The impact of binary interaction on the main-sequence morphology of young star clusters

Dissertation
zur
Erlangung des Doktorgrades (Dr. rer. nat.)
der
Mathematisch-Naturwissenschaftlichen Fakultät
der
Rheinischen Friedrich-Wilhelms-Universität Bonn

vorgelegt von
Chen Wang
aus
Qiqihar, China

Bonn 2021

Angefertigt mit Genehmigung der Mathematisch-Naturwissenschaftlichen Fakultät der Rheinischen Friedrich-Wilhelms-Universität Bonn

1. Gutachter:	Prof. Dr. Norbert Langer
2. Gutachter:	Prof. Dr. Peter Schneider

Tag der Promotion:
Erscheinungsjahr:

Abstract

Star clusters play a vital role in our understanding of stellar physics and evolution, because they are believed to contain stars born at the same time, with the same initial conditions. Therefore, the distribution of the main-sequence (MS) stars of a star cluster in the color-magnitude diagram (CMD) should be characterized by one simple isochrone. However, recent high-precision Hubble Space Telescope (HST) observations found complex MS morphologies in young star clusters, indicating the existence of multiple MS components. Despite more than ten years of effort, the origin of these MS components is still unclear. In this thesis, we reinvestigate this problem by using new state-of-the-art stellar models, considering binary interaction and rotation, both of which are widely accepted to have a significant influence on stellar structure and evolution.

We first explore how binary evolution affects the MS morphology of young star clusters, as most massive stars are proposed to be born with close companions. For this aim, we calculate the evolution of more than 50 000 detailed binary models. To work out the main effects of binary interaction, we assume that the two stellar models composing a binary system are initially rotating synchronized with the orbital motion. We find that binary interaction can reproduce the multiple MS components in young star clusters, including slowly-rotating blue stragglers on the upper left side of the cluster turn-off, which may stem from binary mergers, and near-critically-rotating stars in an extended region on the right side of the cluster turn-off, which our models reproduce as mass gainers of the stable mass transfer.

Our detailed binary models indeed demonstrate that binary evolution greatly impacts the MS morphology of young star clusters. However, binary evolution alone cannot explain all observed MS features, in particular, the double MSs, with the red MS containing the majority of stars and the blue MS containing a minority. There is ample evidence that rotation is responsible for the double MSs, with the fast-rotating stars appearing redder than their slowly-rotating counterparts in the CMD. We find that stellar models with natal rotational velocities of 0-35% of their critical values and 50%-65% of their critical values can explain the observed blue and red MSs, respectively. This bi-modal velocity distribution agrees with the observed velocity distribution of the file A and B type stars.

We propose that the slowly-rotating blue MS stars originate from binary mergers, stimulated by recent finding that binary merger products may rotate slowly and appear younger than other cluster members. In order to explain the number of the observed blue MS stars, we require a high merger rate early during the evolution of the clusters, as predicted by recent binary formation models, and by new cluster observations. Based on our findings, we propose a scenario that can explain all the MS components in young star clusters with coeval stars. We assume that all cluster stars are born with nearly the same rotational velocities (i.e. 50%-65% of their critical velocities), no matter whether they are single stars or in binaries, and populate the red MS. The close binaries merge either during their pre-MS evolution or their early MS evolution, and produce slowly-rotating blue MS stars. The mass gainers in mass transfer systems evolve to near-critically-rotating Be stars. We examine this scenario by computing a large grid of new detailed binary models in which the two components have natal velocities of 55% of their critical values. These models indeed reproduce all observed MS components in the CMD.

However, we find that our models fail to explain the large number of Be stars observed in young star clusters, because many of our binary models lead to mergers during mass transfer, according to our adopted merger criterion. When relaxing the merger criterion, we find that this problem can be alleviated.

Our models predict observational signatures for stars in each MS component. Further observations, especially spectroscopic observations that can obtain rotational rate and binary fraction of the stars in young star clusters, are in high demand to thoroughly test our scenario.

Contents

1 Introduction **1**
1.1 The evolution of single stars 2
  1.1.1 Basic equations 2
  1.1.2 Mixing processes 3
  1.1.3 Wind mass loss and metallicity 5
  1.1.4 A general view of single star evolution 6
1.2 The evolution of rotating stars 6
  1.2.1 Modelling rotating stars 7
  1.2.2 The effect of rotation on stellar structure and evolution 8
  1.2.3 Be stars 8
1.3 The evolution of binary stars 9
  1.3.1 Roche lobe overflow 10
  1.3.2 Stability of mass transfer 13
  1.3.3 A binary evolutionary example 14
1.4 Star clusters 15
  1.4.1 Traditional view of star clusters 16
  1.4.2 Modern view of star clusters 16
1.5 Overview of the chapters in this thesis 19
  1.5.1 Chapter 2: Effects of binary evolution on the main sequence of young star clusters 19
  1.5.2 Chapter 3: Slowly and moderately rotating stars as the constituents of the split main sequences in young star clusters 20
  1.5.3 Chapter 4: Stellar mergers as the origin of the blue main-sequence band in young star clusters 21
  1.5.4 Chapter 5: Upper limit on the fraction of the binary evolution produced Be stars in young star clusters 21

2 Effects of binary evolution on the main sequence of young star clusters **23**
2.1 Introduction 24
2.2 Method and assumptions 24
2.3 Binary-induced main-sequence features 26
2.4 Comparison to single-star models 31
2.5 Comparison to observed star clusters 31
2.6 Concluding remarks 33
2.7 Appendix: Quantitative characterization of the main-sequence features 35
  2.7.1 Appendix A: TBF (Turnoff binary-evolution feature) 35

2.7.2 Appendix B: RBF (Red binary-evolution feature) . . . 35
2.7.3 Appendix C: BBF (Blue binary-evolution feature) . . . 36

3 Slowly and moderately rotating stars as the constituents of the split main sequences in young star clusters 37
3.1 Introduction . . . 38
3.2 Different definitions of the critical rotational velocity . . . 39
3.3 Input physics and assumptions in stellar models . . . 41
3.4 Results and discussions . . . 44
3.4.1 Rotationally-induced color variation . . . 44
3.4.2 Comparison with the main-sequence stars in NGC 1818 in the CMD . . . 45
3.4.3 Implications for the origin of Be stars . . . 49
3.4.4 Comparison with the spectroscopic measurement of the NGC 1818 MS stars 51
3.5 Summary & Conclusions . . . 52
3.6 Appendix . . . 53
3.6.1 Appendix A: Stellar evolutionary examples in the HRD . . . 53
3.6.2 Appendix B: Surface abundance of the star models . . . 55
3.6.3 Appendix C: Degeneracy in rotationally-induced color separation . . . 55
3.6.4 Appendix D: Current surface rotation of the star models and the implications for Be stars . . . 57

4 Stellar mergers as the origin of the blue main-sequence band in young star clusters 61
4.1 Author contributions . . . 61
4.2 Main . . . 62
4.3 Data Availability Statement . . . 70
4.4 Acknowledgments . . . 70
4.5 Supplementary materials . . . 71
4.5.1 A: The main sequence split as a function of stellar rotation . . . 71
4.5.2 B: Distribution of the detailed binary models in the CMD . . . 74
4.5.3 C: Mass functions . . . 79
4.5.4 D: Merger models and merger history . . . 83

5 An upper limit on the fraction of Be stars in young star clusters that are produced by binary evolution 95
5.1 Introduction . . . 96
5.2 Methods . . . 97
5.2.1 Binary fraction and mass ratio distribution . . . 98
5.2.2 Building synthetic star clusters based on merely single star models . . . 100
5.3 Results and comparison with the observations . . . 101
5.3.1 Distribution of the MS stars in the CMD . . . 101
5.3.2 Distribution of the Be star fraction . . . 102
5.4 Summaries and conclusions . . . 105

5.5 Appendix 106
    5.5.1 Appendix A: Binary fraction and mass ratio distribution in NGC 1818, NGC 1755, and NGC 2164 106
    5.5.2 Appendix B: Synthetic clusters resembling NGC 1818, NGC 1755 and NGC 2164 based on merely single star models 106
    5.5.3 Appendix C: Be star fraction in NGC 1818, NGC 1755 and NGC 2164 107

6 Summary and Outlook **117**

A Outcome of the grids of SMC binary models **125**

Bibliography **135**

List of Figures **149**

List of Tables **159**

Acknowledgements **161**

CHAPTER 1

Introduction

Our ancestors started to look into the sky since thousands of years ago, attempting to answer the questions like where we are in the universe; are our earth the center of the universe; and are our earth and sun unique in the universe. In the 4th century BC, two influential Greek philosophers Plato and Aristotle firstly argued that our Earth is the center of the universe, with the sun, moon, and other stars all orbiting around our Earth, which is known as the "geocentric model". Though this model has been superseded, it still reflects our ancestors' intelligence and their interest in the universe. The geocentric model cannot accurately explain the movements of the sun, moon, and planets. Some other theories, including the prototype of the "heliocentric model", were proposed after that. However they were not able to challenge the biblical status of the "geocentric model", not only because the idea that all celestial bodies move around the Earth agrees with people's experiences, but also because it is a religious belief that human is paramount in the universe. "Geocentric model" held sway until the so-called "Copernican Revolution" happened. In 1543, the Renaissance astronomer Nicolaus Copernicus published his mathematical model of a heliocentric system in "De revolutionises erbium coelestium", in which he argued that the Earth and planets revolve around the sun. The "heliocentric theory" dramatically altered people's perspective of the universe. After that, the development of the new theories and inventions, for example, the development of Newton's theory and the invention of the telescope, considerably developed Copernicus's theory. After that, between 1914 and 1919, an American astronomer Harlow Shapley found that the sun is neither the centre of the universe nor the center of our galaxy. Soon after that, another American astronomer Edwin Hubble argued that even our galaxy is not special in the universe. In fact, there are numerous galaxies similar to our galaxy beyond the Milky Way. Now, it has been well understood that the universe is full of stars, galaxies, and other forms of matter and energy. Meanwhile, our universe is not static, but is expanding at an increasing rate since it was created from a big bang (Perlmutter et al., 1999).

In modern astronomy, celestial bodies are studied by applying laws of physics in the experiments on Earth, as Eddinton claimed "what is possible in the Cavendish Laboratory may not be too difficult in the sun". But how do people know that the stars follow the same laws of physics as in the experiments on Earth? In fact, we don't know that in advance. Instead, astronomers firstly study the stars by assuming that the same laws of physics hold, and compare with the observations to see whether the results are sensible. Once the observations contradict the theory, a refinement of the theory is needed. Fortunately, only some refinements into classical physics are required so far, for example, general relativity is proposed to refine Newton's law and has been directly confirmed to be true by the detection of gravitational waves (B. P. Abbott, R. Abbott, T. D. Abbott, Abernathy et al., 2016). In reality, such refinements are believed or have been proposed to hold also in experiments on Earth. It is just that the laboratories on Earth do not have the extreme conditions (for example, extreme temperature and gravity) like our universe, so that we cannot observe some effects, like the bending of a light beam, on Earth. This, in turn, means that the universe provides us with a unique testbed to study physics in extreme conditions.

1.1 The evolution of single stars

In astronomy, a star is a shining, gravitationally self-bound object which is burning nuclear fuel in its center. This definition implies a lower mass limit of $\sim 0.1\,\mathrm{M}_{\odot}$ for an object to be a star, because an object lighter than that cannot start nuclear burning. The upper mass threshold for an object to be a star is controversial, but is usually believed to be $\sim 100\,\mathrm{M}_{\odot}$, above which intense radiation pressure can destroy the object. Stars are the fundamental elements of the galaxies and universe. Therefore, it is vital to understand stars, including their formation, their size, their mass, and there evolution in time. A star's life is a constant struggle against the force of gravity. Therefore, a star's evolution and its final fate are primarily determined by its initial mass (Heger, Fryer et al., 2003; Langer, 2012). An interesting thing in stellar astronomy is that people have achieved a deep understanding of stars' evolution before knowing how they were formed. This is because once a star forms, it settles into the so-called hydrostatic and thermal equilibrium, and keeps no memory of its forming past. Hydrostatic equilibrium means that there is a balance among all the forces exerting on a gas element inside the star. While thermal equilibrium is a stationary state that the nuclear burning rate in the stellar center equals the energy radiation rate at the stellar surface.

1.1.1 Basic equations

A star is usually assumed to be spherical symmetry, such that its physical properties only depend on the radial coordinate, making it possible for us to study 3D stars with 1D models. It is a reasonable assumption as long as the star is not rotating too fast. One can either use the radius of a spherical shell r ($\in 0 \dots R$) to describe stellar physical quantities, known as the Eulerian coordinate system, or use the mass encompassed in a spherical shell m ($\in 0 \dots M$) to describe stellar physical quantities, known as the Lagrangian coordinate system. The Lagrangian coordinate system is more commonly used when building star models because the mass of a star remains almost constant during its evolution if its wind is negligible. In contrast, a star's radius can change dramatically during its entire evolution.

In the case of both hydrostatic and thermal equilibrium, a star's structure can be described by four basic equations. In the Lagrangian coordinate, they are expressed as the following:

$$\frac{dr}{dm} = \frac{1}{4\pi r^2 \rho}, \tag{1.1}$$

where dr represents the thickness of a spherical shell with mass dm at radius r, and ρ is the local density at radius r. The second equation is

$$\frac{dP}{dm} = -\frac{Gm}{4\pi r^4}, \tag{1.2}$$

where dP is the pressure difference between the upper and lower layers of a spherical shell with mass dm at radius r, m is the mass encompassed in the sphere with radius r. The third equation is

$$\frac{dl}{dm} = \epsilon_{\rm nuc} - \epsilon_{\nu}, \tag{1.3}$$

where the left term is the luminosity difference between the upper and lower layers of a spherical shell with mass dm at radius r. $\epsilon_{\rm nuc}$ and ϵ_{ν} indicate the energy produced by nuclear burning and the energy taken away by neutrinos per unit mass per second. The last equation is

$$\frac{dT}{dm} = -\frac{Gm}{4\pi r^4}\frac{T}{P}\nabla \qquad \text{with} \qquad \nabla = \begin{cases} \nabla_{\rm rad} = \frac{3\kappa}{16\pi acG}\frac{lP}{mT^4} & \text{if} \quad \nabla_{\rm rad} \leq \nabla_{\rm ad} \\ \nabla_{\rm rad} = \Delta\nabla & \text{if} \quad \nabla_{\rm rad} > \nabla_{\rm ad} \end{cases} \tag{1.4}$$

where the left term is the temperature gradient. T, P and l are the local temperature, pressure and luminosity at radius r. κ is opacity and a is the radiation constant. The term $\Delta\nabla = \nabla - \nabla_{\rm ad}$ means the difference between the real temperature gradient and the adiabatic temperature gradient.

Equations 1.1 and 1.2 represent the principles of mass conservation and momentum conservation, respectively. They determine the structure of a star in hydrostatic equilibrium. Equation 1.3 is the principle of energy conservation that energy radiates from the stellar surface at a rate equal to the net energy generation rate in the stellar center. Equation 1.4 describes the temperature gradient required to transport luminosity l by radiation or by convection. Equations 1.3 and 1.4 determine the structure of a star in thermal equilibrium. One can construct a star model with these equations by considering the specification of boundary conditions and initial conditions.

1.1.2 Mixing processes

One of the most important physical processes that affects stellar structure and evolution is internal mixing, including convection, overshooting and semiconvection. These mixing processes influence the property of a star by transporting material, energy, and angular momentum. However, a detailed theory of mixing is still missing. To solve this problem, people usually treat mixing as a diffusive process and adopt the "mixing length theory" to compute the heat and angular momentum transferred in the mixing regions when building 1D star models. In this section, we briefly discuss these mixing processes.

Convection

Convection describes bulk motions of gas inside a star. Assuming that a small perturbation moves a mass element upwards by a small distance, the perturbation grows if the density of the mass element is smaller than its surroundings as a consequence of a net upward buoyancy force, which will eventually result in an unstable situation that causes convection. In contrast, the perturbation will be quenched and the mass element will stay in a stable situation if the density of the mass element is larger than its surroundings. In this case, convection does not happen. According to this principle, the condition for convection to occur is given by the following criteria, based on whether the layers are chemically homogeneous (Schwarzschild criterion) or have a chemical gradient (Ledoux criterion):

$$\nabla_{\rm rad} \geq \nabla_{\rm ad} \qquad \text{(Schwarzschild criterion)}, \tag{1.5}$$

and

$$\nabla_{\mathrm{rad}} \geq \nabla_{\mathrm{ad}} + \nabla_{\mu} \quad \text{(Ledoux criterion)}. \tag{1.6}$$

Here ∇_{rad} is the dimensionless radiative temperature gradient (see Eq. 1.4). $\nabla_{\mathrm{ad}} = (\mathrm{d}\log T/\mathrm{d}\log P)_{\mathrm{ad}}$ (here P is used to measure the stellar depth) indicates the adiabatic temperature gradient, which equals 0.4 in ideal gas and 0.25 in radiation-dominated gas. $\nabla_{\mu} = \mathrm{d}\log\mu/\mathrm{d}\log P$ in the Ledoux criterion depicts the mean molecular weight gradient, again using P to measure the stellar depth.

It can be seen in Equation 1.4 that ∇_{rad} describes the temperature gradient required to transport luminosity l with merely radiation. The larger the luminosity needed to be transported, the larger the temperature gradient is required. According to Eqs 1.4 and 1.5, if this required temperature gradient is larger than an upper limit (∇_{ad} in the case of Schwarzschild criterion and $\nabla_{\mathrm{ad}} + \nabla_{\mu}$ in the case of Ledoux criterion), convection will happen and take over the task of energy transport. The combination of Eqs 1.4 and 1.5 implies that convection is prone to happen in layers with a large value of κ (e.g. low-mass star's cool envelope), a large value of l/m (e.g. massive star's hot center), and a small value of ∇_{ad} (e.g. partial ionized stellar surface).

Convection transports energy from the inner layer to the outer layer, because hot bubbles move up, transporting their heat to their surroundings, while cool bubbles move down, absorbing heat from their surroundings until these bubbles are dissolved. The so-called mixing length theory is used to compute the energy transported by convection (Böhm-Vitense, 1958). In this theory, blobs of gas are assumed to travel over a radial distance l_{m} before they dissolve and transport energy to their surroundings. By comparing detailed models with the observations, a mixing length parameter $\alpha_{\mathrm{m}} = l_{\mathrm{m}}/H_{\mathrm{P}}$ of 1.5 – 2 is proposed, where H_{P} is the local pressure scale height. Convection is super efficient at transporting energy, such that a tiny difference between the real temperature gradient and the adiabatic gradient is adequate to transport a large luminosity, implying that the real temperature gradient is almost identical to the adiabatic gradient in convective regions.

Apart from energy, convection also transports material in stellar interiors. In massive stars, convection happens in stellar center, bringing fresh hydrogen fuel to the stellar center, thereby extending its main-sequence (MS) lifetime. While in low-mass stars or giant stars, convection happens in stellar envelops, which may change the stars' surface chemical composition abundance by brining nuclear burning products in stellar center to stellar surface, known as the "dredge-up" process.

Overshooting

The convective eddies cannot stop their upward motion at the boundary between the stable and unstable layers against convection, because they have non-vanishing velocities, though they have zero acceleration. Overshooting describes such an extra upward motion of the convective eddies. Overshooting is usually implemented in star models by increasing the convective region by a certain amount (e.g. Stothers and Chin, 1985). The radial distance of this extended region is expressed as $\alpha_{\mathrm{OV}} H_P$, where α_{OV} and H_P are overshooting parameter and the local pressure scale height, respectively. α_{OV} can be constrained by comparing the widths of the observed MS stars and of the star models, because a larger α_{OV} results in a larger convective core of a star which further means a longer MS lifetime and a larger MS width (Stothers and Chin, 1985; Mermilliod and Maeder, 1986; Maeder and Meynet, 1987; Ekström et al., 2008). Brott et al. (2011) obtained a value of $\alpha_{\mathrm{OV}} = 0.335$ for the $16\,\mathrm{M}_{\odot}$ stars by using the sudden transition in the observed $v \sin i$ and $\log g$ plane as the end of the MS. Claret and Torres (2016) used double-lined eclipsing binaries and found a positive relation between α_{OV} and mass. Convective overshooting can vary stars' evolution significantly by increasing the convective core. Accurate calibration on the overshooting parameter is in high demand.

Semiconvection

Semiconvection is a process happened in stellar layers that would be dynamically unstable according to the Schwarzschild criterion, but is stabilized by a composition gradient (∇_{μ} in Eq. 1.6) on top of the convective core, i.e., is stable according to the Ledoux criterion. An over-stable oscillation happens in semiconvective layers on a thermal timescale, mixing the material and smoothing the composition gradient. Similar to overshooting, semiconvection has been studied since a long time ago (Schwarzschild and Härm, 1958; Chiosi and Summa, 1970; Langer, El Eid and K. J. Fricke, 1985), but its strength is still unknown.

Semiconvection mainly affects a star's post-MS evolution when a chemical composition gradient has been established outside the convective core. Schootemeijer, Langer et al. (2019) found that semiconvection has a profound influence on the formation of blue supergiants (BSGs). Large semiconvection mixing efficiency is prone to produce BSGs. In order to match the ratio between BSGs and red supergiants (RSG) in single star models with the observations, a semiconvection efficiency of $\alpha_{\mathrm{SC}} > 10$ is required (Schootemeijer, Langer et al., 2019). Semiconvection may also affect the flavor of the Wolf-Rayet stars and their subsequent supernova explosions. Efficient semiconvection mixing leads to a larger CO core of a star, which facilitates the formation of the WC/WO type Wolf-Rayet stars. After the Wolf-Rayet phase, if the entire CO core of a star is exposed, a type Ic supernova explosion is expected.

1.1.3 Wind mass loss and metallicity

Hot and luminous massive stars suffer strong stellar winds, taking away their mass and angular momentum, thereby affecting their evolution and final fates. The wind is radiation-driven as it is radiation that accelerates ions. A photon can be absorbed by an atom if the photon energy equals a certain energy level of the atom, during which an electron is lifted to a higher energy level. Then the electron will fall back to its original energy level, emitting a photon in a random direction. During this process, energy and momentum contained in the photon are converted to the ion. Since the direction of the radiation pressure is outward, the ion receives an outward motion. The strength of the wind depends on the strength of radiation (i.e. wind mass loss is more intense in more massive stars) and the abundance of available ions (i.e. wind mass loss is metallicity dependent). Even though hydrogen and helium are the most abundant elements in stellar interiors, they have few available energy levels. In contrast, iron groups contain many thousands of transitions, which allows them to absorb photons of various frequencies. Consequently, iron plays the dominant role in the strength of stellar wind. The stars in high-metallicity environments have stronger winds.

Stellar winds affect the luminosity, effective temperature, lifetime, core mass and evolutionary fate of stars. In general, a stronger stellar wind takes away more mass, eroding to the deeper layer of a star, and thus results in a lower luminosity, higher temperature and a smaller core of the star. The intense stellar wind in massive stars with high metallicity can expel their entire H and even He envelopes, and produce type Ib/Ic supernovae or light black holes. Whereas stars with lower masses in low metallicity environments can retain a fraction of H envelopes and explode as type II supernovae. Stellar wind also affects stars' rotational rate. Massive stars with high metallicity can be spun down significantly due to the intense stellar wind.

Even though the existence and importance of stellar wind have been widely accepted, the strength of stellar wind remains one of the least well-understood problems in astrophysics. In star models, the empirical prescriptions that can fit the observations are adopted. These prescriptions are precarious, yet play a vital role in determining the evolution and outcome of star models.

Metallicity also influences stars' evolution by affecting their opacity. The envelope opacity of a low-metallicity star is small, such that photons can radiate away more easily, resulting in a larger luminosity of the star compared to a high-metallicity star with the same mass. In order to remain thermal equilibrium, a low-metallicity star has to contract more to compensate for the larger radiated energy, therefore, it has a smaller radius and higher effective temperature than its high-metallicity counterpart.

1.1.4 A general view of single star evolution

A star's evolutionary history is a competition history between gravity force and pressure. At first, the ideal gas and radiation pressure resist the gravity force, and later on, the degenerate electrons and neutrons supply the pressure needed to balance the gravity force when a star becomes a compact object. A star cannot stay in its original stage permanently, instead, it has to evolve because it is radiating energy outward. As to a protostar, gravitational energy is used to compensate for the radiated energy, so a protostar contracts as a whole. During this overall contraction, the center temperature of the protostar increases, which can be understood by the virial theorem, and eventually reaches the H burning temperature. Then nuclear-burning energy takes over the task of compensating for the energy lost at the stellar surface. At this point, the overall contraction stops and the star begins its nuclear timescale evolution. When H is depleted in the core, the He core starts to contract due to the lack of nuclear-burning energy. Meanwhile, the H envelope expands, which can be understood by the mirror principle. As soon as the center temperature is hot enough for He ignition, the He core contraction stops. After He exhaustion, the core resumes a contraction until the center temperature is hot enough to burn the next fuel. Stars with core masses lower than the Chadarasika mass can never reach a temperature high enough to burn C in the center. Instead, they evolve to degenerate CO white dwarfs. Stars with massive cores can repeat such cycles of nuclear burning and contraction until they develop an iron core in the center. No further burnings can happen because iron has the largest binding energy per nucleon. Such massive stars will die as neutron stars through supernova explosions or die as black holes through direct collapse.

1.2 The evolution of rotating stars

The discovery of solar rotation can be traced to 1978 (Tassoul, 1978). However the theory of stellar rotation developed slowly after that, because rotation was usually treated as a second-order effect in stellar structure and evolution. On the one hand, rotational energy is generally only a tiny fraction of gravitational energy. On the other hand, according to "Occam's Razor", a theory explaining the observations with the smallest number of hypotheses is optimal. However, a number of discrepancies between stellar models and observations reveal that the role of stellar rotation is overwhelmingly overlooked (see Maeder and Meynet, 2000, and references therein). For example, the peculiar helium and nitrogen abundances found in massive O- and B-type stars and the peculiar distribution of stars in the Hertzsprung-Russell diagram (HRD).

When building star models, people always assume them to be spherical symmetry. In general, it is a good approximation. However, this assumption is inapplicable in rapidly-rotating stars, as the centrifugal force makes the stars oblate, with the equatorial radius larger than the polar radius. From another point of view, rotation can trigger instabilities in stellar interiors, which further affect the structure and evolution of rapidly-rotating stars. These instabilities include the dynamical and secular shear instability in the case of differential rotation (Maeder and Meynet, 1996), the Solberg-Høiland instability (Wasiutynski, 1946), the Eddington-Sweet circulation, which describes the large-scale meridional circulation in rotating-stars (Eddington, 1925), and Goldreich-Schubert-Fricke instability against axisymmetric perturbations (Goldreich and Schubert, 1967; K. Fricke, 1968). These instabilities induce material and angular momentum mixing in stellar interiors. When taking into account magnetic fields, angular momentum can be transported due to the Tayler-Spruit dynamo, which makes a star rotate nearly as a solid body (Spruit, 2002). In star models, people always assume rotational mixing to happen via diffusion and use parameters to characterize the mixing efficiency (Endal and Sofia, 1978; Heger, Langer and Woosley, 2000).

1.2.1 Modelling rotating stars

The real structure of a rotating star is 3D as it deviates from spherical symmetry. In this section, we briefly describe the implementation of rotation in 1D star evolution codes, using MESA, one of the most prevalent stellar evolution code, as an example (Paxton, Cantiello et al., 2013; Paxton, Smolec et al., 2019). The basic idea is to redefine the radial coordinate, such that the basic form of the stellar equations remains the same as in non-rotating stars. Rotating stars are barotropic when reaching hydrostatic equilibrium, i.e. pressure is constant on equipotential. When building star models, people use the so-called shellular rotation law, in which Ω is constant on isobars as a consequence of strong horizontal turbulence. In the framework of shellular rotation, the radius of the isobars are used as the radial coordinate to describe the property of the rotating stars.

To retain the form of the stellar structure equations described in Chapter. 1.1.1 in a rotating star, two factors f_P and f_T are introduced to correct the pressure and temperature, respectively. Equation 1.2 becomes:

$$\frac{\mathrm{d}P}{\mathrm{d}m} = \frac{-Gm}{4\pi r_P^4} f_P, \tag{1.7}$$

where

$$f_P = \frac{4\pi r_P^4}{GmS_P} \frac{1}{< g_{\mathrm{eff}}^{-1} >}. \tag{1.8}$$

Here S_P is the total surface of the isobar and $< g_{\mathrm{eff}}^{-1} >$ is the average of the inverse of surface effective gravity over the equipotential. While the term of ∇_{rad} in Eq. 1.4 becomes:

$$\nabla_{\mathrm{rad}} = \frac{3\kappa}{16\pi acG} \frac{P}{T^4} \frac{l}{m} \frac{f_T}{f_P}, \tag{1.9}$$

where

$$f_T = \frac{4\pi r_P^2}{GmS_P} (< g_{\mathrm{eff}} >< g_{\mathrm{eff}}^{-1} >)^{-1}. \tag{1.10}$$

1.2.2 The effect of rotation on stellar structure and evolution

Rotation has mainly two effects. The first one is that the centrifugal force can reduce a star's effective gravity and luminosity. According to Von Zeipel's theorem that the local temperature of a rotating star is proportional to the effective gravity to the power of one forth (von Zeipel, 1924), the effective temperature of a rotating star is lower than that of a non-rotating star with the same mass. The strength of the centrifugal force is latitude dependent, resulting in the fact that an equator-on star appears cooler and fainter than a pole-on star, which is known as the gravity darkening.

The second effect is that rotation can induce strong mixing in stellar interiors. Rotationally-induced mixing brings fresh nuclear burning fuel to the stellar center, thereby increasing the core size and the MS lifetime of a rotating star. Rotational mixing can also bring central nuclear burning products to the stellar surface, thereby affecting the surface chemical composition abundance and effective temperature of a rotating star. Extremely fast rotating massive stars can even be fully mixed and suffer the so-called chemically homogeneously evolution, during which they remain compact, blue, and luminous (Maeder, 1987; Yoon and Langer, 2005; Marchant, Langer, Podsiadlowski, Tauris and Moriya, 2016). Chemically homogeneously evolution occurs more easily in lower metallicity environments due to the weak stellar wind (Yoon, Langer and Norman, 2006; Brott et al., 2011; Langer, 2012). Rotation also affects a star's post-MS evolution. Generally speaking, a rotating star has a larger He core mass. Therefore, the initial mass for a star to evolve to a Wolf-Rayet star is lower in the presence of rotation. Nevertheless, the impact of rotational mixing in post-MS stars is not as important as in MS stars, because the timescale of the post-MS evolution is usually shorter than the timescale of rotational mixing.

A comparison between the evolution of $5\,\mathrm{M}_\odot$ rotating stars with different velocities and the corresponding non-rotating star is shown in Figure 3.5.

1.2.3 Be stars

Be stars are a set of B-type stars observed with emission lines, which are believed to be associated with circumstellar discs caused by extremely fast rotation. Yet, the rotation threshold for a star to manifest as a Be star is still unclear. Several Be stars have been confirmed to rotate at velocities larger than 90% of their critical values (Domiciano de Souza, Kervella et al., 2003; Carciofi et al., 2008; Domiciano de Souza, Hadjara et al., 2012). Chauville et al. (2001) found that the mean velocity of the Be stars is 75% of their critical velocities from statistical studies of the observations, while W. Huang, Gies and McSwain (2010) found the threshold can be as low as 60% of critical velocities. From another point of view, Ekström et al. (2008) investigated the single star models and proposed that a threshold of 70% of critical velocity is demanded to match the observations.

Be stars can form in either single stars or binaries. Single stars gradually increase their fractional critical velocities across the MS evolution and may finally reach near-critical rotation (Sackmann and Anand, 1970; Ekström et al., 2008; Hastings, C. Wang and Langer, 2020). This is because during the MS evolution, the critical velocity of a star decreases due to its radius expansion, while the equatorial velocity of the star remains almost the same. Whether a star can reach critical rotation at the end of its MS evolution depends on its initial velocity, stellar wind and angular momentum transport. Less massive stars in low-metallicity environments are prone to get higher fractional critical velocities at the end of their MSs, because of the less intense stellar wind. Meanwhile, the stars with rigid rotation are also prone to reach higher rotational rates than the stars with differential rotation, because angular momentum can be transported more efficiently from the stellar center to the stellar surface in rigidly rotating stars.

Be stars can also form in binary systems via accretion. The most compelling evidence for the binary scenario is the discovery of Be/X-ray binaries that contains a Be star and a compact object (Liu, van Paradijs and van den Heuvel, 2006; Langer, 2012; Raguzova and Popov, 2005). The spin-up of the accretor is indeed predicted in detailed binary models (Wellstein, Langer and Braun, 2001; Langer, Wellstein and Petrovic, 2003; Petrovic, Langer and van der Hucht, 2005; Cantiello, Yoon et al., 2007; S. E. de Mink, Cantiello et al., 2009). The accretor in a binary system can reach near critical rotation by accreting small amounts of material (Packet, 1981). Whether the accretor can retain this critical rotation depends on whether the separation between the two stars is wide enough to avoid tidal spin down. Therefore, accretors in wide binaries tend to form critically-rotating Be stars. Meanwhile, the accretor is more difficult to reach critical rotation during Roche lobe overflow if the separation of the two stars is too small, because in this case accretion may happen in a ballistic way, in which less specific angular momentum is transported compared to an accretion via Keplerian disc.

However, whether binary alone can explain all the observed Be stars or whether the single channel is indispensable is still controversial. Based on different assumptions on mass transfer efficiency, either all (Shao and X.-D. Li, 2014), half (Pols et al., 1991) or only a small fraction (van Bever and Vanbeveren, 1997) of galactic Be stars can be explained by binaries. Hastings, Langer et al. (2021) used an analytical way to calculate a stringent upper fraction limit of the binary produced Be stars in young star clusters. They found that binary interaction can account for at most about one third of the Be stars near the turn-off, which roughly agrees with the observations (Milone, Marino, Di Criscienzo et al., 2018). Except for these theoretical studies, J. Bodensteiner, Shenar and Sana (2020) examined the binarity of around 300 Galactic Be stars and found no evidence of the Be binaries with MS companions. It indicates that the single star channel cannot play a significant role in producing Be stars, otherwise the Be binaries with MS companions should be detected due to the fact that the majority of stars are indeed in binaries.

1.3 The evolution of binary stars

A binary is a system of two stars, revolving around their common barycenter. The observation of binary systems started in the 17th century, since the invention of the telescope. Recently, Sana, S. E. de Mink et al. (2012) found that more than 70% of the Galactic massive O stars have companions close enough to interact during their lives. There are plenty of phenomena and objects believed to be related to binary interaction. For example, Algo systems, in which the more evolved star is less massive than the less evolved star, are explained by mass transfer through Roche lobe overflow. The blue stragglers that appear younger than other MS stars in star clusters are proposed to be the merger products of two MS stars (Schneider, Podsiadlowski et al., 2016; C. Wang et al., 2020). There are also cataclysmic variables and X-ray binaries containing a compact object (a white dwarf, neutron star or black hole) and a companion star. In these systems, the gravitational potential energy is converted to radiation, which makes them bright in X-ray and ultraviolet band. Binary is also proposed to be responsible for the formation of the millisecond pulsars. Besides, binary plays an important role in the formation of type Ib/Ic supernovae (Yoon, Woosley and Langer, 2010). In 2015, gravitational waves from the merger of two black holes was detected (B. P. Abbott, R. Abbott, T. D. Abbott, Abernathy et al., 2016). This is a landmark discovery which opens the new era of gravitational wave astronomy. After that, more and more gravitational waves from mergers of two black holes, a black hole and a neutron star and two neutron stars (B. P. Abbott, R. Abbott, T. D. Abbott, Acernese, Ackley, C. Adams, T. Adams, Addesso, Adhikari, Adya, Affeldt, Afrough, Agarwal, Agathos, Agatsuma, Aggarwal, Aguiar, Aiello, Ain, Ajith, B. Allen, G. Allen, Allocca, Altin, Amato, Ananyeva, S. B. Anderson, W. G. Anderson, Angelova et al., 2017; B. P. Abbott et al., 2019; R. Abbott et al., 2021a; R. Abbott et al., 2021b) have been reported. These double compact object systems are binary evolutionary descendants. It is, therefore, crucial to study the evolution of binary stars.

1.3.1 Roche lobe overflow

The two stars in a binary system exchange mass and angular momentum via the so-called Roche lobe overflow. It was Edouard Roche who first studied such close binary interaction. Roche lobe overflow happens when one star in a binary system reaches the L1 point (see Fig. 1.1 for the Roche potential of a binary system), as a consequence of either radius expansion or orbit shrinking. The Roche lobe radius, the radius of a sphere that contains the same volume as the Roche lobe, of the primary star is expressed by an approximate analytic formula (Eggleton, 1983):

$$\frac{R_{L,1}}{a} = \frac{0.49q^{2/3}}{0.6q^{2/3} + \ln(1 + q^{1/3})}. \tag{1.11}$$

Here a is the separation of the two stars, $q = m_1/m_2$ is the mass ratio between the primary star and the secondary star. The Roche lobe radius of the secondary star can be obtained by replacing q with q^{-1}.

There are three types of mass transfer based on when the donor star fills its Roche lobe.

- Case A mass transfer: the mass transfer that happens when the donor star is burning hydrogen. There are two subphases in Case A mass transfer, with an initial fast Case A mass transfer happening in a thermal timescale during which the mass ratio of the system is conversed, followed by a subsequent slow Case A mass transfer happening in a nuclear timescale.
- Case B mass transfer: the mass transfer that happens when the donor star has exhausted hydrogen in the stellar center but has not ignite helium. A donor star typically loses nearly all its H envelope in a stable Case B mass transfer.
- Case C mass transfer: the mass transfer that happens when the donor star has finished helium burning in the stellar center. Case C mass transfer is prone to happen in an unstably way compared to Case A and Case B mass transfer because a donor star in Case C mass transfer usually has a deep convective envelope which makes it expand quickly in response to the mass loss.

Figure 1.2 depicts the radius evolution of a 5 $\mathrm{M}_\odot$ star. The above mentioned three mass transfer phases are indicated.

Even though people have understood well that mass transfer occurs in close binary systems, the mass transfer efficiency which describes how much mass transferred from the donor star can be accreted by the accretor still remains one of the unsolved key questions. In most previous studies, people usually assume that a fixed fraction β of the transferred mass ends up in the mass gainer (De Greve and De Loore, 1992; Chen and Han, 2002). Nevertheless, there is a more physically reasonable way to determine the mass transfer efficiency, that is whenever the mass gainer reaches critical rotation,

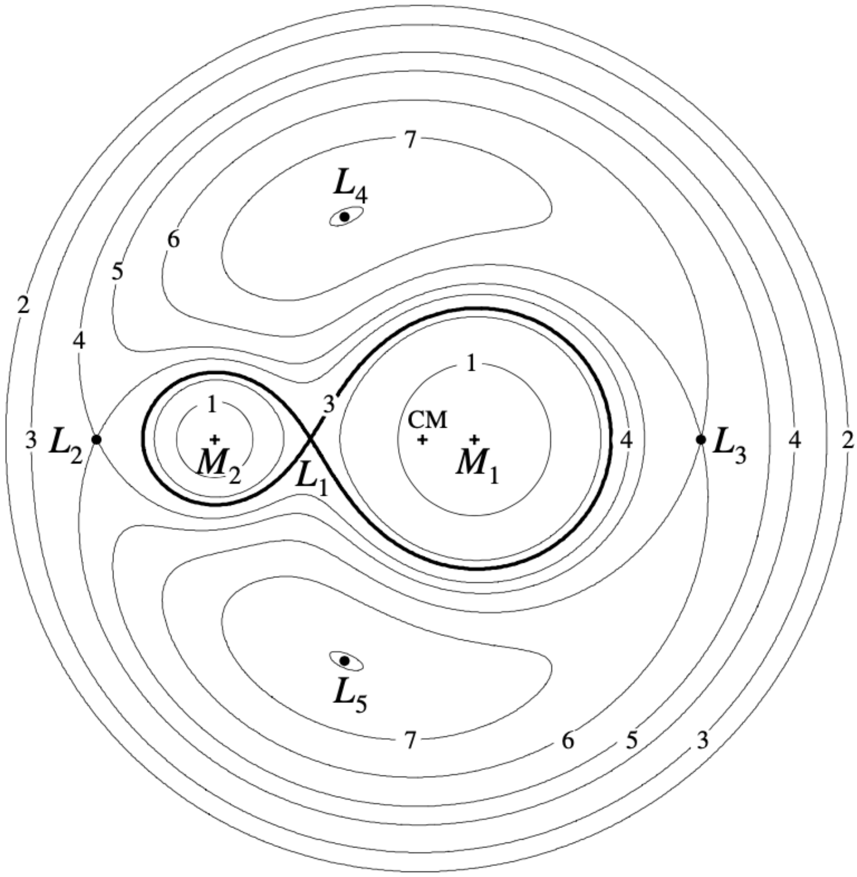

Figure 1.1: The orbital plane of the Roche equipotential for binary systems with a mass ratio of 0.25. M_1 and M_2 are the mass of the two stars, while CM is the center mass of the system. L_1 to L_5 are the Lagrange points. The inner Lagrange point L1 is the place where mass flows from one star to another. Credit: Frank, King and Raine (2002).

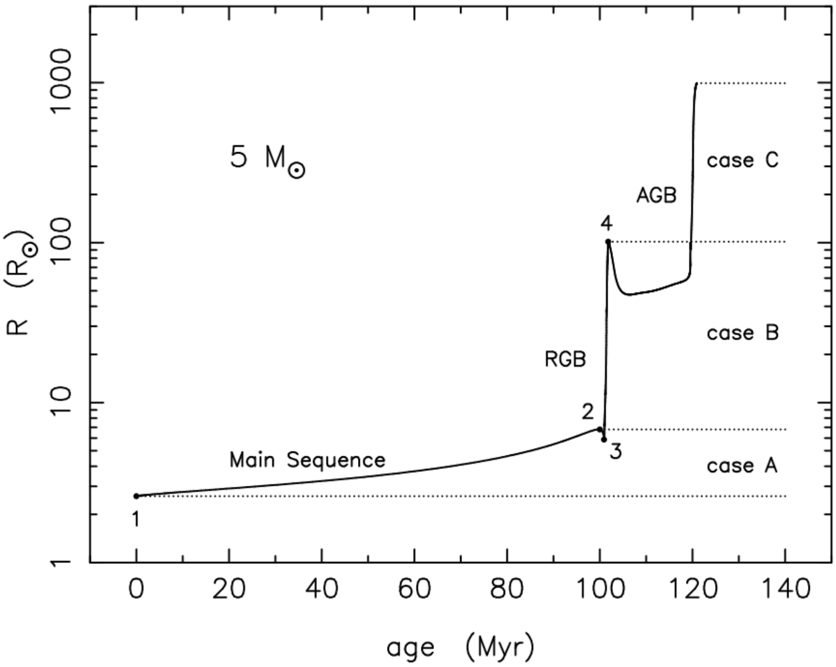

Figure 1.2: Radius evolution as a function of time of a 5 M$_\odot$ star. The evolutionary phases and different types of mass transfer are indicated in the figure. Credit: Tauris and van den Heuvel (2006).

a further accretion is inhibited (Wellstein, Langer and Braun, 2001; Langer, Wellstein and Petrovic, 2003; Marchant, Langer, Podsiadlowski, Tauris, S. de Mink et al., 2017). Based on this assumption, mass transfer efficiency is usually higher in Case A mass transfer than in Case B and Case C mass transfer, because Case A mass transfer happens in a binary system whose separation is small enough for tides to spin down the accretor. C. Wang et al. (2020) found that Case B mass transfer is highly non-conservative and usually results in critically-rotating stars. Nevertheless, some studies proposed that a star may keep on accreting mass when it has reached critical rotation by transporting angular momentum outwards via discs (Popham and Narayan, 1991; Paczynski, 1991). To what extent a star can keep on accretion depends on viscosity.

Binary period changes during mass transfer due to the redistribution of angular momentum. In conservative mass transfer, if mass is transferred from the more massive star to the less massive star, the orbit will shrink, while if mass is transferred from the less massive star to the more massive star, the orbit will expand. This conclusion can be explained by the following equations. The orbital angular momentum J of a binary system is expressed as:

$$J = (M_1 a_1^2 + M_2 a_2^2)\,\omega, \tag{1.12}$$

where $a_1 = (\frac{M_2}{M_1+M_2})a$, $a_2 = (\frac{M_1}{M_1+M_2})a$ are the distances of the two stars from their braycenter, and $\omega = 2\pi/P$ is the binary's angular velocity. Substituting for a_1 and a_2 gives:

$$J = \frac{M_1 M_2}{M_1 + M_2}\omega a^2 = M_1 M_2 (\frac{Ga}{M_1 + M_2})^{(1/2)}. \tag{1.13}$$

Then the following expression is obtained by logarithmically differentiating Eq. 1.13:

$$\frac{\dot{a}}{a} = \frac{2\dot{J}}{J} + \frac{2(-\dot{M}_2)}{M_2}(1 - \frac{M_2}{M_1}). \tag{1.14}$$

In the case of conservative mass transfer, the total mass and angular momentum remain unchanged (i.e. $\dot{M}_1 + \dot{M}_2 = 0$, $\dot{J} = 0$). When treating the secondary star as the donor star, i.e. $\dot{M}_2 < 0$, one obtains the above mentioned conclusion that if $m_2 < m_1$, $\dot{a} > 0$, meaning that the orbit expands, while if $m_1 > m_2$, $\dot{a} < 0$, meaning that the orbit shrinks. Any processes that cause a non-conservative mass transfer ($\dot{J} < 0$) will accelerate the shrinking of the orbit.

1.3.2 Stability of mass transfer

Whether a mass transfer occurs in a stable way or not depends on whether the donor star can just stay within its Roche lobe. Therefore, one needs to compare the change of the donor radius and the change of the Roche lobe radius in response to mass transfer, which are expressed as (see Ivanova, 2014, for more detail):

$$\zeta_{\rm donor} = \frac{{\rm dlog}R_{\rm donor}}{{\rm dlog}M_{\rm donor}}, \quad \zeta_{\rm L} = \frac{{\rm dlog}R_{\rm L}}{{\rm dlog}M_{\rm donor}}. \tag{1.15}$$

Stable mass transfer occurs if $\zeta_{\rm L} \leq \zeta_{\rm donor}$. In the case of conservative mass transfer, $\zeta_{\rm L}$ is expressed as:

$$\zeta_{\rm L} = 2.13q - 1.67, \tag{1.16}$$

where q is the mass ratio between the mass donor and the mass gainer. An unstable mass transfer will happen if the mass ratio is larger than the critical value:

$$q > q_{\rm crit} = \frac{\zeta_{\rm donor}}{2.13} + 0.788. \tag{1.17}$$

The value of $\zeta_{\rm donor}$ depends on whether the donor star is trying to rebuild its hydrostatic equilibrium or thermal equilibrium as both equilibria are disturbed during mass transfer. For the hydrostatic readjustment, the donor's response to mass loss is almost adiabatic and we have:

$$\zeta_{\rm donor} = \zeta_{\rm ad} = (\frac{{\rm dlog}R_{\rm donor}}{{\rm dlog}M_{\rm donor}})_{\rm ad}. \tag{1.18}$$

Whereas for the thermal readjustment, one can define a thermal equilibrium mass-radius exponent:

$$\zeta_{\rm donor} = \zeta_{\rm eq} = (\frac{{\rm dlog}R_{\rm donor}}{{\rm dlog}M_{\rm donor}})_{\rm eq}. \tag{1.19}$$

If $\zeta_{\rm eq} < \zeta_{\rm L} \leq \zeta_{\rm ad}$, mass transfer will happen in thermal timescale. The donor star is out of thermal equilibrium in such a mass transfer case. It is the thermal readjustment that makes the star's radius just fill its Roche lobe. While if $\zeta_{\rm L} \leq \min(\zeta_{\rm eq}, \zeta_{\rm ad})$, mass transfer will happen in a longer timescale. The donor star can remain both hydrostatic and thermal equilibrium. In such a case, it is the nuclear burning induced radius expansion that makes the donor star fill in its Roche lobe. In general, a radiative envelope changes marginally in response to mass loss, therefore, mass transfer happened in donor stars with a deep radiative envelope tends to be stable. In contrast, a star with a deep convective envelope expands rapidly in response to mass loss, usually resulting in an unstable mass transfer.

1.3.3 A binary evolutionary example

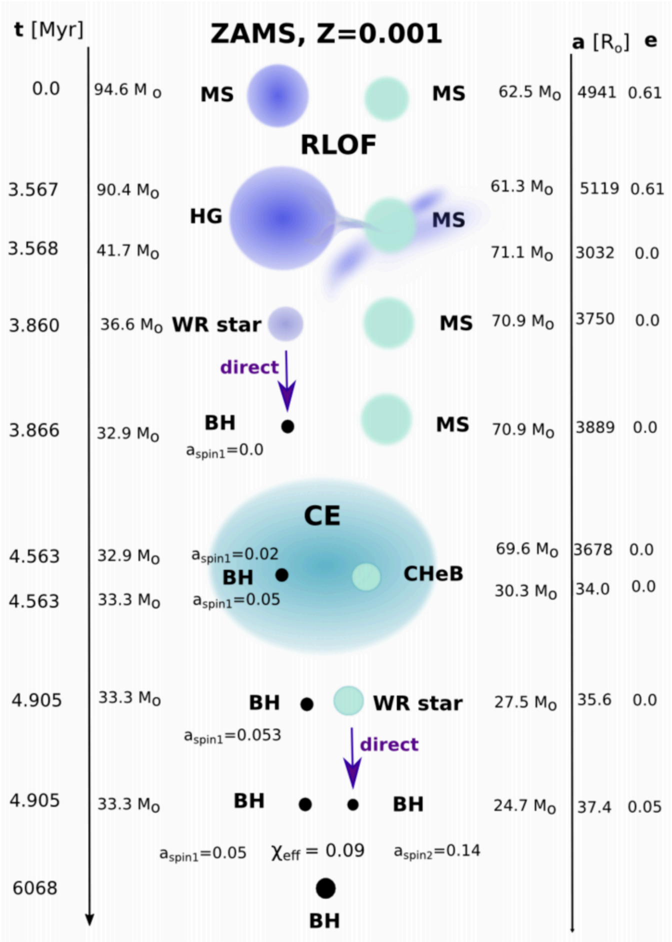
t [Myr]
ZAMS, Z=0.001
a [R$_\odot$] e
0.0
94.6 Mo
MS
MS
62.5 Mo
4941 0.61
RLOF
3.567
90.4 Mo
61.3 Mo
5119 0.61
HG
MS
3.568
41.7 Mo
71.1 Mo
3032 0.0
3.860
36.6 Mo
WR star
MS
70.9 Mo
3750 0.0
direct
3.866
32.9 Mo
BH
MS
70.9 Mo
3889 0.0
a$_{spin1}$=0.0
CE
4.563
32.9 Mo
a$_{spin1}$=0.02
69.6 Mo
3678 0.0
BH
CHeB
4.563
33.3 Mo
a$_{spin1}$=0.05
30.3 Mo
34.0 0.0
4.905
33.3 Mo
BH
WR star
27.5 Mo
35.6 0.0
a$_{spin1}$=0.053
direct
4.905
33.3 Mo
BH
BH
24.7 Mo
37.4 0.05
a$_{spin1}$=0.05
χ$_{eff}$ = 0.09
a$_{spin2}$=0.14
6068
BH

Figure 1.3: A binary evolution example with the StarTrack population synthesis code from the zero-age main sequence (ZAMS) to the merger of the two black holes. The evolution started with two massive stars with masses of $94.6\,\mathrm{M}_\odot$ and $62.5\,\mathrm{M}_\odot$, in a separation of 4941 solar radii. The initial eccentricity is 0.61. In this figure, MS, HG, WR star, BH mean main-sequence, Hertzsprung gap, Wolf-Rayet star and black hole, respectively. CE and CHeB mean common envelope phase and core helium burning phase, respectively. In this binary evolution example, a Wolf-Rayet star is assumed to be directly collapse into a black hole without a supernova after its nuclear burning stage. Credit: Belczynski et al. (2020).

Figure 1.3 shows the evolution of a potential progenitor of the gravitational source GW170104, in which the two black holes have $31.2^{+8.4}_{-6.0}\,\mathrm{M}_\odot$ and $19.4^{+5.3}_{-5.9}\,\mathrm{M}_\odot$ before the coalescence (B. P. Abbott, R. Abbott, T. D. Abbott, Acernese, Ackley, C. Adams, T. Adams, Addesso, Adhikari, Adya, Affeldt, Afrough, Agarwal, Agathos, Agatsuma, Aggarwal, Aguiar, Aiello, Ain, Ajith, B. Allen, G. Allen, Allocca, Altin, Amato, Ananyeva, S. B. Anderson, W. G. Anderson, Antier et al., 2017; Belczynski et al., 2020). The evolution starts with two zero-age MS (ZAMS) stars of masses $94.6\,\mathrm{M}_\odot$ and

$62.5\,\mathrm{M}_\odot$ in a separation of $4941R_\odot$. The initially more massive primary star depletes its center H at about 3.6 Myr, shortly after which Roche lobe overflow happens due to the expansion of the primary star. After the first mass transfer phase, the primary star loses its envelope and becomes a $36.6\,\mathrm{M}_\odot$ hot stripped Wolf-Rayet star, meanwhile the secondary star becomes a $71.1\,\mathrm{M}_\odot$ star. Subsequently, the WR star directly collapses to a BH of around $33\,\mathrm{M}_\odot$. After the secondary star ends its MS evolution, an inverse mass transfer from the secondary star to the BH happens in an unstable way, resulting in a common envelope evolution. The common envelope is successfully expelled in a short time, leaving a tight system containing a BH and a WR star. Then the second WR star collapses to the second BH with a mass of $24.7\,\mathrm{M}_\odot$. The two BHs merge within the age of the universe and create gravitational waves.

1.4 Star clusters

A star cluster is a group of gravitationally bound stars. There are basically two types of star clusters. One is globular clusters in which the stars are tightly bound and are mainly old stars. The other one is open clusters in which the stars are loosely bound and are mainly young stars. Star clusters are crucial to our understanding of stellar physics and evolution. Our lifetimes are a drop in the bucket compared to stars' lifetime, thus we can only observe snapshots of stars. Fortunately, star clusters provide us a circumstance that a group of stars are born simultaneously with nearly identical initial composition, but are currently in different evolutionary stages. By studying these clusters stars, we can learn the evolution of stars.

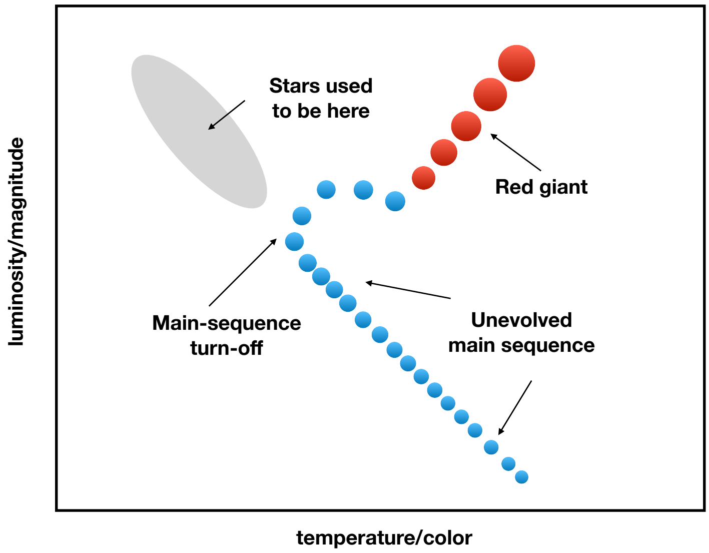

Figure 1.4: Schematic diagram of cluster star distribution in the Hertzsprung-Russell diagram/color-magnitude diagram. Stars in different evolutionary stages are indicated by different markers. In particular, the grey region means that the stars luminous enough to be here have evolved off their main-sequences.

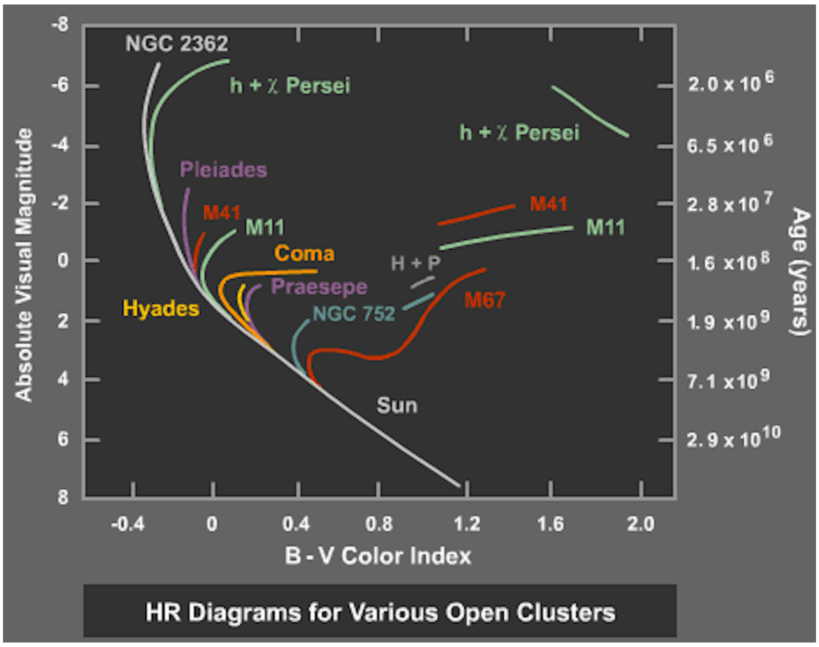

Figure 1.5: Age estimation of various open clusters based on their turn-off positions in the color-magnitude diagram. The lines are the theoretical isochrones that can best fit the observed cluster star distributions. The age of a cluster can be obtained by the right y-axis according to its turn-off. Source: Australia Telescope Outreach and Education; Credit: Mike Guidry, University of Tennessee.

1.4.1 Traditional view of star clusters

In the traditional view, a star cluster is an ensemble of stars born at the same time, with the same initial conditions, including initial chemical composition and initial rotation. Fig. 1.4 schematically illustrates the traditional view of the distribution of the stars in a cluster in the HRD or color-magnitude diagram (CMD). In this perspective, mass is the only parameter that determines the evolutionary stage of the stars. More massive stars evolve faster and end their MS phases earlier, at which time the less massive stars are still on their MSs. This results in a turn-off in the HRD or CMD. All stars above the turn-off have evolved to their late-evolutionary phases or have even evolved to be compact objects. The luminosity of the turn-off star is always used to determine the cluster age. A lower turn-off luminosity means an older cluster age. Fig. 1.5 demonstrates some cluster age estimation examples based on the cluster turn-off luminosities. In this figure, lines correspond to the theoretical isochrones (a line connecting the position of the star models at a specific age) that can best match the observed cluster star distributions in the CMD. The right y-axis shows the age of the isochrones that have corresponding turn-off magnitudes. Among these clusters, NGC 2362 is the youngest (~ 2 Myr), while M 67 is the oldest (several billion years).

1.4.2 Modern view of star clusters

However, recent high-precision observations based on Hubble Space Telescope (HST) reveal that the MS morphology of star clusters is too complex for a simple isochrone to explain (Milone, Bedin, Piotto and J. Anderson, 2009; Milone, Marino, D'Antona, Bedin, Da Costa et al., 2016; C. Li, de

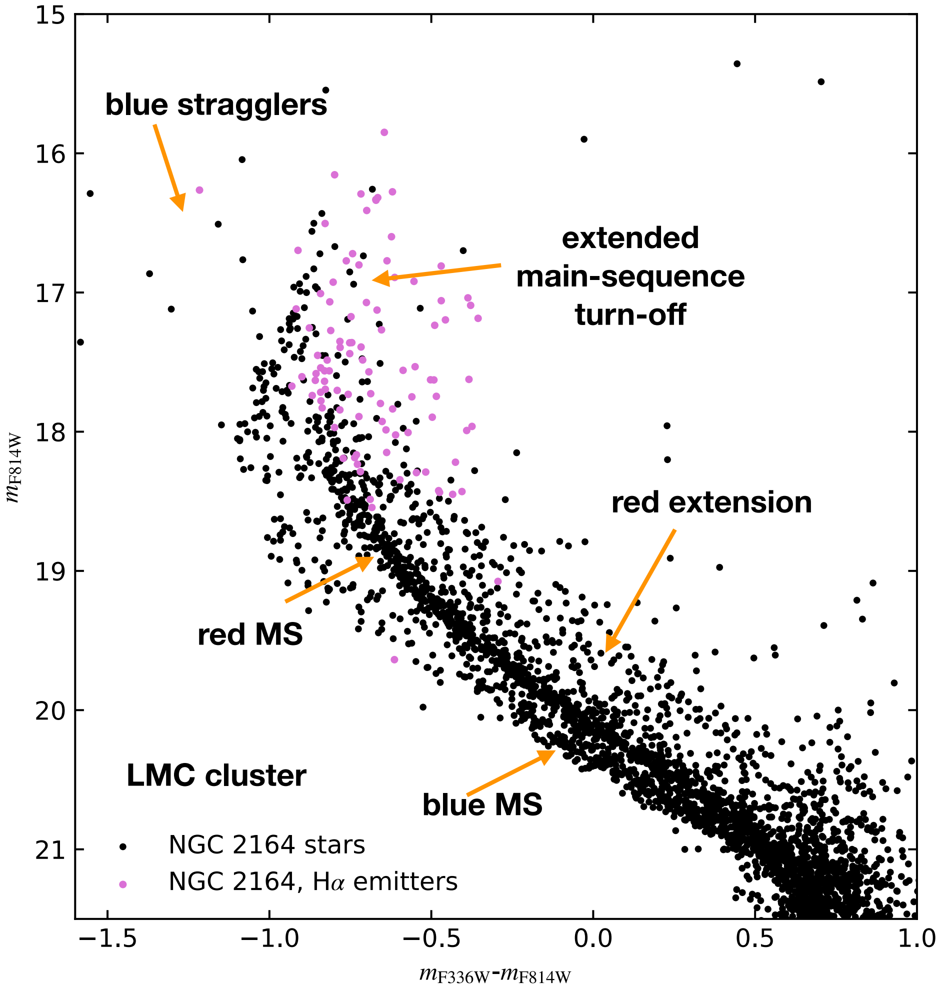

Figure 1.6: Color-magnitude diagram of the main-sequence stars in the Large Magellanic Cloud cluster NGC 2164 observed by Hubble Space Telescope. The black and purple dots correspond to the observed main-sequence stars without and with photometric excess in the narrow Hα band. Distinct main-sequence components are indicated in the figure. Data is from Milone, Marino, Di Criscienzo et al. (2018).

Grijs et al., 2017; Milone, Marino, Di Criscienzo et al., 2018; C. Li, Sun et al., 2019). Figure 1.6 shows the distribution of the MS stars in the LMC cluster NGC 2164 (~ 85 Myr) in the CMD. At least five distinct MS components can be seen. The outstanding red and blue MSs correspond to the so-called split MS in the literature. There is a red extension on top of the red MS. In addition, there are blue stragglers on the upper left side of the turn-off and Hα emitters on the right side of the turn-off, together making the cluster turn-off extended.

Such a complex MS morphology challenges the traditional view that cluster stars are born with the same initial conditions.The multiple MS component feature has been confirmed in both old globular clusters and young open clusters. But their origins are different. In old globular clusters, stars in different MS populations are proposed to have different [Fe/H] abundances, implying that they are in real different generations (Gratton, Carretta and Bragaglia, 2012; Milone, Piotto, Renzini et al., 2017). In contrast, identical chemical composition is found in open cluster stars, indicating that they are indeed coeval stars (Milone, Marino, D'Antona, Bedin, Da Costa et al., 2016; Mucciarelli et al., 2014).

This thesis focuses on the MS stars in young open clusters. Previous interpretations of the origin of the multiple MS components in young star clusters are summarized in the following:

- real age difference: a prolonged period of star formation is the most intuitive way to explain the multi-component feature (Baume et al., 2007; Mackey and Broby Nielsen, 2007; Glatt et al., 2008; Milone, Bedin, Piotto and J. Anderson, 2009; Goudfrooij, Puzia et al., 2011; Correnti, Goudfrooij, Puzia et al., 2015). However, as mentioned above, no evidence of chemical composition difference is found in young cluster stars. Besides, Bastian and Strader (2014) analyzed 12 LMC and 1 SMC young star clusters, and found no evidence for a gas residual or dust, which contradicts the continuous star formation. From another point of view, if a prolonged star formation exits, the escape velocity of a cluster should be larger than the wind velocity of the first-generation stars, such that the material from the first-generation stars can be used to create the second-generation stars. Goudfrooij, Girardi et al. (2014) argued that a lower escape velocity limit of $\sim 15\,\mathrm{km\,s^{-1}}$ is required to explain the extended MS turn-off as extended star formation, which roughly corresponds to a mass threshold of $10^{4.8}\,\mathrm{M_\odot}$. But some of the clusters with confirmed multiple MS component feature are lighter than this threshold, like NGC 1755 ($\sim 10^{3.6}\,\mathrm{M_\odot}$), NGC 1805 ($\sim 10^{3.7}\,\mathrm{M_\odot}$), NGC 1818 ($\sim 10^{4.41}\,\mathrm{M_\odot}$), and NGC 2164 ($\sim 10^{4.18}\,\mathrm{M_\odot}$) (Milone, Marino, Di Criscienzo et al., 2018). Last but not least, from a theoretical point of view, real age difference alone cannot explain the split MS, because unevolved coeval stars with the same initial conditions are nearly located in the same position in the CMD.

- rotation: rotation is proposed to explain both the split MS and extended MS turn-off (eMSTO) (Bastian and S. E. de Mink, 2009; Yang, Bi et al., 2013; Brandt and C. X. Huang, 2015; Niederhofer, Georgy et al., 2015; D'Antona, Di Criscienzo et al., 2015; Correnti, Goudfrooij, Bellini et al., 2017). Rotation influences the distribution of the MS stars in two opposite ways. On the one hand, centrifugal force makes rotating stars cooler and dimmer than their non-rotating counterparts. On the other hand, rotationally-induced mixing may make rotating stars hotter, brighter and living longer as MS stars than their non-rotating counterparts. Therefore, in general, the unevolved/less-evolved rotating stars are redder in the CMD compared to the non-rotating stars as rotational mixing has not played a role. While whether turn-off rotating stars are redder than their non-rotating counterparts depends on the efficiency of rotational mixing. Previous studies have shown that two populations of stars with one containing non-rotating stars and the other one containing near-critically-rotating stars are required to explain the observed blue and red MS stars in young star clusters. Despite the success in explaining the position of the double MSs in the CMD, there are some problems, for example, on how to explain so many stars born as near-critically-rotating stars. In Chapter 3, we reinvestigate how much rotation is needed to explain the observed double MSs with the newly computed rotating single star models.

- binary interaction: binary interaction can produce peculiar stars that cannot be produced in single stars. van Bever and Vanbeveren (1998) found that binary mergers can produce a population of blue stragglers on the upper left of the cluster turn-off with detailed binary models. Later on, Yang, Meng et al. (2011) obtained similar results by using the rapid binary models in which stars are resolved by grid points. Recently, C. Wang et al. (2020) showed

> that binary evolution is able to produce not only the blue stragglers, but also a sequence of near-critically-rotating Be stars, located on the red side of the turn-off, with a range of about 2-3 magnitudes, which agrees well with the observations.

However, to date, no study can reproduce all the observed MS components with coeval star models in a self-consistent way. In this thesis, we use the state-of-the-art star models to investigate the impact of the important physics, such as rotation and binary evolution, on the MS morphology of young Magellanic Cloud clusters.

1.5 Overview of the chapters in this thesis

As binary stars are abundant and binary interaction affects the properties of both stars, it is mandatory to investigate the contribution of binary interaction to the observed MS morphology in young star clusters. However, to date, no thorough comparisons between the detailed binary models and the observations are available in the market. This thesis aims to comprehensively understand the role of binary interaction in shaping the MS morphology in young open star clusters, and to replicate the observed MS components in young star clusters with newly computed detailed binary models. We first explored the binary-induced MS features in young star clusters with our dense grids of binary models in which the two stars are simply assumed to be synchronized at ZAMS. Then we studied the role of rotation in explaining the observed split MS. After that, we investigated the origin of the slowly-rotating stars in young open clusters. At last, we took advantage of all our findings and built new binary models in which the two stars have moderate initial rotation. We compared these rotating binary models with the observed MS stars in young star clusters.

For the binary models, we only consider the SMC-like metallicity. Because in such a low metallicity, the models are barely affected by the uncertain stellar wind, which allows us to single out the binary effects. Whereas for the single star models, we consider both the LMC-like and SMC-like metallicities, because we want to compare our models with the MS stars in both LMC and SMC clusters. We compare our detailed single and binary models with four Magellanic Cloud clusters younger than 100 Myr, namely the SMC cluster NGC 330, and the LMC clusters, NGC 1818, NGC 1755, and NGC 2164. All these clusters exhibit a feature of multi-component in high-precision observations. The advantages of studying Magellanic Clouds clusters include that their distances are well established. The Magellanic Cloud clusters are close to us, such that a detection of individual stars is possible. In addition, both Magellanic Clouds have low metallicity, not only allowing us to circumvent the effect of uncertain stellar wind in massive stars, but also allowing us to understand the stars in the early universe.

1.5.1 Chapter 2: Effects of binary evolution on the main sequence of young star clusters

In this chapter, we explore the binary evolutionary induced MS features in young star clusters. We compute the evolution of more than 50 000 binaries in a large parameter space. The initial primary mass $M_{1,\mathrm{i}}$ ranges from $5\,\mathrm{M}_\odot$ to $100\,\mathrm{M}_\odot$ in intervals of $\log M_{1,\mathrm{i}} = 0.05$. The initial mass ratio ranges from 0.1 to 1 in intervals of 0.05, while the initial period is from 1 day to 3162 days in intervals of $\log P = 0.025$. The two stars in a binary system are assumed to be synchronized at ZAMS. Based on this assumption, most of the stars are slow rotators at ZAMS, which allows us to avoid the influence of star rotation. We trace the evolution of these binary systems from the ZAMS to carbon depletion in both stars.

We display the distribution of our binary models in the HRD at various ages (younger than 30 Myr). We find an explicit feature that the MS turn-off is extended at all analyzed ages. We identify an extended turn-off binary-evolution feature attributed to MS mergers, semi-detached systems, and post-mass-transfer systems. Rejuvenation is the leading cause of the hot temperature of the MS mergers. While the red binary evolutionary induced population contains near-critically-rotating Be stars, which are the accretors survived Case B mass transfer. The luminosity extension of this red binary evolutionary induced population is determined by the least massive stars that can experience a stable Case B mass transfer. We also see a blue binary-evolution feature, mainly related to contact binaries, whose evolutionary phases are uncertain.

Meanwhile, we conduct a population synthesis study to explore the evolution of the binary stars in a cluster with a total mass of $\sim 10^5\,\mathrm{M}_\odot$. We use an animation to show the evolution of our binary models up to 40 Myr. The animation explicitly shows the above-mentioned binary-induced features and the way these features evolve.

This work is the start of our project. We find that binary evolution indeed affects the MS morphology in young star clusters. However, the binary models in this work cannot match the distribution of the observed stars in young star clusters, because rotation is not properly considered.

1.5.2 Chapter 3: Slowly and moderately rotating stars as the constituents of the split main sequences in young star clusters

It is widely accepted that rotation is responsible for the split MS in young star clusters. Previous studies based on the prevalent SYCLIST models argued that stars with zero rotation and near-critical rotation are needed to explain the color split between the observed blue and red MS stars. However, it is unrealistic that so many stars are born with near-critical rotation. Besides, the majority of the stars having near-critical natal spins contradicts the spectroscopic observations. In this chapter, we attempt to address the issue of how much rotation is needed to reproduce the observed color split between the red and blue MS stars in young star clusters.

We compare our MESA rotating single star models with the observations and find that stars with 0-35% of critical rotation and 55-65% of critical rotation are adequate to match the observed blue and red MS stars. These values agree with the observed bi-modal velocity distribution of the field B/A type stars and agree with the spectroscopic measurement of the velocity of the MS stars in NGC 1818.

We find similar results with the SYCLIST models after clarifying the different definitions of critical rotation and removing the influence of models' initial relaxation. However, we find that different star model sets predict different distributions of the turn-off stars. We argue that current observations are not adequate to assess these two model sets.

In addition, we explore the implication of our results on the formation of Be stars. We confirm the previous result that single stars with initial moderate rotation can evolve to Be stars at the end of their MS stages, but binary evolution still plays a vital role in the formation of Be stars. We also check the rotationally induced surface N enrichment in turn-off stars. We find that N is enriched in the turn-off stars whose initial rotational velocities are larger than 40% of their critical values.

1.5.3 Chapter 4: Stellar mergers as the origin of the blue main-sequence band in young star clusters

In Chapter 3, we have proposed that the blue MS in young star clusters should mainly contain slowly-rotating stars. In this chapter, we attempt to address the issue of the origin of these slowly-rotating stars. We propose that the blue MS stars are binary merger products, stimulated by the previous findings that binary merger products are slow rotators and are rejuvenated. We use our single star models to compute the position of the binary merger products created at specific ages. By comparing our results with the observed position of the blue MS stars in the CMD, we derive a potential merger time, which is the time in the binary history when the coalescence happened, for each blue MS star. We find a high merger rate in the early life of star clusters, which peaks at 2 Myr and prevails for tens of Myr. The mergers might be mainly caused by binary orbit decay because the fraction of the binary evolutionary induced mergers is small. Our findings have both theoretical and observational evidence.

We also estimate the mass function of the red and blue MS stars, and find that the mass function of the red MS stars complies well with the Salpeter IMF, while the mass function of the blue MS stars has a much shallower slope. Such dissimilar mass functions imply their different origin mechanisms. We, for the first time, propose that cluster stars gain their rotation in two different ways. All stars are born with nearly the same initial rotation, i.e. roughly half of their critical velocities and populate the red MS. Binary mergers triggered either by orbital shrinking or by binary evolution produce slowly rotating stars that populate the blue MS.

1.5.4 Chapter 5: Upper limit on the fraction of the binary evolution produced Be stars in young star clusters

In Chapter 2, we propose that binary evolution results in a population of near critically-rotating Be stars on the right side of the turn-off with a magnitude range of 2 to 3 mags. However, our detailed binary models fail to reproduce as many such Be stars as the observations. The reason is that a significant amount of binaries merge during Case B mass transfer in our models.

In this chapter, we relax the merger criterion adopted in our detailed binary models, and attempt to explore the maximum fraction of the binary evolutionary induced Be stars in young star clusters. We make a simple assumption that all binaries with mass ratios larger than 0.5 can produce a Be star. The mass ratio threshold is chosen such that the magnitude range of the Be sequence roughly matches the observation. Instead of computing new detailed binary models, which are both time and space consuming, we make use of our single star models described in detail in Chapter 3 to simulate the distribution of binary systems in the CMD. We apply our findings in Chapter 3 and 4 and assume that all stars have natal spins of half of their critical values. We adopt empirical binary initial parameter distributions.

Based on our new merger criterion, we find that the fraction of the binary evolutionary produced Be stars with respect to all the MS stars decreases with increasing magnitude in star clusters, with a maximum value of ~30% near the turn-off, which is considerably larger than the prediction by our detailed binary models in Chapter 2, but is still smaller than the observed Be star fraction near the turn-off (~ 50%). Calculating the Be star fraction as a function of stellar mass, rather than magnitude, may make the predicted fraction more comparable to the observations (Hastings, Langer et al., 2021). Another solution may be fine-tuning the initial binary parameter distributions, which will be considered in our future studies. Nevertheless, the most plausible explanation for the deficiency of the predicted Be star fraction is that single star evolutionary induced Be stars should be considered, as previous studies have shown that initially moderately fast rotating single stars can achieve near critical rotation at the end of their MS evolution. However, we find that the fraction of the single evolutionary induced Be stars depends highly on the uncertain stellar wind. In our single star models, the stars with masses of around $10\,\mathrm{M}_\odot$ suffer very intense stellar wind near the end of their MS evolution due to the bi-stability jump, avoiding reaching critical rotation. Therefore, in star clusters with ages of $\sim$30 Myr (the turn-off mass is $\sim 10\,\mathrm{M}_\odot$), single star evolution only accounts for a minor fraction of the Be stars near the turn-off. In contrast, in star clusters with ages between $\sim$ 50 and 100 Myr, single star evolution can contribute to a significant fraction of Be stars. Further studies on both single and binary star evolution, including the mass transfer stability, the stellar wind and accompanied angular momentum loss, are in high demand to understand the formation of the Be stars.

CHAPTER 2

Effects of binary evolution on the main sequence of young star clusters

Chen Wang, Norbert Langer, Abel Schootemeijer, Norberto Castro, Sylvia Adsheid, Pablo Marchant, and Ben Hastings

Astrophysics Journal: Letters, 2020, 888, 12

Author contributions: C.W. performed the stellar evolution calculations and analysed the results, based on earlier work by P.M. and his advice. N.L. interpreted the results, together with C.W., A.S., B.H.. S.A. performed an earlier pilot study and contributed to interpreting the results. N.C. interpreted the related observations. C.W. and N.L. wrote and edit the paper. All authors reviewed the manuscript.

Abstract

Star clusters are the building blocks of galaxies. They are composed of stars of nearly equal age and chemical composition, allowing us to use them as chronometers and as testbeds for gauging stellar evolution. It has become clear recently that massive stars are formed preferentially in close binaries, in which mass transfer will drastically change the evolution of the stars. This is expected to leave a significant imprint in the distribution of cluster stars in the Hertzsprung-Russell diagram. Our results, based on a dense model grid of more than 50,000 detailed binary-evolution calculations, indeed show several distinct, coeval main-sequence (MS) components, most notably an extended MS turnoff region, and a group of near-critical rotating stars that is spread over a large luminosity range on the red side of the classical MS. We comprehensively demonstrate the time evolution of the features in an animation, and we derive analytic expressions to describe these features. We find quantitative agreement with results based on recent photometric and spectroscopic observations. We conclude that while other factors may also be at play, binary evolution has a major impact on the MS morphology of young star clusters.

2.1 Introduction

The stellar main sequence (MS) in the Hertzsprung-Russell (HR) diagram, which was discovered (Russell, 1914) before it was known that stars are powered by nuclear fusion (Atkinson and Houtermans, 1929), is the backbone of our knowledge of stars. Until today, the analysis of star clusters has given essential clues for understanding the internal structure and evolution of stars. Research in recent years has shown that the MSs of star clusters are not simple one-dimensional structures; rather, they contain distinct features that still need to be deciphered.

In studies of star clusters, frequent key assumptions are that the stars in a cluster are coeval, have the same initial chemical composition, are not affected by rotation, and are single stars. All four assumptions are currently being challenged by modern, high-precision observations. Recently, photometric studies using the Hubble Space Telescope revealed that the MS of young and intermediate age star clusters (14-600 Myr) in the Magellanic Clouds and in the Galaxy is split into two distinct MSs, as well as an extended MS turnoff region (D'Antona, Milone et al., 2017; Milone, Marino, Di Criscienzo et al., 2018; C. Li, Sun et al., 2019, and references therein). Furthermore, the young clusters show distinct groups of emission-line stars, extending more than two magnitudes below the turnoff (Milone, Marino, Di Criscienzo et al., 2018), most of which are spectroscopically identified as Be stars (J. Bodensteiner et al., 2019).

In this situation, it appears worthwhile to investigate binary-evolution effects. The observed binary incidence and binary properties of massive stars imply that an isolated life of a massive star is the exception, the rule being that its evolution will be strongly affected by a binary companion (Sana, S. E. de Mink et al., 2012). Simplified binary population synthesis calculations in which binary evolution is approximated based on single-star models, have shown that binary evolution can produce a rapidly rotating sub-population (S. E. de Mink, Langer et al., 2013), and that it can account for the so-called blue stragglers, i.e., cluster stars above the apparent cluster turnoff, in Galactic open clusters with ages of up to ~ 1 Gyr (Yang, Meng et al., 2011; Schneider, Izzard, Langer et al., 2015). However, such so called rapid binary-evolution models are not able to predict reliable effective temperatures of post-interaction stars. To understand the MS morphology of young star clusters, it is therefore necessary to investigate the effects of close binary evolution based on dense grids of detailed binary-evolution models (van Bever and Vanbeveren, 1998).

Here, we provide such grids, which include differential rotation, rotationally induced internal mixing, and magnetic angular momentum transport as used by Marchant, Langer, Podsiadlowski, Tauris, S. de Mink et al. (2017) and use them to investigate the effects of close binary evolution on the MS morphology of young star clusters. In Sect. 2.2 we describe the adopted physics to compute binary models, and we present our main results in Sect. 2.3. We provide a comparison with single-star models in Sect. 2.4, and with observed star clusters in Sect. 2.5. In Sect. 2.6, we give our concluding remarks.

2.2 Method and assumptions

We use the detailed one-dimensional stellar evolution code MESA (Paxton, Bildsten et al., 2011; Paxton, Cantiello et al., 2013; Paxton, Marchant et al., 2015), version 8845, to compute our binary-evolution models. The stellar models contain physics assumptions that are identical to the rotating single-star models of Brott et al. (2011), and include differential rotation, rotationally induced internal mixing, magnetic angular momentum transport, stellar wind mass loss, and non-equilibrium CNO nucleosynthesis. Our assumptions on binary physics are as those described by Marchant, Langer, Podsiadlowski, Tauris, S. de Mink et al. (2017). Below, we emphasize the most relevant physical assumptions for convenience.

We use the standard mixing-length theory to model convection with a mixing-length parameter of $\alpha = l/H_P = 1.5$, where H_P denotes the local pressure scale height, which allows for inflated envelopes in models near their Eddington limit (Sanyal, Grassitelli et al., 2015; Sanyal, Langer et al., 2017). To determine the boundaries of convective zones, we adopt the Ledoux criterion, where we include convective core overshooting as a step function with $\alpha_{\mathrm{OV}} = 0.335$ (Brott et al., 2011). We include semiconvective mixing in superadiabatic layers if they are stable according to the Ledoux criterion using $\alpha_{\mathrm{sc}} = 1$ (Langer, K. J. Fricke and Sugimoto, 1983), and thermohaline mixing as used by Cantiello and Langer (2010) with $\alpha_{\mathrm{th}} = 1$. Rotationally induced mixing is modeled as a diffusive process (Heger, Langer and Woosley, 2000). We take into account the effects of dynamical and secular shear instabilities, the Goldreich-Schubert-Fricke instability, and Eddington-Sweet circulations. The efficiency parameter of rotational mixing is $f_c = 1/30$ as proposed by Chaboyer and Zahn (1992). We also include the Tayler-Spruit dynamo for the transport of angular momentum (Spruit, 2002; Heger, Woosley and Spruit, 2005).

The detailed structure of both binary components is computed simultaneously with the orbital evolution. We assume circular orbits and adopt initial spins such that the rotation period of both stars is synchronized to the orbital period of the binary on the zero-age MS. During the evolution, the effects of tidally induced spin-orbit coupling (Detmers et al., 2008) are included. We compute mass and angular momentum transfer arising from Roche-lobe overflow. We assume the specific angular momentum accreted by the secondary star depends on whether the accretion is ballistic or occurs via a Keplerian disk, and restrict the mass accretion of the mass gainer when it has reached near-critical rotation (Petrovic, Langer and van der Hucht, 2005). We do so by adopting a rotational enhancement of the stellar mass-loss rate, which prevents models from exceeding critical rotation (Langer, 1998; Langer, 2012; Paxton, Marchant et al., 2015). When the energy contained in the combined luminosity of both stars is insufficient to drive the mass out of the binary at a rate equal to the mass loss rate, we assume that both stars are engulfed in the excess material, with a binary merger ensuing.

For contact phases, we employ the scheme described by Marchant, Langer, Podsiadlowski, Tauris and Moriya (2016) to model the mass-transfer phase. We assume both stars to merge when they both fill their Roche volumes and mass outflow through the second Lagrangian point is obtained. When a binary merger is assumed to happen for a given binary model while both stars still burn hydrogen in their cores, we calculate its further evolution by adopting a single-star model with the appropriate mass and age. We assume that the internal structure fully rejuvenates, and adopt an initial central hydrogen abundance of the merger product according to Schneider, Podsiadlowski et al. (2016). Mergers are treated as non-rotating stars, following Schneider, Ohlmann, Podsiadlowski, Röpke, Balbus, Pakmor and Springel (2019).

The evolution of the binary models is started by considering both stars on the zero-age MS. We then follow the evolution of both components, as long as one of the two stars is still on the MS. We compute our models until core carbon exhaustion. If at that stage the core of a model exceeds the Chandrasekhar mass, we assume that it produces a supernova explosion, and compute the continued evolution of its core hydrogen burning companion in isolation.

We adopt a metallicity of $Z_{\mathrm{SMC}} = 0.002179$ appropriate for young stars in the SMC, a helium abundance of $Y = 0.25184$, and a distribution of heavy elements as used by Brott et al. (2011).

Our model grid covers initial primary star masses between 5 $M_\odot$ and 100 $M_\odot$, initial mass ratios of 0.95-0.3, and initial orbital periods of 1 day-8.6 yr. We cover the initial parameter space with more than 50,000 binary-evolution models, using 26 different initial primary masses and 140 initial period values, both distributed evenly in log-space, and 14 evenly distributed initial mass ratios.

We compute a second suite of binary models in order to predict the distribution of stars in the HR diagram of a star cluster with a total mass of 10^5 $M_\odot$ in stars between 100 $M_\odot$ and 0.8 $M_\odot$. This leads to 2078 binary systems with primary masses larger than 5 $M_\odot$. We use a Monte Carlo simulation to generate initial binary systems adopting a Salpeter initial mass function (IMF) (Salpeter, 1955), a flat distribution of initial mass rations q_i, and a flat distribution of log P_i, within the initial mass ratio and period ranges as described above. We assume a binary fraction of one, i.e., we do not consider additional single stars in our cluster model. We use the MESA code to evolve the generated 2078 binary systems in time. In this way, the time dependence of the HRD distribution of the cluster stars can be simulated without the need to interpolate between different binary-evolution models. An interpolation in time is still necessary, which, due to the high time resolution of the MESA models, does not lead to noticeable errors.

2.3 Binary-induced main-sequence features

Figure 2.1 shows the locations of our models in the HR diagram for selected ages. Each of the ~50,000 detailed binary evolutionary sequences provides one dot in each figure, as long as at least one of the two stars still undergoes core hydrogen burning. We only plot the visually brighter component of each system, as in most cases the fainter one is either unevolved, lost its envelope, or terminated its evolution (S. E. de Mink, Sana et al., 2014). Statistical probabilities due to the IMF or initial binary parameter distributions are not taken into account, but the figure is meant to demonstrate which parts of the HR diagram are covered by models in the different evolutionary branches. In this figure, we distinguish models in four different evolutionary branches, as indicated.

The pre-interaction binaries (blue) in Fig. 2.1 are located on a single line, which represents the corresponding single-star isochrone (SSI). As most of our pre-interaction stars rotate slowly by construction, the rotational broadening of the SSI is small, even near the turnoff (see Figure 7 of Brott et al., 2011). This ensures that all other features that are visible in Fig. 2.1 are induced by binary evolution, and not an effect of the initial distribution of rotational velocities.

We distinguish three prominent features in the distribution of stars in Fig. 2.1. First, at all times, the turnoff region is extended beyond the SSI, mostly to higher luminosities and temperatures (we call this the turnoff binary-evolution feature, TBF). Second, for ages above ~ 4 Myr, a distinct red MS appears (red binary-evolution feature, RBF), whose lower part is well separated from the SSI. Third, at all times, MS stars to the blue side of the SSI appear. They form a separated blue MS for ages above ~ 10 Myr and merge with the TBF at high luminosities (blue binary-evolution feature, BBF). We indicate these features in Panel (d) of Fig. 2.1. None of these three features has been described by detailed binary-evolution models before.

The evolution of exemplary binary models in the HR diagram in Fig. 2.2 helps reveal the origin of the MS features. Binaries that undergo mass transfer while both stars fuse hydrogen in their cores (Case A mass transfer) evolve into semi-detached systems. This occurs because Case A mass transfer comprises a nuclear timescale mass-transfer phase, whereas otherwise mass transfer occurs on the much shorter thermal or even on the dynamical timescale. As shown in Fig. 2.1, the semi-detached

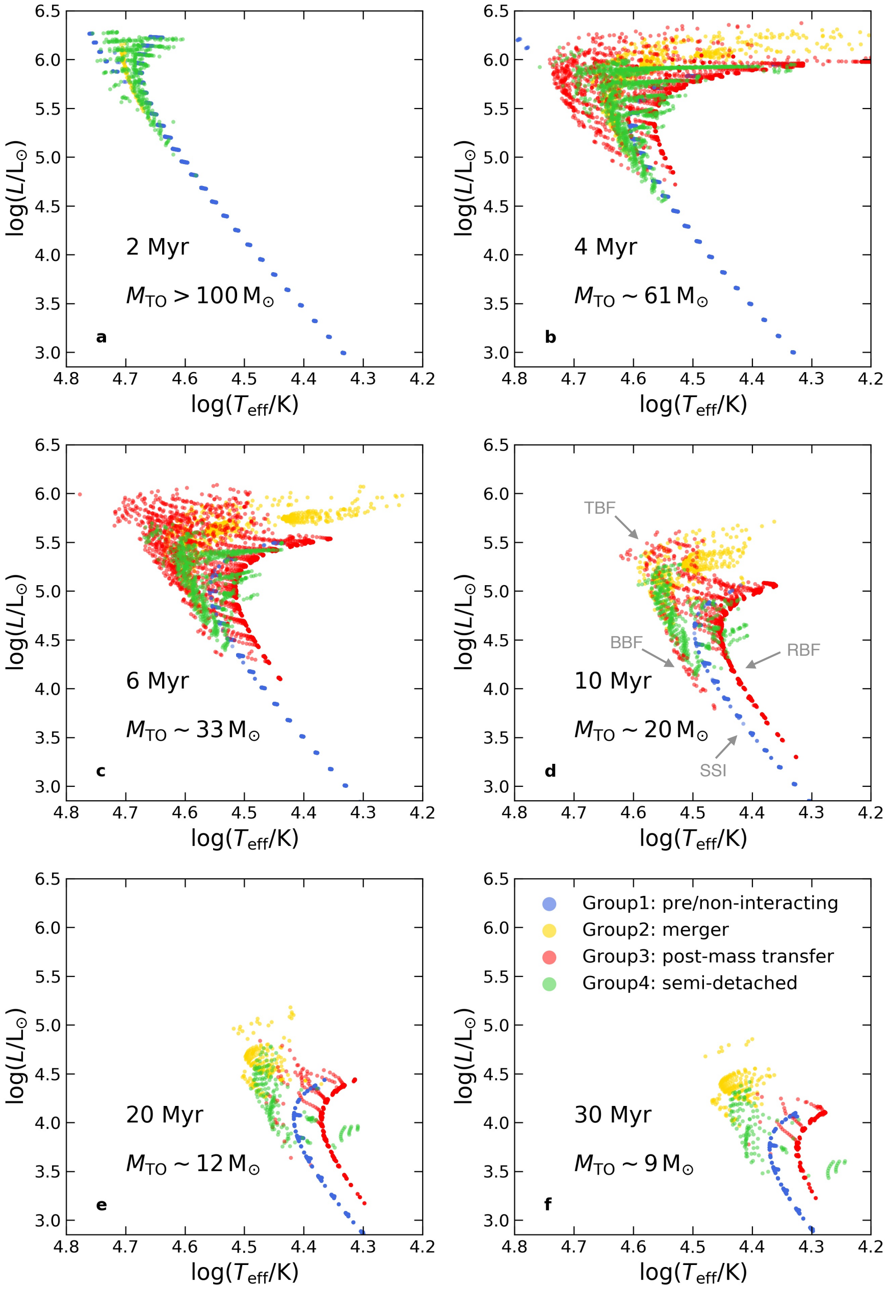

Figure 2.1: Distribution of our binary models in the Hertzsprung-Russell diagram at six different times, as indicated. Only the visually brighter component of each binary is plotted, for all models where at least one of the two stars still undergoes core hydrogen burning. Dark blue dots correspond to models that have not yet interacted with a companion. Yellow dots indicate the products of the merger of two core hydrogen burning stars. Red dots indicate stars that have undergone rapid (thermal timescale) accretion of matter from a companion. Green dots represent stars undergoing nuclear timescale accretion at the selected time. Below the age, we indicate the approximate MS turnoff mass for the non-interacting stars. We indicate the binary produced MS features in Panel (d).

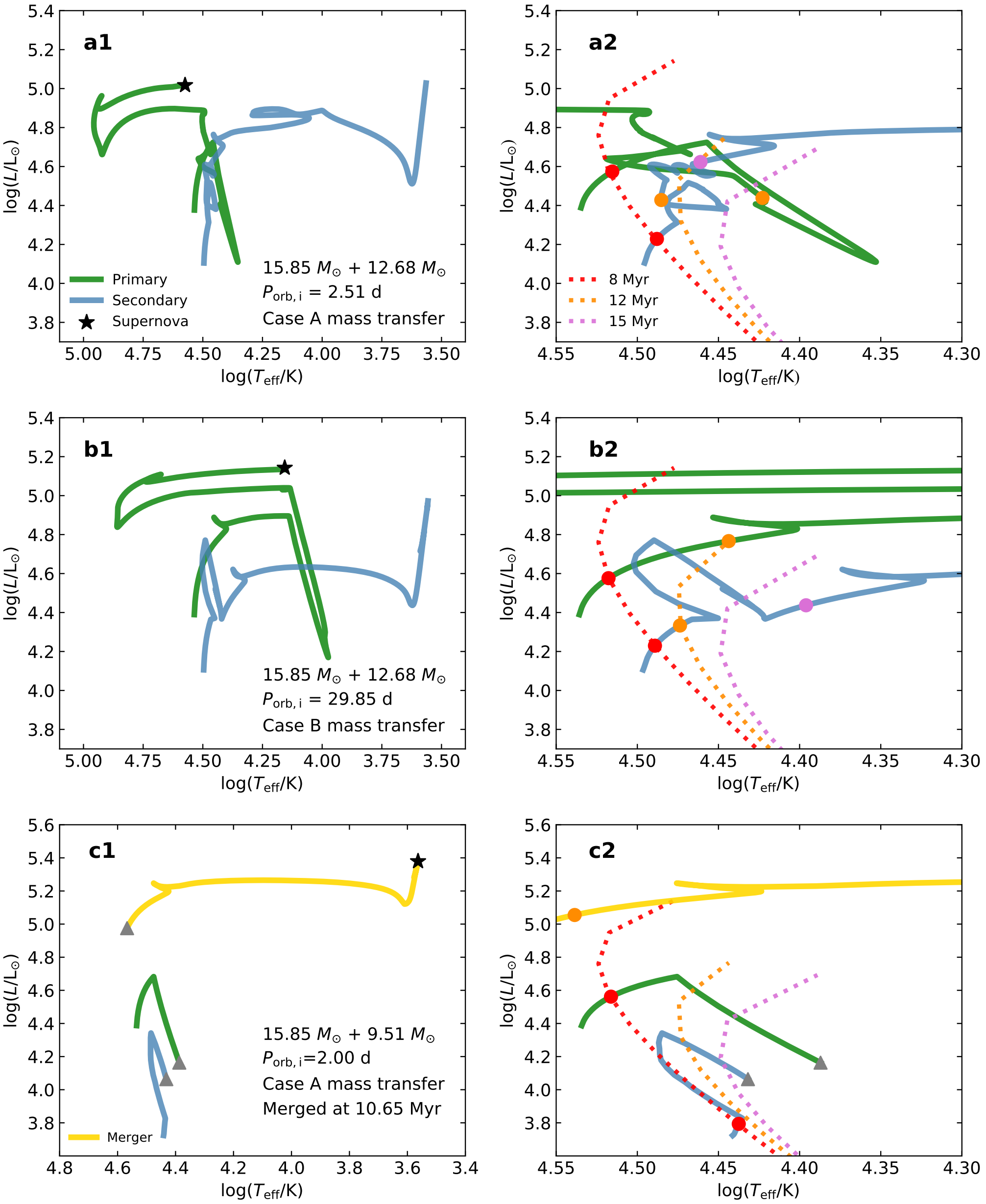

Figure 2.2: Evolution of both components of three example binary models in the HR diagram (left panels), with a zoom of the MS region (right panels). All three models start with the same primary model (donor star, green lines) of 15.85 $M_\odot$. The initial mass of the secondary stars (mass gainer, blue lines) is 12.68 $M_\odot$ in the top two systems, and 9.51 $M_\odot$ in the third. The dashed lines in the right panels represent single-star isochrones for 8, 12, and 15 Myr, and solid dots on the evolutionary tracks with the corresponding colors mark the positions of the binary components at these ages. The black star symbols mark the pre-supernova position of the primary stars. The gray triangles in the bottom panels mark the merger event. The donor stars in the top and the bottom models start mass transfer during core hydrogen burning (Case A mass transfer), and the donor in the middle model starts mass transfer after core hydrogen exhaustion (Case B mass transfer).

models do not give rise to a sharp feature in the HR diagram, since their locations are quite spread out, and overlap strongly with those of the mergers and post-mass-transfer systems. These together produce the TBF. They are mostly located above and to the left of the line formed by the pre-interaction stars because their mass ratios are inverted, since the former secondary stars have accreted substantial amounts of matter in a preceding thermal timescale Case A mass transfer. If the secondary's mass has been increased to values above the mass corresponding to the single-star turnoff, it will be brighter than any of the pre-interaction stars at the given age. The internal process of rejuvenation, i.e., the mixing of fresh fuel toward the centre due to an increase of the mass of the convective core, makes it look younger, i.e., leads to a higher surface temperature than that of a comparable pre-interaction star (Schneider, Izzard, Langer et al., 2015). After the mass donor in a Case A binary system ends its core hydrogen burning, its post-MS expansion will give rise to another rapid, thermal timescale, mass-transfer phase, after which we consider the binary a post-mass-transfer system.

Our Case A binaries produce a rich spectrum of observable features. The BBF, as described above, is exclusively due to Case A mass transfer. Whereas models in the extended turnoff region are blue mainly because they are rejuvenated, the fainter blue MS stars of the BBF, which are most pronounced for ages in the range of 10-20 Myr, have higher surface temperatures because their envelopes are significantly enriched in helium. They originate from the binaries with the shortest initial periods and smallest initial mass ratios, which undergo contact evolution but avoid merging (Marchant, Langer, Podsiadlowski, Tauris and Moriya, 2016). Furthermore, we find some detached systems in between fast and slow Case A mass transfer, which share their HR diagram positions with the semi-detached systems. At the highest masses, strong stellar winds can lead to a widening of the orbit after the fast Case A mass transfer. This may detach the mass donor from its Roche lobe for some time (Petrovic, Langer and van der Hucht, 2005). At lower masses, the orbital period of systems right after the fast Case A mass transfer can be short enough that tidally induced spin-orbit coupling leads to an expansion of the orbit, which again allows the primary stars to detach from their Roche lobe for about 0.1-0.2 Myr before the slow Case A mass transfer begins. We also find some semi-detached binary models in which the mass donor is still the brighter of the two stars. These donor stars, which are in thermal equilibrium, can be significantly cooler than the single-star terminal age MS. In Fig. 2.1, we see these models sticking out on the cool side of the RBF about 0.5 dex below the turnoff. We note that such systems have been identified by Howarth et al. (2015) and Mahy et al. (2019). Finally, our merged stars behave similar to near-conservative Case A mass-transfer systems. They populate the brightest part of the extended turnoff region and overlap strongly with the post-mass-transfer mass gainers (Fig. 2.1).

The group of post-mass-transfer systems is dominated by initially wider binaries, which undergo thermal timescale mass transfer only after the primary star exhausted hydrogen in its core (Case B mass transfer). As their large orbital separations render tides ineffective on the mass gainers, these are quickly spun up to near-critical rotation, after which their accretion efficiencies are strongly reduced (see Section 2.2). Many Case B mass gainers end up naturally in this situation, as critical rotation is reached after only accreting a few percent of their initial mass (Packet, 1981), if the orbits are wide enough to avoid tidal spin-down (Langer, 2012). These models populate the RBF, and are approximately 15% cooler than the correspondingly luminous models on the SSI due to the action of their centrifugal force on their structure (Paxton, Smolec et al., 2019). The RBF becomes more distinct and spreads over a larger luminosity range for larger ages. The RBF shows a temperature offset from the SSI of approximately 15%. Our models are spun up to as fast a rotation as is numerically allowed, i.e., 98% of critical rotation, and they mostly remain at this level for their remaining hydrogen burning

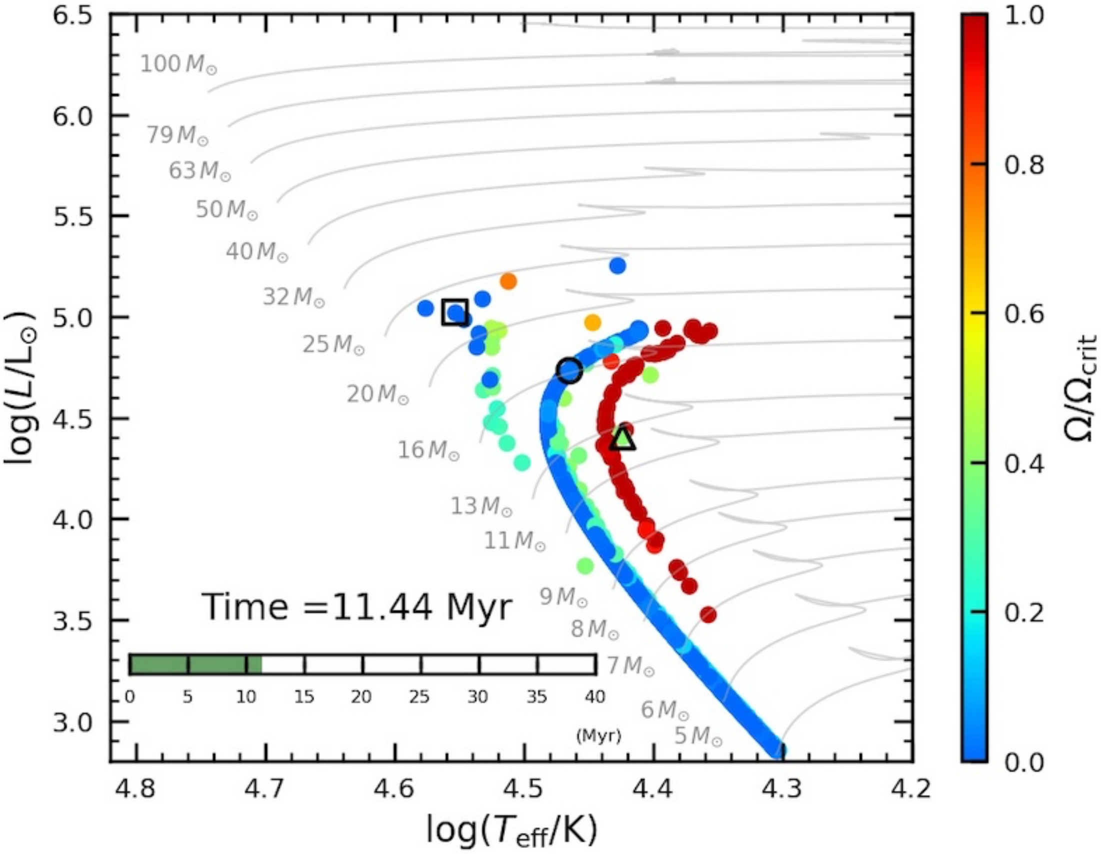

Figure 2.3: Star cluster animation to show their evolution in the Hertzsprung-Russell diagram, with colors indicating the ratio of rotation to critical rotation velocity. Evolutionary tracks of non-rotating single stars are shown as gray lines, with initial masses quoted. We evolve our cluster from an age of 0.02 Myr up to 40 Myr, corresponding to a turnoff mass of ~ $8\,\mathrm{M}_\odot$. The three example binaries shown in Fig. 2.2 are marked with special symbols, such that triangles, circles and squares indicate examples a, b, and c, respectively. The video duration is 20 s.

lifetimes. Only the most massive fast rotators ($M \gtrsim 20\,\mathrm{M}_\odot$) have strong enough stellar winds to spin down (Langer, 1998). This leads them to slowly evolve off the RBF towards the blue side. The RBF extends a factor of 30 or more in luminosity below the turnoff region. We show in Sec. 2.7.2 that the minimum luminosity of the RBF is set by the minimum initial mass ratio for which a merging of the two stars is avoided.

We provide an animation [1] of our population synthesis study (Fig. 2.3) to demonstrate the time evolution of the various binary-induced morphological MS features of young star cluster. In this animation, different colors correspond to different fractions of critical rotation. A slow forwarding of the image sequence therefore allows tracing of the evolution of the brighter stars in the HR diagram, as well as the evolution of their rotation velocities.

---

[1] The animation can be downloaded at https://doi.org/10.5281/zenodo.3598691

2.4 Comparison to single-star models

Figure 2.4 shows the result of a population synthesis for single-star models (Brott et al., 2011) with an age of 15 Myr, for which we adopted the initial rotational velocity distribution of Dufton et al. (2013) and the Salpeter IMF. It demonstrates that rapidly rotating single-star models are significantly bluer than the spun-up mass gainers. Since the rotation rate of the RBF models was ordinary before accretion, they have established a strong chemical gradient in their interior, which prevents rotational mixing from affecting their chemical structure. The situation is different in rapidly rotating single stars, where helium mixed into the stellar envelopes (Brott et al., 2011; Georgy, Ekström, Eggenberger et al., 2013) can cause the star to evolve to a higher effective temperature (Maeder, 1987). Furthermore, rapidly rotating stars would only form a discrete MS line if their initial rotation rates were nearly identical, since the amount of mixing is a sensitive function of the rotation rate.

Figure 2.4 shows also that rotational mixing in single stars can produce an extended turnoff region similar to the TBF. However, the presence of the single-star feature depends on the number of stars that rotate very rapidly initially. If the rapidly rotating single stars were in fact binary products, as suggested by S. E. de Mink, Langer et al. (2013) and Ramírez-Agudelo et al. (2015), binaries would be the only way to produce an extended MS turnoff. As shown by our models, a TBF is in fact unavoidable for a non-vanishing binary fraction.

2.5 Comparison to observed star clusters

Within the last decade or so, it has become evident that extended MS turnoffs are a ubiquitous feature of young star clusters (C. Li, Sun et al., 2019, and references therein). In a broader sense, this includes the phenomenon of the blue stragglers, which is found for clusters of all ages (Ahumada and Lapasset, 2007). For young clusters, extended turnoffs are often explained by the presence of stars with a wide range of rotation rates (D'Antona, Milone et al., 2017, and references therein). However, simplified binary-evolution population synthesis demonstrates that binary evolution may also be able to lead to extended turnoffs (Yang, Meng et al., 2011; Schneider, Izzard, S. E. de Mink et al., 2014).

Our binary-evolution models allow us to obtain a reliable quantification of the extent of the TBF. We derived the apparent age difference Δt between the SSI and an SSI that fits either the bluest or the brightest member of the coeval binary population in our simulated cluster (see Fig.2.3), as a function of its true age t. Figure 2.5 shows that the apparent age difference can be approximated by a linear function, i.e., $\Delta t \propto t/2$. This corresponds well to our analytic estimate in Sec. 2.7.1 of $\Delta t \propto 0.58t$. As shown in Fig. 2.5, our result is compatible with the recent observational estimates by Beasor et al. (2019) and Britavskiy et al. (2019). Our analytic result also agrees with corresponding estimates for clusters up to 1000 Myr (see Figure 2 of Niederhofer, Georgy et al., 2015).

In fact, any process that enriches the core with a fixed fraction of the hydrogen mass of the envelope of a MS star will give rise to a linear relation between the apparent age difference at the turnoff and the turnoff age of the non-enriched stars, be it binary rejuvenation as in our case, or rotationally induced mixing (Niederhofer, Georgy et al., 2015). However, our simple result, i.e., that the apparent cluster age is about half the true age, is a natural consequence that binary evolution can lead to stars with a mass of about twice the single-star turnoff mass. While rotational mixing can lead to a similar result, a tuning of the rotation rate and/or of the mixing efficiency is required, since the amount of mixed material depends on both parameters. In any case, it appears likely that binary evolution provides a

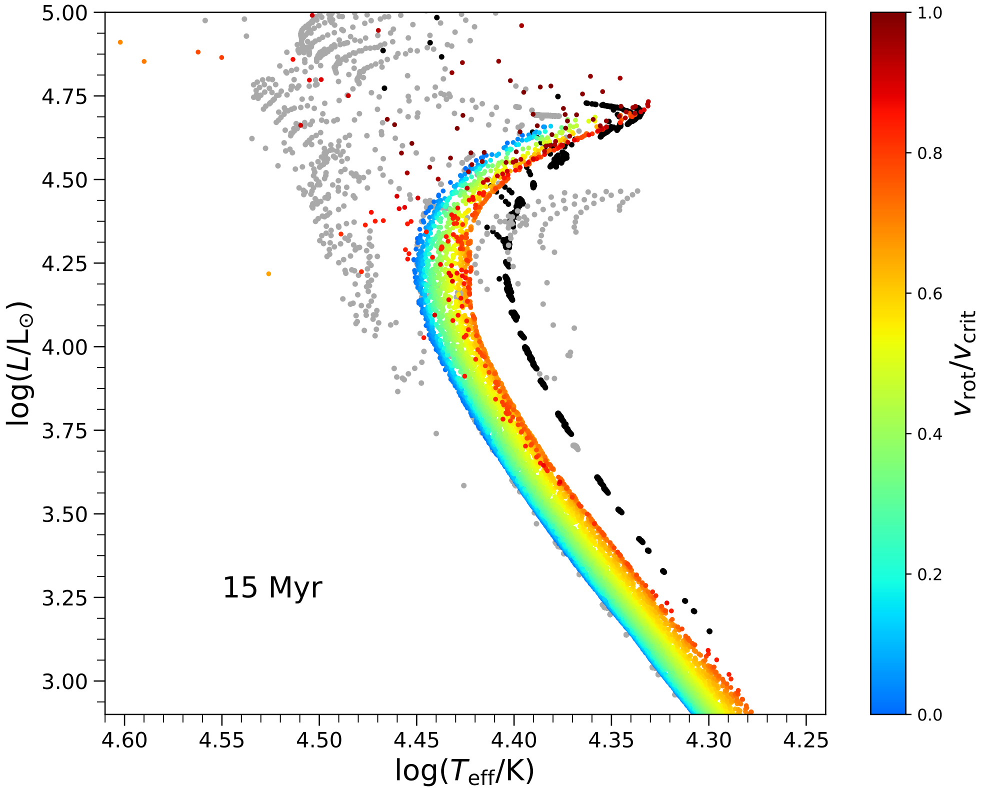

Figure 2.4: Distribution of 10,000 simulated single stellar models (colored dots) obtained from interpolating in the dense grid of the single-star evolution model of Brott et al. (2011), taking into account the initial mass function and the distribution of the initial rotation velocities derived by Dufton et al. (2013), at 15 Myr. The color represents the ratio of rotation to critical rotation velocity at an age of 15 Myr, according to the color bar to the right. Overlaid are our binary-evolution models models using grey and black dots, at the same age, with black indicating a ratio of rotation to critical rotation velocity above 0.98.

significant, perhaps dominant, contribution to the extended turnoffs in young star clusters.

The occurrence of the RBF in our models is a genuine binary-evolution effect and does not depend on the choice of initial rotation rates. The effectiveness of accretion-induced spin-up in nature is demonstrated by the observed group of Be/X-ray binaries, which are understood as rapidly rotating B stars that have accreted from the progenitors of neutron star companions (L. Wang, Gies and Peters, 2018). We therefore identify our RBF models, which all rotate extremely rapidly (see Fig. 2.3), as Be stars (Pols et al., 1991). Recent photometric and spectroscopic results show that a significant fraction of the MS stars in young clusters ($\lesssim$ 100 Myr) within two to three magnitudes below the turnoff are Be stars (Milone, Marino, Di Criscienzo et al., 2018; J. Bodensteiner et al., 2019). As demonstrated by our animation (Fig. 2.3), noting that a difference of 2.5 mag corresponds to a factor of 10 in luminosity, this brightness range is well reproduced by our binary models. In Sect. 2.7.2 we relate this range analytically to the minimum mass ratio of stable Case B mass transfer, which thus can be directly determined from the quoted observations.

It has been shown by Ekström et al. (2008) that if stellar winds are not too strong, rotating single stars increase their fraction of critical rotation during the MS evolution, which may lead the initially fastest rotators to become Be stars. However, the transition to the Be stage occurs mostly at the end of core hydrogen burning. As shown by Hastings, C. Wang and Langer (2020), this would place the single Be stars very close to the cluster turnoff, which seems to disagree with the quoted observations. The only way to obtain single Be stars a factor of 10-30 below the turnoff luminosity in star clusters is that they are born with near-critical rotation. According to McSwain and Gies (2005), the number of such stars appears to be small. We conclude that it appears likely that binary evolution provides a significant, perhaps dominant, contribution to the Be star population in young star clusters, as suggested by Schootemeijer, Götberg et al. (2018) and Klement et al. (2019).

2.6 Concluding remarks

Our binary-evolution models produce several distinct morphological features of the MSs of star clusters younger than about 40 Myr. Given that our results emerge from generic binary-evolution model calculations, without applying any fine-tuning, it is striking that they quantitatively reproduce several of the main characteristics of observed MSs of open star clusters. This refers in particular to the extended turnoff region and the corresponding apparent age spread, as well as to the luminosity range of the Be stars in young clusters. Both effects are comprehensively demonstrated by our animation (Fig. 2.3).

This does not preclude the possibility that other factors are also important. As discussed above, the role of rapidly rotating single stars depends critically on the initial distribution of rotation rates. Also, non-coevality or differences in the initial chemical composition of the cluster stars may be important in some clusters. Our results imply that binary evolution is likely to play a major role in shaping the MSs of star clusters, as long a substantial fraction of the stars are born in binary systems. A detailed population synthesis study including all of the above factors will help us to confirm this picture, and will have strong implications for our understanding of star and binary formation and evolution, including the origin of the mass ratio and orbital period distribution of close binaries, and the IMF of stars.

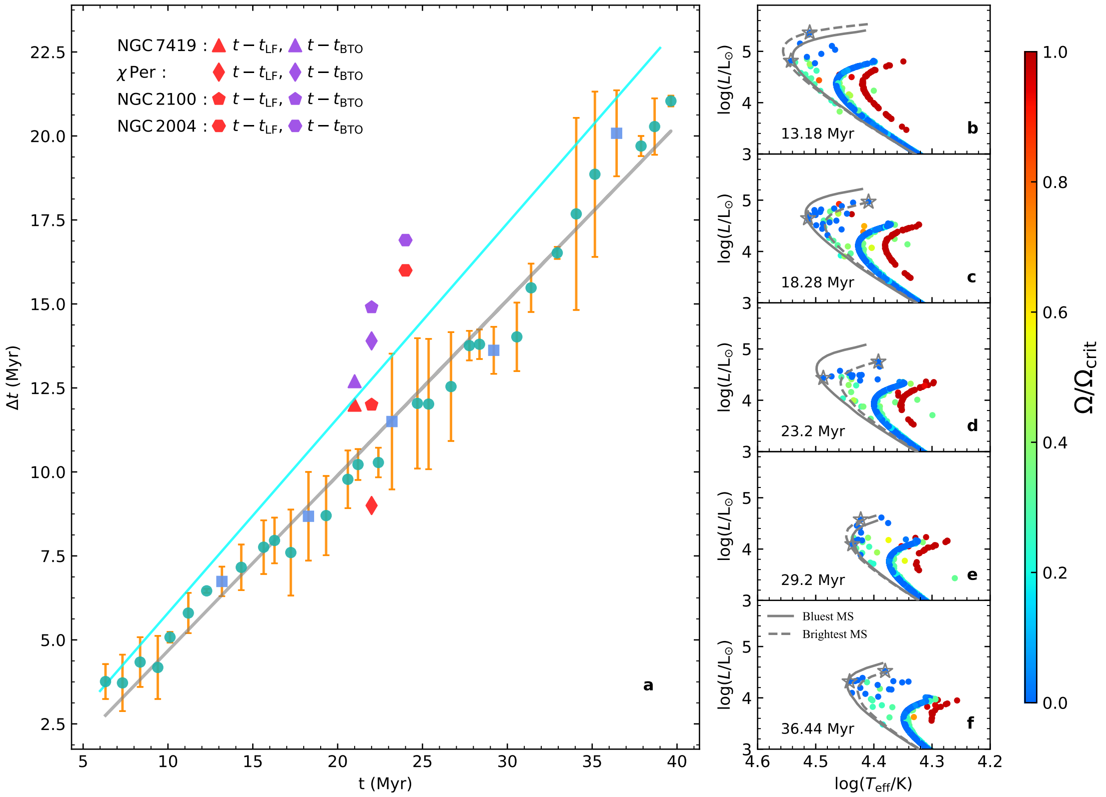

Figure 2.5: Age spread Δt inferred by the extended MS turnoff from the binary models as a function of cluster age t. To determine the apparent age of the extended turnoff stars in our simulated clusters, we first generate a series of single-star isochrones and then fit these isochrones via two methods, first, using the bluest MS star, and second, using the brightest MS star as to be fitted by the isochrone. Examples are shown in Panels (b) to (f), where the solid gray line describes the best-fitting isochrone for the first, and the dashed gray line describes the best-fitting isochrone for the second method. The model stars used for these fits are indicated by grey star symbols. In Panel (a) we show average of the result from the two methods for 33 different times as green symbols, where the examples from Panels (b) to (f) are marked by blue squares. The error bars represent the difference in the results from the two methods. The gray straight line represents a linear fit to the data as $\Delta t = 0.518t - 0.510$. We also show the results for two Galactic and two LMC clusters of Beasor et al. (2019). Here, we took the age derived from the lowest luminosity red supergiant as the true cluster age (Beasor et al., 2019; Britavskiy et al., 2019), and show the age discrepancy with the ages derived from the stellar luminosity function (red) and the brightest turnoff star (purple). We display our analytic estimate (Eq. 2.1) with a cyan line.

2.7 Appendix: Quantitative characterization of the main-sequence features

We quantify the features of the TBF, RBF, and BBF described in Fig. 2.1 in Section 2.7.1, 2.7.2, and 2.7.3, respectively.

2.7.1 Appendix A: TBF (Turnoff binary-evolution feature)

The apparent age spread indicated by the extended turnoff region is about half of the true age of the simulated stars (see Figure 2 of Niederhofer, Georgy et al., 2015). This compares well with simple estimates of the binary rejuvenation due to mass accretion and stellar mergers. For a mass-luminosity relation as $L \propto M^{\alpha}$, and a hydrogen burning lifetime of a star of mass M as $\tau \propto M/L$, the lifetime ratio of two stars is $\tau_1/\tau_2 = (M_1/M_2)^{1-\alpha}$, while their luminosity ratio is $L_1/L_2 = (\tau_1/\tau_2)^{\alpha/(1-\alpha)}$. The maximum possible stellar mass in a cluster with a single-star turnoff mass of $8\,\mathrm{M}_\odot$ (corresponding to M_1 in the equations above), will be about $14.4\,\mathrm{M}_\odot$ ($= M_2$), i.e., the result a merger of two $8\,\mathrm{M}_\odot$ stars (90% of $16\,\mathrm{M}_\odot$). Therefore, we obtain an equation for the apparent age spread $\tau_1 - \tau_2$ in our cluster with an age τ_1 that is linear in τ_1, as

$$\tau_1 - \tau_2 = \left[1 - \left(\frac{M_1}{M_2}\right)^{\alpha-1}\right]\tau_1, \tag{2.1}$$

and for $M_1/M_2 = 8/14.4$ and for $\alpha = 2.5$, which holds approximately for stars of $14\,\mathrm{M}_\odot$ and is only a weak function of the mass (see Figure 17 of Köhler et al., 2015), we obtain $\tau_1 - \tau_2 = 0.58\tau_1$.

2.7.2 Appendix B: RBF (Red binary-evolution feature)

We note that our MESA models may underestimate the effect of the centrifugal force on the outermost parts of the stellar models for a rotation faster than about 90% of critical rotation (Paxton, Smolec et al., 2019). Furthermore, they do not account for the presence of a decretion disk, which may make the star appear redder than predicted here (Rivinius, Carciofi and Martayan, 2013). This does induce an uncertainty in the predicted effective temperature, or any magnitude or color computed from it.

The extent of the RBF in luminosity is determined by the minimum mass ratio for stable mass transfer. For example, at a turnoff masses of $20\,\mathrm{M}_\odot$ (corresponding to $t \simeq 10\,\mathrm{Myr}$), the minimum initial mass ratio $q_{\mathrm{min,B}}$ for which a merger during the Case B mass transfer is avoided is $q_{\mathrm{min,B}} \simeq 0.3$, i.e., the minimum stellar mass on the RBF is about $6\,\mathrm{M}_\odot$ (as little mass is accreted). Just from the mass difference, using the mass-luminosity relation of the form $L \propto M^{\alpha}$ with $\alpha \simeq 2.5$ (Köhler et al., 2015) implies a luminosity ratio between the brightest and the dimmest RBF star of 20 (1.31 dex). However, due to the large mass difference, while the brightest RBF star is about to finish core hydrogen burning, the dimmest ones are essentially unevolved. We therefore need to consider the difference in the average mean molecular weight μ of the stars, which contributes to the luminosity difference as $L \propto \mu^{\beta}$. An initial mean molecular weight of $\mu_{\mathrm{SMC}} = 0.59$, the mean molecular weight of helium as $\mu_{\mathrm{He}} = 4/3$, and an average convective core mass fraction of $q_{\mathrm{core}} = 0.25$, yield an average mean molecular weight of our brightest RBF star of $\bar{\mu} = 0.69$, which, with $\beta \simeq 4.5$ (see Figure 17 of Köhler et al., 2015), yields another factor of 2.02 (0.31 dex) for the luminosity ratio, resulting in a total of 41 (1.61 dex), i.e., in more general terms, the luminosity ratio between the brightest and the dimmest RBF star is

$$\frac{L_{\rm top}}{L_{\rm bottom}} = \left(\frac{\mu_{\rm He}}{\mu_{\rm SMC} q_{\rm core} + \mu_{\rm He}(1 - q_{\rm core})}\right)^{\beta} \left(\frac{1}{q_{\rm min,B}}\right)^{\alpha} . \tag{2.2}$$

Considering the dependence of $q_{\rm min,B}$ on cluster age, i.e., for $t \lesssim 15$ Myr we have $q_{\rm min,B} \lesssim 0.3$, which rises to $q_{\rm min,B} \lesssim 0.6$ at 20 Myr and 0.7 at 30 Myr and beyond, the above equation leads to a good characterization of the RBF for the different times shown in Fig. 2.1.

Due to mass accretion during Case B, the fraction of RBF stars near the turnoff region will be naturally close to one, as observed in many young clusters. At lower luminosities, the RBF star fraction will be proportional to the fraction of Case B binaries that avoid merging.

The temperature separation between RBF and SSI cannot be predicted well by our models. The reason is that the RBF stars rotate at more than 0.98% of critical rotation. The outer layers of current rotating 1D models are not well described for models beyond 0.90% of critical rotation (Paxton, Smolec et al., 2019).

2.7.3 Appendix C: BBF (Blue binary-evolution feature)

The BBF merges with extended turnoff stars at the highest luminosities. The minimum luminosity is determined in our models by the minimum initial mass ratio for which Case A contact evolution is avoided for at least a fraction of core hydrogen burning, which is $q_{\rm min,A} = 0.7$ for an initial donor mass of $M_{\rm 1,i} = 10\,{\rm M}_{\odot}$, and $q_{\rm min,A} = 0.35$ for an initial donor mass of $M_{\rm 1,i} = 20\,{\rm M}_{\odot}$. We note that our predictions for the evolution of contact systems must be considered as very uncertain, as our models do not allow for heat flows between the two components. Therefore, the more realistic values of $q_{\rm min,A}$, as well as the number of blue MS stars, may differ significantly from those obtained in our calculation.

CHAPTER 3

Slowly and moderately rotating stars as the constituents of the split main sequences in young star clusters

Chen Wang, Ben Hastings, Abel Schootemeijer, Norbert Langer, and Pablo Marchant

To be submitted

Author contributions: C.W. and B.H. performed the analyses on the single star models computed by A.S.. N.L. contributed to interpret the results. P.M. performed early work on computing star models with MESA code. C.W. wrote the original draft. B.H., A.S. and N.L. contributed to polish and improve the draft.

Abstract

Spectroscopic studies in young open clusters have revealed that the distribution of stellar rotational velocities shows evidence of a dichotomy, with 10~30% of stars rotating slowly and the remaining 70~90% rotating fairly rapidly. At the same time, accurate photometry of young star clusters shows a split main sequence, which is again interpreted as a spin dichotomy. Whereas recent papers suggest that extreme rotation is required to retrieve the photometric split, we use both our new grid of rotating MESA models and the prevalent SYCLIST models to show that slow (0−30% of critical velocities) and intermediate (50−60% of critical velocities) rotation are able to explain the photometric split. These values are consistent with the spectroscopic studies of field stars and cluster stars. We argue that these values resemble the birth spin distributions of upper main sequence stars. Our models with initial velocities larger than 40% of their break-up values exhibit a notable surface nitrogen enrichment at the end of their main-sequence evolution. Consistent with previous studies, we find that initially moderately rotating single stars are able to achieve near critical rotation before they finish hydrogen burning. However, this only happens near the end of their main-sequence evolutions, which implies that binary interaction is indispensable in explaining the observed faint Be stars up to two magnitudes below the turn-off in young star clusters.

3.1 Introduction

Rotation has a profound impact on stellar structure and evolution (see Maeder and Meynet, 2000, for a review). On the one hand, it makes a star oblate, reducing its effective gravity, thereby reducing the flux and temperature at its equator, as described by von Zeipel theorem (von Zeipel, 1924). On the other hand, rotation is also predicted to trigger internal mixing in the stellar interior (Endal and Sofia, 1978), during which fresh hydrogen is injected into the stellar center, while nuclear-burning products are dragged up to the stellar surface. As a consequence, rotationally-induced mixing extends the main-sequence (MS) lifetime of a rotating star and makes it more luminous and hotter than its non-rotating counterpart. The position of a rotating star in the Hertzsprung-Russell diagram (HRD) or color-magnitude diagram (CMD) is determined by the competition between these two opposite effects.

A bimodal equatorial rotational velocity distribution has been found in early B type stars ($7-15\,\mathrm{M}_\odot$) in the Tarantula nebula, peaking at $0 \leq v_\mathrm{e} \leq 100\,\mathrm{km\,s^{-1}}$ and $200 \leq v_\mathrm{e} \leq 300\,\mathrm{km\,s^{-1}}$ (Dufton et al., 2013). It is similar to the previously reported bimodal distribution in the Galactic field late B- and early A-type stars in a range of $2.5-4\,\mathrm{M}_\odot$ (Zorec and Royer, 2012). Differently, stars with masses between $1.6\,\mathrm{M}_\odot$ and $2.3\,\mathrm{M}_\odot$ are found to have unimodal distribution with a lack of stars slower than $50\,\mathrm{km\,s^{-1}}$ (Zorec and Royer, 2012). The existence of a substantial fraction of rapid rotators has implications for star clusters that are believed to be composed of simple single non-rotating stars in one starburst. For example, it will affect the accuracy of cluster age estimation in which non-rotating star models are employed (Beasor et al., 2019).

Recent high-precision photometric studies from Hubble Space Telescope (HST) have indeed shown that cluster components cannot be described by one simple isochrone in both old (~10 Gyr) massive globular clusters in our Milky Way (see Bastian and Lardo, 2018, for a review) and in young and intermediate-age (from 14 Myr to 2 Gyr) star clusters in the Large and Small Magellanic Clouds (LMC and SMC, respectively) (Milone, Bedin, Piotto and J. Anderson, 2009; Milone, Bedin, Piotto, Marino et al., 2015; Milone, Marino, D'Antona, Bedin, Da Costa et al., 2016; Milone, Marino, D'Antona, Bedin, Piotto et al., 2017; Milone, Marino, Di Criscienzo et al., 2018; C. Li, de Grijs et al., 2017; C. Li, Sun et al., 2019; D'Antona, Milone et al., 2017; Bastian, Kamann, Cabrera-Ziri et al., 2018; Lim et al., 2019). In the CMD, this phenomenon is characterized by a split of the MS, with the blue MS containing 10-30% stars and the red MS containing 70-90% stars (for clusters younger than 1 Gyr), and an extended main sequence turn-off (eMSTO) (for clusters younger than 2 Gyr). In addition, Cordoni et al. (2018) analyzed Gaia data and found that the eMSTO is also seen in Galactic open clusters younger than 2.5 Gyr, while the feature of the split MS only occurs in clusters younger than 700 Myr. These findings challenge our traditional view that star clusters are made up of stars of the same age, chemical composition and rotation. Despite a great deal of theoretical work, the physical mechanism leading to such a complex MS morphology in young Magellanic Cloud clusters remains unclear.

A prolonged star formation history is one of the most intuitive ways to explain the perceived age spread within the star clusters (Mackey, Broby Nielsen et al., 2008; Goudfrooij, Puzia et al., 2011). Whereas the old massive globular clusters of our Milky Way are found to comprise at least two distinct stellar populations with different chemical compositions (Bastian and Lardo, 2018), stars in the young and intermediate-age LMC and SMC clusters have been shown to have nearly the same chemical composition (Mucciarelli et al., 2014), which argues against real age differences. Besides, though age difference can produce an eMSTO, it cannot explain the observed split MS because unevolved MS stars occupy nearly the same positions at different ages.

Rotation is proposed as an alternative scenario to interpret the MS morphology, including both the eMSTO and the split MS, in young star clusters (Bastian and S. E. de Mink, 2009; Yang, Bi et al., 2013; Brandt and C. X. Huang, 2015; Niederhofer, Georgy et al., 2015; D'Antona, Di Criscienzo et al., 2015; Correnti, Goudfrooij, Bellini et al., 2017). For the eMSTO, rotation alone is not enough to explain the observed large extended distribution of the turn-off stars, and an additional age difference is usually required (e.g. D'Antona, Milone et al., 2017; Gossage et al., 2019). As to the split MS, no consensus on how much rotation is needed to match the observed color split has been achieved. By comparing the prevalent single star models SYCLIST [1] (Georgy, Ekström, Granada et al., 2013) with observations, it has been proposed that two populations consisting of non-rotating stars and stars with 90% of critical angular velocities are required (see D'Antona, Milone et al., 2017; Milone, Marino, Di Criscienzo et al., 2018, and references therein). This interpretation is supported by the large fraction of the Be stars observed in the young massive LMC clusters NGC 1850 and NGC 1856 (Bastian, Cabrera-Ziri et al., 2017). However, it is unlikely that the majority of stars are born with near-critical rotation. In reality, a B-star study of W. Huang, Gies and McSwain (2010) has reported that non-evolved critically rotating stars should be scarce ($< 1.3\%$). From the observational side, the detected Be stars in young star clusters are almost all located within two magnitudes below the turn-off, which contradicts the idea that unevolved stars are critically rotating. Meanwhile, the peak of the fast component in the above-mentioned bimodal distribution for B/A-type stars (Zorec and Royer, 2012; Dufton et al., 2013) only corresponds to 50-60% of critical rotation. The strongest evidence that opposes the red MS comprising near-critical rotating stars arises from the spectroscopic measurements of the red MS stars in young and intermediate-age clusters, which find a mean equatorial rotational velocity $v \sin i$ of $\sim 202 \pm 23\,\mathrm{km\,s^{-1}}$, much smaller than the critical velocities ($\sim 400 - 500\,\mathrm{km\,s^{-1}}$) of these stars (Marino et al., 2018; Sun, de Grijs et al., 2019; Sun, C. Li et al., 2019; Kamann, Bastian, Gossage et al., 2020).

In this paper we propose that slow and intermediate rotation are sufficient to explain the split MSs. We will show that, counter-intuitively, this is in agreement with previously inferred near-critical rotation velocities, and that the differences are the result of, firstly, how the fraction of critical rotation is defined and, secondly, an early spin-down phase of the SYCLIST models. We have computed new rotating stellar models with MESA that include efficient core-envelope coupling mediated by internal magnetic fields, which is not included in the SYCLIST models. We compare our models with both photometric and spectroscopic observations of the MS stars in the LMC cluster NGC 1818. Thereby, we attempt to constrain the rotational velocities of the red and blue MS stars in young Magellanic Cloud clusters and discuss their implications on the formation of Be stars. The layout of the paper is as follows. Section 3.2 explains different definitions of the critical rotational velocity. Section 3.3 describes the physics and assumptions used in computing our single star models. Our results and comparisons with the observations are presented in Section 3.4. At last, we summarise our conclusions in Section 3.5.

3.2 Different definitions of the critical rotational velocity

Several definitions of the critical velocity of a rotating star exist. Here, we differentiate them and attempt to eliminate misunderstandings. Rivinius, Carciofi and Martayan (2013) have clarified different types of critical rotational velocities and their relations. Here, we briefly summarize their definitions using SYCLIST and MESA star models as examples.

---

[1] https://www.unige.ch/sciences/astro/evolution/en/database/syclist/

The critical velocity used in SYCLIST models and most of the literature is computed in a critically rotating star model, i.e., the supposed equatorial radius the star model would have at critical rotation is used. It takes into account the fact that a star increases its radius as it approaches critical rotation. The critical velocity under this definition, in the framework of the Roche approximation, is expressed as:

$$v_{\mathrm{crit,SYCLIST}} = \sqrt{\frac{GM}{R_{\mathrm{e,crit}}}} = \sqrt{\frac{2}{3}\frac{GM}{R_{\mathrm{p,crit}}}}, \tag{3.1}$$

in terms of linear rotational velocity, and

$$\Omega_{\mathrm{crit,SYCLIST}} = \sqrt{\frac{GM}{R^3_{\mathrm{e,crit}}}} = \sqrt{\frac{8}{27}\frac{GM}{R^3_{\mathrm{p,crit}}}}, \tag{3.2}$$

in terms of angular rotational velocity. Here $R_{\mathrm{e,crit}}$ and $R_{\mathrm{p,crit}}$ are the equatorial radius and the polar radius of a critically-rotating star, respectively. The factor $2/3$ comes from the relation $R_{\mathrm{e,crit}} = 3/2R_{\mathrm{p,crit}}$ in a critically rotating star, in the framework of the Roche approximation. In general, the variation of the polar radius due to rotation is marginal, such that we can use $R_{\mathrm{p,crit}}/R_{\mathrm{P}} \simeq 1$ as a good approximation, where R_{P} is the polar radius of a star with an arbitrary rotational rate. Thus it is possible to calculate $\Omega_{\mathrm{crit,SYCLIST}}$ and $v_{\mathrm{crit,SYCLIST}}$ without a numerical model of a critically-rotating star.

However, MESA adopts a different definition, in which current equatorial radius R_{e} is used. The critical velocity and critical angular velocity are expressed as:

$$v_{\mathrm{crit,MESA}} = \sqrt{\frac{GM}{R_{\mathrm{e}}}} \quad \text{and} \quad \Omega_{\mathrm{crit,MESA}} = \sqrt{\frac{GM}{R^3_{\mathrm{e}}}}, \tag{3.3}$$

which are denoted by v_{orb} and Ω_{orb}, respectively, in Rivinius, Carciofi and Martayan (2013). The velocity in Eq. 3.3 corresponds to the Keplerian circular orbital velocity at the equator of a rotating star. Though this definition is not commonly used in literature, it perhaps is more physically meaningful when discussing Be stars as it directly tells us the required velocity of a star to eject material to its closest possible orbit just on top of the photosphere. Another set of single star models, MIST [2], built with MESA also uses this definition.

When describing how fast a star rotates, the ratio between the rotational velocity and the critical velocity is used more often than the absolute rotational velocity. One also needs to distinguish between linear velocity and angular velocity under this circumstance. Under the SYCLIST definition, the relation between the fractional linear critical velocity and the fractional angular critical velocity is given by:

$$\frac{v_{\mathrm{e}}}{v_{\mathrm{crit,SYCLIST}}} = \frac{\Omega_{\mathrm{e}} R_{\mathrm{e}}}{\Omega_{\mathrm{crit,SYCLIST}} R_{\mathrm{e,crit}}} = \frac{\Omega_{\mathrm{e}}}{\Omega_{\mathrm{crit,SYCLIST}}} \frac{R_{\mathrm{e}}}{R_{\mathrm{P}}} \frac{R_{\mathrm{p}}}{R_{\mathrm{p,crit}}} \frac{R_{\mathrm{p,crit}}}{R_{\mathrm{e,crit}}} \simeq \frac{2}{3} \frac{R_{\mathrm{e}}}{R_{\mathrm{p}}} \frac{\Omega_{\mathrm{e}}}{\Omega_{\mathrm{crit,SYCLIST}}}. \tag{3.4}$$

---

[2] http://waps.cfa.harvard.edu/MIST/

Here v_e and Ω_e are the equatorial linear and angular velocities, respectively. It can be seen that, in general, the fractional linear velocity is smaller than the fractional angular velocity, unless a star is a non- or critically-rotating star. Whereas under the MESA definition, the fractional linear and angular velocities are identical, i.e., $v_\mathrm{e}/v_\mathrm{crit,MESA} = \Omega_\mathrm{e}/\Omega_\mathrm{crit,MESA}$. For non-critically rotating stars, one has $v_\mathrm{e}/v_\mathrm{crit,MESA} < v_\mathrm{e}/v_\mathrm{crit,SYCLIST} < \Omega_\mathrm{e}/\Omega_\mathrm{crit,SYCLIST}$.

In this work, we always refer to the MESA definition when discussing critical rotation, i.e, $v_\mathrm{crit} = v_\mathrm{crit,MESA}$, because we mainly use our MESA models to investigate the role of rotation in splitting the cluster MS. In order to compare the results from our models with those from the SYCLIST models, we convert $\Omega_\mathrm{e}/\Omega_\mathrm{crit,SYCLIST}$ and $v_\mathrm{e}/v_\mathrm{crit,SYCLIST}$ in the SYCLIST models to $v_\mathrm{e}/v_\mathrm{crit,MESA}$ with the following equation (Rivinius, Carciofi and Martayan, 2013):

$$\frac{v_\mathrm{e}}{v_\mathrm{crit,MESA}} = \sqrt{\left(\frac{v_\mathrm{e}}{v_\mathrm{crit,SYCLIST}}\right)^3 \frac{\Omega_\mathrm{crit,SYCLIST}}{\Omega_\mathrm{e}}}. \tag{3.5}$$

We found that SYCLIST star models with formally labeled $\omega_\mathrm{label} = \Omega_\mathrm{e}/\Omega_\mathrm{crit,SYCLIST} = 0.9$ are in fact not rotating near-critically due to two issues. The first one is that SYCLIST rotating models have a relaxation phase at the very beginning of their MS evolution, during which their rotational velocities drop dramatically as meridional circulation transports angular momentum from the outer layers of the star to the inner layers (Ekström et al., 2008). After such relaxation, the formally labelled $\omega_\mathrm{label} = 0.9$ models drop to $\Omega_\mathrm{e}/\Omega_\mathrm{crit,SYCLIST} \sim 0.8$. The relaxation period lasts for a few percent of the stars' MS lifetimes. The decrease of the surface rotational velocity is more substantial in models with higher initial ω_label values. The second one is that 0.8 in terms of critical angular velocity fraction under the SYCLIST definition roughly corresponds to 0.5 in terms of critical linear (as well as angular) velocity fraction under the MESA definition. In reality, recent MIST models have indeed proven that the color difference between star models with 50% of critical rotation and zero rotation is sufficient to explain the observed color split in a ~ 200 Myr LMC star cluster NGC 1866 (Gossage et al., 2019). However, they focus their attention on the eMSTO region that is affected by gravity darkening, internal mixing, Be stars, and post-interaction binaries (Yang, Meng et al. 2011; Schneider, Izzard, Langer et al. 2015; Yang 2018; Hastings, C. Wang and Langer 2020; C. Wang et al. 2020), and thus cannot explicitly decipher the impact of rotation on the distribution of the MS stars in young star clusters.

3.3 Input physics and assumptions in stellar models

We use the detailed one-dimensional stellar evolution code MESA, version 12115, (Paxton, Bildsten et al., 2011; Paxton, Cantiello et al., 2013; Paxton, Marchant et al., 2015; Paxton, Smolec et al., 2019) to compute single star models. The stellar models include differential rotation, rotationally induced internal mixing, magnetic angular momentum transport, stellar wind mass loss, and non-equilibrium CNO nucleosynthesis. The adopted physics are based on Brott et al. (2011) and are identical to those utilised in Schootemeijer and Langer (2018) and the rotating models in Schootemeijer, Langer et al. (2019), except for a mass-dependent overshooting parameter and that we disable the controls that govern time smoothing in rotational mixing. We briefly summarise the most relevant assumptions here and compare them with those used in other model sets.

We use the standard mixing-length theory to model convection with a mixing length parameter of $\alpha = l/H_\mathrm{P} = 1.5$, where H_P is the local pressure scale height. The boundary of the convective core is determined by the Ledoux criterion. Convective eddies penetrate deeper into the radiative zone due to their non-zero velocities at the boundary, known as convective overshooting. It introduces a large uncertainty in stellar internal mixing and consequently affects stellar evolution. We adopt step-overshooting that extends the convective zone by $\alpha_{\rm OV}H_{\rm P}$, where $\alpha_{\rm OV}$ increases linearly from 0.1 at $1.66\,\mathrm{M}_\odot$ to 0.3 at $20\,\mathrm{M}_\odot$, because $\alpha_{\rm OV}$ is thought to be lower at lower mass (Claret and Torres, 2016). Below $1.66\,\mathrm{M}_\odot$, $\alpha_{\rm OV}$ linearly decreases more rapidly such that it reaches zero at $1.3\,\mathrm{M}_\odot$ (where the convective core disappears). In the SYCLIST modes, the same expression is used a fixed $\alpha_{\rm OV}$ of 0.1. While in the MIST models, an exponentially decaying diffusion coefficient is applied, which is roughly equivalent to $\alpha_{\rm OV} = 0.2$ in terms of step overshooting. A larger convective overshooting parameter results in a larger convective core and a longer MS lifetime as a consequence. We adopt a semiconvection mixing efficiency parameter of $\alpha_{\rm SC} = 10$ (Schootemeijer, Langer et al., 2019), and a thermohaline mixing efficiency of $\alpha_{\rm th} = 1$ (Cantiello and Langer, 2010).

The rotationally enhanced mixing is modelled as diffusive processes (Heger, Langer and Woosley, 2000) with parameters of f_c that scales the efficiency of composition mixing with respect to angular momentum transport, and f_μ that describes the stabilizing effect of mean molecular weight gradients. We adopt values of $f_c = 1/30$ (Chaboyer and Zahn, 1992; Marchant, Langer, Podsiadlowski, Tauris and Moriya, 2016) and $f_\mu = 0.1$ (Yoon, Langer and Norman, 2006), while the MIST models use the same f_c, but a different f_μ value of 0.05. A smaller f_μ value means a stronger rotational mixing even in the presence of a stabilizing chemical gradient. The effects of the dynamical and secular shear instabilities, the Goldreich-Schubert-Fricke instability, and Eddington-Sweet circulations are included. In the SYCLIST models, a more efficient diffusive-advective approach is taken when modeling rotational mixing, which makes their fast rotators brighter and hotter compared to our models and the MIST models with the same initial parameters. As to angular momentum transport, the implementation of the Tayler-Spruit dynamo (Spruit, 2002) in our MESA models imposes a strong coupling between the contracting core and the expanding envelope during stars' MS evolution, making our MESA models rotating nearly as solid-bodies. This process is not considered in the SYCLIST models, and consequently, the SYCLIST models rotate differentially and spin down more quickly at the surface than their MESA counterparts (Choi et al., 2016; Hastings, C. Wang and Langer, 2020). Differential rotation in the SYCLIST models leads to a strong shear mixing, which causes efficient rotational mixing in the SYCLIST models. These different implementations in different model sets are all able to explain some observations but struggle with others (see Choi et al., 2016, for example), meaning that the current observations cannot uniquely constrain the uncertain physics in star models.

The stellar structure of a rapidly rotating star deviates from spherical symmetry due to the presence of centrifugal force. In a one-dimensional stellar evolution code, this problem is circumvented by solving the stellar structure equations on the isobaric shells that have constant angular velocities (Meynet and Maeder, 1997). The radius coordinate is redefined as the radius of a sphere containing the same volume as the isobar. Within the framework of the Roche approximation that assumes all mass is concentrated in the stellar center, the ratio between the equatorial radius and the polar radius of a critically rotating star is 3/2. In MESA, two factors f_T and f_P, are introduced to correct the temperature and the pressure of a rotating star, such that the regular form of equations of non-rotating stars is retained (Endal and Sofia, 1976; Paxton, Cantiello et al., 2013). In MESA old versions, f_T and f_P are limited to specific values to ensure numerical stability, limiting the accuracy of computing the star models rotating at more than 60% of their critical velocities. However, in version 12115, which is the one we use, a new implementation of centrifugal effects allows for a precise calculation of stars up to 90% of their critical velocities (Paxton, Smolec et al., 2019).

We compute single star models with both LMC-like metallicity $Z_{\mathrm{LMC}} = 0.004841$ and SMC-like metallicity $Z_{\mathrm{SMC}} = 0.002179$. The helium abundance is assumed to decrease linearly from its primordial value $Y = 0.0.2477$ at $Z = 0$ (M. Peimbert, Luridiana and A. Peimbert, 2007) to $Y = 0.28$ at the solar metallicity of $Z = 0.017$ (Grevesse, Noels and Sauval, 1996). Thus we have $Y_{\mathrm{LMC}} = 0.2569$ and $Y_{\mathrm{SMC}} = 0.2518$. The abundances of the heavy elements are the same as those described in Brott et al. (2011). We build single star models of initial masses between 1.05 and 19.95 $\mathrm{M}_{\odot}$, which securely cover the magnitude range of the MS stars in the clusters studied in this paper (LMC cluster NGC 1818), with intervals of $\log M = 0.04$. For each mass, we construct nine evolutionary tracks with initial rotational velocities $W_{\mathrm{i}} = v_{\mathrm{e}}/v_{\mathrm{crit,MESA}}$ ranging from 0 to 0.8, in intervals of 0.1. We compute models from the zero-age MS (ZAMS) to the end of the central He burning phase.

We notice that our MESA models do not achieve thermal equilibrium initially, which causes wobbles in stellar radius, and in turn affects their critical velocities and rotational velocities. Unlike the SYCLIS models, the change of the rotational rate during this relaxation period in our MESA models is marginal, due to the implementation of a strong core-envelope coupling. To eliminate this initial relaxation, we redefine the ZAMS as the time when 3% of hydrogen is burnt in the core. We use the rotational velocity at that time as the initial velocity. To do this, we first remove all the MESA models before our redefined ZAMS phase and then assign the rotational velocity $W_{\mathrm{i}} = v_{\mathrm{e}}/v_{\mathrm{crit,MESA}}$ at the newly defined ZAMS as the new initial rotation. At last, we do interpolation to get star models rotating with precise W_{i} values between 0 to 0.75, in intervals of 0.05. To construct isochrones of the star models, we use the interpolation method described in (C. Wang et al., 2020) to obtain the stellar properties at certain ages.

To do temperature-luminosity to color-magnitude conversion, we obtain the absolute magnitude of a single star by $M = M_{\mathrm{bol}} - BC$, where $M_{\mathrm{bol}} = M_{\mathrm{bol},\odot} - 2.5\log(L/L_{\odot})$ is the bolometric magnitude of a star, BC is the bolometric correction. We use the same bolometric correction tables tailored for HST F814W and F336W filters as the MIST models [3], which are computed from 1D atmosphere models based on ATLAS12/SYNTHE (Kurucz, 1970; Kurucz, 1993). We adopt $M_{\mathrm{bol},\odot} = 4.74$ (Mamajek et al., 2015). The absorption coefficients are $A_{\mathrm{F814W}} = 2.04E(B-V)$ and $A_{\mathrm{F336W}} = 5.16E(B-V)$ (Milone, Marino, Di Criscienzo et al., 2018), where $E(B-V)$ describes the extinction.

We compare our models with the SYCLIST and MIST models. We first obtain the appropriate SYCLIST evolutionary tracks and isochrones with marked ω_{label} from 0.0 to 0.95. As mentioned in Sec. 3.2, the SYCLIST models use different definitions of critical rotational velocity from the MESA models. To achieve a coherent comparison between the MESA and the SYCLIST models, we also redefine the SYCLIST models' ZAMS phases and their initial rotational velocities, such that they have the same definition as our MESA models. We use Eq. 3.5 to do the conversion. We also do interpolation to the SYCLIST models to obtain the models rotating at the precisely required values. Since the MIST models only have two values of rotation $W_{\mathrm{i}} = 0.0$ and $W_{\mathrm{i}} = 0.4$ available to the public, we decide not to do any interpolation. Leaving the MIST models as their original results does not affect our comparison, because the MIST models have the same definition of critical velocity as our MESA models, and meanwhile the initial relaxation phase before ZAMS only affects the rotational velocity of these models marginally. We need to point out that in the SYCLIST models, metallicities $Z_{\mathrm{LMC}} = 0.006$ and $Z_{\mathrm{SMC}} = 0.002$ are tailored for the LMC and SMC stars. The MIST models have multiple metallicities available. We chose two values that are most similar to the adopted values in our MESA models, which are $Z_{\mathrm{LMC}} = 0.0452$ and $Z_{\mathrm{SMC}} = 0.00254$ for the LMC and SMC stars, respectively. We also need to point out that apart from different Z values, the abundance ratio of the heavy elements are also different in the SYCLIST models and our MESA models. The SYCLIST models simply use solar-scaled abundance ratios, while our models follow the initial chemical compositions in Brott et al. (2011) that are intended to match the observed OB stars in the LMC and SMC in the FLAMES survey (C. J. Evans et al., 2005). We find that the evolution of the MIST models and our MESA models are quite similar (see Fig. 3.5). Therefore, we focus on our MESA models and the SYCLIST models in this work.

---

[3] http://waps.cfa.harvard.edu/MIST/model_grids.html#bolometric

3.4 Results and discussions

3.4.1 Rotationally-induced color variation

We have discussed in Sec. 3.1 that the observed split MS in young star clusters can be interpreted by stars with different rotation. The evolutionary examples for stars with different rotation are shown in Sec. 3.6.1. But how much rotation is demanded to explain the observed color disparity between the red and blue MSs in young star clusters is controversial. In this section, we reinvestigate this problem by comparing the rotationally-induced color variation in the star models with the observations.

In Fig. 3.1, we show the color difference between the rotating stars and the non-rotating stars in our MESA models and the SYCLIST models at four evolutionary times, which are ZAMS, 80 Myr, 100 Myr and 200 Myr, with the last three times corresponding to the estimated age of the three LMC clusters, NGC 1755, NGC 2164 and NGC 1866, whose split MS features have been studied in detail (see fig. 5 in Milone, Marino, D'Antona, Bedin, Da Costa et al. 2016 for NGC 1755, fig. 13 in Milone, Marino, Di Criscienzo et al. 2018 for NGC 2164 and fig. 6 in Milone, Marino, D'Antona, Bedin, Piotto et al. 2017 for NGC 1866, respectively). We make use of the established density distribution of the red and blue MS stars in these studies and plot the color difference between the peak of the red and blue MS star distributions with color dots and error bars in corresponding panels. The error bars on the x-axis represent photometric color error at corresponding magnitudes. The lines with caps on the y-axis correspond to the magnitude intervals. We convert the apparent magnitude of the observations to absolute magnitude using the distance modulus and reddening parameters provided in Milone, Marino, Di Criscienzo et al. (2018). We only show the unevolved/less-evolved observed stars, because the bright blue MS stars have a quite extended distribution and are proposed to be related to binary mergers (Schneider, Podsiadlowski et al., 2016; C. Wang et al., 2020).

For our MESA models, we also examine the influence of gravity darkening, which describes the dependence of a rotating star's brightness on its orientation. Gravity darkening makes a rotating star hotter and brighter if we see it pole-on, while cooler and dimmer if we see it equator-on. We use Eqs. 44 and 45 in Paxton, Smolec et al. (2019) to calculate this effect. The results are shown by shaded areas in Fig. 3.1, in which the left and right boundary represent pole-on and equator-on detection, respectively. At ZAMS, the effect of gravity darkening is more significant in more rapidly rotating stars, as anticipated. But the effect of gravity darkening also seems to be more outstanding in less massive stars. We argue that this is just a geometric consequence. Because the isochrones of stars with different initial rotational rates are almost parallel along the oblique direction (see Fig. 3.2); thus the horizontal color difference is larger in the low-mass star region where the slopes of the isochrones are shallower. While at other ages, the effect of gravity darkening first becomes smaller and then larger again from the bottom to the turn-off region. This is because gravity darkening either makes a star hotter and brighter if we see it pole-on, or cooler and dimmer if we see it equator-on. Therefore the net effect of gravity darkening shifts a star roughly along the direction of its isochrone. After the ZAMS, the isochrones near the turn-off bend towards the red side, making the net effect of gravity darkening outstanding.

Figure 3.1 yields three conclusions. Firstly, rotationally-induced color variations of the unevolved/less-evolved star models in our MESA models and the SYCLIST models are almost identical (see also Sec. 3.6.1). Secondly, after the ZAMS, Δcolor of the SYCLIST models decreases with decreasing magnitude, even to negative values, where the rotating models are bluer than their non-rotating counterparts. This is caused by the strong surface He enrichment in the SYCLIST models (see Sec. 3.6.1 and 3.6.2). In contrast, our rotating models are always redder than the non-rotating models. Finally, the color difference between the models with 50% of critical rotation, rather than the previously proposed near critical rotation, and the models with zero rotation is adequate to match the observed color split. We remind the reader here that 50% of critical rotation under the MESA definition roughly equals 60% of critical linear velocity and 75% of critical angular velocity under the SYCLIST original definition.

We notice that other combinations of initial rotation velocities of the blue and red MS may also explain the observed color split. We also use star models with $W_\mathrm{i} = 0.2$ and $W_\mathrm{i} = 0.3$ to anchor the blue MS and compute the color difference between these models and the models with more rapid rotation. The results are shown in Sec. 3.6.3. We do not consider even faster rotation for the blue MS, because spectroscopic measurements report a low average velocity for the blue MS stars (see Fig. 3.4). We find that $W_\mathrm{i} \sim 0.55$ and $W_\mathrm{i} \sim 0.6$ are required to retrieve the observed color split of the red and blue MS if we use $W_\mathrm{i} = 0.2$ and $W_\mathrm{i} = 0.3$ as anchors for the blue MS stars.

3.4.2 Comparison with the main-sequence stars in NGC 1818 in the CMD

In this section, we conduct a comparison between the theoretical isochrones and the LMC cluster NGC 1818 red and blue MS stars in the CMD, using what we have learned in Sec. 3.4.1. We show the distribution of the NGC 1818 normal MS stars and Hα emitters in the CMD in the left panel of Fig. 3.2 and perform the isochrone fitting in the right panel. We first reproduce the fitting in Milone, Marino, Di Criscienzo et al. (2018), who employ 40 Myr isochrones of the SYCLIST star models rotating at labelled 90% and 0% critical angular velocities, shown by the solid orange and dashed green lines, respectively. The adopted distance modulus and reddening are listed both in the figure and in Tab. 3.1. As mentioned above, the labelled 90% of critical angular velocities in the SYCLIST models roughly corresponds to half of the critical linear velocities under the definition of Eq. 3.3.

Then we utilize our MESA models with $W_\mathrm{i} = 0.5$ to fit the observed red MS. We adapt the isochrone age, distance modulus and reddening, such that the isochrone of such models can fit the observed red MS equally well as the SYCLIST models, in a visual inspection (see the solid red line in the right panel of Fig. 3.2). We find that a younger isochrone is required when using our MESA models than using the SYCLIST models, because strong rotational mixing makes the SYCLIST models appear younger than our MESA models near the turn-off. It implies that different conclusions may be drawn when using different model sets to evaluate a cluster's age. We notice that the derived distance modulus $\mu = 18.28$ from our MESA models is smaller than the measured LMC distance modulus of 18.48 (Pietrzyński et al., 2013; Inno et al., 2016). Distance moduli of 18.48 and 18.28 correspond to distances 49.7 kpc and 45.3 kpc away from us. The diameter of the LMC is around 5.2 kpc (Gaia Collaboration, Helmi et al., 2018), which is slightly small to explain the above mentioned distance

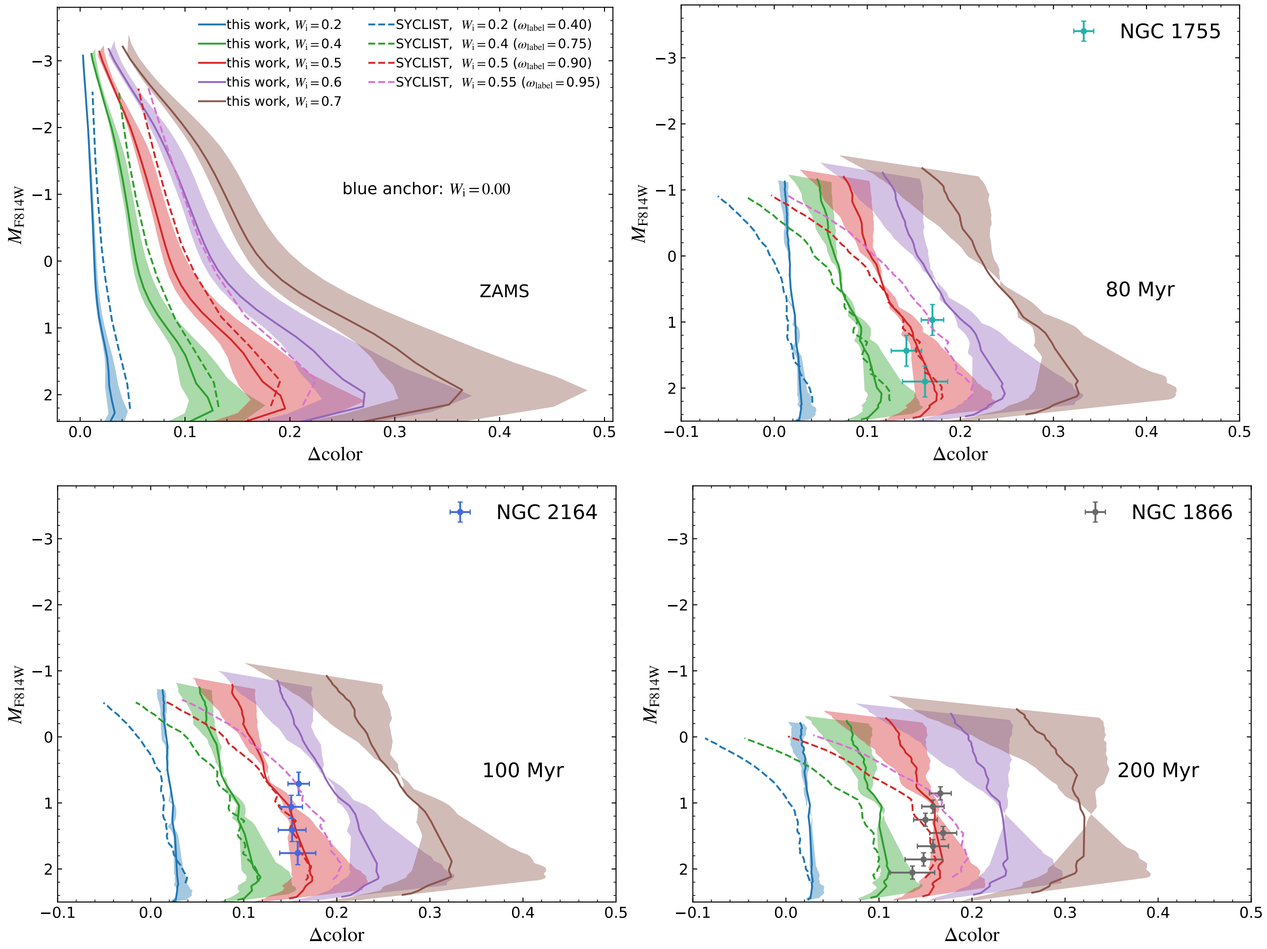

Figure 3.1: Color difference between the rotating and non-rotating LMC models as a function of magnitude at four different ages, which are ZAMS and the derived ages for three young LMC clusters NGC 1755 (80 Myr), NGC 2164 (100 Myr) and NGC 1866 (200Myr) (Milone, Marino, Di Criscienzo et al., 2018). The solid and dashed lines denote our MESA models and the SYCLIST models, respectively, with color indicating initial rotational rate. The formally labelled fractional critical angular velocities for the SYCLIST models in their web interface are shown in the parentheses. Shaded areas exhibit the effect of gravity darkening. Dots with error bars in the last three panels indicate the color difference between the star number distribution peaks of the observed blue and red main-sequence stars in the above-mentioned three clusters (see fig. 5 in Milone, Marino, D'Antona, Bedin, Da Costa et al. 2016 for NGC 1755, fig. 13 in Milone, Marino, Di Criscienzo et al. 2018 for NGC 2164, and fig. 6 in Milone, Marino, D'Antona, Bedin, Piotto et al. 2017 for NGC 1866 on the number distribution of the blue and red main-sequence stars, respectively).

difference. Nevertheless, we point out that the derived distance modulus is sensitive to the star models, especially the metallicity of the models. The SYCLIST models have higher metallicity than our MESA models. Meanwhile, the derived distance modulus and reddening depend also highly on the accuracy of the bolometric correction table. Any small changes in metallicity or bolometric correction values can cause a large difference in the derived distance modulus and reddening. The grey arrow in the right panel of Fig. 3.2 indicates how an isochrone will change if the reddening is increased by 0.05. After obtaining the parameters that can best match the observed red MS with our $W_\mathrm{i} = 0.5$ models, we apply them to the non-rotating models and plot the corresponding isochrone with the dashed dark blue line in the right panel of Fig. 3.2.

Figure 3.2 straightforwardly confirms our previous conclusion that stars with 50% and zero critical rotation are able to explain the observed red and blue MSs, in both the SYCLIST models and our MESA models. As expected, the SYCLIST isochrone of the fast-rotating models crosses the isochrone of the slowly-rotating models near the turn-off due to strong rotational mixing. It seems that our MESA models with inefficient mixing match the turn-off region better. However, considering the fact that the turn-off stars might be a mixture of fast rotating stars, whose positions are highly affected by gravity darkening, and binary interaction products, we cannot discard strong rotational mixing in the stellar interior. A plausible way to assess the efficiency of rotational mixing is to examine the surface abundance enrichment of the H burning products. We check the surface He and N enrichment of our rotating models and the SYCLIST models in Sec. 3.6.2. We find that both models exhibit strong N enrichment. While the strong surface He enrichment is only seen in the SYCLIST models. Further spectroscopic measurements on the surface abundance of the turn-off stars are needed to constrain rotational mixing efficiency.

As pointed out in Sec. 3.4.1, degeneracies exist when explaining the color split with rotation. The color separation between the models with $W_\mathrm{i} = 0.55$ and $W_\mathrm{i} = 0.20$, and between the models with $W_\mathrm{i} = 0.60$ and $W_\mathrm{i} = 0.30$ can also match the observed color difference between the red and blue MSs. In Fig. 3.10, we also exhibit the isochrone fitting with our MESA models based on these two combinations of initial rotation velocities. We see that they can fit the observed red and blue MSs equally well. Therefore, one cannot accurately determine the rotational velocities for the red and blue MS stars based on merely their positions in the CMD. Nevertheless, the conclusion that a bimodal distribution of the initial rotation with both slow and intermediate components is demanded to explain the split MS in young star clusters is rigid.

We notice that the red MS stars' distribution in the CMD in quite narrow, indicating that the red MS stars in young star clusters are born with nearly identical rotation, i.e. around 50% to 65% of their critical linear velocities. One may wonder whether we can predict the initial rotation distribution of the observed MS stars according to their positions in the CMD. Unfortunately, it is impossible at this moment because rotation is not the only factor relevant for the distribution of the observed MS stars. Unresolved binaries and photometric errors prevent us from such a prediction.

The significant population of sources above the red MS are probably unresolved binary systems. The presence of a second star in a coeval pre-interaction binary system makes the binary appear redder and brighter than its primary star alone. The stars on the left side of the $W_\mathrm{i} = 0.0$ isochrones are hot blue MS stars, which are proposed to be binary merger products that have experienced rejuvenation processes (Schneider, Podsiadlowski et al., 2016; C. Wang et al., 2020). There is also a population of Hα emitters on the top right side of the CMD down to around two magnitudes below the turn off. They are proven to be Be stars with Hα emitters, which are related to near critical rotation. We discuss the predictions of our MESA models on these Be stars in the next section.

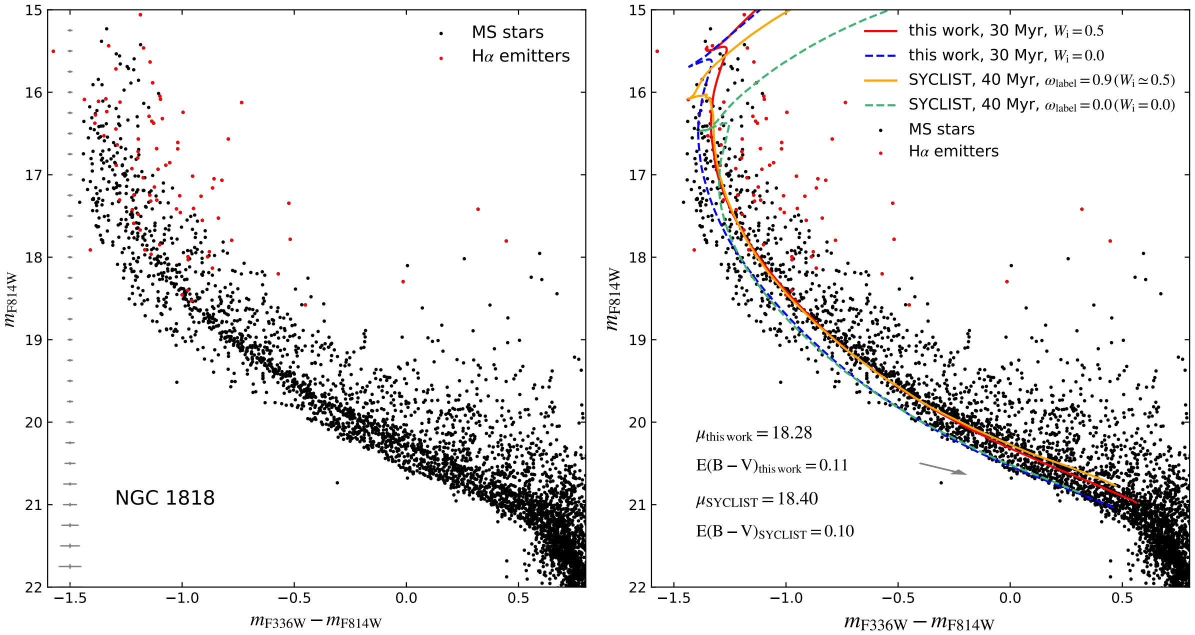

Figure 3.2: Left: high-precision HST observation of the LMC cluster NGC 1818. The black and red dots are normal main-sequence stars and stars with a brightness excess in the Hα narrow band filter. The red errorbars on the left indicate one sigma photometry error at corresponding magnitudes. Right: isochrone fit for the red and blue main sequences of NGC 1818, using the SYCLIST models and our MESA models. For the SYCLIST models, we take the fit in Milone, Marino, Di Criscienzo et al. (2018), using 40 Myr isochrones of the non-rotating models and the models with labelled 90% of critical angular velocities (roughly equal to 50% of critical linear velocities under the MESA definition) to fit the observed blue and red main sequences, indicated by the solid orange line and the dashed green line, respectively. While for our MESA models, we employ 30 Myr isochrones of the non-rotating models and the models with 50% of critical linear velocities to fit the observed blue and red main sequences, denoted by the solid red line and the dashed blue line, respectively. The adopted distance modulus and reddening in each fit are listed. The small grey arrow shows how the isochrones will move if we add 0.05 to $E(B-V)$.

Table 3.1: The adopted fitting models and the corresponding parameters for the LMC cluster NGC 1818.

Cluster	Galaxy	Fitting model	$W_{\rm i}$ for the red MS	$W_{\rm i}$ for the blue MS	Age (Myr)	μ	$E(B-V)$
NGC 1818	LMC	This work	0.5	0.0	30	18.28	0.11
NGC 1818	LMC	This work	0.55	0.2	30	18.29	0.09
NGC 1818	LMC	This work	0.60	0.3	30	18.31	0.09
NGC 1818	LMC	SYCLIST	0.5	0.0	40	18.40	0.10

3.4.3 Implications for the origin of Be stars

Two plausible ways are proposed for the formation of Be stars, i.e. the single star channel and the binary channel. Single stars can approach near-critical rotation at the end of their MS evolution, mainly due to the decrease of their critical velocities (Ekström et al., 2008; Hastings, C. Wang and Langer, 2020). While the accretors in binary systems spin up during mass transfer (Pols et al., 1991; Langer, 2012; C. Wang et al., 2020). The most compelling evidence supporting the binary channel is the detection of Be/X-ray binaries made up of a Be star and a compact object (Raguzova and Popov, 2005; Liu, van Paradijs and van den Heuvel, 2006). In this section, we examine to what extent the single channel may contribute to the origin of Be stars with our newly computed single star models with different initial rotation.

To achieve this goal, we investigate the minimum initial rotational rates required for single stars with different masses to reach velocities superior to particular values before they end their MS evolution. The results are shown in Fig. 3.3. We consider both our LMC and SMC models and consider different evolutionary stages (1% or 0.1% center H left) as the end of the MS evolution. Similar to Ekström et al. (2008) and Hastings, C. Wang and Langer (2020), we find that in general, more massive stars reach high velocities more easily, as can be seen by their smaller required initial rotational velocities to reach velocities superior to particular values at the end of their MS evolution, due to more efficient meridional mixing. We also find that mass loss plays an essential role in determining how fast a star can rotate. However, different from Ekström et al. (2008) and Hastings, C. Wang and Langer (2020) that reveal only the stars massive than ~20 $\mathrm{M}_\odot$ are spun down by the strong stellar wind, our models suffer strong stellar wind caused by the bi-stability jump, which happens at the end of the evolution of the stars in a mass range of 7 to 15 $\mathrm{M}_\odot$. Such strong stellar wind prevents the related models from rotating near critically, as can be seen in the first panel of Fig. 3.3, that no star models with masses between 8 and 14 $\mathrm{M}_\odot$ in our LMC grids can reach $v/v_{\mathrm{crit}} = 0.8$ at the end of their MS evolution. We remind the reader that we compute star models up to $W_{\mathrm{i}} = 0.75$. We do not attempt to assess different model sets as the adopted wind mass loss rate, the metallicity, chemical composition abundances and angular momentum transport are different in different model sets. Nevertheless, we agree with the previous studies that initially moderately rotating single stars are able to reach higher rotational rates at the end of their MS evolution.

The velocity threshold for a star to be a Be star is still unclear, which can be as low as $v/v_{\mathrm{crit}} = 0.65$ depending on the star's mass and the temperature (W. Huang, Gies and McSwain, 2010; Rivinius, Carciofi and Martayan, 2013, and references therein). If a threshold of $v/v_{\mathrm{crit}} = 0.7$ is adopted, Fig. 3.3 shows that in general stars with initial rotational rates of 40% to 50% of their critical values are able to evolve to Be stars. Lower initial rotational rates are required in more massive stars and in more metal-poor environment. In Sections 3.4.2 and 3.6.3, we have shown that the red MS stars in young star clusters should have natal spins of 50% -60% of their critical values, meaning that all these red MS stars are able to produce Be stars at the end of their MS evolution.

However, as Hastings, C. Wang and Langer (2020) has pointed out, the single channel can only account for the Be stars near the turn-off, and the dim Be stars down to two magnitudes below the turn-off can only be explained by the binary channel. We also examine this with our newly computed single star models and the SYCLIST models (see Sec. 3.6.4). We plot the current rotational velocities of our rotating models and the SYCLIST models as a function of magnitude in Sec. 3.11. Our results are in high agreement with Hastings, C. Wang and Langer (2020) that single star models only increase their rotational rates near the turn-off, below which they almost persist their initial spins. Therefore, single stars cannot explain the Be stars dimmer than around one magnitude below the turn-off, unless they are born to be Be stars. But then the question is why people rarely observe Be stars fainter than two magnitudes below the turn-off. From another point of view, if the Be stars produced by the single channel is prevalent, one would expect to detect a large amount of detached binary systems comprised of a Be star and a normal MS star or another Be star. However, J. Bodensteiner, Shenar and Sana (2020) reported a lack of MS companions to Be stars after examining 287 Galactic Be stars. Therefore, current theories and observations seem to advocate that binary channel plays the dominant role in producing Be stars.

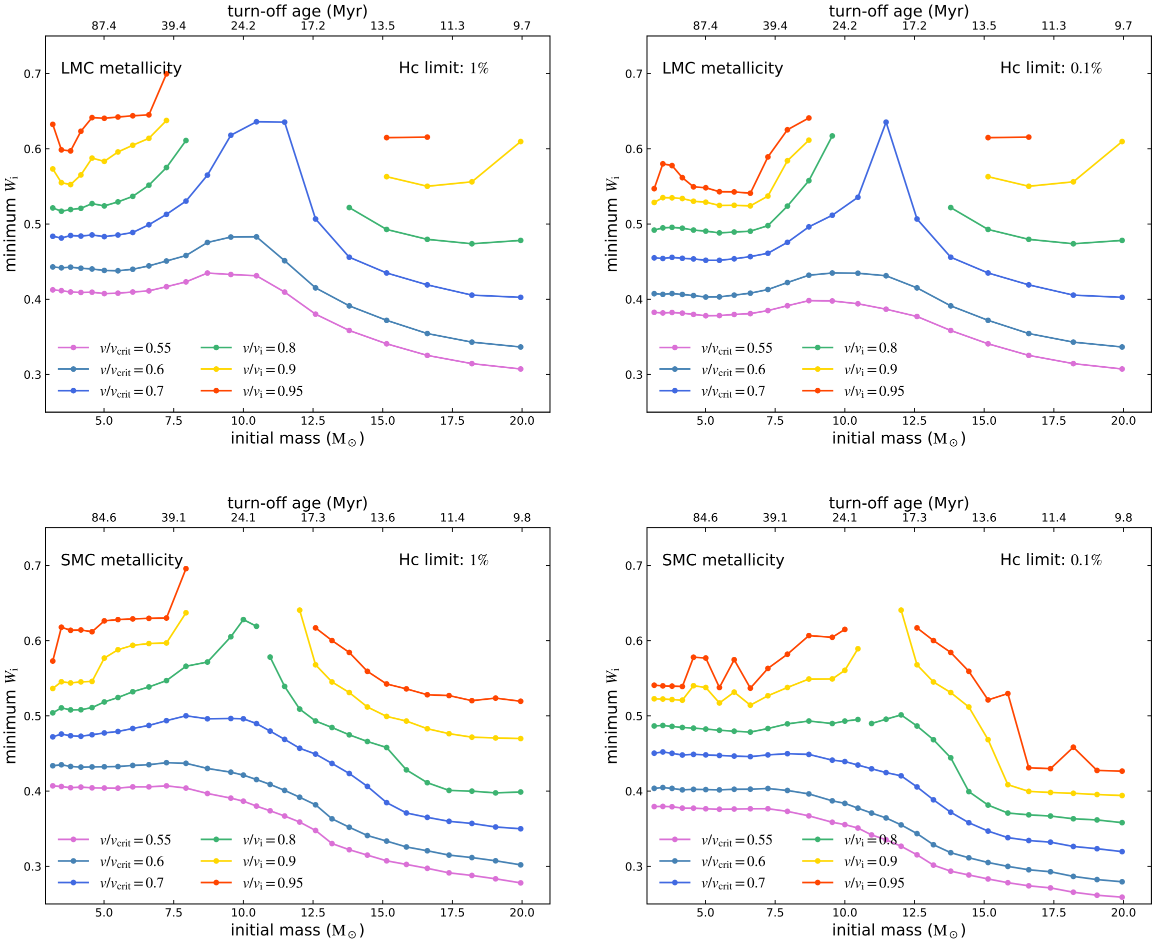

Figure 3.3: Minimum initial velocity for a star to reach a specific velocity at the end of its main-sequence evolution. The upper left and right panels show the results of our LMC metallicity models by assuming 1% of center H or 0.1% of center H left as the criterion of the terminal-age main sequence, respectively. While the lower panels correspond to the results of our SMC metallicity models under different terminal-age main sequence criteria. Colors indicate the velocity of a star at its terminal main sequence. Each dot on the lines represents one mass in our single star model grids. The top x-axis indicates the corresponding turn-off age of each mass in models with $W_i = 0.5$.

3.4.4 Comparison with the spectroscopic measurement of the NGC 1818 MS stars

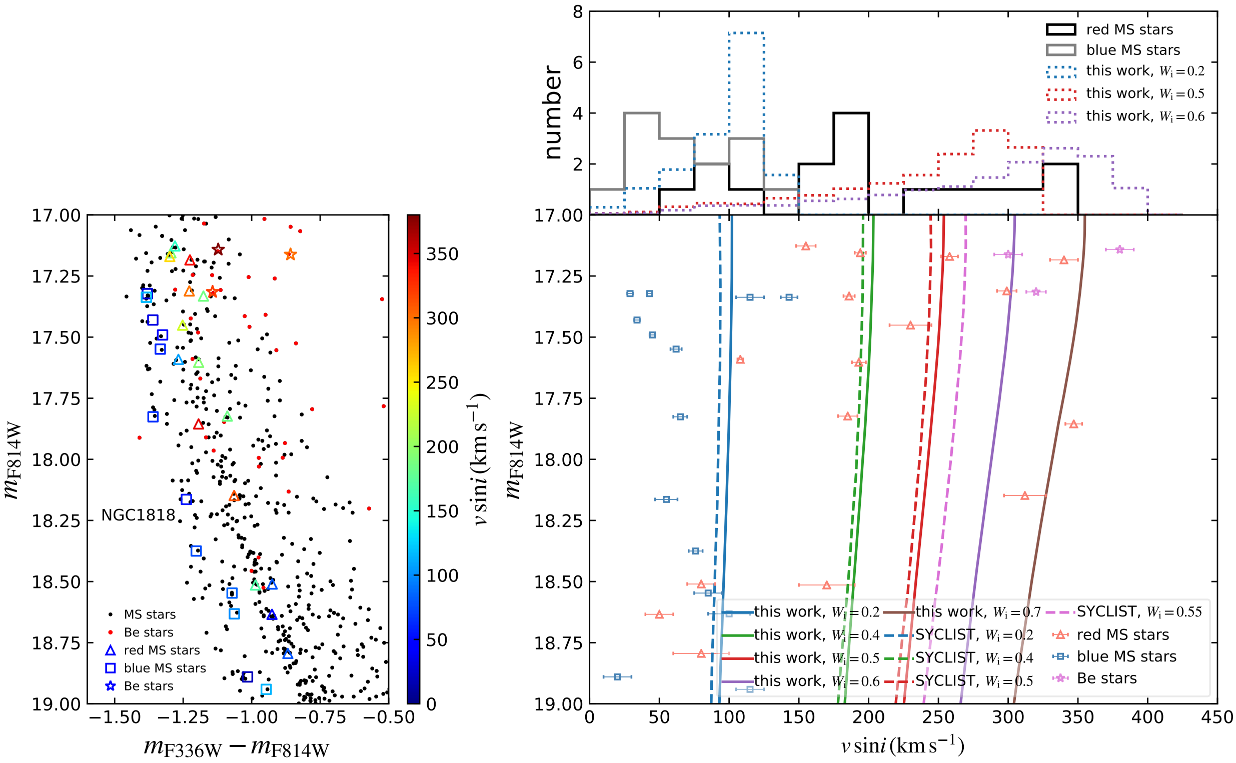

Figure 3.4: Left: distribution of the main-sequence stars with spectroscopic measurement (Marino et al., 2018) in the CMD. The red main-sequence stars, blue main-sequence stars, and Be stars with Hα emission lines are designated by triangles, squares and asterisks, respectively, with color indicating the measured $v\sin i$ values. The main-sequence stars and the Hα emitters observed by the Hubble Space Telescope are shown by the black and red dots, respectively. Lower right: comparison between the model predicted average surface equatorial velocity and the spectroscopic measurements. The symbols with error bars correspond to the observations, using the same symbol types as the left panel. The solid lines and dashed lines represent the average surface equatorial velocity (times $\pi/4$ to account for a random orientation) of our MESA models at 30 Myr and the SYCLIST models at 40 Myr (the ages used in the isochrone fitting in Fig. 3.2). Color coding is the same as Fig. 3.1. Upper right: comparison between our theoretical predicted $v\sin i$ distributions (color dotted steps) and the observed $v\sin i$ of the red (solid black steps) and the blue (solid grey steps) main-sequence stars. For the theoretical predictions, we perform a Monte Carlo simulation by assuming a random orientation angle distribution and normalise the results to a total number of 15 for each initial rotation, which is similar to the number of the blue (14) and red main-sequence (16) stars with spectroscopic analysis.

All our above analyses are based on comparing the theoretical models with the photometric observations that do not contain direct information of the stellar rotational velocities. Recently, several high-resolution spectroscopic studies have been performed in young and intermediate-age clusters, providing an unprecedented opportunity to study the impact of rotation in the formation of the double MS (Dupree et al., 2017; Kamann, Bastian, Husser et al., 2018; Bastian, Kamann, Cabrera-Ziri et al., 2018; Marino et al., 2018; Kamann, Bastian, Gossage et al., 2020). Among them, NGC 1818 is the youngest cluster studied so far, and is a perfect case to test our theory. The left panel of Fig. 3.4 shows the position of the NGC 1818 MS stars. The open symbols mark out the stars that have spectroscopically measured velocities in Marino et al. (2018), with colors indicating the measured $v \sin i$ values. The triangles, squares, and asterisks correspond to the red MS, blue MS, and Be stars, respectively. We plot the $v \sin i$ distribution as a function of magnitude for these observed stars in the lower right panel with the same markers. But the color in this panel does not refer to the stars' velocities, with blue, red, and purple representing the blue MS, red MS, and Be stars, respectively. The mean measured velocities of the red and blue MS stars are $202 \pm 23\,\mathrm{km\,s^{-1}}$ and $71 \pm 10\,\mathrm{km\,s^{-1}}$, respectively, with the red MS stars having a more dispersed velocity distribution. The three red MS stars with the smallest velocities are all faint. Large systematic errors at such high magnitudes may affect the accuracy of the estimated velocities of these stars. The difference in the measured velocities of the red and blue MS stars provides compelling evidence that rotation plays an essential role in the split MS in young star clusters. We then plot the average surface rotational velocity of the SYCLIST (dashed lines) models and our MESA models (solid lines) (times $\pi/4$ to account for a random orientation) in this panel. The mean velocities of the observed red and blue MS stars agree well with our $W_\mathrm{i} \sim 0.5$ and $W_\mathrm{i} < 0.2$ models. In the upper right panel of Fig. 3.4, we plot the number distribution of the observed red and blue MS stars as a function of $v \sin i$, indicated by the dark and grey steps, respectively. For comparison, we plot such a distribution for our MESA models with $W_\mathrm{i} = 0.2$, $W_\mathrm{i} = 0.5$, and $W_\mathrm{i} = 0.6$ by assuming a random orientation distribution. A random orientation distribution means that $\cos i$ is evenly distributed between 0 and 1, and thus there is a higher opportunity to observe a star equator-on than pole-on. We normalise the theoretical predictions to a total number of 15, which is similar to the number of the analyzed red (16) and blue (14) MS stars. The range of the velocity distribution of the observed blue and red MS stars agrees well with the predictions from our $W_\mathrm{i} = 0.2$ and $W_\mathrm{i} = 0.6$ models, but the observed velocity peaks are smaller than the predictions from our models with these two rotations. This might be attributed to the small observation samples. Thus, we would encourage researchers to observe more stars, also in more clusters to examine our theory thoroughly.

3.5 Summary & Conclusions

Previous studies have proven rotation to be responsible for the recently discovered split MS in young star clusters. However, these studies argue that most of the stars should be born with near-critical rotation to match the observed red MS stars, which seems unrealistic. We have reinvestigated this problem and have found that it is merely a consequence of how and when critical rotation is defined. After clarifying the definition of critical rotation and eliminating the influence of initial model relaxation, we show that the previously believed near-critically rotating SYCLIST models are, in reality, rotating at a rotational velocity of $\sim 50\%$ of their critical linear velocities, under the definition of Eq. 3.3.

Then we have explored how much rotation is adequate to reproduce the observed color split by constructing new grids of rotating single star models with MESA. We found consistency between our MESA models and the SYCLIST models, that a bimodal velocity distribution with a fast component of 50% to 60% critical linear rotational velocities (corresponding to $\sim 60\% - {\sim}70\%$ critical linear rotational velocity, and ${\sim}75\% - {\sim}85\%$ critical angular velocity in terms of the origin SYCLIST definition) and a slow component of 0 to 30% critical linear rotational velocities can retrieve the color disparity between the observed red and blue MS stars. This distribution not only agrees well with the bimodal velocity distribution found in B/A type stars (Dufton et al., 2013; Zorec and Royer, 2012), but also agrees well with the current spectroscopic measurements of the blue and red MS stars in young star clusters (Marino et al., 2018).

The conclusion that slow and intermediate rotations are able to reproduce the split MS in young star clusters is robust, regardless of the adopted star models. However, we have indeed seen a difference between our MESA models and the SYCLIST models. We found that the isochrones of the fast-rotating and slowly-rotating SYCLIST models cross with each other near the MS turn-off due to a strong rotational mixing. In contrast, our rotating models are always redder than their non-rotating counterparts because rotational mixing is inhibited by chemical composition gradients. Interestingly, we found that the surface N abundance is enriched in the turn-off rotating models in both model sets, while the surface He abundance is only enriched in the turn-off rotating SYCLIST models, which make them much bluer than our MESA models. It seems that our MESA models match the observation in the turn-off region in the CMD better. But we cannot discard the validity of the SYCLIST models, or precisely speaking, efficient rotational mixing, because the star ingredients in the turn-off region is complex. It reminds us that we should restrict to the unevolved/less-evolved stars when investigating the role of rotation in shaping the MS morphology in young star clusters. Future studies on measuring the surface chemical abundances of the turn-off stars may help us better constrain the strength of rotational mixing.

Finally, we have explored the contribution of single-star evolution to the observed Be stars in young star clusters. We found consistency with the previous findings that the single stars increase their fractional critical velocities as they evolve along the MS, and may finally reach near-critical rotation. However, how fast rotation a star can achieve depends highly on stellar wind. We find that all the red MS stars that are proposed to have 50%-60% of their critical velocities can become Be stars at the end of their MS evolution, based on the assumption that the stars rotating faster than 70% of their critical velocities manifest themselves as Be stars. We also found consistency with the previous studies that the single channel can only interpret the Be stars in the vicinity of the cluster MS turn-off. A detailed study on the binary evolutionary produced Be stars is in high demand to thoroughly understand the Be star formation.

3.6 Appendix

3.6.1 Appendix A: Stellar evolutionary examples in the HRD

In Fig. 3.5, we show the evolution of 5 $M_\odot$ star models with different initial rotational velocities in the HRD, with the left and right panels corresponding to the LMC and SMC metallicity, respectively. The precise adopted metallicities in the three model sets are listed in the legend. As mentioned in Sec. 3.3, the metallicity Z tailored for the LMC stars in the SYCLIST models is larger than in our MESA models and the MIST models; thus, the SYCLIST ZAMS models are cooler than the corresponding MESA ZAMS models in this work and the MIST ZAMS models (see the left panel of Fig. 3.5). While similar metallicities are used for the SMC star models in different model sets, all the ZAMS models occupy similar positions in the HRD in the right panel of Fig. 3.5. For the SYCLIST models we recalculate their initial spins in the same way as our MESA models (see Sec. 3.3). For reference, we show the corresponding nearest initial $\omega_{\text{label}} = \Omega_{\text{e}}/\Omega_{\text{crit, SYCLIST}}$ in the SYCLIST model web interface in the brackets.

Fig. 3.5 illustrates that fast-rotating models are cooler than the slowly-rotating models at ZAMS in all three model sets, with similar rotation disparities leading to similar temperature differences. This means that before the evolutionary effect kicks in, the influence of rotationally-induced deformation of stellar temperature is identical in the three model sets. Nevertheless, after the ZAMS, the evolutionary tracks of the three model sets are different, even for the non-rotating models, as a consequence of different adopted mixing assumptions. The difference of the adopted α_{OV} parameter dominates the dissimilarity of the non-rotating models. α_{OV} roughly equals 0.1, 0.15 and 0.2 in terms of step overshooting for a $5\,\mathrm{M}_{\odot}$ star in the SYCLIST models, our MESA models and the MIST models, respectively. Consequently, the SYCLIST non-rotating models have the smallest turn-off luminosities and MS lifetimes, while the MIST non-rotating models have the largest turn-off luminosities and MS lifetimes with both the LMC and SMC metallicities. In contrast, the diverse evolution of the rotating models in the three model sets is mainly caused by the different adopted rotational mixing parameters. The most noticeable difference between the three model sets is that the SYCLIST fast-rotating models progressively evolve towards the hotter side along their MS evolution and finally cross with the non-rotating models near the turn-off, due to a substantial surface He enrichment induced by efficient rotational mixing. On the contrary, the MIST models and our MESA models show very similar surface He abundances between the rotating and non-rotating models because rotational mixing is assumed to be inhibited by chemical composition gradient. Therefore, the MIST rotating models and our MESA rotating models are always cooler than their non-rotating counterparts.

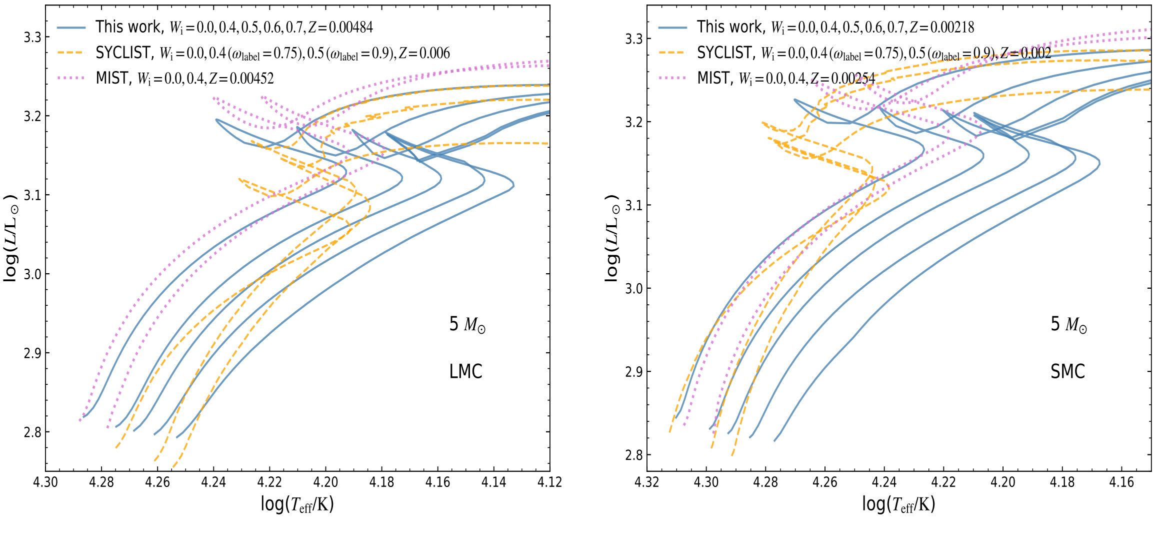

Figure 3.5: Evolutionary tracks of $5\,\mathrm{M}_{\odot}$ star models with LMC-like (left) and SMC-like (right) metallicities. The solid blue, dashed orange and dotted purple lines denote our MESA models, the SYCLIST models, and the MIST models, respectively. The adopted metallicity Z in different model sets are listed in the legend. In each model set, stellar evolutionary tracks from left to right correspond to models with increasing initial rotational velocity, with values listed in the legend. Numbers in the parentheses indicate the formally labelled fractional critical angular velocities in the SCYLIST web interface.

3.6.2 Appendix B: Surface abundance of the star models

Rotational mixing can bring H burning products from the stellar center to the stellar surface. Therefore, one can use the enrichment of the surface abundance of H burning products as a proxy for the strength of rotational mixing. Massive stars burn H via the CNO cycle, in which C, N and O are used as catalysts. The reaction between ^{14}N and ^{1}H is the slowest during the CNO cycle, resulting in an increased abundance of ^{14}N in layers where this process takes (or has taken) place. Rotational mixing can mix these ^{14}N (as well as He) enriched layers to the stellar surface.

In Fig. 3.2, we have shown that both our MESA models and the SYCLIST models can fit the observations well, even though they adopt different rotational mixing efficiencies. In this appendix, we aim to explore the surface abundance of He and N in these two model sets. In Fig. 3.6 we show the surface He and N abundances as a function of magnitude for the models shown in Fig. 3.2 that are used to fit the observed red and blue MSs. We see a similar surface N abundance enrichment in our MESA rotating models and the SYCLIST rotating models. On the contrary, the significant enrichment of surface He abundance only happens in the SYCLIST rotating models. This is because He is produced more slowly than ^{14}N. When He is produced, a strong chemical composition gradient has been created near the convective core, prohibiting the mixing of He to the stellar surface, which is the case in our MESA models. But the SYCLIST models allow for efficient mixing even in the presence of a strong chemical composition gradient. Therefore, the SYCLIST rotating models have higher surface He abundances and higher surface temperatures than our MESA rotating models. Future observations on the surface chemical composition abundance of the blue and red MS stars in young star clusters are encouraged to constrain rotational mixing.

Figure 3.7 displays the N abundance of our rotating models at their turn-offs. We see that the higher the initial rotation and the larger the initial stellar mass, the stronger the surface N enrichment is predicted, which agrees well with the results in Hastings, C. Wang and Langer (2020). The single star models with natal spins larger than 40% of their critical velocities all display a significant N enrichment at the end of their MS evolution. Since the stars with such initial rotation have a large probability to evolve to Be stars (see Sec.3.4.3), we argue that all the single-channel produced Be stars should have outstanding surface N enrichment. However, the Be stars created in binary systems might not be N enriched, as the predecessor of the Be star, i.e. the accretor in a binary system, rotates at a normal velocity until mass transfer happens, at which time a strong chemical composition has been established and thus, a strong rotational mixing is impeded.

3.6.3 Appendix C: Degeneracy in rotationally-induced color separation

Degeneracy exits when comparing the rotationally-induced color separation of the theoretical models with the observed color split between the red and blue MSs, because different combinations of rotation can cause similar color separation. In Fig. 3.8, we show the color difference between the rotating models and the models with $W_{\mathrm{i}} = 0.20$. Fig. 3.9 is similar to Fig. 3.8, but we compute the color separation of our rotating models with respect to the $W_{\mathrm{i}} = 0.30$ models. We find that $W_{\mathrm{i}} \sim 0.55$ and $W_{\mathrm{i}} \sim 0.60$ are required to retrieve the color separation between the observed red and blue MSs if the blue MS stars are anchored to stars with $W_{\mathrm{i}} = 0.20$ and $W_{\mathrm{i}} = 0.30$.

In Fig. 3.10, we do isochrone fitting for the NGC 1818 red and blue MS stars in the CMD, using our MESA models with the above mentioned two pairs of rotation. As expected, we fit the observations in Fig. 3.10 equally well as in the right panel of Fig. 3.2 by adjusting distance modulus and reddening

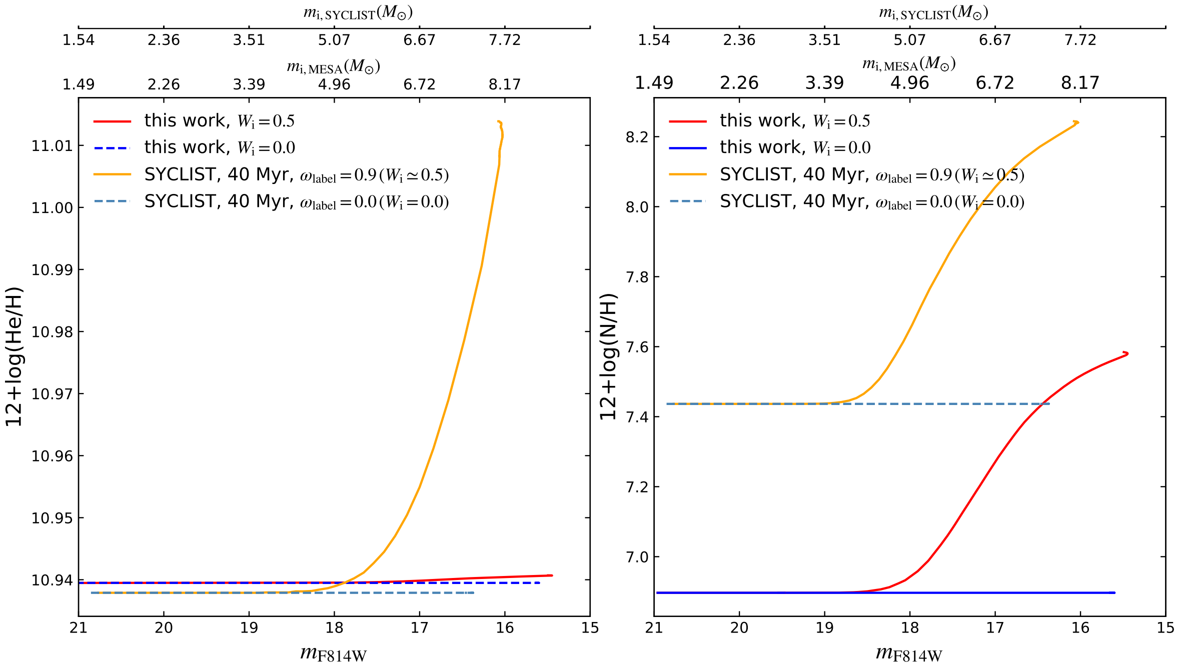

Figure 3.6: Current surface He (left) and N (right) abundances as a function of magnitude of our MESA models and the SYCLIST models shown in Fig. 3.2. The upper two x-axis show the corresponding mass derived from our MESA models and the SYCLIST models that are used to fit the red main-sequence.

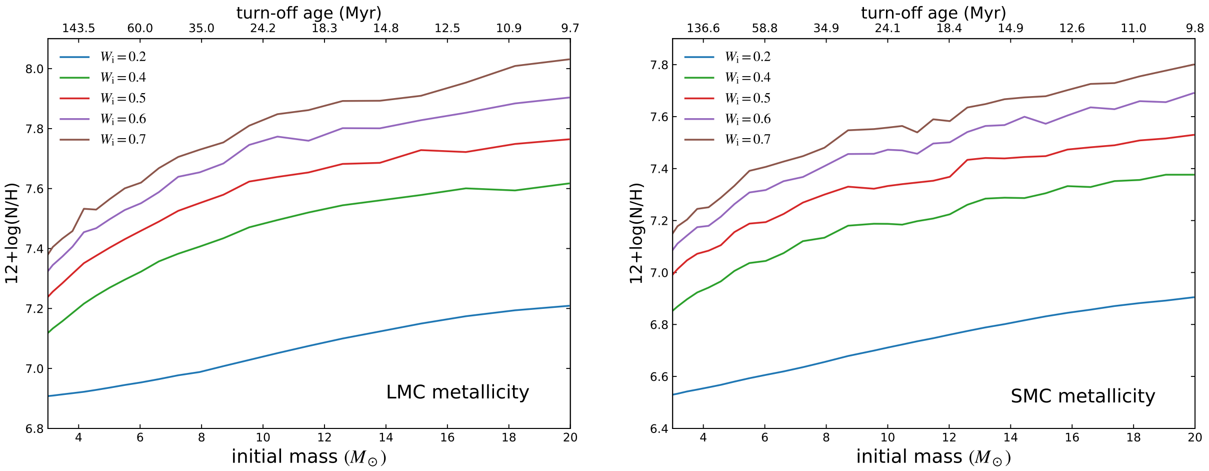

Figure 3.7: Surface N abundances of our MESA models with LMC metallicity (left) and SMC metallicity (right) at the end of their main sequences (when 1% of H is left in the center). The x-axis shows models' initial mass, with corresponding turn-off ages showing on the top x-axis. The solid lines with different colors indicate different initial rotational rates.

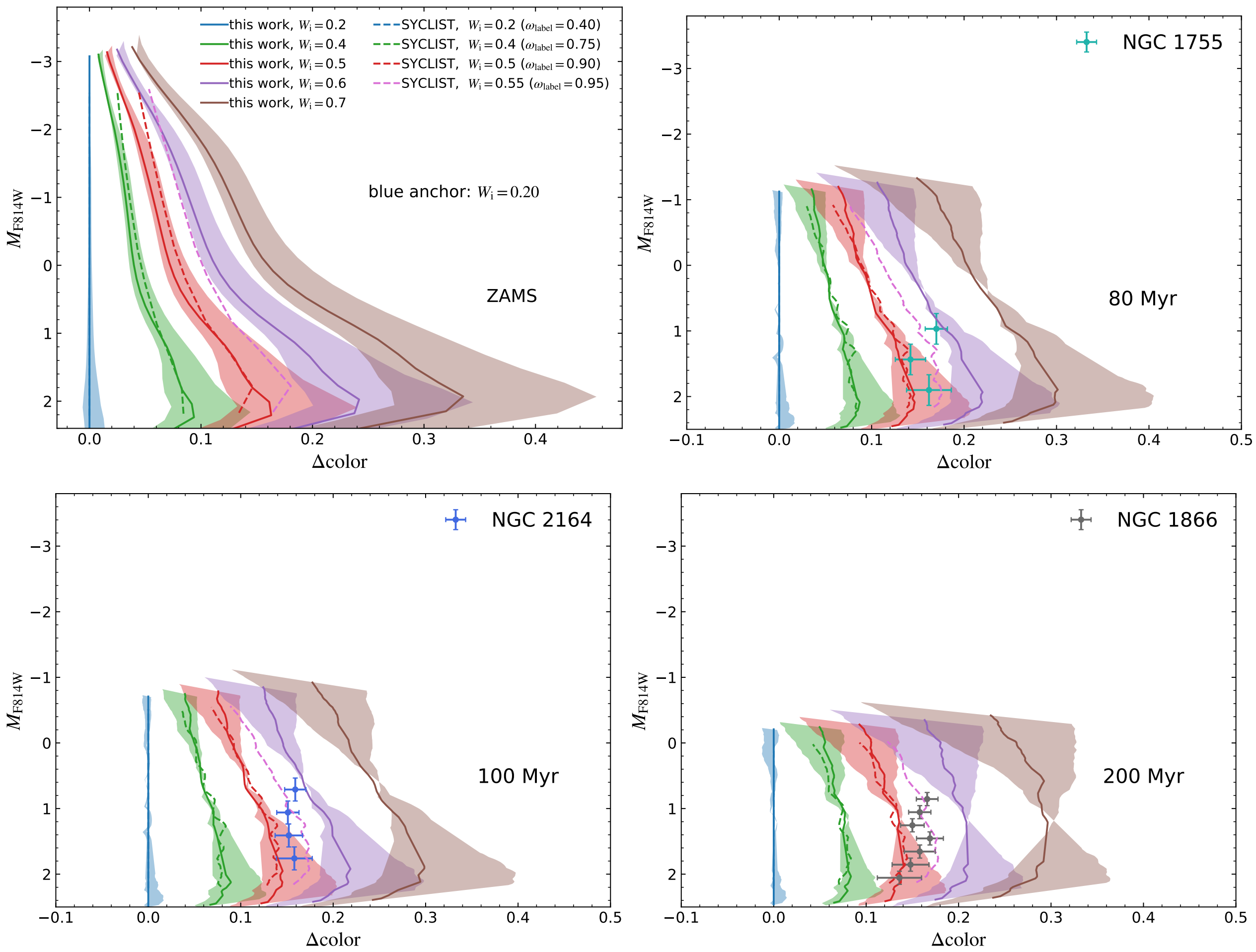

Figure 3.8: Same as Fig. 3.1, but color differences are calculated with respect to the W_i = 0.2 models.

(see Tab. 3.1). It means that one cannot evaluate the actual rotation for the blue and the red MS stars with only photometric observations. The spectroscopic $v \sin i$ measurements in NGC 1818 seem to support 10% to 20% of critical rotation for the blue MS stars (Marino et al., 2018), which is slow, yet non-vanishing. Future spectroscopic observations are urgent to help us determine the rotational rates of the red and the blue MS stars more accurately.

3.6.4 Appendix D: Current surface rotation of the star models and the implications for Be stars

Figure. A1 of Hastings, C. Wang and Langer (2020) shows that a 15 $M_\odot$ model with initial rotation of 60% critical can spend a significant time rotating at velocities larger than 80% of their critical values, and can finally evolve to more than 90% of their critical values near the terminal-age MS. Therefore, the Be stars close to the turn-off could originate from single stars, whereas those Be stars with magnitudes two mags below the turn-off are unlikely to. In Sec.3.4.3, we have displayed the required initial spin of a star to become a Be star. In this appendix, we directly compare the single

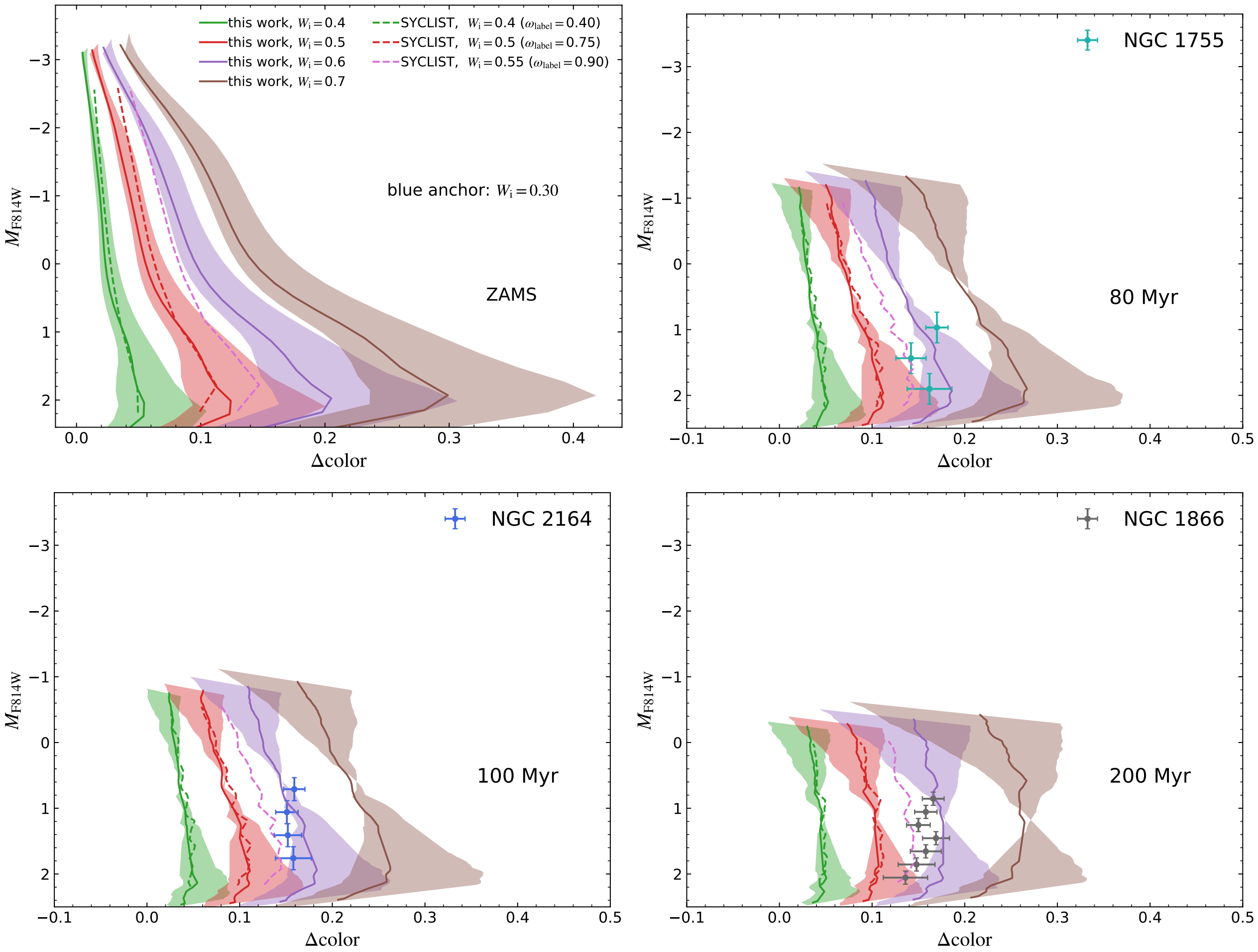

Figure 3.9: Same as Fig. 3.1, but color differences are calculated with respect to the $W_i = 0.3$ models.

star models with the Be stars in NGC 1818 to address the issue that the observed Be stars in which magnitude range can be explained by single star evolution.

We plot the current rotational rates v/v_{crit} of our MESA models and the SYCLIST models at an age corresponding to the derived age of NGC 1818 as a function of magnitude in Fig. 3.11. The adopted ages, distance moduli and reddenings for our MESA models and the SYCLIST models are the same as in Fig. 3.2. We only show the MS models that have at least 0.1% H left in the core. Again, our results agree well with Ekström et al. (2008) and Hastings, C. Wang and Langer (2020) in the sense that v/v_{crit} increases gradually from the high magnitude (unevolved) part to the low magnitude (evolved) part until the turn-off region where the increase of v/v_{crit} accelerates. However, unlike the results in Hastings, C. Wang and Langer (2020) that used models in Brott et al. (2011), our MESA models and the SYCLIST models hardly reach 80% of their critical rotation near the end of their MSs if their initial spins are smaller than 70% of their critical values. We find that wind mass loss in the temperature range for the bi-stability jump to occur (~24 kK) plays an essential role in determining the surface velocity of our star models. Our MESA models suffer a stronger wind mass loss compared to the models in Brott et al. (2011), because they smooth the wind mass loss rate in a more extensive

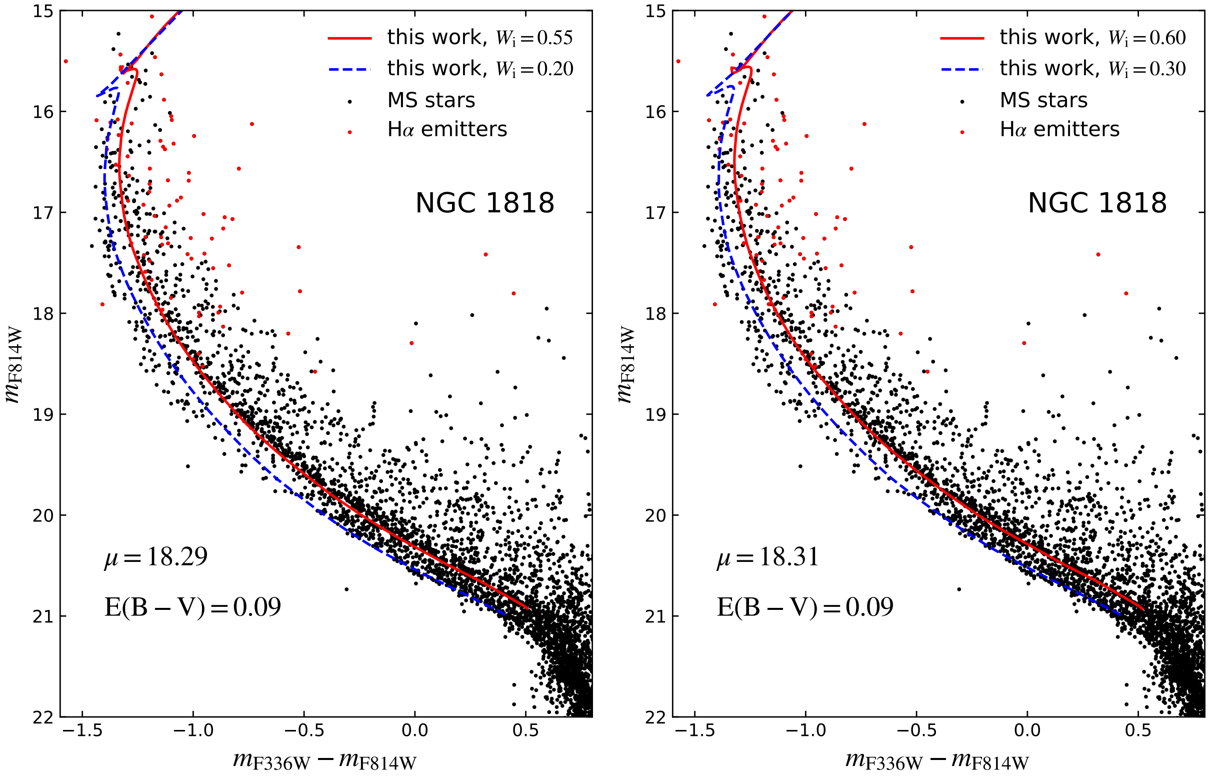

Figure 3.10: Same as Fig. 3.2, but we only show our MESA models and use pairs of isochrones of the $W_i = 0.55$ and $W_i = 0.20$ models (left), and the $W_i = 0.60$ and $W_i = 0.30$ models (right) to fit the the observed red and blue main sequences in NGC 1818.

temperature range near the bi-stability jump. Unfortunately, the turn-off stars (~8 $M_\odot$) in clusters with ages similar to NGC 1818 happen to fall into the bi-stability jump region. The bump in the purple and brown solid line near 16.5th magnitude is indeed caused by the bi-stability jump related enhanced wind mass loss.

The importance of Fig. 3.11 is that it straightforwardly demonstrates that our single star models with an initial rotational rate of $W_i \sim 0.6$ are only able to explain the observed Be stars up to 1.5 magnitudes below the turn-off, given 70% of critical rotation as the threshold for a star to be a Be star. We do not expect the majority of stars to rotate even faster than $W_i \sim 0.6$, because it not only contradicts the previously reported velocity distributions of the B/A type stars (Zorec and Royer, 2012; Dufton et al., 2013), but also contradicts the fact that Be stars are rarely found at magnitudes higher than two magnitudes below the turn-off. Therefore, the presence of dim Be stars ~2 mags below the turn-off in, for example, NGC1818 may advocate the binary channel as the main scenario for the formation of Be stars.

We point out that we cannot quantitatively compare the difference between our MESA models and the SYLICT models in Fig. 3.11 as they have different ages, rotational mixing efficiencies, and rotationally-induced angular momentum transfer, meaning that the models with the same mass at the corresponding ages are in different evolutionary phases. In addition, rotationally-induced angular momentum transfer is also different in the two model sets.

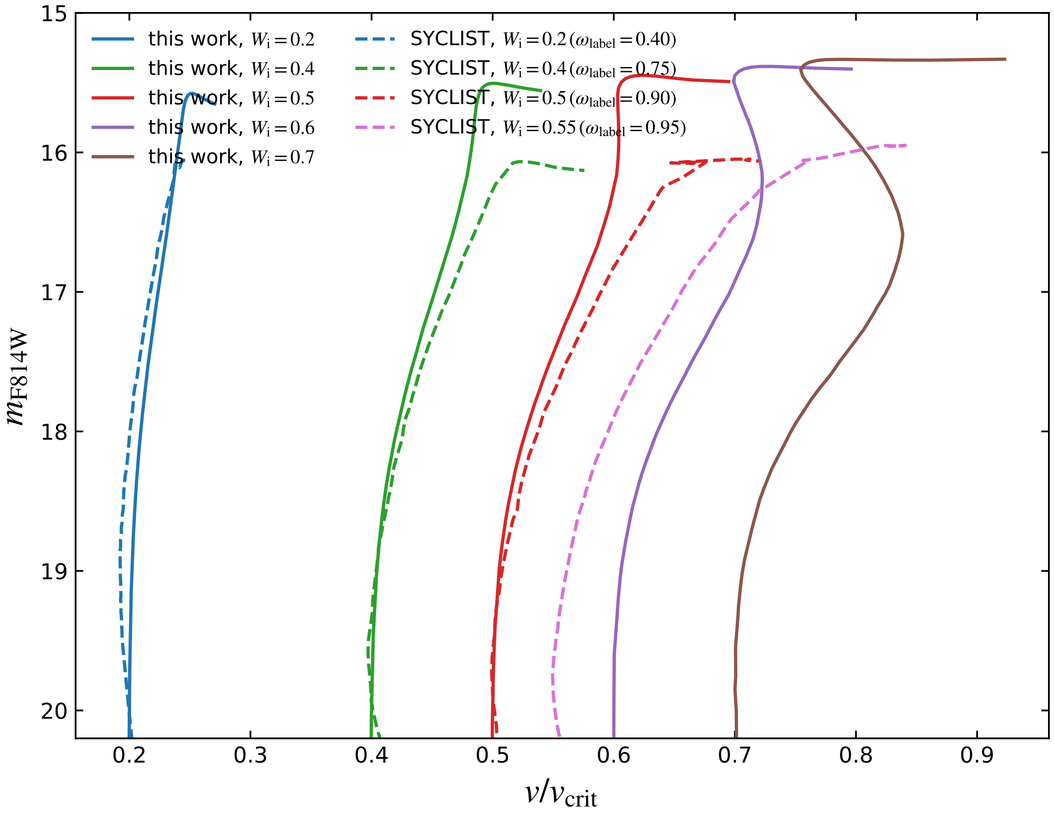

Figure 3.11: Ratio between current surface rotation velocity and the critical velocity as a function of magnitude for our our MESA models at 30 Myr (solid line) and the SYCLIST models at 40 Myr (dashed line). Colors indicate the ratio between the initial rotation velocity and the critical velocity, which is the same as Fig. 3.1.The adopted model age, distance modulus and reddening for each model set are the same as the right panel of Fig. 3.2.

CHAPTER 4

Stellar mergers as the origin of the blue main-sequence band in young star clusters

Chen Wang, Norbert Langer, Abel Schootemeijer, Antonino Milone,
Ben Hastings, Xiao-Tian Xu, Julia Bodensteiner, Hugues Sana,
Norberto Castro, D. J. Lennon, Pablo Marchant, A. de Koter, Selma E. de Mink
Submitted to Nature Astronomy

4.1 Author contributions

CW, AS, BH, X-TX performed the stellar evolution calculations, based on earlier work by PM and his advice. NL worked out the analysis interpretation of the results, together with CW, AS, BH and SdM. AM, JB, HS, NC, DL, AdK provided an interpretation of the related observations. All authors reviewed the manuscript.

Abstract

Recent high-quality Hubble Space Telescope (HST) photometry shows that the main sequences (MS) stars of young star clusters (younger than $\sim 600\,$Myr) form two discrete components in the color-magnitude diagram (CMD). Based on their distribution in the CMD, we show that stars of the blue MS component can be understood as slow rotators originating from stellar mergers. We derive the masses of the blue MS stars, and find that they follow a nearly flat mass function, which supports their unusual formation path. Our results imply that the cluster stars gain their mass in two different ways, by disk accretion leading to rapid rotation, contributing to the red MS, or by binary merger leading to slow rotation and populating the blue MS. We also derive the approximate merger time of the individual stars of the blue MS component, and find a strong early peak in the merger rate, with a lower level merger activity prevailing for tens of Myr. This supports recent binary formation models, and explains new velocity dispersion measurements for members of young star clusters. Our findings shed new light on the origin of the bi-modal mass, spin, and magnetic field distributions of main-sequence stars.

4.2 Main

The main sequence (MS) of star clusters is a cornerstone of stellar formation and evolution (Iben, 1967; Gaia Collaboration, Babusiaux et al., 2018). In the last decade, the simple picture of star clusters as an ensemble of coeval stars born with identical initial conditions has been challenged. Old and very massive globular clusters host multiple stellar populations, with differences in chemical compositions(Gratton, Carretta and Bragaglia, 2012; Milone, Piotto, Renzini et al., 2017). Recent Hubble Space Telescope (HST) observations have also revealed that the MSs of young open star clusters (with ages between ∼ 15 Myr and ∼ 600 Myr) are composed of several discrete components(Milone, Bedin, Piotto and J. Anderson, 2009; Milone, Marino, D'Antona, Bedin, Da Costa et al., 2016; C. Li, de Grijs et al., 2017; Milone, Marino, Di Criscienzo et al., 2018; C. Li, Sun et al., 2019), but with identical chemical composition (Milone, Marino, D'Antona, Bedin, Da Costa et al., 2016; Mucciarelli et al., 2014). In the color-magnitude diagram (CMD), this is characterised by a split MS from the vicinity of the turn-off all the way to a faint magnitude, with the red MS component containing more stars than the blue MS (e.g. NGC 1755 in Fig. 4.1). The emergence of a sub-population of blue MS stars is ubiquitous in Magellanic Cloud clusters younger than ~600 Myr (Milone, Marino, Di Criscienzo et al., 2018).

In this paper, we use the ∼ 60 Myr old Large Magellanic Cloud (LMC) cluster NGC 1755 as an example to investigate the origin of its split MS, with three more clusters, that are NGC 1818, NGC 2164 in the LMC and NGC 330 in the Small Magellanic Cloud (SMC), discussed in the supplementary materials. The MSs in these clusters all show a distinct blue component in the CMD. In NGC 1755, the color difference between the blue component and the well-defined red (major) MS is up to 0.25 magnitudes (Milone, Marino, Di Criscienzo et al., 2018) (see panel a of Fig. 4.1). The lower portion of the blue MS is the narrowest, while the upper portion is more diffuse. The blue MS stars comprise roughly 20% of the cluster stars.

There is well-founded observational evidence that supports rotation being responsible for the split MS, with blue MS stars rotating significantly slower than other cluster stars (designated here as red MS stars) (Bastian and S. E. de Mink, 2009; Dupree et al., 2017; Marino et al., 2018; Milone, Marino, Di Criscienzo et al., 2018; Bastian, Kamann, Cabrera-Ziri et al., 2018; Sun, C. Li et al., 2019; Kamann, Bastian, Gossage et al., 2020). In particular, the spectroscopically measured average projected rotation velocity of red MS stars in NGC 1818 was found to be 202 ± 23 $\mathrm{km\,s^{-1}}$, while it was only 71 ± 10 $\mathrm{km\,s^{-1}}$ for the blue MS stars in this cluster (Marino et al., 2018). While previous studies suggest that extremely rapid rotation (∼ 90% of initial critical rotation) of the red MS stars may be required to account for the color difference between blue and red MS (D'Antona, Milone et al., 2017; Milone, Marino, Di Criscienzo et al., 2018), our stellar models show that adopting ~65% of initial critical rotation for the red MS stars and ~35% for the blue MS stars provides indeed a good fit to the observed red MS and to the best discernible part of the blue MS (panel b of Fig. 4.1 and Sec. 4.5.1). This also agrees with the currently available, although sparse spectroscopic rotational velocity measurements (Marino et al., 2018; Sun, C. Li et al., 2019; Kamann, Bastian, Gossage et al., 2020), and, notably, with the bi-modal distribution of the rotation rates of B and A-type field MS stars, in which the average projected rotational velocities of the slow and fast components are ∼ 20 − 100 $\mathrm{km\,s^{-1}}$ and 180 − 250 $\mathrm{km\,s^{-1}}$, respectively (W. Huang, Gies and McSwain, 2010; Zorec and Royer, 2012; Dufton et al., 2013).

Other scenarios for the origin of blue MS stars have been proposed. Suggestions that the blue MS stars formed in a second burst of star formation after the formation of the majority of the cluster stars

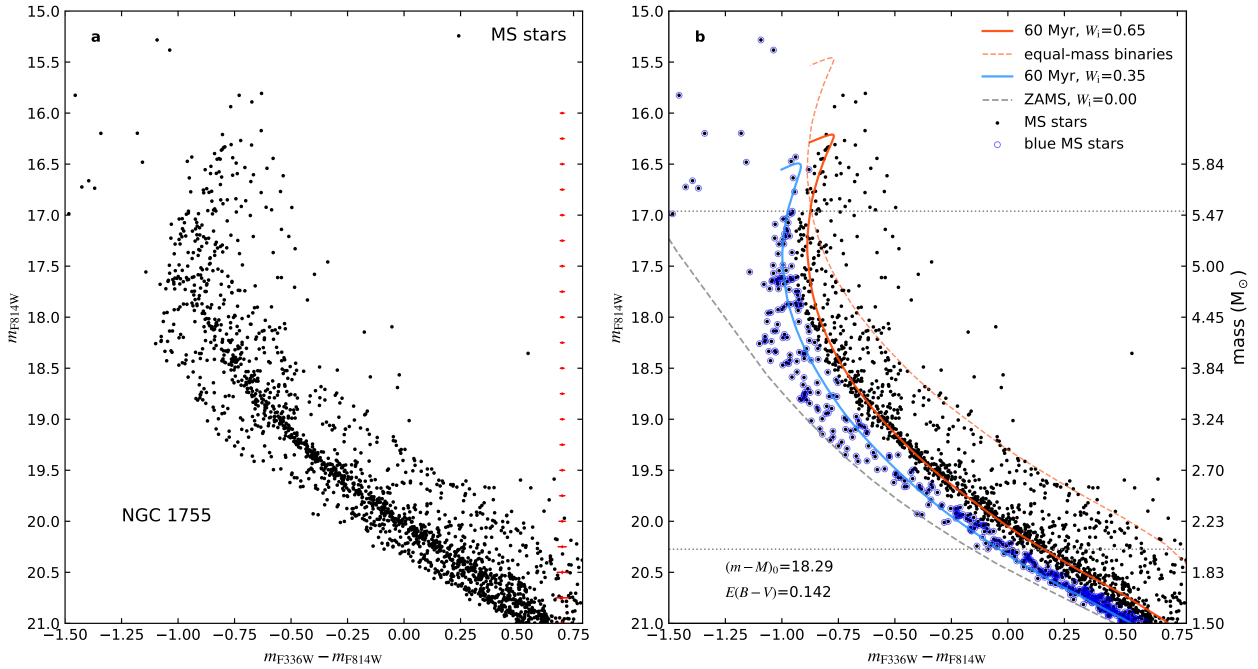

Figure 4.1: **a**: Color-magnitude diagram of the stars (black dots) in the main-sequence region of the Large Magellanic Cloud open star cluster NGC 1755 based on high-quality HST photometry (Milone, Marino, Di Criscienzo et al., 2018). Typical errors at different magnitudes are shown with red error bars on the right. **b**: Isochrone fit for the red (major) main sequence of NGC 1755, signified by the densest stellar concentration, using stellar models with a rotation parameter of $W_i = 0.65$ (red solid line), and identification of the blue main-sequence stars (blue circles; cf., Sec. 4.5.1). The solid blue line represents the corresponding isochrone of single star models with $W_i = 0.35$ Here, $W_i = v_{\mathrm{rot,i}}/v_{\mathrm{crit,i}}$ is the ratio between rotational velocity and break-up velocity at the zero-age main sequence. The red dashed line shows the positions of the equal-mass binaries in which both components have $W_i = 0.65$. The grey dashed line indicates the zero-age main-sequence line of non-rotating stars. The adopted age, distance modulus $(m - M)_0$ and reddening $E(B - V)$ are indicated. The stars between the two thin horizontal dotted lines are used in our mass function analysis (see Sec. 4.5.3). The right y-axis shows the stellar mass according to the mass-magnitude of the fast rotating stellar models.

(Goudfrooij, Puzia et al., 2011; Correnti, Goudfrooij, Bellini et al., 2017) are in conflict with the persisting color difference between blue and red MS even far below the turn-off, since the faintest stars are essentially unevolved. Similarly, the trend that the apparent cluster age spread measured from the MS widths near the turn-off increases for older Magellanic Cloud and Galactic star clusters cannot be explained by a second star burst (Niederhofer, Hilker et al., 2015; Niederhofer, Georgy et al., 2015; Cordoni et al., 2018).

It has further been proposed that the blue MS stars were born with similar rotational velocities as the red MS stars, but that their rotation has slowed down subsequently due to tidal braking (D'Antona, Milone et al., 2017). Whereas tidal braking of close binaries provides a viable spin-down mechanism, it does not produce enough blue MS stars, since most close binaries will appear redder than non-rotating single stars regardless of the rotation rate of their components, due to the presence of two stars in the observed point source. Only very low-mass ratio binaries containing slow rotators are expected to contribute to the blue MS stars. The blue MS has also been suggested to originate from a combination of MS stars with He-star companions and stellar mergers, where the MS split is explained by a bi-modal distribution of post-merger masses (Yang, 2018). Bi-modal disk-locking during the star formation process has also been suggested to explain the observed MS dichotomy (Bastian, Kamann, Amard et al., 2020). In this model, the blue MS stars are slow rotators due to a longer disks-locking time during their pre-MS accretion phase, compared to the red MS stars. While this may reproduce the rotation dichotomy, it cannot explain that closer to the turn-off, more and more of the blue MS stars are located to the blue side of the blue MS isochrone.

Binary mergers offer a natural way to create the blue MS population. A binary merger creates a star that is more massive than either of its progenitor stars, with a core hydrogen content that is higher than that of an equally old single star of the same mass. Thus, merger products may have the same age as all other cluster stars, but appear younger in the CMD, signified by their bluer color. Previous studies have shown that tight binary stars which merged as a consequence of the expansion of their component stars during hydrogen burning evolution form the blue stragglers that are brighter and bluer than the turn-off stars in star clusters (Schneider, Izzard, Langer et al., 2015; C. Wang et al., 2020) (see also Sec. 4.5.2 for the simulation based on detailed binary models). The continuity in the CMD between the blue stragglers and the fainter blue MS stars displayed in several clusters (NGC 1866, NGC 1856, NGC 294, KRON 34, with ages between 200 Myr to 500 Myr) (Milone, Marino, Di Criscienzo et al., 2018) provides us a further clue for the merger origin of the latter. We demonstrate in Section 4.5.2 that, based on large grids of detailed binary evolution models, evolutionary channels which can produce stars to the blue side of the major MS, e.g., binaries consisting of a MS star and a hot stripped companion star, or short period binaries with tidally spun-down components, only account for an insignificant fraction of the observed blue MS stars.

Further evidence for a merger origin of the blue MS stars is provided by analysing their mass functions. We fit the CMD positions of blue and red MS stars, i.e., the magnitude of the individual stars along the constructed isochrones, with single star models of the appropriate spin and age to obtain a measurement of the stellar mass (Sec. 4.5.3). We then fit the mass distributions of both groups of stars with power laws. For the red MS stars, the derived power law exponent of $\gamma \simeq -2.30 \pm 0.08$ is close to that of a Salpeter law ($\gamma = -2.35$) in the mass range of $5.5 \ldots 2\,\mathrm{M}_\odot$. In the same mass range, the mass function of the blue MS stars, however, is found to follow a power law with an exponent of $\gamma = -0.52 \pm 0.50$, representing a much shallower mass distribution (Fig. 4.2). Similar results are obtained for the other clusters investigated (Sec. 4.5.3). This indicates that the blue MS stars are not formed by the same mechanism as the red MS stars, just at a later time, but that both groups emerge from different formation mechanisms. The shallow slope of the mass function of the blue MS stars is in fact consistent with their merger origin, as it may be the result of the observed decreasing close binary fraction with decreasing stellar mass (Schneider, Izzard, Langer et al., 2015). This is also expected according to recent binary formation models (Tokovinin and Moe, 2020).

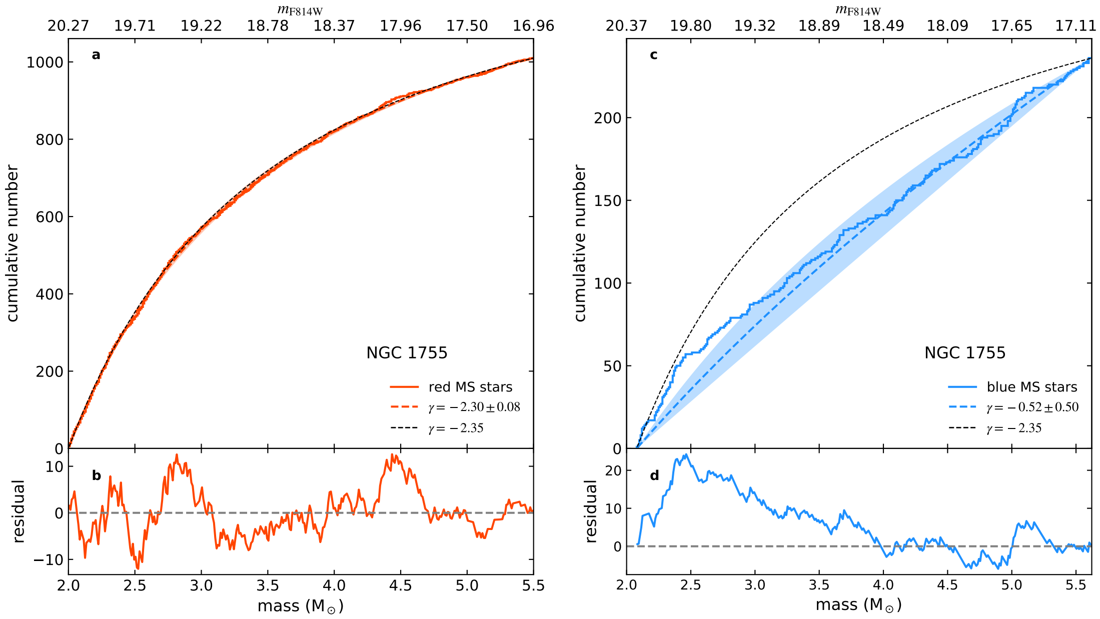

Figure 4.2: **a** and **c**: Cumulative number distribution of red main-sequence (red lines) and blue main-sequence stars (blue lines) in NGC 1755 as a function of their mass, as derived from the stellar model isochrones. Dashed lines display distributions according to the best-fitting power-law mass function. The shading reflects one sigma errors of our power-law fitting, and correspond to the error of the power law indices given in the legend. The dashed black lines show the distributions predicted by a power law with index $\gamma = -2.35$ (the traditional Salpeter IMF), assuming the same total number of stars as the corresponding number in the observed populations. We show the apparent magnitudes for given masses on the top of the figures. **b** and **d**: Residuals, i.e., difference between the colored solid and dashed lines in Panels a and c, as a function of mass, with a residual of zero indicated by the grey dashed lines.

A merger origin of the blue MS stars may also hold the clue for their slow rotation (Marino et al., 2018; Kamann, Bastian, Gossage et al., 2020). While initially, a stellar binary merger contains a large angular momentum surplus due to the orbital angular momentum, recent hydrodynamic binary merger calculations show that the merger product loses most of that in a puffed-up stage right after the merger, such that it settles as a slow rotator on the MS after a Kelvin-Helmholtz time scale (Schneider, Ohlmann, Podsiadlowski, Röpke, Balbus, Pakmor and Springel, 2019). These simulations suggest that large-scale magnetic fields form in the merger product, such that a further spin-down due to magnetic wind braking may occur subsequently.

Unlike previously discussed scenarios, the merger origin of the blue MS stars provides a coherent explanation of the dichotomies in color, rotation, and mass function slope, and of the peculiarly wider blueward extension of the blue MS for brighter magnitudes. It leads us to the exciting conclusion that stars come to accumulate their mass in two fundamentally different ways. On the one hand, the majority of stars form by accretion of gas via accretion disks, which is the dominant path, leading to a well populated red MS with a rotation rate of slightly larger than half of critical rotation. On the other hand, a fair fraction of the so created stars merge with a similar mass companion and produce a blue MS star, rotating significantly slower and obeying a different initial mass function than the red MS stars. This bi-modality in the star formation process may therefore be at the root of the observed bi-modalities in stellar spins (Zorec and Royer, 2012; Dufton et al., 2013), magnetic fields (Donati and Landstreet, 2009), and mass functions (Milone, Marino, Di Criscienzo et al., 2018), and of course location in the CMD. In the following, we shall discuss these aspects in more detail.

The narrowness of the red MS (panel a of Fig. 4.1) implies that potentially, accretion induced star formation may result in a rather narrow distribution of MS rotational velocities in the considered mass range, with a peak near 65% of critical rotation, which is in agreement with considerations of gravitational torques between stars and disks (Lin, Krumholz and Kratter, 2011), and also in agreement with the spectroscopic measurements of both the red MS stars in young star clusters (Marino et al., 2018; Sun, C. Li et al., 2019; Kamann, Bastian, Gossage et al., 2020) and the B and A-type field stars (W. Huang, Gies and McSwain, 2010; Zorec and Royer, 2012; Dufton et al., 2013). Furthermore, there is evidence for stars in binaries being born with very similar spins as single stars (Ramírez-Agudelo et al., 2015). Whereas the information about the initial spins of the stars which merged to become blue MS stars is wiped out in the merger process, these stars appear to rotate so slowly that their color is largely unaffected by rotation (Fig. 4.6). While we see a significant number of MS stars with extreme rotation, most notably the Be stars, which are likely evolved MS stars which are spun-up either by mass transfer from a binary companion (C. Wang et al., 2020) or as single stars by their contracting cores (Ekström et al., 2008; Hastings, C. Wang and Langer, 2020), it is thus conceivable that upper MS stars are formed either rotating slowly, or about half critically.

Binary mergers of MS stars have also been suggested to be responsible for the generation of the large scale B-field found in about 10% of the upper MS stars (Ferrario et al., 2009), and magnetohydrodynamic (MHD)-simulations of the merger process appear to support this idea (Schneider, Ohlmann, Podsiadlowski, Röpke, Balbus, Pakmor and Springel, 2019). According to our analysis, the fraction of merger stars ($\sim 20\%$) is larger than the observed fraction of magnetic stars (Petit et al., 2013). This means that either not every merger event leads to a magnetic star, or that the merger generated B-fields decay on a timescale comparable to the nuclear time scale of the stars. The fact that the topological requirement of intertwined toroidal and poloidal field components (Braithwaite and Spruit, 2004) is not a guaranteed outcome of the turbulent merger phase provides evidence for the former scenario, while the distribution of the fractional MS ages of magnetic massive stars (Fossati et al., 2016) justifies the latter.

Furthermore, our results have implications for the understanding of the stellar initial mass function (IMF). They imply that the IMF when measured from field stars consists of two components with largely different slopes. In star clusters, on the other hand, the stellar mass function is not static as often assumed, but it may evolve as the merger rate changes with time, offering a challenging but feasible way to test the proposed interpretation.

To quantify the consequences of stellar mergers, we construct simple merger models following the scheme of Schneider, Podsiadlowski et al. (2016). The strongest apparent rejuvenation of merger products, as measured by time difference between the cluster age and the apparent age of the merger product identified through single star models, occurs in binaries with a mass ratio of one (Sec. 4.5.4). Fitting models of equal-mass mergers to an individual blue MS star in the CMD therefore allows us to obtain a lower limit to its merger time, i.e., the moment in the cluster history when it formed through the coalescence of its progenitor binary. Figure 4.3 shows lines of constant merger time for equal mass binaries, indicating the current positions of merger products which were created at the indicated times, in the CMD of NGC 1755. These lines extend from the blue MS, for a merger time corresponding to the time of cluster formation (defined here as $t = 0$), almost all the way to the zero age MS for a merger time close to the cluster age ($t = 60$ Myr). Notably, the lines of constant merger time cover most blue MS stars brighter than ~ 19.5 mags. Blue MS stars to the red side of the line for $t_{\text{merge}} = 0$ may have a slightly faster initial rotation than $W_{\text{i}} = 0.35$ (see Fig. 4.6). We note that this applies in particular to blue MS stars below ~ 19.5 mags, or $\sim 2.5\,\text{M}_{\odot}$, which is analogous to the disappearance of the slowest rotators in Galactic field stars (Zorec and Royer, 2012).

Assuming equal-mass binary mergers, we can constrain the history of stellar merger events in NGC 1755 and other clusters. The unknown exact rotation rate of the blue MS stars remains the dominant error source in deriving their merger time from their positions in the CMD. We therefore derive the merger time of each blue MS star for different assumptions on the rotational rate (see panel b of Fig. 4.4 and Sec. 4.5.4), which yields representative uncertainties of the merger times. For stars fainter than ~ 19 mags, we cannot constrain the merger times any more. Panel a of Fig 4.4 shows the result of integrating over Gaussian merger time probability distributions for each star, with the shaded area indicating the 1σ bootstrapping envelope (see Sec. 4.5.4). Figure 4.4 implies that the merger rate was largest within the first few Myrs of the cluster evolution, after which it dropped considerably. However, on a reduced but substantial level, the merging activity prevailed for several tens of Myr. Since by adopting equal-mass binary mergers, we only obtain lower limits to merger time of each star, the true merger times might be somewhat larger than implied by Fig. 4.4. However, varying the mass ratio of the pre-merger binaries only has a limited effect (see Sec. 4.5.4). In fact, it is the relative distance between each blue MS star to the blue MS isochrone that determines its merger time. That the star density is the highest in the vicinity of this isochrone unambiguously implies an early peak in the merger rate. In addition, we find a moderate positive correlation between merger time and stellar brightness (see Sec. 4.5.4), which is consistent with recent binary formation simulations that suggest binaries with higher masses to merge earlier than binaries with lower masses (Korntreff, Kaczmarek and Pfalzner, 2012). We repeated the analysis for the three other clusters (see Sec. 4.5.4) and found very similar results.

Binary evolution driven by the nuclear timescale expansion of the individual stellar components can not account for the large number of observed blue MS stars, particularly far below the turn-off, since stellar expansion starts very slowly during hydrogen burning (C. Wang et al., 2020) (see also Sec. 4.5.2). Therefore, a merger fraction of the order of 20% all along the MS can only be produced by decaying binary orbits. In fact, there are multiple lines of evidence for this. Tidal forces imposed by the circum-binary matter from which the stars formed are known to induce a drastic decay of the binary orbit (Korntreff, Kaczmarek and Pfalzner, 2012). Recent binary formation models indeed predict about 30% of binary B stars to merge during the pre-MS evolution or shortly thereafter (Tokovinin and Moe, 2020). Orbit decay is also required to explain the high observed fraction of very close massive binary systems (Sana, S. E. de Mink et al., 2012). Direct evidence for pre-MS binary orbit decay is provided from observations of pre-MS binaries in a nearby star forming region (Sana, Ramírez-Tannus et al., 2017). More quantitatively, the strong peaks at early time in our derived merger histories appear consistent with the observed rapid rise of the velocity dispersions in star clusters during their first few million years of evolution (Ramírez-Tannus et al., 2021). Notably, this timescale corresponds to the duration of the pre-main sequence phase of stars in the considered mass range, during which time they are bloated and thus more prone to tidal effects.

The derived merger activity on a timescale at least ten times longer is more difficult to understand.

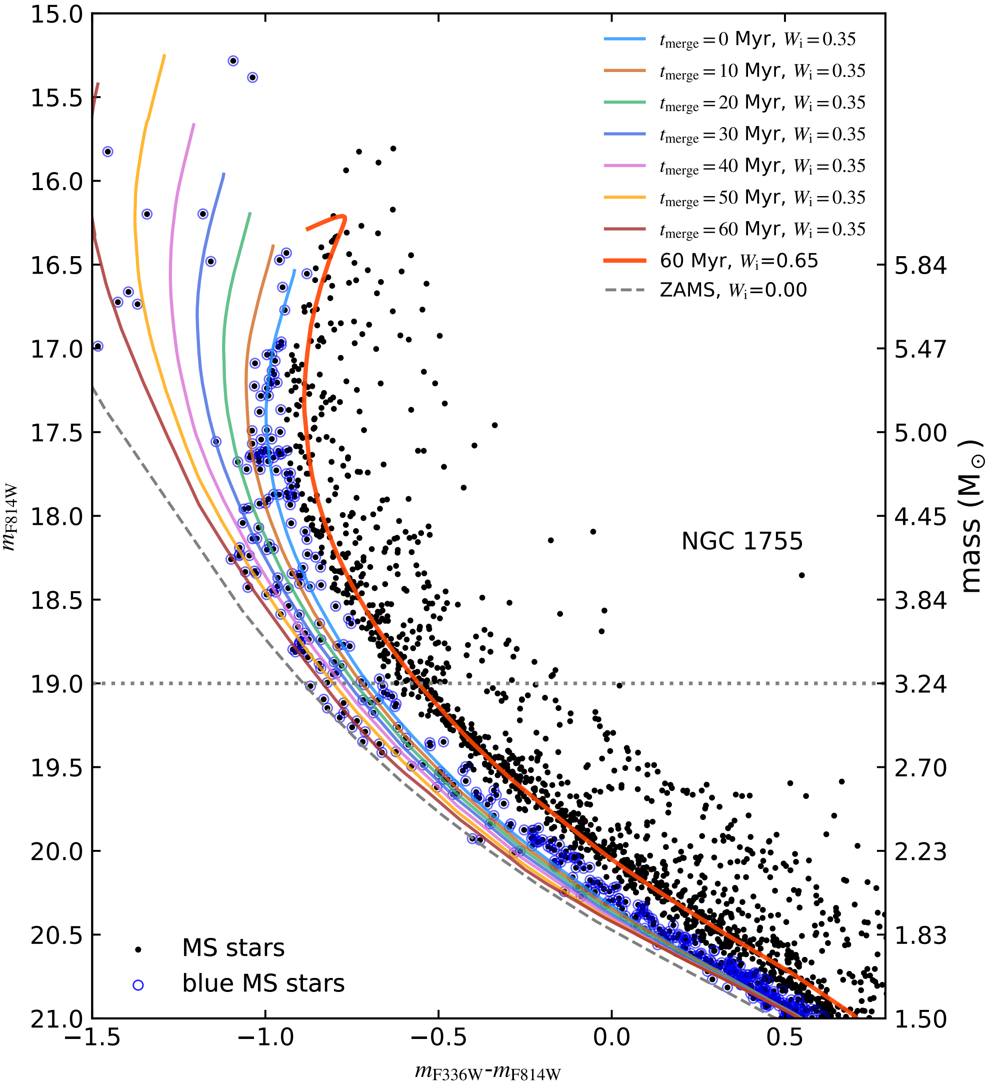

Figure 4.3: Color-magnitude diagram with lines of constant merger times, overplotted on the distribution of the main-sequence stars in NGC 1755, with blue open circles indicating blue main-sequence stars. Solid lines of given colors provide the location of merger products which formed from equal-mass binaries at the indicated time (see color scale) and were then evolved to the current cluster age. The merger products have 35% critical rotation immediately after the merger event. The blue main-sequence stars above the grey horizontal dotted line are considered in the merger time estimation (see Sec. 4.5.2). The isochrone fitting to the red MS (solid red line), the zero-age main-sequence line (dashed grey), and the adopted distance modulus and reddening are the same as panel b of Fig. 4.1.

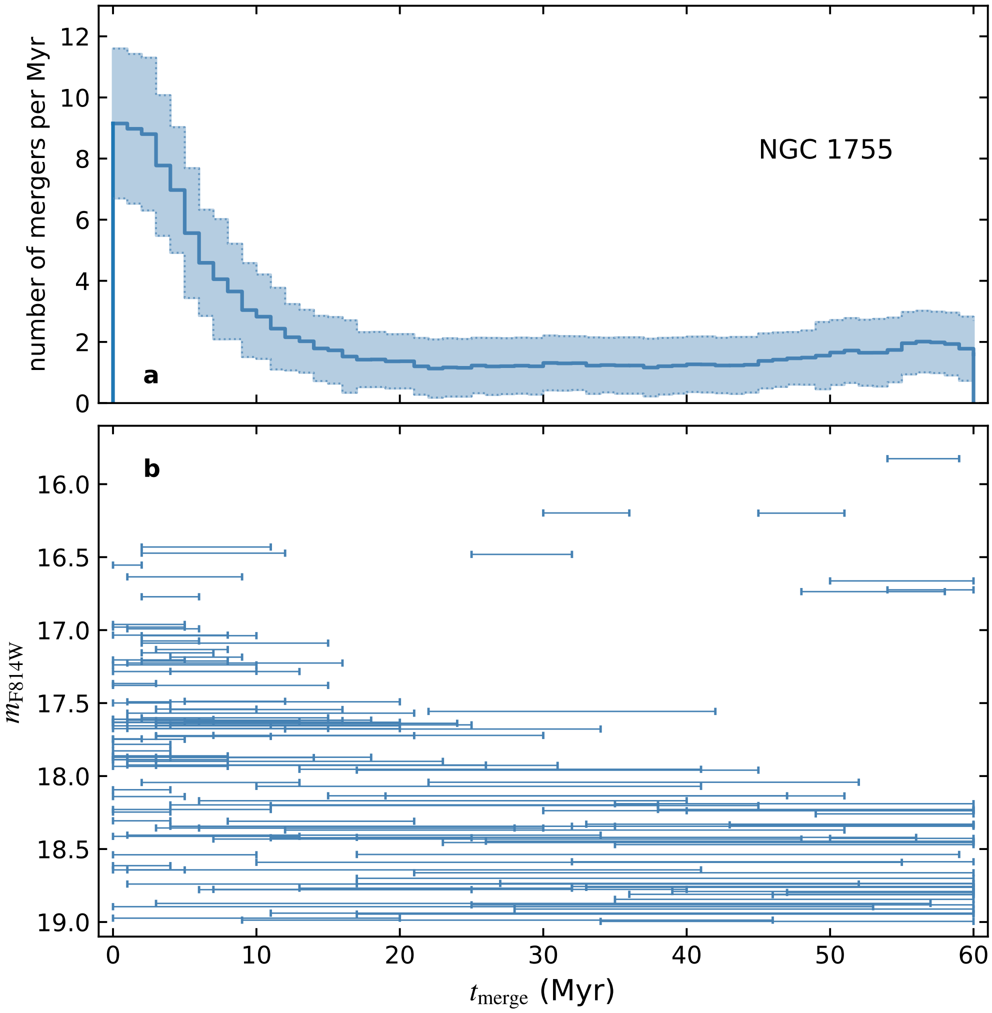

Figure 4.4: **a** (upper panel): Merger rate, expressed as number of merger events per Myr, as function of time, as derived for NGC 1755. This histogram is obtained by taking in to account a Gaussian probability distribution of the merger rotation over the time range displayed in Panel b for each star, and summing up their contributions in each time bin of width 1 Myr. The shaded area indicates bootstrapped 1σ estimates. **b** (bottom panel): Magnitude versus merger time of the blue main-sequence stars in NGC 1755 (blue horizontal error bars). Magnitude errors are small and are not shown here (see Fig. 4.1). The upper and lower limits of the merger time are derived from the minimum and maximum rotation velocities consistent with the color, individually for each star. A time of 60 Myr corresponds to today.

The similarity of this timescale to the timescale of violent relaxation of star clusters, on which they re-virialise after expelling the gas left over after star formation ended, suggests that dynamical processes may play a role. While stellar encounters can lead to binary hardening, the stellar density in the investigated clusters is too small to render this process efficient (Baumgardt and Klessen, 2011). It appears more likely that triple and higher-order multiple system can foster the merging of their inner binary components, e.g. via Lidov-Kozai cycles (Kozai, 1962; Eggleton and Kiseleva-Eggleton, 2001) or by passing stars (Wu et al., 2018) that can cause a high eccentricity of the inner binaries and trigger the subsequent tidal friction. Indeed, we show in Sec. 4.5.4 and Fig. 4.19, that even today, after most of the mergers may have occurred, the CMDs of the discussed young star clusters bear evidence for a current fraction of triple and higher order multiple systems of at least of $\sim 5\%$, which may imply that the corresponding merger activity is still ongoing.

In our analysis, we consider clusters younger than 100 Myr. However, our conclusion that binary mergers account for the split MS may apply to clusters with ages up to $\sim$ 700 Myr (with a turn-off mass of $\sim 2\,\mathrm{M}_{\odot}$), the limit up to which the MS morphology as considered here is observed (Milone, Marino, Di Criscienzo et al., 2018). The mechanisms for orbit decay and merging may also act on lower-mass stars. Unfortunately, for these stars, the information on their birth spins and large scale B-fields are erased by their convective envelopes, which produce their own magnetic activity and lead to magnetic spin-down.

4.3 Data Availability Statement

The observational data in this work is available from Antonino Milone on reasonable request. The MESA inlist files used to compute the single and binary star models in this work can be downloaded at: https://doi.org/10.5281/zenodo.5233209.

4.4 Acknowledgments

The research leading to these results has received funding from the European Research Council (ERC) under the European Union's Horizon 2020 research and innovation programme (grant agreement numbers 772225: MULTIPLES). CW acknowledges funding from CSC scholarship. This work has received funding from the European Research Council (ERC) under the European Union's Horizon 2020 research innovation programme (Grant Agreement ERC-StG 2016, No 716082 'GALFOR', PI: Milone, http://progetti.dfa.unipd.it/GALFOR). APM acknowledges support from MIUR through the FARE project R164RM93XW SEMPLICE (PI: Milone) and the PRIN program 2017Z2HSMF (PI: Bedin). HS and JB acknowledge support from the FWO Odysseus program under project G0F8H6N. NC gratefully acknowledges funding from the Deutsche Forschungsgemeinschaft (DFG) - CA 2551/1-1. PM acknowledges support from the FWO junior postdoctoral fellowship No. 12ZY520N. SdM acknowledges funding by the Netherlands Organization for Scientific Research (NWO) as part of the Vidi research program BinWaves with project number 639.042.728.

4.5 Supplementary materials

4.5.1 A: The main sequence split as a function of stellar rotation

The main characteristic feature in the distribution of the cluster stars in the CMD, which is the basis for our work, is that the MS band is split into two distinct components. This is a striking feature not only visible in the CMD of MS stars in NGC 1755, but rather a common feature detected in Magellanic Cloud star clusters younger than ~ 600 Myr (Milone, Marino, Di Criscienzo et al., 2018). In this work, we fix our attention on clusters younger than 100 Myr, whose distinct components can be compared with our models of stars exceeding 2 $M_\odot$. Currently, high-quality data exists for six clusters younger than 100 Myr in the LMC and the SMC (NGC 330, NGC 1818, NGC 1805, NGC 1755, NGC 1850 and NGC 2164), five of which are shown to exhibit the split MS (excluding NGC 1805), but one of them (NGC 1850) is composed of two sub-clusters (Milone, Marino, Di Criscienzo et al., 2018). We investigate all the remaining four clusters in this work, which are the LMC clusters NGC 1755, NGC 1818, NGC 2164 and the SMC cluster NGC 330. We use the observational data published in Milone, Marino, Di Criscienzo et al. (2018) which includes corrections for differential reddening. We use the same method as in that work to eliminate the contamination from the foreground and background field stars. Rotation is widely accepted to be responsible for the split MS (Bastian and S. E. de Mink, 2009; Niederhofer, Georgy et al., 2015; Correnti, Goudfrooij, Bellini et al., 2017). We explore how much rotation is required to retrieve the color split by comparing our rotating single star models with the MS components in the above mentioned four clusters. We next describe the physics and assumptions adopted while computing the single star models.

We use the detailed one-dimensional stellar evolution code MESA (Paxton, Bildsten et al., 2011; Paxton, Cantiello et al., 2013; Paxton, Marchant et al., 2015; Paxton, Smolec et al., 2019). Most of the physical assumptions are identical to those utilized in Brott et al. (2011). The exception is that we use a mass-dependent overshooting parameter $\alpha_{\rm ov}$ (i.e., the number of pressure scale-heights by which the hydrogen-burning core is extended). For an initial mass of 20 $M_\odot$ we use $\alpha_{\rm ov} = 0.3$ (Brott et al., 2011). Below that, $\alpha_{\rm ov}$ decreases linearly such that it reaches a value of $\alpha_{\rm ov} = 0.1$ at 1.66 $M_\odot$ (Claret and Torres, 2016). Below 1.66 $M_\odot$, $\alpha_{\rm ov}$ has an even steeper linear decrease such that it equals zero at 1.3 $M_\odot$ (where the convective core disappears). This mass-dependence accounts for the trend that the width of the distribution of field MS stars in the CMD increases with mass (Castro et al., 2014; Claret and Torres, 2016; Schootemeijer, Langer et al., 2019). The adopted $\alpha_{\rm ov}$ in this work are similar to the findings in Martinet et al. (2021). We emphasize here that although overshooting still remains poorly constrained, and it can affect the location of the turn-off stars in the CMD, the uncertainty of overshooting does not play a role in explaining the observed double MS (Yang and Tian, 2017). We include differential rotation, rotationally induced internal mixing, magnetic angular momentum transport, stellar wind mass loss, and non-equilibrium CNO nucleosynthesis. We use the standard mixing-length theory to model convective mixing with a mixing-length parameter $\alpha_{\rm MLT} = 1.5$. The Ledoux criterion is used to determine the boundaries of convective zones. In the superadiabatic layers that are stable according to the Ledoux criterion but unstable according to the Schwarzschild criterion, we assume that semiconvection occurs with a mixing parameter of $\alpha_{\rm SC} = 10$ (Schootemeijer, Langer et al., 2019). We model rotational mixing as a diffusive process (Heger, Langer and Woosley, 2000), taking into account the effects of dynamical and secular shear instabilities, the Goldreich-Schubert-Fricke instability (Goldreich and Schubert, 1967; K. Fricke, 1968), and the Eddington-Sweet circulations (Eddington, 1925). The efficiency parameter of rotational mixing is

$f_c = 1/30$ as proposed in Chaboyer and Zahn (1992). We include the Tayler-Spruit dynamo for the transport of angular momentum (Spruit, 2002; Heger, Woosley and Spruit, 2005).

We follow the mass-loss recipe used in Brott et al. (2011): for hydrogen-rich stars with surface hydrogen mass fraction $X_s \geq 0.7$, the wind prescription of Vink, de Koter and Lamers (2001) is used, while for hydrogen-poor stars with $X_s \leq 0.4$, the WR mass-loss prescription of Hamann, Koesterke and Wessolowski (1995) is used. For intermediate surface hydrogen abundances $0.4 < X_s < 0.7$, we linearly interpolate the value of $\log \dot{M}$ between the two prescriptions. The metallicity-dependent stellar winds scale as $\dot{M} \propto Z^{0.85}$ (Vink, de Koter and Lamers, 2001).

We consider both LMC and SMC metallicity, with $Z_{\rm LMC} = 0.00484$ and $Z_{\rm SMC} = 0.00218$ (Brott et al., 2011). We compute single star models in a mass range of $1.05\,{\rm M}_\odot$ and $20\ {\rm M}_\odot$ in a dense grid with $\Delta \log m_{\rm i} = 0.02$, from the zero-age MS, which is defined at the position where 3% of hydrogen is burnt to avoid the initial model relaxation, until well beyond core hydrogen exhaustion. We define a stellar model's initial fractional critical rotation as $W_{\rm i} = v_{\rm rot,i}/v_{\rm crit,i}$, where $v_{\rm rot,i}$ and $v_{\rm crit,i}$ are its average surface rotational velocity and its break-up velocity at the zero-age MS , respectively. We follow MESA definition of the critical velocity $v_{\rm crit} = \sqrt{Gm/R_{\rm eq}}$, where m and $R_{\rm eq}$ are the mass and equatorial radius of the stellar model, respectively. Then for each mass, we compute model sequences for $W_{\rm i}$ ranging from 0.15 to 0.75, in intervals of 0.1, as well as non-rotating models. We did not go higher than that because we encounter numerical problems when computing stellar models with $W_{\rm i} > 0.75$.

To construct the stellar distribution in the CMD, we first calculate the absolute magnitude of a star in a given filter F as $M_{\rm F} = M_{\rm bol} - BC_{\rm F}$, where $M_{\rm bol} = M_{\rm bol,\odot} - 2.5\log{(L/L_\odot)}$ is the bolometric magnitude of a star, $BC_{\rm F}$ its bolometric correction for the adopted filter, and $M_{\rm bol,\odot} = 4.74$ mag (Mamajek et al., 2015). The bolometric correction is obtained by interpolating tables computed from 1D atmosphere models based on ATLAS12/SYNTHE (Kurucz, 1993; Kurucz, 1970) for either the HST/WFC3 F814W or F336W filters as these correspond to observations used in this paper. The absorption coefficients are $A_{F814W} = 2.04\,E(B-V)$, $A_{F336W} = 5.16\,E(B-V)$ (Milone, Marino, Di Criscienzo et al., 2018), where $E(B-V)$ is the reddening. The apparent magnitude is then obtained by $m_{\rm F} = M_{\rm F} + A_{\rm F} + (m-M)_0$, where $(m-M)_0$ is the distance modulus.

In the framework of a single star-burst forming a star cluster, (i.e., all stars are born at the same time), we attempt to use the isochrones constructed from our stellar models to fit the observations. The observations show a narrow red MS band, which marks the peak of stellar density in the CMD. In particular below 19th magnitude, the CMD of NGC 1755 (see panel a of Fig. 4.1) shows a clear gap between the red MS and bluer stars. We start the isochrone fitting by adopting the parameters (isochrone age, distance modulus and reddening) derived in (Milone, Marino, Di Criscienzo et al., 2018). Since we are using different stellar models, we then need to adapt these parameters together with the stellar rotation parameter gradually until we obtain a pair of isochrones with the same age, but with different initial rotational velocities that can simultaneously best match the red MS and the blue MS bands, by visual inspection. We find that stellar models with $W_{\rm i} = 0.65$ and $W_{\rm i} = 0.35$ can fit the observed red and blue MSs equally well in all the clusters analyzed here (see panel b of Fig. 4.1 and Figs. 4.5). The adopted parameters in the isochrone fitting, as well as the mass of the studied clusters provided in Milone, Marino, Di Criscienzo et al. (2018) are listed in Tab. 4.1. The adopted parameters in our work are slightly different from Milone, Marino, Di Criscienzo et al. (2018), as a consequence of different employed star models, with slightly different initial chemical composition and adopted physics parameters. The resulting small differences in the fit parameters of the employed isochrone are not significant, because only the relative distance between red and blue isochrone below well the turn-off is important for our analysis. The bluer isochrone identifies the bulk of blue MS stars to the blue of the red isochrone, with, however, more and more stars falling to its blue side with higher brightness. In this paper, we consider stars as blue MS stars if their colors are bluer than the median color of the two isochrones at corresponding magnitudes, marked by the open blue circles in the CMD.

The stars to the red (right) side of the red MS are most likely unresloved close binaries, which are expected to lie in between the red MS and the corresponding equal-mass binary line, constructed by adding 0.75 magnitudes to the isochrone fitting the red MS, corresponding to a factor of two in flux (red dashed line in panel b of Fig. 4.1 and Figs. 4.5). This interpretation is strengthened by a rather sharp drop in stellar density to the red side of the equal-mass binary line seen in all the analyzed clusters. Finally, we expect that most of these unresolved binaries, as most stars in these clusters generally, are rapid rotators, since the rapidly-rotating equal-mass binary isochrone does indeed fit the red edge of the red MS nicely. Redder stars are likely to be Be stars when near the turn-off (Milone, Marino, Di Criscienzo et al., 2018), or higher order multiple systems otherwise.

We notice that the stars to the red (right) side of the red MS may also be explained by stars rotating with even faster velocities. Figure 4.6 shows a comparison of isochrones derived from our single star models computed with different initial rotational rates, with the MS stars of NGC 1755. The adopted age, distance modulus and reddening are the same as in Fig. 4.1. We see that the faster rotating stellar models are redder than the slower rotating ones, due to their lower effective gravity. For slow rotation, an increase of the rotation parameter W_i by 0.1 has only a small effect on the isochrone color. However, it becomes progressively larger for faster rotation. The isochrone of our fastest rotating models ($W_\mathrm{i} = 0.75$) overlaps the CMD region populated by suspected unresolved binaries (with large mass ratios). However the majority of the stars redder than the red MS can not be interpreted as extremely fast rotating stars, otherwise it contradicts the observed rotational velocity distributions of the B-type and A-type stars (W. Huang, Gies and McSwain, 2010; Zorec and Royer, 2012; Dufton et al., 2013) and the fact that Hα emitters have only been detected in the region within two magnitudes below the turn-off (Milone, Marino, Di Criscienzo et al., 2018).

Figure 4.6 can also be used to constrain the width of the rotational velocity distribution of the stars on the red MS. Its broadening can be delineated well by single stars with W_i from 0.45 to 0.65. Even though binaries composed of two slow rotators can also occupy the red MS, we do not expect them to play an important role if most slow rotators originate from binary mergers, after which most of them should be single stars. Nevertheless, low-mass ratio tidally-locked binaries may provide a small contribution to the red MS population (see Sec. 4.5.2 and Fig. 4.8).

The choice of the rotation parameter for the isochrone fitting of the red MS is slightly degenerate, such that slightly smaller rotation parameters may also provide acceptable fits. We investigate how a different choice of W_i would impact our conclusion for the four clusters in Fig. 4.7. The adopted parameters are listed both in the figure and in Tab. 4.1. We again use the median color between the blue and red isochrones to distinguish the blue and red MS stars. Even though rotation parameters of $W_\mathrm{i} = 0.55$ and $W_\mathrm{i} = 0.15$ can retrieve the observed color split of the red and blue MS equally well compared to the values of $W_\mathrm{i} = 0.65$ and $W_\mathrm{i} = 0.35$, the former lead to several stars being bluer than the zero-age MS line in NGC 1755, NGC 330 and NGC 1818, which could not be interpreted by stellar rejuvenation caused by binary mergers. Notably, the remaining degeneracy of the rotation parameter and age for the isochrone fitting does not affect our main conclusions, because it is not the precise values of these two parameters, but the gap in the CMD which determines our results. E.g., the

Table 4.1: Basic information of the studied clusters and the parameters adopted in fitting the observed red and blue main sequences with our single star models.

Cluster	Galaxy	$\log(M/M_\odot)$	W_i for red MS	W_i for blue MS	Age (Myr)	$(m-M)_0$	$E(B-V)$
NGC 330	SMC	4.61	0.65	0.35	40	18.85	0.079
NGC 1818	LMC	4.41	0.65	0.35	40	18.31	0.067
NGC 1755	LMC	3.60	0.65	0.35	60	18.29	0.142
NGC 2164	LMC	4.18	0.65	0.35	85	18.32	0.103
NGC 330	SMC	4.61	0.55	0.15	30	18.82	0.110
NGC 1818	LMC	4.41	0.55	0.15	35	18.32	0.096
NGC 1755	LMC	3.60	0.55	0.15	50	18.28	0.174
NGC 2164	LMC	4.18	0.55	0.15	85	18.28	0.125

derived mass functions of the red and blue MS stars change only marginally for different isochrone fits (see Sec. 4.5.3 and Fig. 4.13). We show in Sec. 4.5.4 that our conclusion of a high frequency of stellar merger events during the early cluster evolution also holds for different isochrone fits.

While it is not in the focus of this work, it is worth mentioning that the bi-modal distribution of rotation rates as adopted here is well suited to lead to an extended main sequence turn-off as it is observed in most of the young open clusters. While binary evolution is known to also contribute substantially (C. Wang et al., 2020), an initial rotational velocity of around 50% of critical is large enough to considerably widen the turn-off region (see Sec. 4.5.2 and Fig. 4.8). The reason is that MS stars increase the ratio of rotation to critical rotation velocity during their evolution (Ekström et al., 2008; Hastings, C. Wang and Langer, 2020), such that the extended main sequence turn-off will be significantly enhanced by the inclination dependence of gravity darkening.

4.5.2 B: Distribution of the detailed binary models in the CMD

In the main text, we have proposed that single and binary stars in young star clusters are born with nearly the same velocities with values slightly larger than half of their break-up velocities. In this section, we examine the distribution of the detailed binary models, built with MESA version 8845, in the CMD, attempting to inspect the contribution of binary evolution to blue MS stars. These newly computed binary models are an extension of the binary models in C. Wang et al. (2020), but assuming that both binary components start with 55% of their critical rotation velocities at the zero-age MS. The physics assumptions adopted in each star model otherwise are the same as in the single star models of this work. We use SMC-like metallicity for our binary models, because the metallicity-dependent stellar wind is weak, such that any differences between binary and single star models are mainly caused by binary interaction. We briefly describe the physics and assumptions adopted for the binary interactions in the following.

We simultaneously compute the detailed structure of both components, together with the orbital evolution. We assume the orbit to be circular. Our binary models are not synchronized initially but have 55% of their critical velocities ($W_\mathrm{i} = 0.55$), as we have shown in the last section that single stars with this velocity are consistent with the observed red MS of young star clusters. The two stars in each

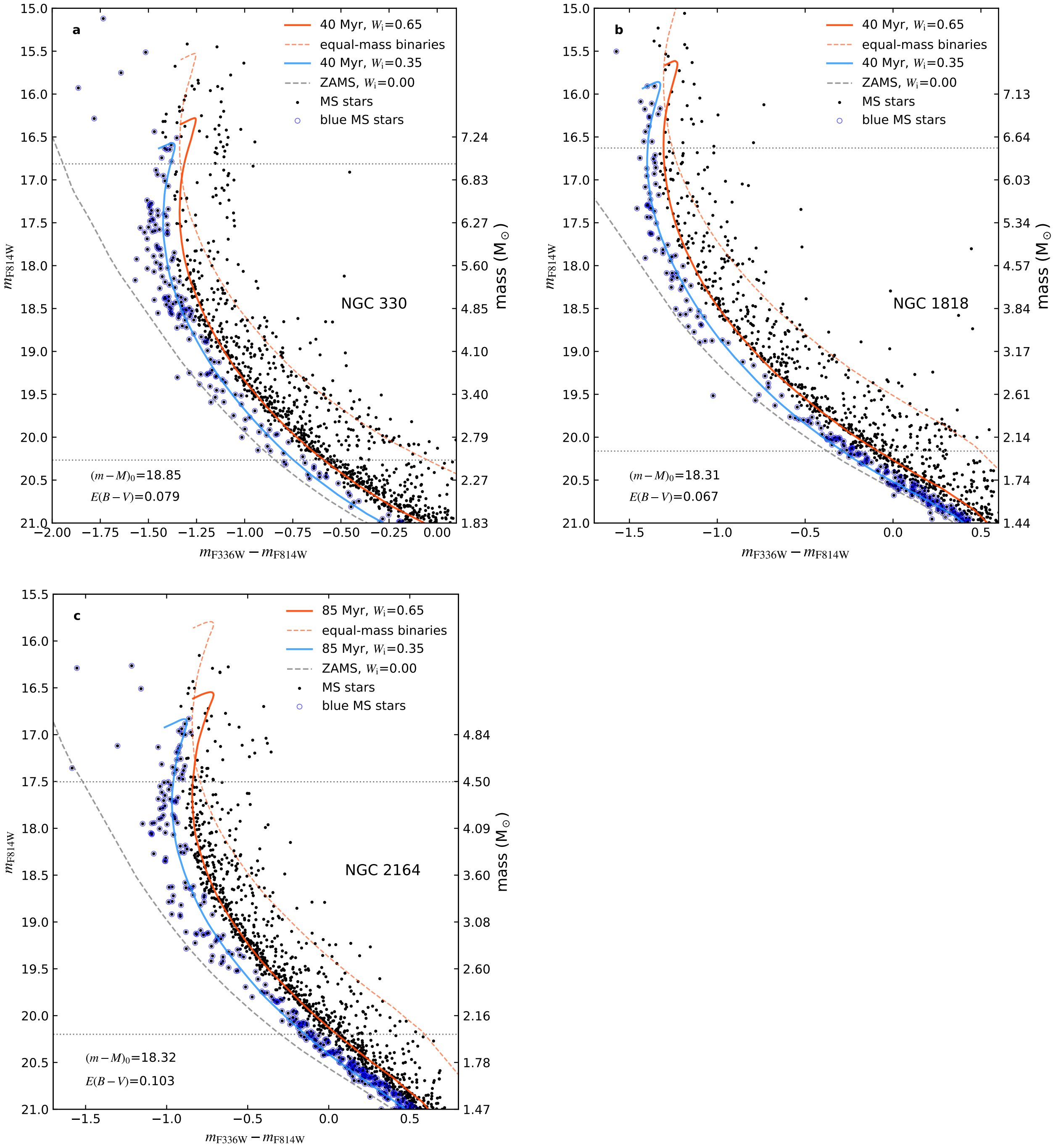

Figure 4.5: As panel b of Fig. 4.1, but for the Small Magellanic Cloud cluster NGC 330 and the Large Magellanic Cloud clusters NGC 1818 and NGC 2164. The adopted distance moduli and reddenings are indicated (see also Tab. 4.1).

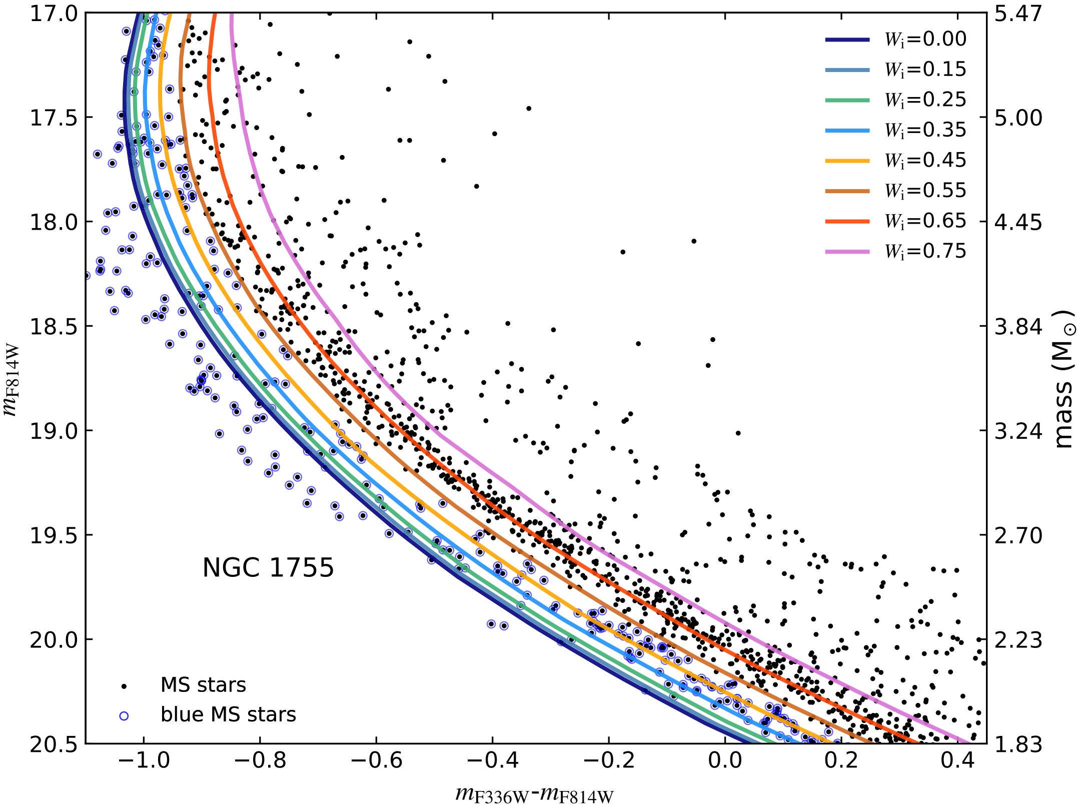

Figure 4.6: Color-magnitude diagram of NGC 1755, with isochrones derived from our single star models with different initial rotational rates, as indicated in the legend. The adopted distance modulus and reddening are the same as panel b of Fig. 4.1, as are the isochrones with a rotation parameter of W_i = 0.35 and W_i = 0.65. The right y-axis displays the stellar masses derived from the mass-magnitude relation of the models with 65% of critical rotation initially.

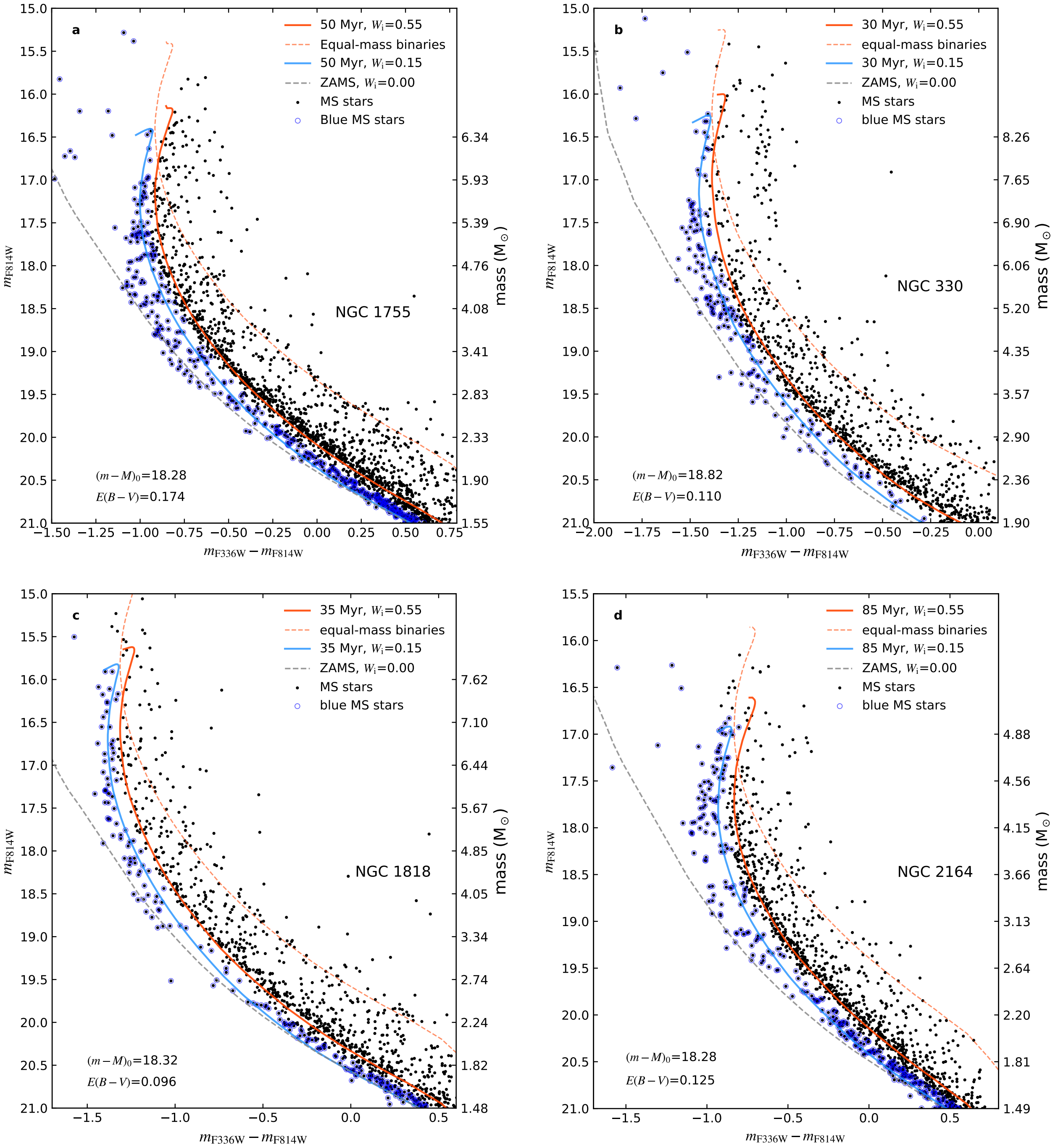

Figure 4.7: As panel b of Fig. 4.1 but for the indicated stars clusters, where stellar models with different initial rotational velocities ($W_i = 0.55$ and $W_i = 0.15$) are employed to fit the red and blue main-sequences of the clusters (see legends). The adopted distance moduli and reddenings are indicated both in the figure and in Tab. 4.1.

binary model can exchange mass and angular momentum via Roche lobe overflow. The mass transfer rate is implicitly adjusted such that the radius of the donor star is restricted to its Roche lobe radius (Wellstein and Langer, 1999). The specific angular momentum accreted by the secondary star depends on whether the accretion is ballistic or occurs via a Keplerian disk. If the orbit of a binary system is wide enough to avoid tidal spin-down, the accretor can reach critical rotation by accreting only a few percent of its initial mass. When this happens, we enhance the mass-loss rate of the accretor (Langer, 1998; Paxton, Marchant et al., 2015) such that it remains rotating just below critical. We assume radiation as the driving force of the enhanced wind. If the required mass loss is beyond the radiative capability of the system, we assume that the binary is engulfed in the excess material, and merges as a consequence. The merger models are computed with the method described in detail in Sec. 4.5.4. We assume the merger products to have an initial spin of 15% of critical rotation ($W_\mathrm{i} = 0.15$), which is consistent with the blue MS when single star models with $W_\mathrm{i} = 0.55$ are used to reproduce the red MS.

We use a Monte Carlo scheme to generate the initial parameters of 3500 binaries, representing a cluster of $7.7 \times 10^4\,\mathrm{M}_\odot$, with a binary fraction of 1 and the least star mass being $0.8\,\mathrm{M}_\odot$. The initial primary mass varies from $3\,\mathrm{M}_\odot$ to $100\,\mathrm{M}_\odot$, following a Salpeter IMF with an exponent of -2.35, while the initial mass ratio ranges from 0.1 to 1, obeying a flat distribution. The initial period varies from a minimum value, at which the two stars would encounter Roche lobe overflow at zero-age MS to 3162 days, following a flat distribution in logarithmic space.

We follow the evolution of these binaries from the zero-age MS to core carbon exhaustion. If the core mass of the primary star exceeds the Chandrasekhar mass at the time of carbon depletion, we assume that a supernova explosion happens, and compute the remaining evolution of its companion as single star.

In Fig. 4.8, we show the CMD distribution of our binary models and binary-evolutionary products at 30 Myr. The magnitude of each binary model is obtained by adding the fluxes of the two components in the corresponding filter bands. The effect of gravity darkening is implemented according to Espinosa Lara and Rieutord (2011) and Paxton, Smolec et al. (2019) by assuming a random orientation for the rotational axis of a star model. We assume that the orbit and spin vectors have the same orientation. We assign an additional shift to each binary model (or binary merger product) in the CMD by considering a Gaussian distribution for the photometric errors at the corresponding magnitudes. For comparison, we overplot the observed MS stars in NGC 330. We do not normalize the total number of our binary models to the observed number of stars, because a concrete quantitative comparison between our binary models and the observations is beyond the scope of this work.

In agreement with C. Wang et al. (2020), we see in Fig. 4.8 that MS mergers produce a population of blue stragglers on the left side of the turn-off, between the zero-age MS line and the solid blue line. We find a deficit of MS merger products fainter than ~18.5 mags at this age, because the faint stars far below the turn-off hardly have time to expand and undergo mass transfer. Besides, our models predict very few MS merger products near the solid blue line, due to the same reason. Therefore, orbit decay during the early evolution of the binaries (see the main text) is mandatory to explain the observed dense distribution of the blue MS stars near the solid blue line. The modelling of this orbit decay is beyond the capabilities of current stellar evolution calculations.

Similar to the results in C. Wang et al. (2020), our newly computed binary models predict a sequence of critically-rotating stars to the red side of the turn-off region. These are the mass gainers of Case B mass transfer, which reach critical rotation and avoid tidal spin down, and likely correspond to Be stars. To account for the flux contribution from the decretion disk of these stars, we increase their red magnitude by 0.2 mags (Labadie-Bartz et al., 2017; Hastings, Langer et al., 2021).

In our shortest period binary evolution models, the rotation of the two components is affected by tides after the zero-age MS. Fig. 4.8 shows a population of tidally-braked binary models, in which the two stars rotate at velocities lower than their initial values. Such systems, if they have small mass ratios, may be located in positions in the CMD that we assign to hold blue MS stars. Additionally, some of our binary models contain a MS star and a stripped, hot helium burning star, which can also contribute to the observed blue MS stars. To explore the degree of contamination of blue MS from these binaries, we calculate the fraction of our detailed binary models (MS+MS binaries and MS+He burning star binaries) which would be classified as blue MS stars, with respect to the total number of binary models. We use the same criterion as in our previous analysis to identify blue MS stars, i.e. counting stars bluer than the median color between the two isochrones at the corresponding magnitude. We do this calculation for our detailed binary models for ages from 15 to 100 Myr. The result is shown in Fig. 4.9.

We perform this analysis only for binary models which are at least one magnitude below the cluster turn-off, since blue and red MSs become undistinguishable near the turn-off (Fig. 4.8). This happens because the isochrone in this region is almost vertical, and as a consequence, the unresolved binaries (with whatever rotation) may be bluer than their single counterparts and contribute to the blue MS stars. In addition, the effect of gravity darkening is more pronounced near the turn-off, resulting in a large spread of the fast-rotating stars.

In Fig. 4.9, we see that for all considered ages, the fraction of binaries that contribute to blue MS stars remains below 3%, which is small compared to the fraction of the observed blue MS stars (~20%). Also Fig. 4.8 shows that the majority of the tidally-braked binaries are still found above the red MS, due to the presence of a companion, despite their slow rotation.

This result is consistent with an analysis of the initial binary parameters. According to our initial period distribution, we find that only 4.6% of the binaries hold two stars rotating at velocities lower than 15% of their critical velocities due to tides. We find that, in general, these slowly-rotating binaries can be classified as blue MS stars only if their initial mass ratios are smaller than 0.25. Assuming a flat mass ratio distribution, we conclude that only ~0.77% of the MS binaries can contaminate the blue MS stars. This simple analysis agrees well with the results in Fig. 4.9. Therefore, we conclude that the contribution of tidally-braked binaries to the observed blue MS stars is marginal.

4.5.3 C: Mass functions

In this section, we investigate the mass functions for the red and blue MS stars in the above mentioned young star clusters. We employ stars between the two grey dashed, horizontal lines in the CMD figures (panel b of Fig. 4.1, Figs. 4.5), because the red and the blue MS can not be well distinguished either above the upper grey dashed line due to the complexity of the turn-off stars, or below the lower grey dashed line due to the large photometric errors. The blue MS stars are those marked by blue circles, while the red MS stars are those not classified as blue MS stars.

Taking NGC 1755 as an example, we plot the cumulative number distribution of the identified red and blue stars with the solid red and blue lines in panel a of Fig. 4.2 and panel c of Fig. 4.2. We use the mass-magnitude relation contained in the isochrones of the $W_{\mathrm{i}} = 0.35$ and $W_{\mathrm{i}} = 0.65$ single star models to convert the magnitude of the identified blue and red MS stars to mass. We assume that stars in each population obey a power-law mass function $N(m)\,\mathrm{d}m \propto m^{\gamma}$, where m means the mass and $N(m)\,\mathrm{d}m$ means the number of stars with masses in the range m to $\mathrm{d}m$. We then find the γ value that

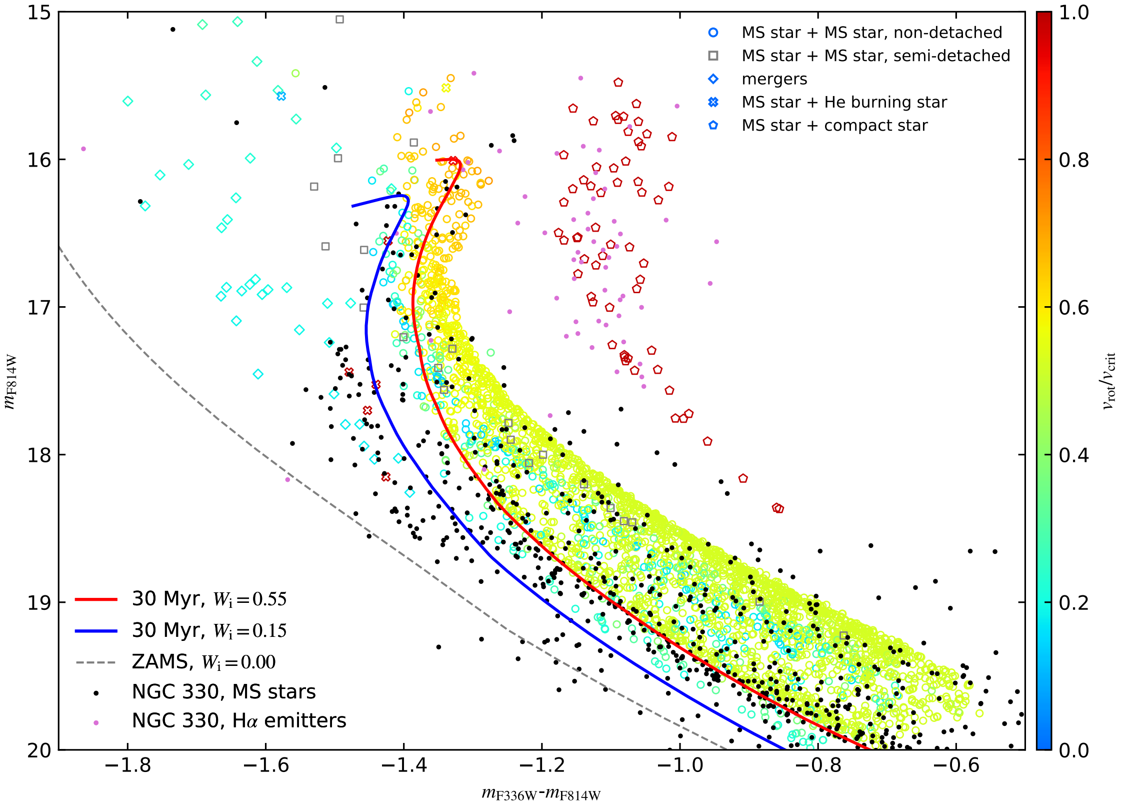

Figure 4.8: Distribution of our detailed binary evolution models in the color-magnitude diagram at an age of 30 Myr. Distance modulus and reddening are assumed as panel b of Fig. 4.7. Each open symbol indicates a binary model (or a binary merger product), showing the combined magnitude and color of the two stars (or the magnitude and color of the binary merger product). Circles indicate detached binary models containing two main-sequence stars, while squares correspond to semi-detached binary models containing two main-sequence stars. Diamonds designate main-sequence merger products. Crosses correspond to binary models containing a main-sequence star and a stripped helium burning star, while pentagons denote binary models containing a main-sequence star and a compact companion. The semi-detached systems are marked in grey, while the color for other open symbols shows the current rotational velocity of either the visually brighter component in a binary model or of a binary merger product. The observed main-sequence stars and Hα emitters are overplotted with small black and purple dots, respectively. The isochrones and zero-age main-sequence line are the same as those in panel b of Fig. 4.7.

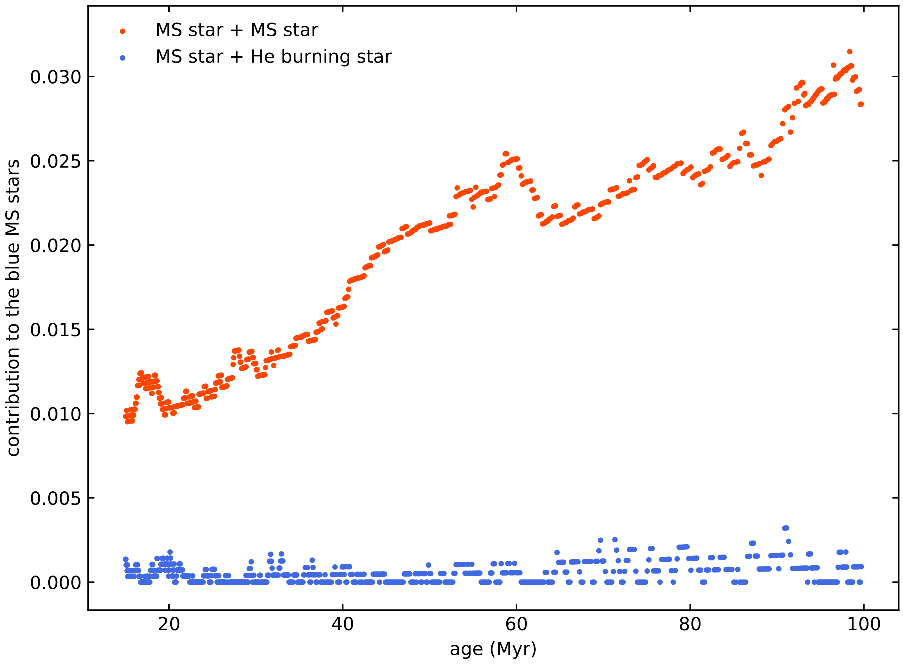

Figure 4.9: Contamination of the blue main-sequence from binary evolution (non-mergers) at different ages. Red and blue dots correspond to the fraction of binary models containing two main-sequence stars and binary models containing a main-sequence star and a He burning star, that will be classified as blue main-sequence stars, with respect to all the binary models, respectively.

can best fit the cumulative distribution of the observed stars in each population. We do the fitting in the cumulative distribution plane to avoid the uncertainties introduced by mass bins. The results are shown with color dashed lines in panel a of Fig. 4.2 and panel c of Fig. 4.2, with the values of the mass function slopes and one sigma errors listed. One sigma error is calculated such that 68.3% of the observed distribution (solid color line) is covered, shown by the colored shaded area. The residuals that describe the difference between the observed distribution and the predicted distribution are shown in panel b of Fig. 4.2 and panel d of Fig. 4.2 for the red and blue MS stars, respectively. It is clearly seen that even though the mass distribution of the blue MS stars smaller than $\sim 2.5\,\mathrm{M_\odot}$ can be comparable to the Salpeter IMF and the red MS stars, the distribution of the higher mass blue MS stars ($> 2.5\,\mathrm{M_\odot}$) is significantly flatter. The shallow slope for the blue MS stars may relate to the fact that the binary fraction is larger for more massive stars. Additionally, a shallow slope may also result from binary orbital decay simulations suggesting that binaries with higher masses are more likely to merge than binaries with lower masses (Korntreff, Kaczmarek and Pfalzner, 2012).

The derived mass function slope depends on the considered mass or magnitude range. We notice that in three of the four analysed clusters (NGC 1755, NGC 1818 and NGC 2164), the mass functions of the blue MS stars below $\sim 2.5\,\mathrm{M_\odot}$ become close to a Salpeter IMF. At the same time, the split MS persists until a brightness corresponding to stars of $\sim 1.5\,\mathrm{M_\odot}$.

For our main result, we consider masses above $\sim 2\,\mathrm{M}_\odot$. Interestingly, Zorec and Royer (2012) found that in galactic field MS stars below $\sim 2.5\,\mathrm{M}_\odot$, the slowest rotators have a significantly larger spin than above $\sim 2.5\,\mathrm{M}_\odot$, consistent with the redder color of the blue MS stars below $\sim 2.5\,\mathrm{M}_\odot$ in the clusters considered here. These findings imply an intrinsic difference in star formation of the slowly-rotating stars above and below $\sim 2.5\,\mathrm{M}_\odot$, perhaps caused by a mass dependent pre-MS evolution, which changes from Henyey-type (horizontal tracks in the HRD) to Hayashi-type (vertical tracks in the HRD) near this mass (Palla and Stahler, 1993; Railton, Tout and Aarseth, 2014). Due to the lack of spectroscopic observations and the larger photometric errors for the stars below $2\,\mathrm{M}_\odot$, we do not include them in our analysis. Nevertheless, the mass functions of the blue MS stars above $\sim 2.5\,\mathrm{M}_\odot$ undoubtedly reveal a discrepancy with the Salpeter IMF, i.e. our conclusion that the red and blue MS stars have different mass functions is robust for stars whose masses are larger than $\sim 2.5\,\mathrm{M}_\odot$.

We do the same experiment for the SMC cluster NGC 330 and the LMC clusters NGC 1818 and NGC 2164. The results are shown in Fig. 4.10, Fig. 4.11, and Fig. 4.12, respectively. For NGC 330, we use a larger lower mass limit of $2.5\ \mathrm{M}_\odot$, because the distance modulus of the SMC is larger than the distance modulus of the LMC. By doing so, we adopt nearly the same higher magnitude limit for all these clusters. We summarize the derived slopes and errors of the MS star mass functions for different clusters in Tab. 4.2. Even though the error of the derived slope of the blue MS stars in NGC 2164 is large, the slope distinction between the red and blue MS stars clearly exists. We found no significant differences between the mass function slopes measured across the four clusters, thus we argue that the mass function dichotomy is ubiquitous in all the studied clusters.

To assess to what extent the derived γ values are affected by blue MS star classification, we examine different boundary lines to define the red and the blue MS stars. We consider boundary lines to lie on the right side of the isochrone for the blue MS, with a color difference equal to a fraction Q of the color separation between the isochrones for the red and the blue MSs. Q ranges from 0 to 1, in intervals of 0.2, with $Q = 0$ ($Q = 1$) representing the extreme case that all stars on the left side of the isochrone for the blue (red) MS are assigned as blue MS stars. The variation of the derived γ values with respect to Q in the four clusters is shown in Fig. 4.13. We also add the results at $Q = 0.5$, which is the value used in our previous analysis. Figure 4.13 reveals that the mass function of the blue MS stars becomes steeper as we use redder boundary lines. Nevertheless, the disparity between the mass function of the blue MS stars and the Salpeter IMF exists even in an extreme case of $Q = 1$.

At last, we use the same stars as we employed in mass function estimation to calculate the fraction of the blue MS stars. The results are shown in Tab. 4.2, with the mean values obtained by assuming $Q = 0.5$ when computing the borderline between the red and the blue MS stars, and the lower and upper errors obtained by assuming $Q = 0$ and $Q = 1$, respectively. We found that the ratio of the blue MS stars is almost identical in all four clusters.

Table 4.2: Slopes γ and uncertainties of the mass functions derived for the red and blue main-sequence stars in four clusters. The last column shows the number ratio between the blue main-sequence stars and all stars.

Cluster	Galaxy	γ for the red MS stars	γ for the blue MS stars	$N_{\mathrm{blue\,MS}}/(N_{\mathrm{blue\,MS}}+N_{\mathrm{red\,MS}})$
NGC 330	SMC	-2.44 ± 0.31	0.64 ± 0.40	$0.19^{+0.18}_{-0.07}$
NGC 1818	LMC	-2.23 ± 0.26	-0.85 ± 0.75	$0.16^{+0.15}_{-0.09}$
NGC 1755	LMC	-2.30 ± 0.08	-0.52 ± 0.50	$0.19^{+0.25}_{-0.10}$
NGC 2164	LMC	-1.92 ± 0.36	-0.38 ± 1.24	$0.17^{+0.24}_{-0.09}$

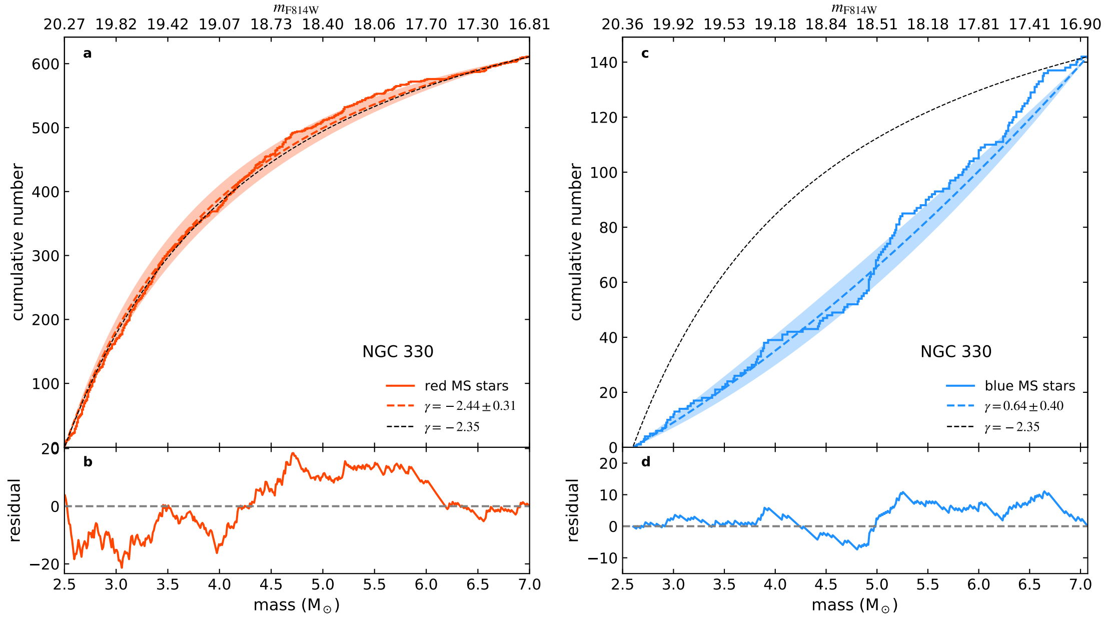

Figure 4.10: As Fig. 4.2, but for the Small Magellanic Cloud cluster NGC 330.

4.5.4 D: Merger models and merger history

We suggest that MS mergers are responsible for the formation of the blue MS stars, according to the fact that they can produce blue stragglers (C. Wang et al., 2020) that appear younger than the other cluster stars. In this scenario, we can estimate the possible merger time t_{merge} of each blue MS star, which is the time in the cluster history when the merger happens, by comparing its distribution in the CMD with the theoretical merger models. We next describe in detail how we do this.

We follow the method in Schneider, Podsiadlowski et al. (2016) to compute models of the merger product of two MS stars. There, it is assumed that the chemical structure of the merger star adjusts itself to that of an ordinary single star with the appropriate mass and age. Whereas the details of the internal mixing process during a stellar merger event are clearly more complex, the major aspect of the our simplified models is confirmed by multi-dimensional merger simulations and detailed follow

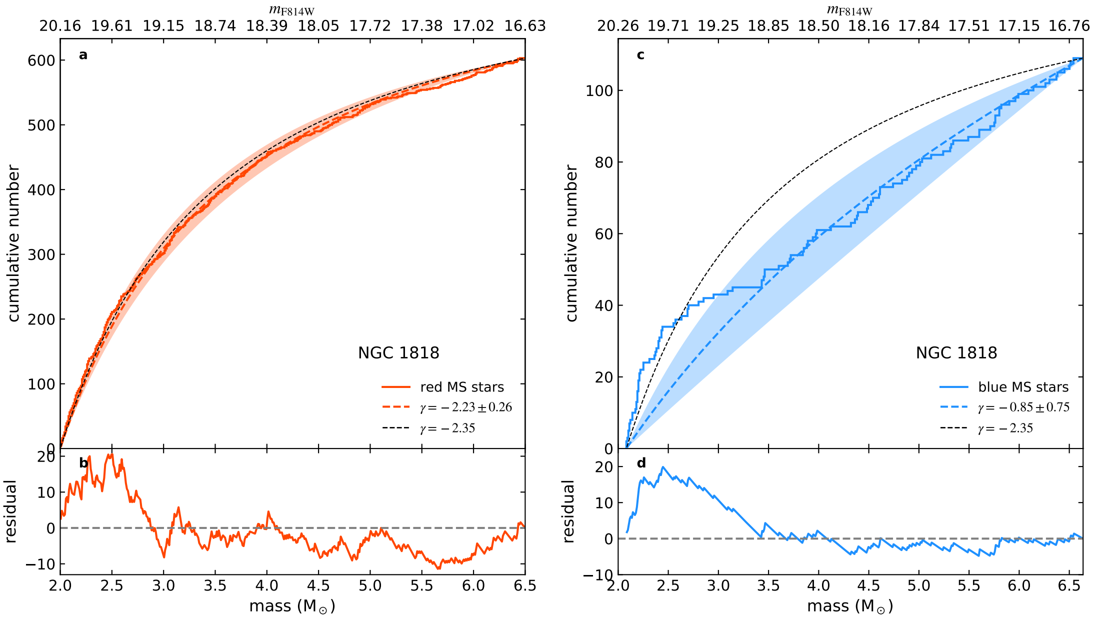

Figure 4.11: As Fig. 4.2, but for the Large Magellanic Cloud cluster NGC 1818.

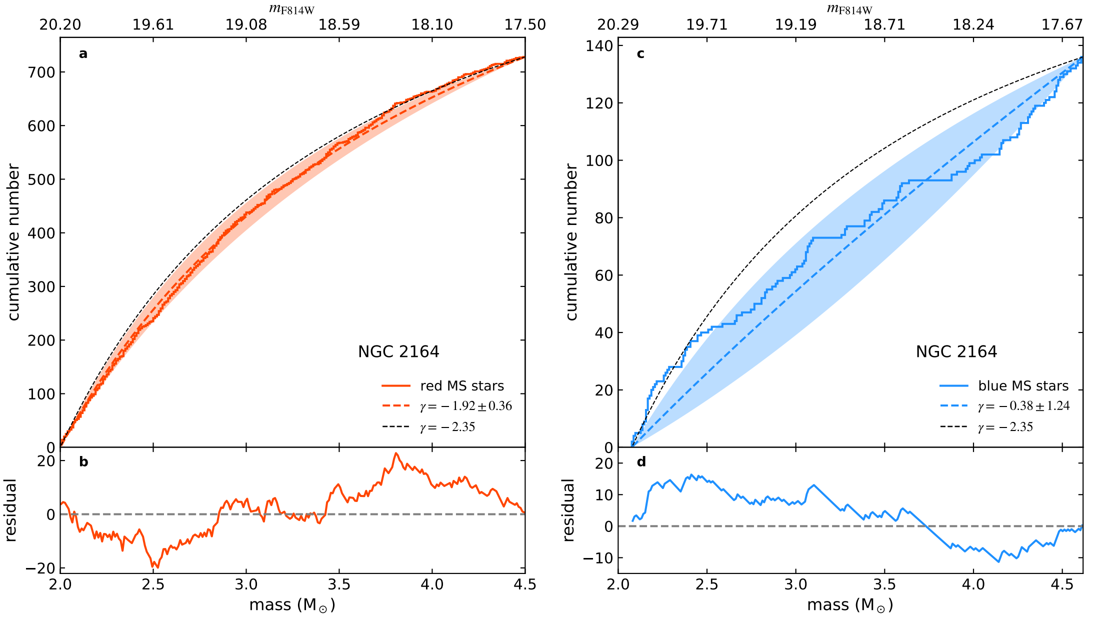

Figure 4.12: As Fig. 4.2, but for the Large Magellanic Cloud cluster NGC 2164.

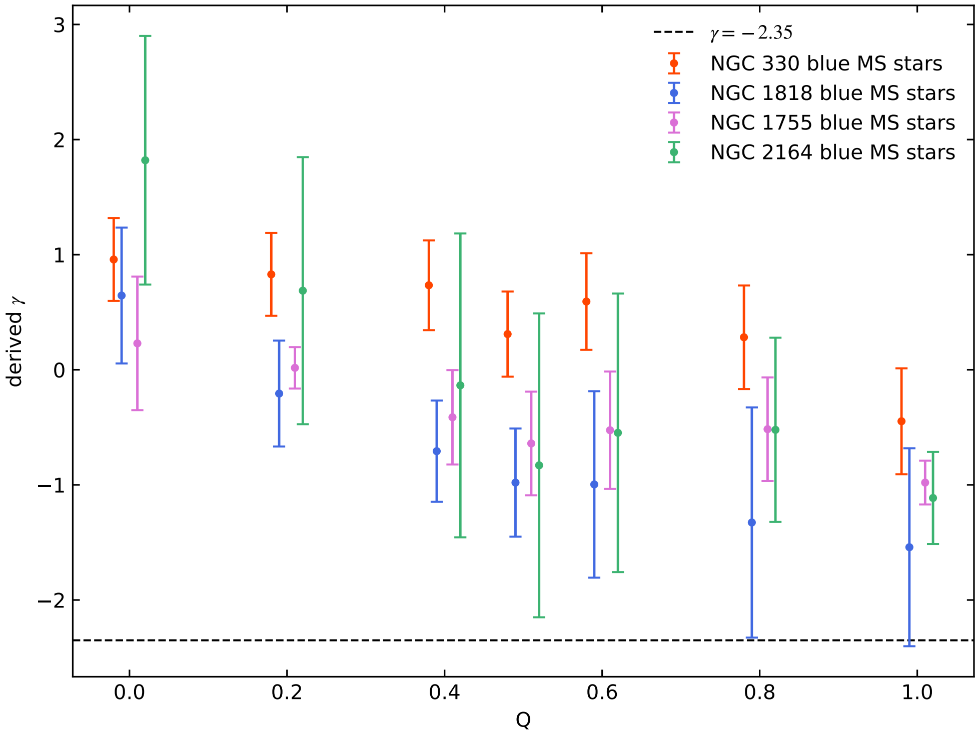

Figure 4.13: Dependence of the derived mass function slope on the borderline between the blue and the red main-sequence stars. The borderline is obtained by shifting the isochrone for the blue main sequence by Q times the color separation between the isochrones for the blue and the red main sequences. We consider Q values between 0 and 1, in intervals of 0.2, as well as $Q = 0.5$. Different errorbars correspond to different clusters. We avoid to plot the errorbars at the same Q values to make them distinct. The black dashed line marks the slope of the Salpeter IMF $\gamma = -2.35$.

up calculations (Glebbeek, Gaburov et al., 2013; Schneider, Ohlmann, Podsiadlowski, Röpke, Balbus, Pakmor and Springel, 2019; Schneider, Ohlmann, Podsiadlowski, Röpke, Balbus and Pakmor, 2020). These studies show that the convective core mass of the merger product increases to a mass found in single star models of the post-merger stellar mass. This increase in convective core mass brings fresh hydrogen to the center of the star which is responsible for the rejuvenation process.

We assume that all stars are born with moderate rotation (i.e., $W_{\rm i} = 0.65$, see Sec. 4.5.1 for the reason), and use corresponding single star models to obtain the masses M_1 and M_2 of the two stars in a binary system immediately before the merger. The mass of the merger product M is expressed as

$$M = (1 - \Phi)\,(M_1 + M_2),$$

where $\Phi = 0.3\,q/(1+q)^2$ with $q = M_2/M_1$ describes the fraction of the mass lost by the binary in the merger event (Glebbeek, Gaburov et al., 2013) . We assume that the lost material has the same composition as the initial composition of the two stars. We then compute the average hydrogen mass fraction of the two stars $\overline{X_1}$ and $\overline{X_2}$ immediately before the merger. The hydrogen mass after and before the merger are connected through

$$M\,\overline{X} = M_1\,\overline{X_1} + M_2\,\overline{X_2} - (M_1 + M_2)\,\Phi\,X_0,$$

where $\overline{X}$ is the average hydrogen mass fraction of the merger product and X_0 is the initial hydrogen mass fraction of the stars. We use our single star models to identify the one which has the same mass and average hydrogen mass fraction as the merger product, and treat it as the starting model of the merger product evolution. The age of this starting model denotes the apparent age $t_{\rm app}$ of the merger product immediately after the coalescence. We then follow the evolution of the merger product until the required age (i.e., the age of the cluster). This means that we evolve the merger model further for a time equal to the difference between the cluster age and the age at which the coalescence happens.

The rotation rate of the merger products, which has not been constrained well to date, plays the dominant role in affecting their positions in the CMD at a given $t_{\rm merge}$. Even though results of MHD simulations have suggested mergers to be slow rotators (Schneider, Ohlmann, Podsiadlowski, Röpke, Balbus, Pakmor and Springel, 2019), seldom faster-rotating stars are detected among blue stragglers (Kamann, Bastian, Gossage et al., 2020). Current available velocity measurements of the blue stragglers report $v \sin i$ values to be between 20 and 270 $\,\rm km\,s^{-1}$, significantly smaller than those of most other cluster members (Sills, T. Adams and Davies, 2005; Rain et al., 2021). In Fig. 4.6, we see that when the red MS is fitted with $W_{\rm i} = 0.65$, all blue MS stars correspond to slow rotators with $W_{\rm i} \lesssim 0.55$. Based on the rotational velocities considered in our single star model grids, we build grids of merger models with birth fractional critical rotational rates of 0, and from 0.15 to 0.55, in intervals of 0.1.

For each initial rotation, we construct a series of lines in the CMD that represent the current positions of the merger products whose progenitors coalesced at given times in the past, from 0 Myr after starburst to the age of the cluster, in intervals of 1 Myr. Figure. 4.3 shows some representative lines by assuming rotational velocities of 35% of the break-up velocities for the merger products. We then use the nearest line to determine the $t_{\rm merge}$ for each observed blue MS star. The adoption of faster rotating merger models results in a larger $t_{\rm merge}$ for a given observed blue MS star, because faster rotating merger models are redder than the slower rotating ones with the same $t_{\rm merge}$. Figure 4.3 indicates that most of the observed blue MS stars can be covered by merger models with a rotation parameter of $W_\mathrm{i} = 0.35$, however, there are outliers to the right and left of the family of lines, indicating that somewhat larger or slower rotation is required for these cases. For example, the blue MS stars between the two isochrones that are used to fit the observed blue and red MS stars (see panel b of Fig. 4.1) cannot be reproduced by merger models with a rotational rate smaller than 35% of their critical velocities. For those stars, we calculate the maximum and minimum rotational rates with which merger models can reach these stars in the CMD.

The derived t_merge for the NGC 1755 blue MS stars are shown in panel b of Fig. 4.4 (lower panel), with the lower limits determined by the merger models with the maximum allowed rotation and the upper limits determined by the merger models with the minimum allowed rotation. We only include stars brighter than 19th magnitude, because we lose diagnostic power beyond that as the fastest rotating merger models produced at 60 Myr are bluer than the slowly rotating merger models produced at 0 Myr. We also exclude the brightest blue MS stars whose magnitudes are smaller than 15.5, because they are brighter than all our merger models. Perhaps they are extremely fast rotating stars which may be subject to strong gravity darkening/brightening. Finally, we compute the merger history by assuming a Gaussian distribution within the allowed merger velocities, with a mean value of $W_\mathrm{i} = 0.35$ and a standard deviation of $W_\mathrm{i} = 0.2$. This distribution is chosen because the isochrone with $W_\mathrm{i} = 0.35$ can fit the blue MS well, and the width of this Gaussian distribution can cover all the identified blue MS stars. This leads to the merger event history of the blue MS stars of NGC 1755 as shown in panel a of Fig. 4.4 (upper panel). The time resolution is 1 Myr, which is governed by the t_merge interval used when we build the merger models. We perform a bootstrapping analysis to obtain the uncertainty of the derived merger time distribution. We randomly assign a rotational velocity for each blue MS star following a Gaussian distribution, and derive its corresponding merger time. We repeat this process 10 000 times, and determine the 1σ uncertainty as the place where 68% of the 10 000 obtained number of mergers per Myr is included in each t_merge bin. The result is shown by the shaded area in panel a of Fig. 4.4. Our results reveal that merger events should be prevalent in the first tens of Myrs, with a peak at 0 Myr to 2 Myrs, to account for the many observed stars near the blue MS.

The distribution of the blue MS stars in the CMD indicates an earlier merger time for brighter stars (see the blue MS stars with magnitudes between 16.5 and 18 near the $t_\mathrm{merge} = 0$ line in Fig. 4.3). In order to examine the correlation between the derived merger time and magnitude, we calculate the Spearman's rank correlation coefficient between these two variables in all 10 000 bootstrapping simulation. The obtained coefficient ranges from 0.31 to 0.54, with an average value of 0.44, indeed indicating a moderate positive correlation. Such a correlation may be consistent with the results of recent binary orbit decay simulations, which propose that more massive binaries are expected to merge earlier than binaries with lower massive stars due to their larger angular momentum and energy loss rates caused by dynamical friction (Korntreff, Kaczmarek and Pfalzner, 2012).

In order to check whether the derived merger rate history is affected by our isochrone fitting, we do the same experiment using the isochrones shown in Fig. 4.7. The results are shown in Fig. 4.14. This time, we consider the merger products to have 0 to 45% of their critical velocities, following a Gaussian distribution with a peak at $W_\mathrm{i} = 0.15$ and a width of $W_\mathrm{i} = 0.3$. These values are chosen such that the rotation peak matches the rotation of the single star models that are used to fit the blue MS, and all blue MS stars are covered, except for several stars which fall on the blue side of the zero-age MS line in Panel a of Fig. 4.7. The rise of the merger event rate at recent times in Fig. 4.14 is caused by ample blue MS stars that can only be reached by non/slowly rotating mergers formed very recently. These blue MS stars have smaller derived rotational rates and t_merge range, thus a larger probability in each allowed t_{merge} bin. However, our main conclusion that merger events are most prevalent in the first tens of Myr remains intact. The Spearman's rank correlation coefficient in this case is 0.34.

We use the same method to estimate the merger history of the blue MS stars in the SMC cluster NGC 330 and the LMC clusters NGC 1818 and NGC 2164, with the results shown in Fig. 4.15. The isochrone fitting is done by employing $W_{\text{i}} = 0.65$ and $W_{\text{i}} = 0.35$ models. We see that our conclusion that mergers happen frequently in the first tens of Myr holds in all the studied clusters. Besides, the derived merger event frequencies in these three clusters all show a continuously decreasing trend. The derived Spearman's rank correlation coefficients are 0.13, 0.60 and 0.47 for clusters NGC 330, NGC 1818 and NGC 2164, respectively, all implying a moderate positive correlation between the derived t_{merge} and magnitude.

In the above analysis, we only consider binary mergers from equal-mass binaries, which possess the strongest rejuvenation. In the following, we examine how the mass ratio of the merger progenitors affects our results. We first quantify the relation between the apparent rejuvenation (how much younger the star looks than it really is) and the mass ratio. We describe the apparent rejuvenation as $(t - t_{\text{app}})/t$, where t is the time at which a merger happens, and t_{app} is the apparent age of the merger product. We consider binaries with primary masses between 2.1 $\text{M}_{\odot}$ and 10 $\text{M}_{\odot}$ in intervals of 0.5 $\text{M}_{\odot}$, and mass ratios between 0.2 and 1 in intervals of 0.2. We assume mergers happen at 60 Myr (i.e., the derived age of cluster NGC 1755), and show the result in Fig. 4.16. It can be seen that rejuvenation increases with increasing mass ratio. For example a 5 $\text{M}_{\odot}$ merger product can be rejuvenated to $\sim$ 40% and $\sim$ 80% younger than its progenitors if it is produced by a $q = 0.2$ and a $q = 1$ binary, respectively. In order to perform this examination, we extend our single star models to 0.4 $\text{M}_{\odot}$. But we only build and use the zero-age MS models for such low-mass stars, as they hardly evolve in young star clusters.

We show the distribution of our merger products created at 60 Myr from binaries with different mass ratios in the CMD in Fig. 4.17, and the resulting merger history in Fig. 4.18. We only include blue MS stars that can be covered by our merger models in this check. It leads to different integral number of the derived merger events under the assumption of different mass ratios. The merger models constructed with low mass ratios are redder in the CMD compared to their high mass-ratio counterparts, thus can cover fewer observed blue MS stars. In Fig. 4.17 and Fig. 4.18, we see that results for mass ratios larger than 0.6 are nearly identical. The rate of the merger events increases after $\sim$ 56 Myr when adopting mass ratios smaller than 0.6, because more blue MS stars have smaller derived rotational rate and t_{merge} ranges. Nevertheless, our main conclusion that merger events should occur at early times is robust, regardless of the binary mass ratio.

Apart from the above-mentioned uncertainties, the derived merger times may also be affected by additional mixing during the merger process, which can make a merger product appear even younger (1.14 times for stars above 5 $\text{M}_{\odot}$ and 1.43 times for stars below 5 $\text{M}_{\odot}$) than in the case of fully rejuvenation (Glebbeek and Pols, 2008; Glebbeek, Gaburov et al., 2013). However, this additional mixing does not significantly affect the distribution of early mergers in the CMD, as the long-lasting later evolution of the merger product after it has been created washes out this small natal difference. Whereas potential surface He enhancement may also impact the distribution of the merger products, it is not found in both theoretical simulations or spectroscopic observations (Sills, Faber et al., 2001; Glebbeek, Gaburov et al., 2013; Carini et al., 2020)

We have proposed in the main text that orbital decay in multiple systems happens probably via Kozai-cycles. A glimpse of the MS distribution in the CMD at the present clusters gives us the impression that there are many suspected triples or higher-order multiples (see panel b of Fig. 4.1

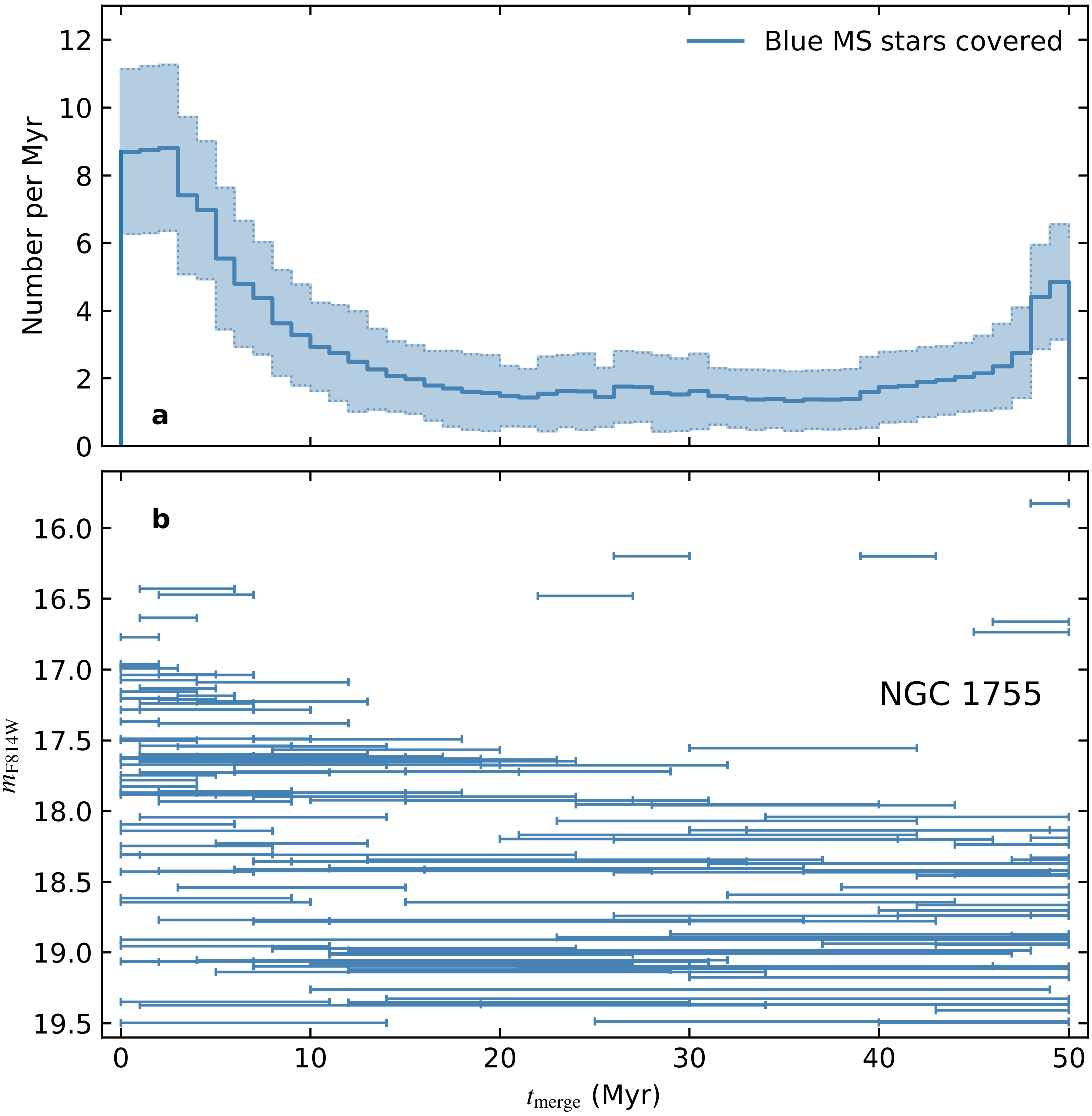

Figure 4.14: As Fig. 4.4, but the results are derived based on the isochrone fitting and blue main-sequence star identification shown in the top left panel of Fig. 4.7.

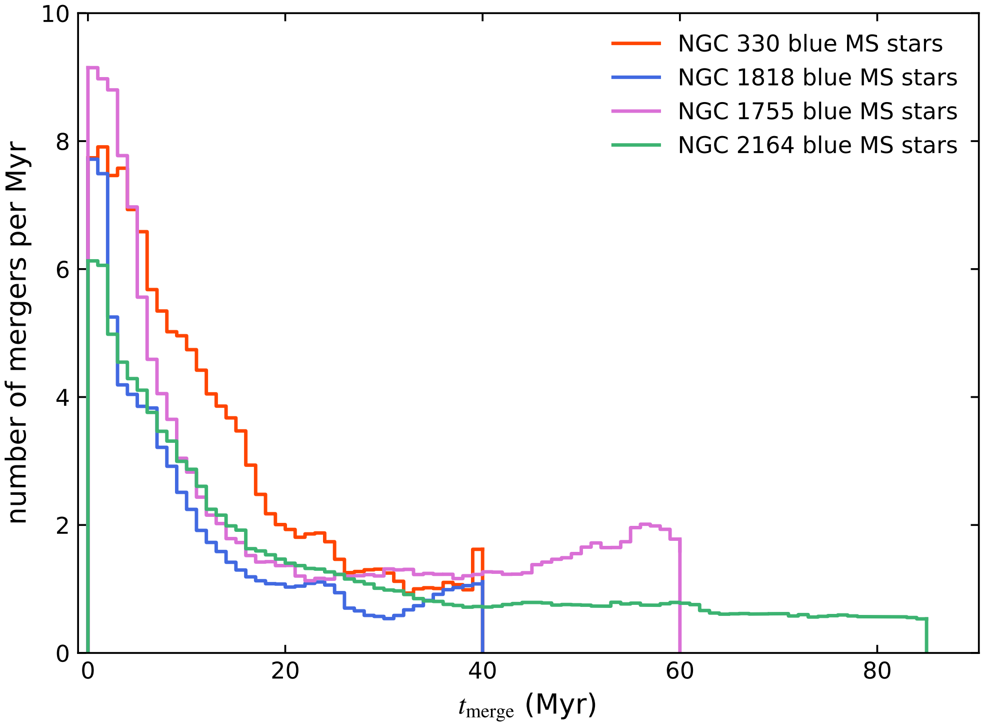

Figure 4.15: As panel b of Fig. 4.4, but for all four clusters: the Small Magellanic Cloud cluster NGC 330, and the Large Magellanic Cloud clusters NGC 1818, NGC 1755 and NGC 2164.

and Figs. 4.5, those with colors redder than the equal-mass binary line red shifted by three times the photometric error). To indicate this, we derive the fraction of the suspected triple or higher-order multiples with respect to all MS stars in three clusters, one SMC cluster NGC 330, and two LMC clusters, NGC 1818 and NGC 1755. In figures comparing our theoretical isochrones with the observations in the CMD (panel b of Fig. 4.1 and Figs. 4.5), we count the stars on top of the equal-mass binary lines shifted redwards by three times the photometric errors as the suspected triple or higher-order multiples. The results are shown in Fig. 4.19. We use absolute magnitude such that we can directly compare clusters with different ages in different galaxies. We use isochrones of $W_{\rm i} = 0.65$ single star models that can best fit the red MS in each cluster to convert the apparent magnitude to the absolute magnitude. We consider stars whose absolute magnitudes are 2 mags larger than the turn-off magnitude to exclude the probable contaminations from critically rotating Be stars. At the low-brightness end, we cut at $M_{\rm F814W} = 2$, which roughly corresponds to an apparent magnitude of 20.5 in these clusters. We show our results in different magnitude intervals. The error bars on the x-axis reflect the magnitude intervals, while the error bars on the y-axis reflect the Poisson error. In general, the fraction of the suspected triples decreases with increasing magnitude. We point out that these values should only be the lower limit, as we miss the low mass ratio multiple systems whose positions are below the boundary lines.

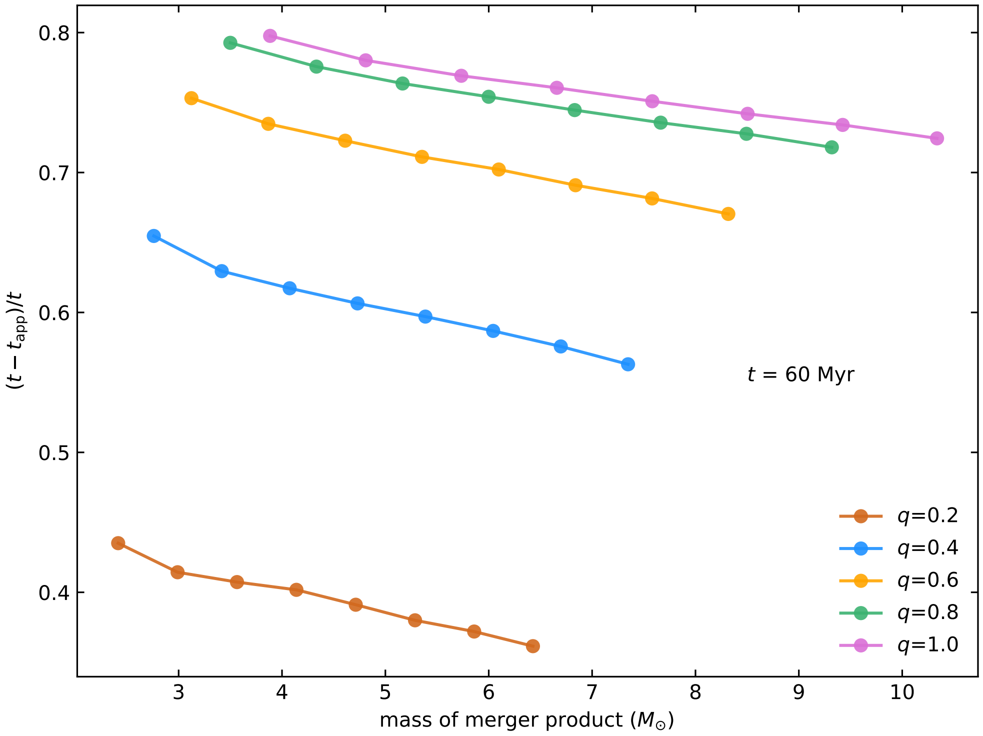

Figure 4.16: Relative rejuvenation versus post-merger stellar mass. t is the cluster age of NGC 1755, which also indicates the most recent incidence time of the merger. t_{app} is the apparent age of the merger product as measured by single star isochrones, for a fixed merger time of $t = 60$ Myr. The five lines correspond to five different mass ratios as indicated by their color (see legend). Each dot on the line corresponds to one computed binary model (see Sec. 4.5.4).

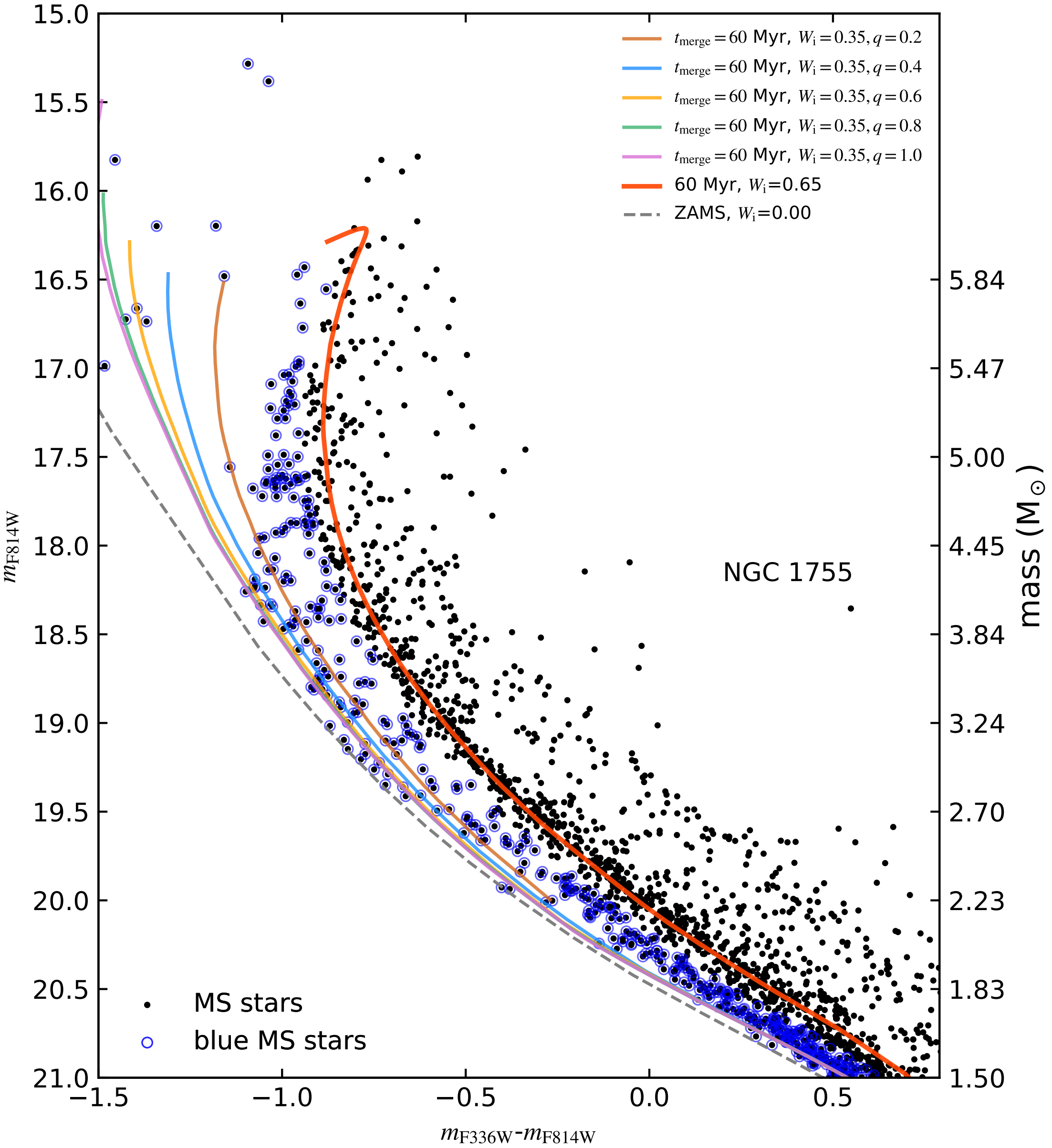

Figure 4.17: As Fig. 4.3, but adopting different mass ratios for the precursor binaries of the merger models. The thin solid lines correspond to the merger models rotating at 35% of their critical velocities. We only show models of mergers for a merger incidence time of 60 Myr. The isochrone for the red MS (thick solid red line), and the zero-age main-sequence line (dashed grey) are the same as in panel b of Fig. 4.1.

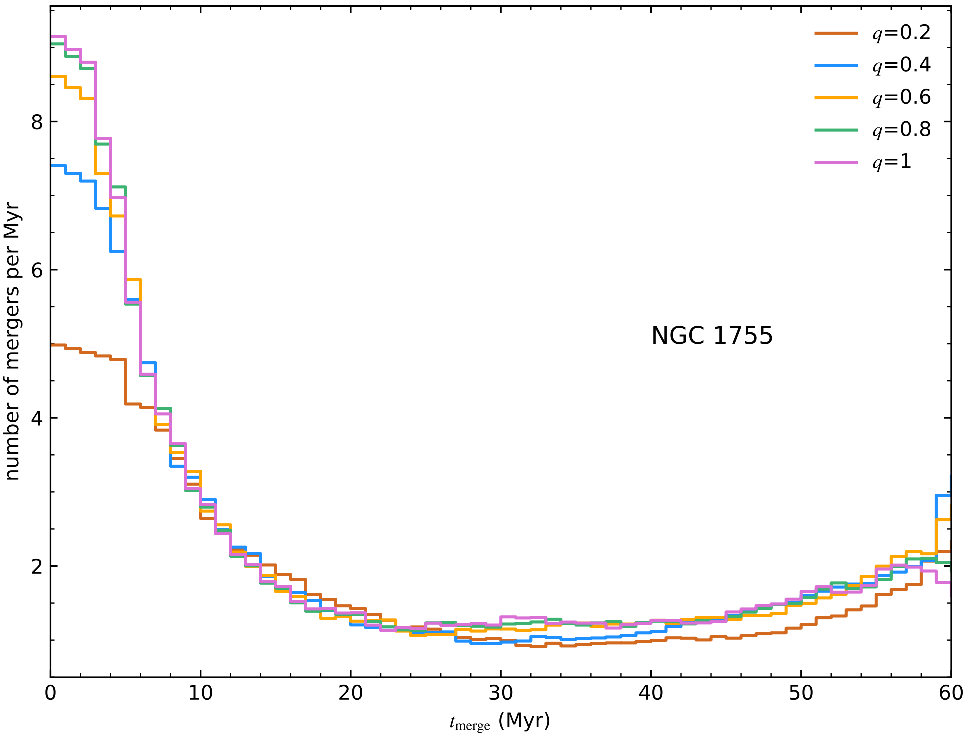

Figure 4.18: As panel b of Fig. 4.4, also showing lines for models resulting from mergers with mass ratios (q) of 0.2, 0.4, 0.6 and 0.8.

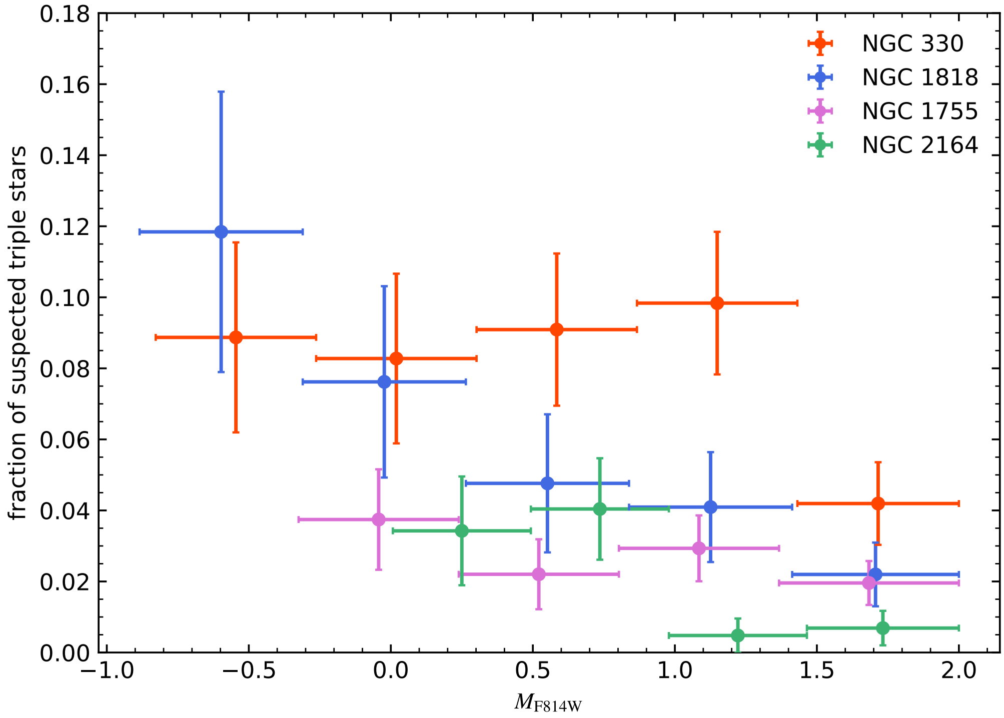

Figure 4.19: Fraction of the suspected triple stars or higher order multiples out of all main-sequence stars, based on the equal-mass binary lines in the CMDs (see panel b of Fig. 4.1, and Fig. 4.5), as function of absolute magnitude for stars in four young Magellanic Cloud clusters in different magnitude intervals. The horizontal width of the error bars correspond to the magnitude intervals, while the vertical error bars reflect the Poisson error.

CHAPTER 5

An upper limit on the fraction of Be stars in young star clusters that are produced by binary evolution

Abstract

In the previous chapters in this thesis, we have proposed that binary evolution can produce a sequence of near-critically-rotating Be stars on the right side of the turn-off in young star clusters, with a magnitude range of 2-3 mags. The predicted Be stars in our detailed binary models agree with the distribution of the observed Be stars in young Magellanic Cloud clusters in terms of the magnitude range and the trend that the Be star fraction increases with decreasing magnitude. However, the predicted Be star fraction near the turn-off in our detailed binary models is less than 10%, much smaller compared to the observed value of $\sim$ 50%. The reason is that the majority of our binary models merge during Case B mass transfer according to our merger criterion. In this chapter, we aim to derive an upper limit on the production of Be stars from binary evolution by relaxing the previously adopted merger criterion. Instead of building new detailed binary models, we propose a method to use merely single star models to simulate the distribution of the binaries and binary evolutionary products in young star clusters. By assuming that all Case B mass transfer binaries with initial mass ratios larger than 0.5 can produce a Be star, we find that at most 30% of the main-sequence stars near the cluster turn-off are binary evolutionary induced Be stars. This number is still smaller than the observed Be star fraction ($\sim$ 50%) near the turn-off, which implies that the single evolution channel for the formation of Be stars has to be invoked. However, we find that the fraction of the Be stars produced by the single evolution channel depends highly on the uncertain stellar wind mass loss and the accompanied angular momentum loss. Further theoretical studies on the single and binary star evolution and observational studies on the Be stars and their companions are required to understand the origin of Be stars.

5.1 Introduction

Be stars are a peculiar group of B-type stars with hydrogen emission lines. The emission lines come from the decretion-disc, which is believed to be associated with extreme fast rotation (see Rivinius, Carciofi and Martayan, 2013, for a review). Two formation scenarios have been proposed for Be stars. One is the so-called single evolution channel, in which a Be star is produced by an initially fast/moderately fast rotating single star achieving near critical rotation at the end of its main-sequence (MS) evolution, mainly due to the decrease of the critical rotational velocity (Ekström et al., 2008; Hastings, C. Wang and Langer, 2020). The other one is the so-called binary evolution channel, in which a Be star is produced in a binary system via accretion (Pols et al., 1991; Liu, van Paradijs and van den Heuvel, 2006; Langer, 2012; C. Wang et al., 2020). The most compelling evidence supporting the binary channel is the detection of Be X-ray binaries that contain a Be star and a compact object (Liu, van Paradijs and van den Heuvel, 2006; Langer, 2012; Raguzova and Popov, 2005). However, whether the binary channel alone is adequate to explain all of the Be stars, or the single channel has to be invoked is still unknown (Pols et al., 1991; van Bever and Vanbeveren, 1997; Shao and X.-D. Li, 2014).

Be stars have been identified in young Magellanic Cloud star clusters via their photometry excess in the narrow Hα band in the Hubble Space Telescope (HST) (Milone, Marino, Di Criscienzo et al., 2018). These Be stars provide us a unique opportunity to study the formation mechanism of Be stars, as the cluster stars are believed to be born in a single starburst. The fact that all the confirmed Be sequences extend to 2-3 magnitudes below the turn-off advocates the binary channel, as the unevolved single stars cannot evolve to Be stars, unless these single stars are born as extremely fast rotating stars, which is not real (W. Huang, Gies and McSwain, 2010).

In the previous chapters in this thesis, we have shown that our detailed binary models indeed produce a Be sequence with a magnitude range of 2-3 mags, which agrees with the observations. They are the mass gainers that used to experience a stable Case B mass transfer, during which they achieved critical rotation and avoided tidal spin down. However, the fraction of the Be stars in our binary models is much smaller than the observed fraction. It is because that the merger fraction is high in our binary models. We assume that the mass gainer cannot keep on accreting mass once it reaches critical rotation during mass transfer. The excess material is thrown away in the form of an enhanced wind mass loss. We assume that it is the combined radiation pressure of the two stars that is used to sustain this enhanced wind mass loss. If the radiation pressure is not large enough, the two stars will be engulfed by the excess material and merge as a consequence. However, whether the mass gainer is able to continue accretion after it achieves critical rotation is debated. Viscous coupling of the accretion disk and the critically-rotating accretor can help to transport angular momentum outward, allowing the accretor to evolve without a devastating merger (Popham and Narayan, 1991; Paczynski, 1991). In addition, radiation from the hot spot produced by the accretion stream hitting the accretor may also make further accretion possible (van Rensbergen et al., 2011).

Therefore, it is reasonable to relax the merger criterion adopted in our detailed binary models. We do not carry out a concrete study on the mass transfer stability. Instead, we make a simple assumption that all Case B mass transfer binaries with mass ratios larger than 0.5 can produce a Be star, thereby we can obtain the upper limit for the binary evolutionary produced Be stars. Here, the mass ratio threshold is chosen such that the predicted Be star magnitude range roughly match the observed magnitude range in young star clusters. Even though assuming a lower mass ratio threshold (or even no mass ratio threshold) can result in more Be stars near the turn-off, the resultant Be star magnitude range is too large to be comparable to the observations. Meanwhile, due to the steep initial mass function, the contribution from the low mass ratio binaries to the turn-off Be stars is negligible (compare Fig. 5.3 with Fig. 5.4).

We use single star models to simulate the evolution of binaries and build synthetic star clusters, taking into account our previous findings that all stars in a star cluster are born with around half of their critical velocities. Hastings, Langer et al. (2021) derived a stringent upper limit of one third of all MS stars being Be stars near the cluster turn-off with an analytical method, based on similar assumptions (but both Case A and Case B mass transfer systems are able to produce Be stars). The simple analytical method is very useful in examining the upper limit on the binary evolutionary induced Be star fraction in young star clusters, however, our work based on detailed single star models is important in the sense that we take into account the effect of physics (e.g. rotation and wind mass loss) on the stellar evolution. In addition, we can replicate the distribution of the MS stars (not only the Be stars) in young star clusters in the color magnitude diagram (CMD) with our method.

In Section 5.2, we describe the method we use to perform population synthesis simulations based on merely single star models. In Section 5.3, we display the distribution of the synthetic MS stars in a cluster resembling cluster NGC 330 in the color-magnitude diagram (CMD) and the Be fraction in our synthetic star cluster. We also compare our results with the observations in this section. At last, in 5.4, we summarize our conclusions.

5.2 Methods

In this work, we employ the single star models with different rotation, which are described in detail in Chapter 4.5.1 to build synthetic star clusters. These single star models are computed by MESA version 12115 (Paxton, Smolec et al., 2019). We do not repeat the description of the single star models in this section, instead, we focus on the explanation of how we build synthetic star clusters with merely single star models. We make use of our previous findings that all stars (including single stars and binaries) in a star cluster are born with 55% of their critical velocities. The fast-rotating single stars in star clusters are easy to be simulated by our fast-rotating single star models. While to obtain the distribution of binaries with simply single star models, we need to make the following assumptions. We assume that the two components in a binary evolve in isolation, with the period unchanged, until the more massive star fills in its Roche lobe. The position of a pre-interaction binary is then determined by the combined fluxes of the two single components. While after the more massive star fills in its Roche lobe, we do not compute the detailed mass transfer processes. Instead, we make a simple assumption that if the first Roche lobe overflow happens when both the two components are burning H, a MS merger is produced immediately. While if the first Roche lobe overflow happens after the initially more massive star has finished H burning in the center, we assign a mass ratio threshold of 0.5, above which a stable Case B mass transfer will occur and produce a critically-rotating Be star immediately without any mass accretion, and below which an unstable Case B mass transfer will occur and produce a post-MS merger product.

Even though such a simulation based on merely single star models cannot predict the properties of the binary evolutionary products accurately, it has many advantages, for example, it is time saving, thereby facilitating initial binary parameter study, and allowing us to examine the adopted physics assumptions in binary evolution, like the merger criterion. The fact that this method cannot predict the CMD positions of the semi-detached systems and post Case A mass transfer systems does not destroy our result and conclusion, because the fraction of the semi-detached systems and the Case A mass transfer systems in a star cluster is low (smaller than ~ 10%, Sen et al. in prep, see also Fig. 4.8).

To perform such a population synthesis simulation, it is firstly crucial to know the inputs, i.e. initial binary fraction and the distribution of the binary parameters. In the following, we apply the method in Milone, Piotto, Bedin et al. (2012) to derive the binary fraction and binary mass ratio distribution of the MS stars in young star clusters by studying their positions in the CMD.

5.2.1 Binary fraction and mass ratio distribution

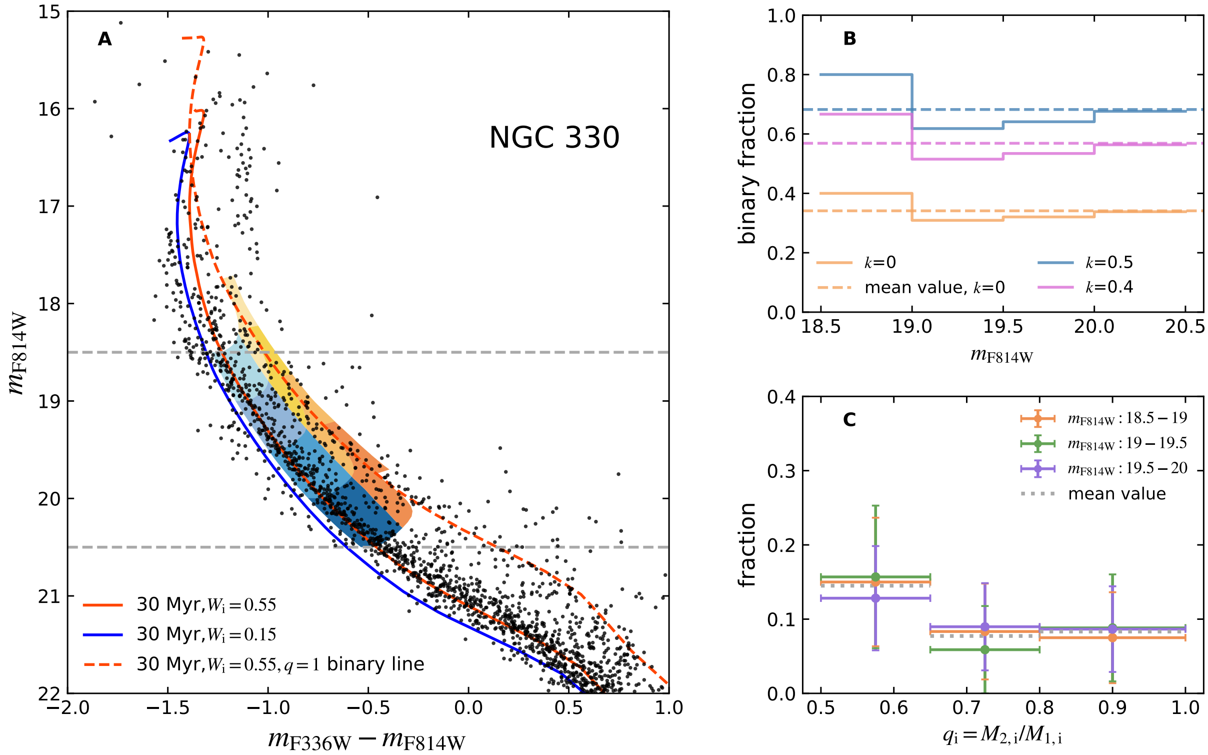

Figure 5.1: Estimate of binary fraction and mass ratio distribution in NGC 330. Shadow areas in Panel A delineate the stars employed. The boundary of these areas is explained in detail in the text. The red and blue solid lines correspond to the isochrones of 30 Myr fast-rotating and slowly-rotating single stars, respectively, while the red dashed line shows the position of the equal-mass binaries comprised of two fast-rotating stars. Panel B displays the derived binary fraction, with different colors representing different fractions of initially synchronized binaries that contain two slowly-rotating stars. Dashed lines express the mean binary fractions in the whole considered magnitude range. In Panel C, we exhibit the normalized fraction of high mass ratio binaries ($q \geq 0.5$) in three bins of $0.5 \leq q < 0.65$, $0.65 \leq q < 0.8$ and $0.8 \leq q \leq 1$. Different colors correspond to different magnitude intervals. The fraction is normalized such that the mass ratio bin is 0.05, and the sum of the fraction in the considered mass ratio range is 1 in each magnitude interval. The grey dashed lines are the mean values in the three magnitude intervals.

Figure 5.1 describes how we derive the binary fraction and mass ratio distribution in NGC 330 and the results we obtain. Stars in color shaded areas are involved in this estimation. The blue area contains most of the single stars and low mass ratio binaries ($q < 0.5$). Its blue boundary is red-shifted from the blue solid line by three times the color error, while its red edge is the locus of binaries formed by two red MS stars with $q = 0.5$. The orange area contains large mass ratio binaries ($q \geq 0.5$). Its red borderline is determined by the red dashed line shifted towards the red by five times the color error. The bright and faint boundaries of the two areas correspond to the locations of $W_{\mathrm{i}} = 0.55$ binaries whose primaries have luminosities of $m_{\mathrm{F814W}} = 18.5$ and $m_{\mathrm{F814W}} = 20.5$, respectively. We then count the number of the stars in the blue and orange areas as $N_{q<0.5}$ and $N_{q\geq0.5}$, respectively. We use a threshold of $q = 0.5$ because $W_{\mathrm{i}} = 0.55$ binaries with mass ratios larger than this value are well separated from single stars and tidally-locked slow rotating binaries, meaning that most of the stars in the orange region are large mass ratio unresolved binaries that are not tidally-locked. Assuming a binary fraction of f_{bin} and a fraction k of the binaries are synchronized, we have

$$\frac{5}{9}(1-k)f_{\mathrm{bin}}(N_{q<0.5}+N_{q\geq0.5}) = N_{q\geq0.5}.$$

Here 5/9 is from the fact that if we assume a flat mass ratio distribution, 5/9 of the binaries with q from 0.1 to 1 have $q \geq 0.5$. Panel B shows the derived values of f_{bin} from different k values in a magnitude range of 18.5-20.5 with intervals of 0.5. Dashed lines with corresponding colors are the average values in the whole considered magnitude range. We see that f_{bin} increases from ~ 40% at $k = 0$ to ~ 70% at $k = 0.5$, which is consistent with the observed high binary fraction in massive stars (Sana, S. E. de Mink et al., 2012). Similar results are obtained in NGC 1818, NGC 1755, and NGC 2164 (see Fig. 5.5, Fig. 5.6 and Fig. 5.7, respectively).

A similar idea is used to estimate the mass ratio distribution, but only high mass ratio binaries (stars in the orange area) are involved. We further divide them into three subgroups, $0.5 \leq q < 0.65$, $0.65 \leq q < 0.8$, and $0.8 \leq q \leq 1$. The fraction of binaries in each subgroup is obtained by dividing the number of stars in that group by the total number of high-mass-ratio binaries in the studied magnitude range. We do this in the upper three magnitude intervals, namely from 18.5 to 20. The result for NGC 330 is shown in Panel C of Fig. 5.1. We normalize the derived fraction to a mass ratio bin of 0.05 to eliminate the impact of different mass ratio intervals introduced in the three subgroups. For example, the leftmost orange dot and error bars indicate that the fractions of stars with $0.5 \leq q < 0.55$, $0.55 \leq q < 0.6$, and $0.6 \leq q < 0.65$ are all ~10% with respect to all high mass ratio binaries. In general, we find a flat mass ratio distribution in NGC 330, as well as in the other three clusters analyzed in this work (see Figs. 5.5 for NGC 1818, 5.6 for NGC 1755, and 5.7 for NGC 2164, respectively). This agrees with the previously reported uniform distribution from the investigation of 59 Galactic globular clusters (Milone, Piotto, Bedin et al., 2012). Therefore, in the following population synthesis calculations, we assume that the mass ratio is evenly distributed between 0.1 and 1.

The method used here relies on high photometric quality, high resolution, accurate analysis of photometric errors, and a correct estimate of field contamination. Even though all the above conditions are satisfied, it would still be difficult to give anything like a precise estimate, because the progenitors of the observed stars are not unique, due to degeneracies from rotation, gravity darkening, synchronized binaries, as well as observational errors. Therefore, the derived binary rates and mass ratio distribution should be taken with some caution. Despite the caveats, it is still a reasonable and efficient way to grasp the binary population in star clusters in the first place.

5.2.2 Building synthetic star clusters based on merely single star models

In this section, we describe in detail how we build a synthetic star cluster resembling NGC 330 with merely single star models. We first extend our single star models to 0.3 $\mathrm{M}_{\odot}$, such that we can reproduce faint stars. We obtain the properties of even lighter stars by extrapolation. For each cluster, we perform a Monte Carlo simulation to generate 10^6 initial binary systems, whose primary masses are from 1.5 $\mathrm{M}_{\odot}$ to 20 $\mathrm{M}_{\odot}$, following the Salpeter IMF with an exponent of -2.35. We adopt a flat mass ratio distribution from 0.1 to 1 as obtained in Sec. 5.2.1. While for the period distribution, we adopt the following formula (Moe in private communication):

$$f(\log P)\,\mathrm{d}\log P = [0.16 + b * (\log P - 4)]\,\mathrm{d}\log P,$$

where $b = 0.038 - 0.048 * \log(M_1/M_{\odot})$ across $\log P(\mathrm{days}) = -0.5 - 3$. Under this assumption, binaries with primary masses larger than 6 $\mathrm{M}_{\odot}$ tend to have short periods, while binaries with primary masses smaller than 6 $\mathrm{M}_{\odot}$ tend to have long periods.

We introduce a period threshold of $\log P = 0.8$ ($P < 6.3$ days), below which binaries are assumed to be synchronized. This threshold is roughly the boundary between the synchronized and non-synchronized binaries in our detailed binary models (see Section 4.5.2). If a binary is synchronized, the rotational rates of the two star ingredients are determined by their initial periods, i.e. binaries with smaller periods have higher natal spins, using the relation between our binary models' (the binary models described in Section 4.5.2) initial spins and periods. While above this period threshold, both binary members are assumed to rotate at 55% of their critical velocities at zero-age MS (ZAMS). Under this assumption, we find an overall fraction of ~ 40% stars to be initially synchronized. Therefore, we consider a binary fraction of 0.6 (see Fig. 5.1), and populate 6667 single star models with 55% of critical velocities whose initial masses are from 1.5 to 20 $\mathrm{M}_{\odot}$, obeying the Salpeter IMF.

Then we follow the evolution of the generated star models till the required ages. In a binary system, if the primary star fills its Roche lobe during H burning, we assume a merger happens immediately and use the method described in Sec. 4.5.4 to compute the evolution of the merger product. In contrast, if a primary star fills its Roche lobe after H exhaustion, we adopt a mass ratio threshold of 0.5, above which the secondary star is assumed to evolve to a critically-rotating Be star without any mass increase, and below which the two stars merge to be a post-MS star. We do not trace the evolution of the post-MS stars in this work.

We need to point out that we do not have real critically rotating star models. Therefore, to obtain the temperature and luminosity of a binary-evolutionary-produced Be star, we make use of our detailed binary models. We calculate the temperature difference between the $W_{\mathrm{i}} = 0.55$ single star models and the binary-evolutionary-produced Be star models with the same mass. Then the temperature of the critically-rotating Be star in the population synthesis in this chapter is obtained by subtracting the corresponding temperature difference from the temperature of the secondary star immediately before mass transfer. We assume that the luminosity of the Be star is the same as the corresponding secondary star immediately before mass transfer, since we assume that no mass is accreted to the secondary star. At last, in the CMD, we subtract 0.2 mag from the obtained m_{F814W} for the binary evolutionary induced Be stars as what we do in Fig. 4.8, to account for the disk contribution and to better separate the Be stars from the normal MS stars.

5.3 Results and comparison with the observations

5.3.1 Distribution of the MS stars in the CMD

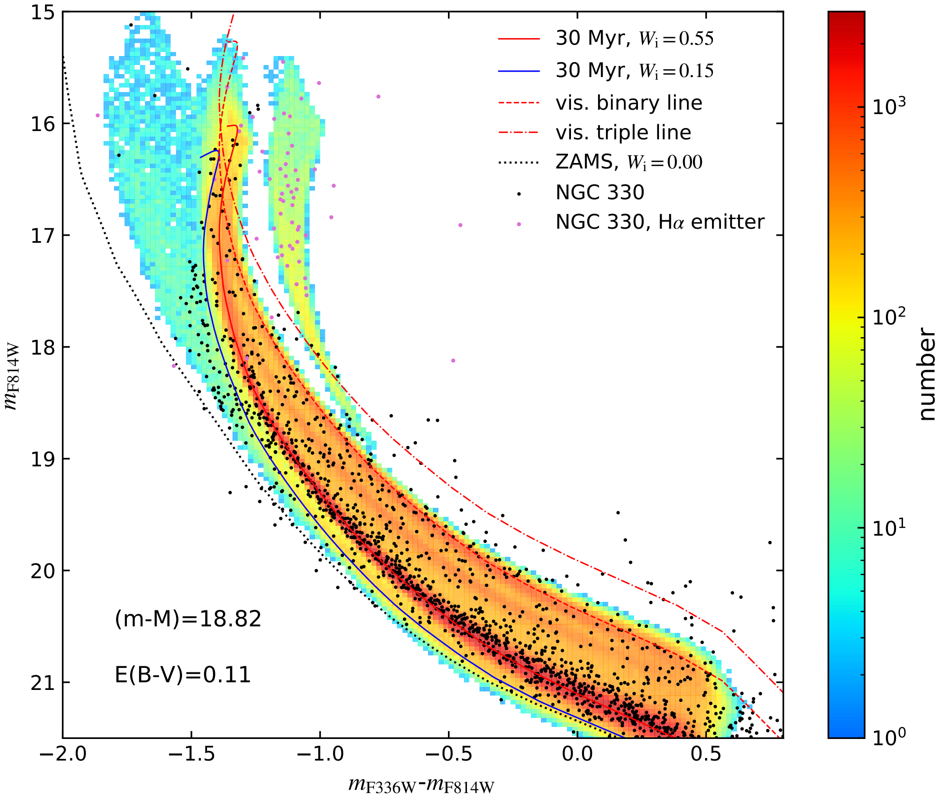

Figure 5.2: The synthetic star cluster resembling NGC 330 based on merely single star models. Color indicates the number of the simulated stars in each pixel. Observed main-sequence stars with and without Hα emission are overplotted with the black and purple dots, respectively. The binary evolutionary induced Be star models are shifted upwards and rightwards by 0.2 mag to better match the position of the observed Hα emitters. We do not normalize the number of the simulated stars to the number of the observed stars to avoid producing discrete main-sequence features in the color-magnitude diagram. The solid red and blue lines correspond to the isochrones of the fast- and slowly-rotating star models, respectively. While the dashed and dotted dashed red lines show the positions of the fast-rotating equal-mass binary and triple star models, respectively.

Fig. 5.2 shows the distribution of our synthetic MS stars that resemble NGC 330 stars in the CMD. The adopted age, distance modulus and reddening are the same as panel b of Fig. 4.7 and are listed in Tab. 4.1. Colors indicate the relative number of the star models in each pixel. We do not normalize the total number of our star models to the number of the observed MS stars to avoid discrete MS features caused by low statistics. Gravity darkening and the magnitude-dependent photometric errors are taken into account. The observed NGC 330 MS stars with and without Hα emission are overplotted by the black and purple dots, respectively, for comparison.

Similar to the synthetic star cluster based on detailed binary models, our synthetic star cluster based on merely single star models also exhibit nearly all the observed MS components with appropriate positions, except for the blue outliers that are bluer than the ZAMS line and the red outliers on top of the visual equal-mass binary line. According to our theory, the blue outliers are probably binary systems containing a He-burning star and a MS star, which can only be produced in detailed binary models. The red outliers are expected to be triples or multiples of higher-orders. There are two peaks in the distribution of the pre-interaction binaries in the CMD, which are from the synchronized and non-synchronized large mass-ratio binaries. We point out here that the unresolved binaries are not equally separated according to their mass ratios. Binaries with $q > 0.8$ are located in similar positions near the equal-mass binary isochrone. Another interesting feature in our synthetic cluster is that the MS mergers stretch out all the way from the isochrone of the slowly-rotating single star models to the ZAMS line. In contrast, the observed hot blue MS stars pile up at 0.5 to 1 magnitude below the turn-off and are generally in the vicinity of the isochrone of the slowly-rotating single star models. As we have argued in Chapter 4 that the blue MS stars are from binary MS mergers, mainly caused by orbit decay, which is beyond our capability to model. All the blue MS star models in Fig. 5.2 are binary evolutionary induced MS mergers, whose fraction (~2% in stars with $m_{\mathrm{F814W}} \leq 21$) is much smaller than the fraction of the observed blue MS stars (~20% in stars with $m_{\mathrm{F814W}} \leq 21$).

The magnitude range of the synthetic Be stars in the CMD is slightly larger than the magnitude range of the observed Hα emitters in Fig. 5.2. It may indicate that using a mass ratio of 0.5 as the threshold for the stable and unstable Case B mass transfer is not adequate. In fact, our detailed binary models show a mass-dependent mass ratio threshold for the stable and unstable Case B mass transfer (see Appendix A). Further studies on the stability of Case B mass transfer are in high demand. In this work, we do not compare the results from other mass ratio thresholds with the observations, because another aspect needs to be noticed: the critically-rotating stars with lower masses may not be able to ionize their decretion disks, which is mandatory in producing emission lines. This means that low-mass critically rotating stars in young star clusters may not manifest as Be stars. Therefore, without a thorough understanding of such an ionizing effect, it is impossible to ultimately gauge the stability of binary mass transfer by the distribution of the Be stars in young star clusters.

5.3.2 Distribution of the Be star fraction

In this section, we examine the fraction of the synthetic Be stars as a function of magnitude and compare our results with the observations. The result for the synthetic cluster resembling NGC 330 is shown in Fig. 5.3. The solid and dashed lines indicate the predicted Be star fraction under the assumption of a binary fraction of 0.6 (meaning that we take into account all the populated stars in Fig. 5.2), and a binary fraction of 1 (meaning that we only consider the binary population in Fig. 5.2), respectively. A binary fraction of 1 gives the upper limit on the Be star fraction in young star clusters. We also distinguish the production of the Be stars from merely the binary evolution channel (red lines) and from both the single and binary evolution channels (blue and green lines). When the single evolution channel is included, we check two velocity thresholds ($v_{\mathrm{th}} = v_{\mathrm{rot}}/v_{\mathrm{crit}} = 0.75$ and 0.70) for a star to be a Be star. As expected, the Be star fraction near the turn-off is increased when the single evolution channel is considered.

Our simulation shows that the fraction of the near turn-off Be stars produced by binary evolution is at most ~ 30%, consistent with the result in Hastings, Langer et al. (2021). This value is smaller than

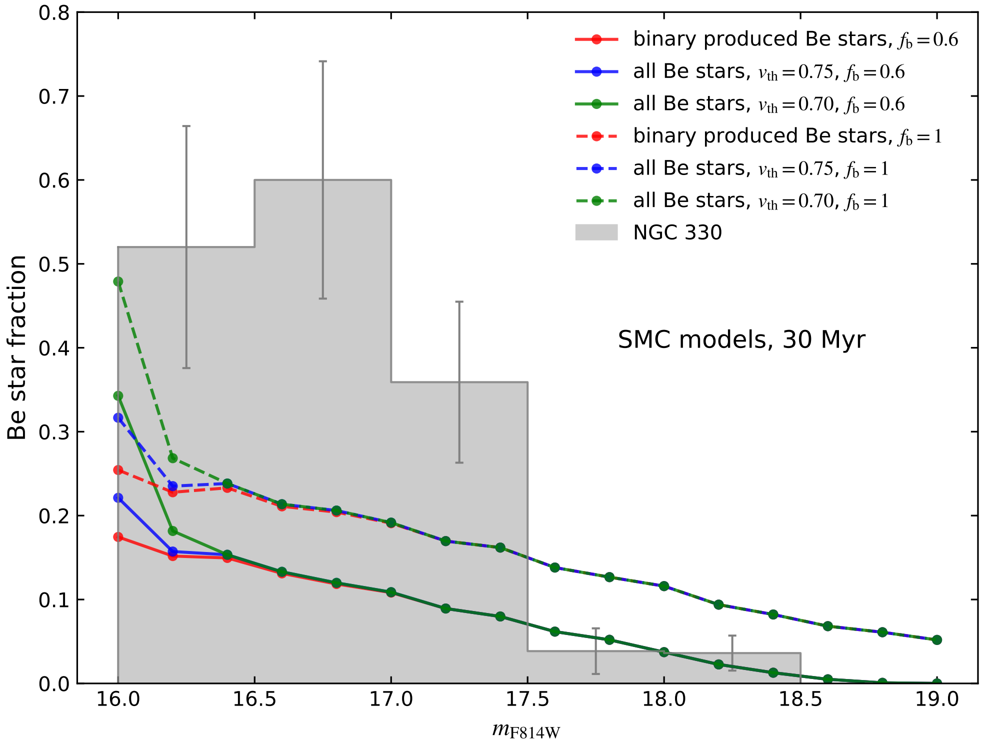

Figure 5.3: Predicted and observed Be fraction in NGC 330 as a function of magnitude. The solid and dashed lines correspond to the predictions based on binary fractions of 0.6 and 1, respectively. The red lines mean that we only consider binary produced Be star models, while the blue (green) lines mean that we treat all star models with velocities larger than 75% (70%) of their critical values as Be star models, regardless of their origins. The grey bars illustrate the observed Be star fraction with the Poisson errors plotted on top.

the observed Be star fraction of ~50% near the turn-off in NGC 330. In Fig. 5.4, we check whether the predicted binary evolutionary induced Be star fraction can be increased if we remove the limit of the mass ratio threshold for the stable and unstable Case B mass transfer, i.e. we assume that all Case B mass transfer binaries can produce a Be star. It is seen that the only significant difference between Fig. 5.4 and Fig. 5.3 is that the predicted fraction of the faint Be stars increases when we remove the mass ratio limit. The predicted fraction of the turn-off Be stars is not sensitive to the adopted mass ratio threshold (if it is not too large), because the contribution of the binaries with small mass ratios to the turn-off Be stars is marginal as a consequence of the steep initial mass function.

Therefore, it seems necessary to invoke the single evolution channel for the formation of Be stars to explain the high fraction of the observed Be stars near the turn-off. However, as we have mentioned in Chapter 3.4.3, the number and magnitude distribution of the single evolutionary induced Be stars in the LMC and SMC clusters are highly affected by the strength of stellar wind related to the bi-stability jump. Fig. 3.3 shows that all single star models between 3 $M_\odot$ and 20 $M_\odot$ with initial velocities of 55% of critical values can reach velocities larger than 70% of critical values at the end of their MS

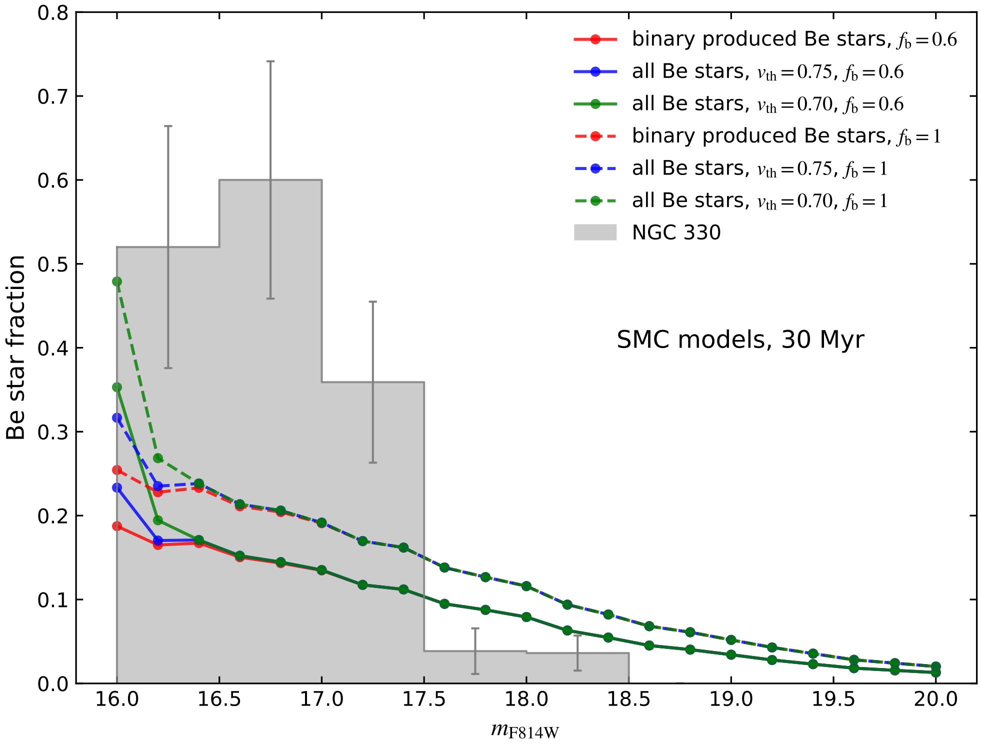

Figure 5.4: Similar as Fig. 5.3, but the mass ratio threshold for the stable and unstable mass transfer is removed in the simulation.

evolution. While Fig. 3.11 shows that among the 30 Myr LMC single star models with initial velocities of 60% of the critical values, only those brighter than ~ 1 mag below the turn-off magnitude can reach velocities larger than 70% of the critical values. The fact that our single star models with masses near 10 $M_\odot$ are significantly affected by the strong stellar wind related to the bi-stability jump leads to a low predicted turn-off Be star fraction in the clusters with ages near 30 Myr. In Fig. 5.3 we see that when we apply a low velocity threshold of $v_{\mathrm{th}} = 0.7$ for the Be stars, the predicted turn-off Be star fraction can reach 50%, which roughly matches the observation. However, the predicted fraction of the Be stars in the magnitude range of 16.5 to 17.5 remains considerably lower than the observed fraction. While the single star models below 6 $M_\odot$ are not affected by the bi-stability jump, meaning that fainter Be stars are easier to form in older clusters. Therefore, we see that the predicted turn-off Be star fraction in clusters older than 50 Myr increases significantly when we take into account single evolutionary induced Be stars and consider a low velocity threshold of $v_{\mathrm{th}} = 0.7$ (see Fig 5.12 and Fig. 5.13).

We need to point out here that in Hastings, Langer et al. (2021), the predicted and observed Be star fraction is compared as a function of mass rather than magnitude, in other words, they count the Be stars in bins that are sloped to the x-axis. This is because due to the effect of the centrifugal force and the luminosity form the decretion disk, a Be star appears redder and brighter than its normal B-type counterpart. This may partly explain the high fraction of the observed near turn-off Be stars in Fig. 5.3, as we are comparing the number of the Be stars with the number of the normal B-type stars with higher masses and thus lower numbers. In the future, we should also compare the Be star fraction from the theory and observations as a function of mass.

Our predictions for the Be star fraction in other three clusters studied in this thesis are shown in Fig. 5.11 for NGC 1818, Fig. 5.12 for NGC 1755, and 5.13 for NGC 2164, respectively. The observed Be star fraction in each cluster is plotted with the grey bars. Unfortunately, we do not have the Hα emission information for the NGC 1755 stars. We find that the binary evolution channel leads to at most 30% of the MS stars near the turn-off being Be stars in all the clusters analyzed in this thesis. After taking into account the single evolution channel, the predicted Be star fraction near the turn-off can be as high as 80%, depending on the cluster age and the adopted Be star velocity threshold.

In this work, we derive the upper fraction limit of the Be stars produced by binary evolution in young star clusters by assuming that all Case B mass transfer binaries with mass ratios larger than 0.5 can avoid merging. A more realistic mass-dependent binary merger criterion may be obtained by comparing the distribution of the simulated Be star fraction with the observations. However, the uncertainties in the derived fraction of the Be stars produced by the single evolution channel will affect the real fraction of the Be stars produced by the binary evolution channel. Therefore, without observational confirmation on the origin of each Be star, it is impossible for us to gauge the stability of binary mass transfer from the Be star distribution in young star clusters.

Further observations that can help us distinguish these two formation channels are, therefore, important to constrain the physics in both single and binary star evolution. If a Be star is produced by the single evolution channel, we would expect to see a MS companion star, due to the fact that the majority of stars are in binaries. However, J. Bodensteiner, Shenar and Sana (2020) analyzed 287 Galactic Be stars and found no Be binaries with MS companions. Meanwhile, if a Be star is originated from single star evolution, its surface nitrogen abundance ought to be enriched due to rotational mixing (see Section 3.6.2). In contrast, if it is from binary evolution, we do not expect a considerable N enrichment, firstly because a strong chemical composition gradient which can prevent further rotational mixing has established before mass transfer, and secondly because the mass gainer can only accrete tiny amounts of material from the donor's envelope. Dunstall et al. (2011) found similar surface N abundances for the B-type and Be stars in the LMC and SMC clusters in the VLT-FLAMES survey of massive stars, which contradicts the single evolution channel for the Be stars. However, the observations are still sparse. More observations on the companion of the Be stars and the surface chemical composition of the Be stars are needed to help us understand the origin of Be stars and stellar evolution.

5.4 Summaries and conclusions

In Chapters 2 and 4, we use our detailed binary models to show that binary evolution can produce a sequence of Be stars with a magnitude range of 2-3 below the turn-off, which matches the magnitude range of the observed Hα emitters in young star clusters well. However, our detailed binary models predict that less than 10% of the MS stars near the turn-off can be Be stars, which is much lower than the observed near turn-off Be star fraction of ~50%. The reason is that most of our binaries merge during Case B mass transfer. We assume that the mass gainer in a binary system cannot keep accreting once it reaches critical rotation. In such a case, we assume that if the radiation pressure from the two stars are not able expel the excess material, the two stars will merge. However, other mechanisms may help to stabilize the mass transfer phase, for example, the outward angular momentum transport in accretion disks.

In this work, we mainly investigate the upper limit on the binary evolutionary induced Be star fraction in young star clusters by relaxing the merger criterion used in our detailed binary models. Instead of computing new binary models, which is both time and space consuming, we perform population synthesis simulations using only single star models with different initial rotation. We make simple assumptions to compute the properties of the post-mass transfer binaries with single star models. We assume that all Case B mass transfer binaries with mass ratios larger than 0.5 can create a Be star without any mass accretion. After relaxing the merger criterion, we find that binary evolution can results in at most 30% of all turn-off MS stars being Be stars, which agrees with the results in Hastings, Langer et al. (2021) that used a model-independent analytical method to derive the upper limit of the Be stars that can be produced by binary evolution in young star clusters.

The fact that the maximum fraction of the binary evolutionary induced Be stars is smaller than the observed fraction near the turn-off indicates that the single evolution channel for the formation of Be stars is indispensable. However, the number of the Be stars produced in single star evolution channel is sensitive to wind mass loss and angular momentum loss. To thoroughly understand the formation of Be stars and gauge single and binary star evolution, we need more studies from both the theoretical side and the observational side. The theoretical work includes detailed studies on the stability of mass transfer in binaries and more accurate constraints on stellar wind mass loss. While the observational work includes the detection of the companions of the Be stars and the measurement of the surface chemical composition of the Be stars.

5.5 Appendix

5.5.1 Appendix A: Binary fraction and mass ratio distribution in NGC 1818, NGC 1755, and NGC 2164

In this appendix, we use the method in Section 5.2.1 to estimate the binary fraction and binary mass ratio distribution in three LMC clusters, NGC 1818, NGC 1755, NGC 2164. The results are shown in Figs. 5.5 to 5.7. The adopted distance moduli and reddenings are listed in Tab. 4.1. We find a high binary fraction and a rather flat mass ratio distribution in all these clusters.

5.5.2 Appendix B: Synthetic clusters resembling NGC 1818, NGC 1755 and NGC 2164 based on merely single star models

Figures 5.8 to 5.10 show our synthetic clusters with ages and metallicity in accordance with LMC clusters NGC 1818, NGC 1755 and NGC 2164, using the method described in Section 5.2.2. The adopted distance moduli and reddenings are listed both in the figures and in Tab. 4.1. In all the three clusters, we reproduce the MS components with positions consistent with the observations.

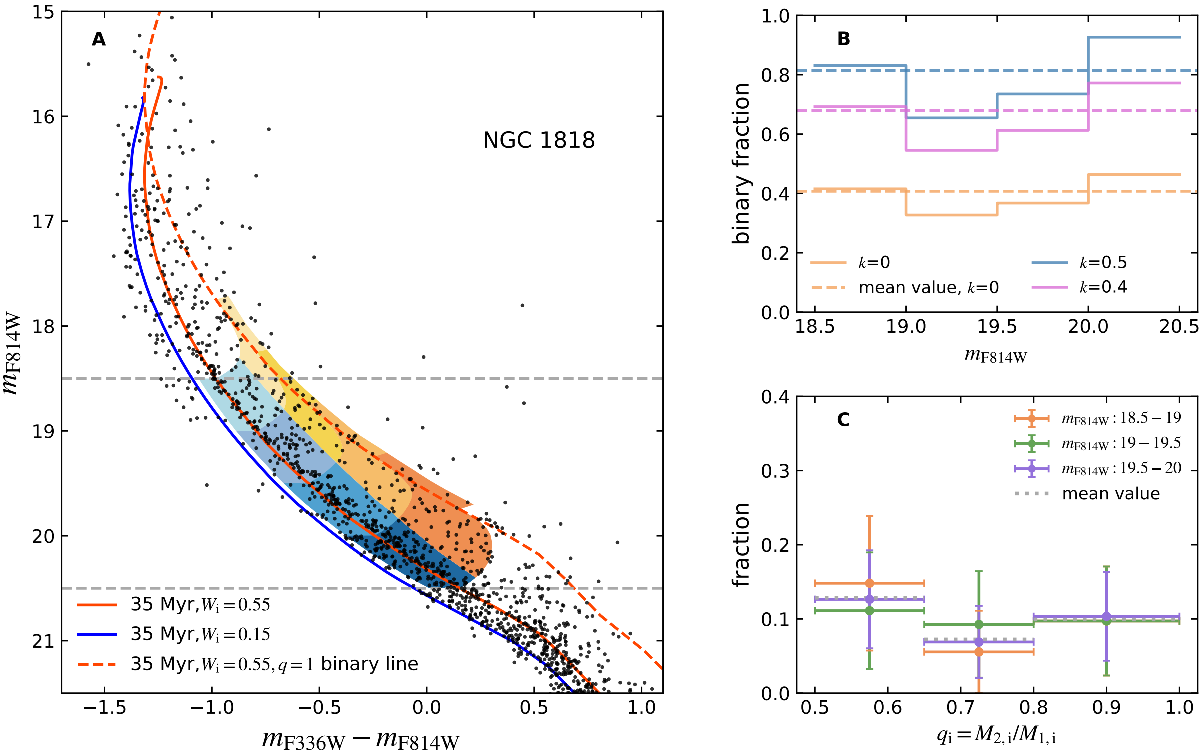

Figure 5.5: The same as Fig. 5.1, but for the LMC cluster NGC 1818.

5.5.3 Appendix C: Be star fraction in NGC 1818, NGC 1755 and NGC 2164

Figures 5.11 to 5.13 show the fraction of the Be stars with respect to all MS stars as a function of magnitude in our synthetic clusters based on merely single star models for three LMC clusters, NGC 1818, NGC 1755 and NGC 2164. The observed fractions in NGC 1818 and NGC 2164 are shown by the grey histograms, with errorbars indicating the Poisson error. We do not have the information of whether a star is a Be star in NGC 1755.

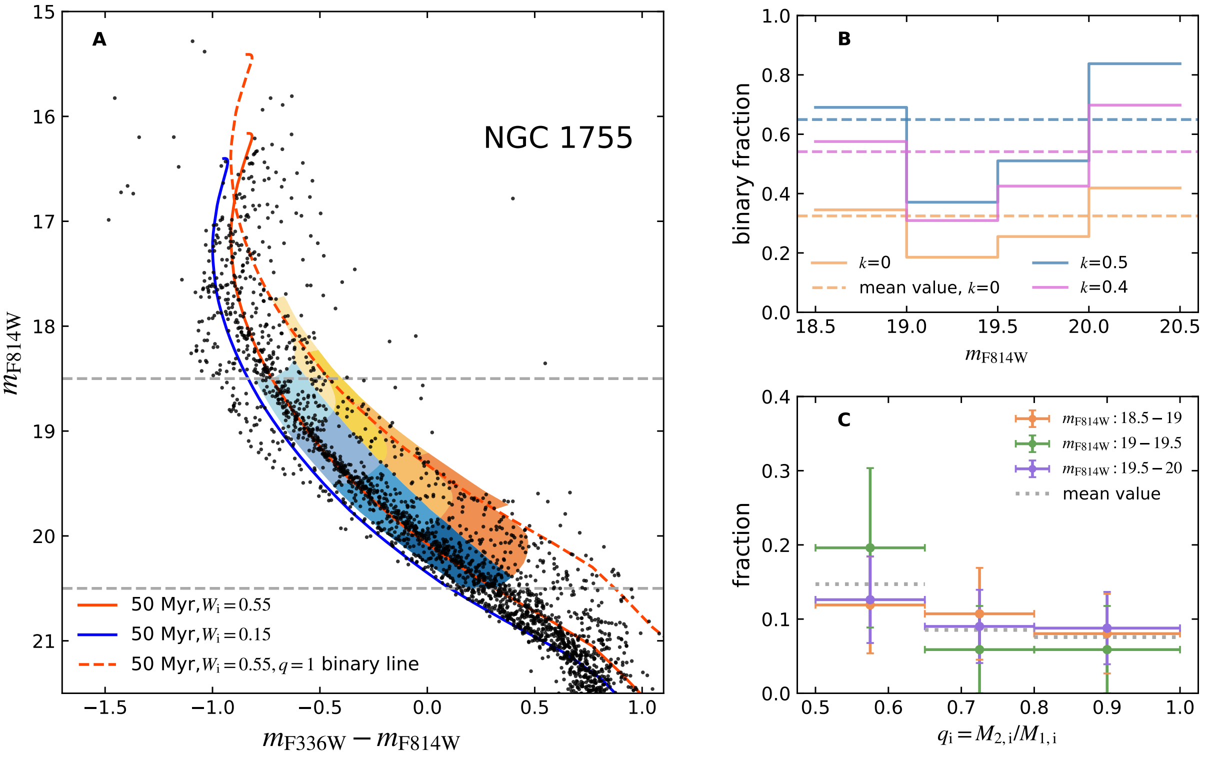

Figure 5.6: The same as Fig. 5.1, but for the LMC cluster NGC 1755.

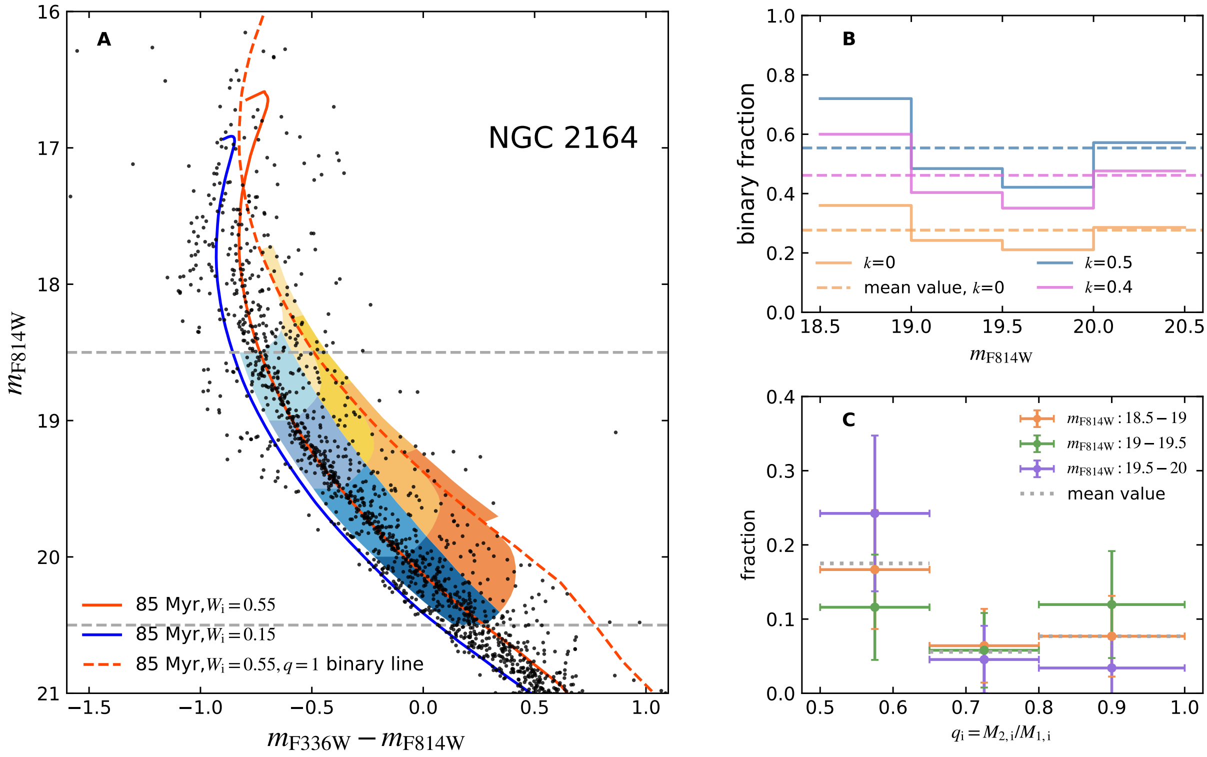

Figure 5.7: The same as Fig. 5.1, but for the LMC cluster NGC 2164.

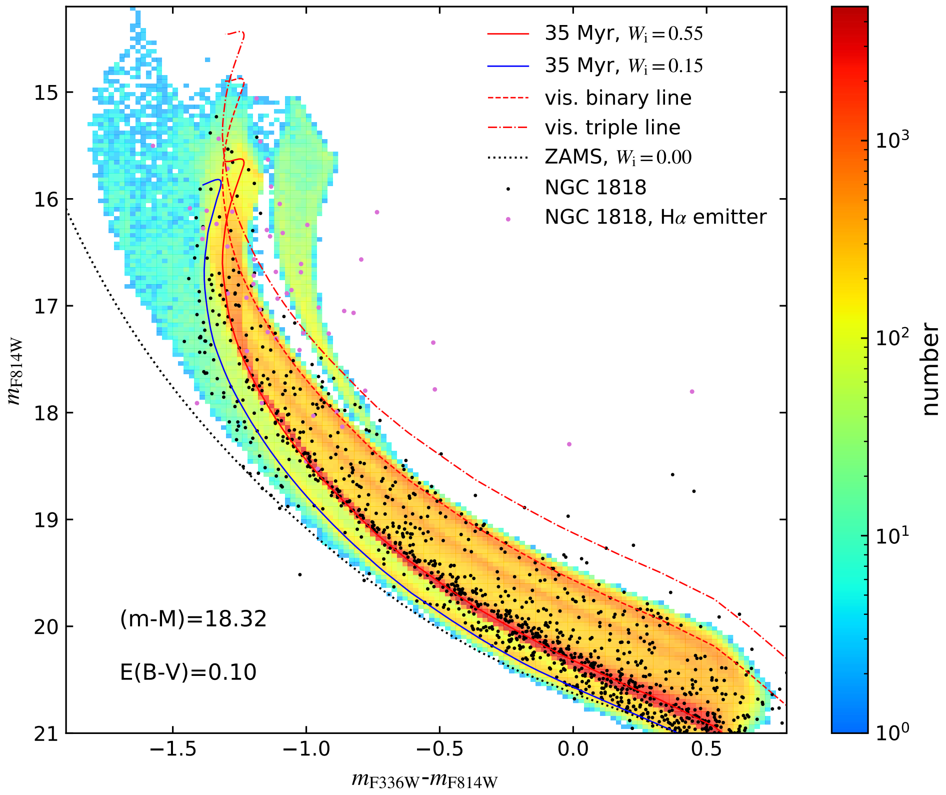

Figure 5.8: The same as Fig. 5.2, but for the synthetic cluster resembling the LMC cluster NGC 1818.

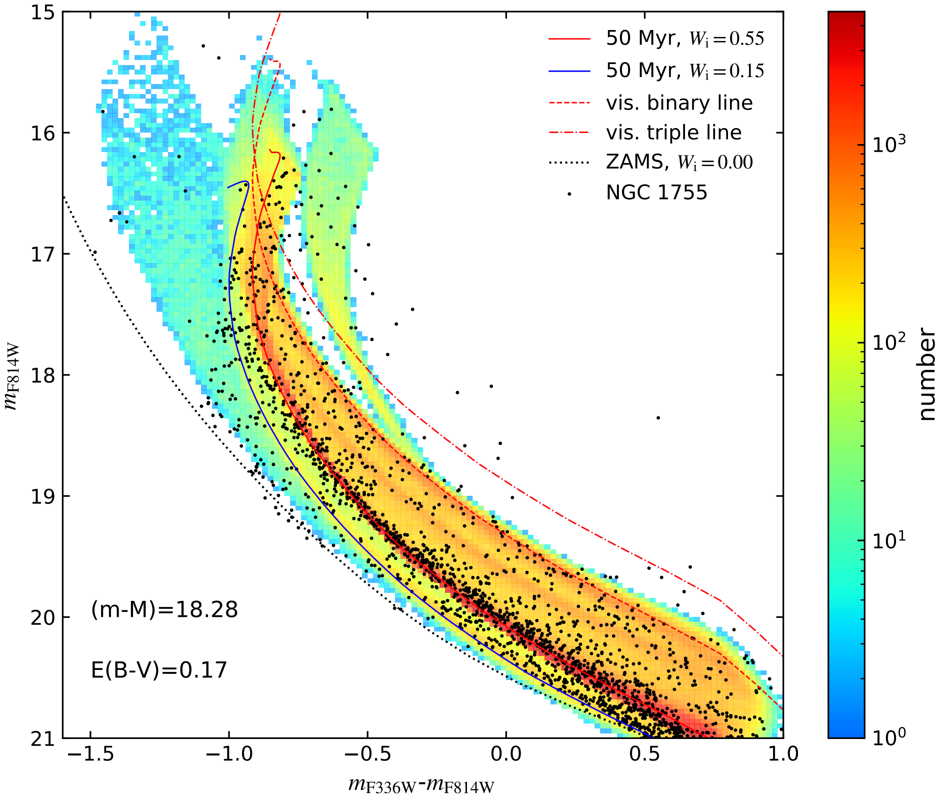

Figure 5.9: The same as Fig. 5.2, but for the synthetic cluster resembling the LMC cluster NGC 1755.

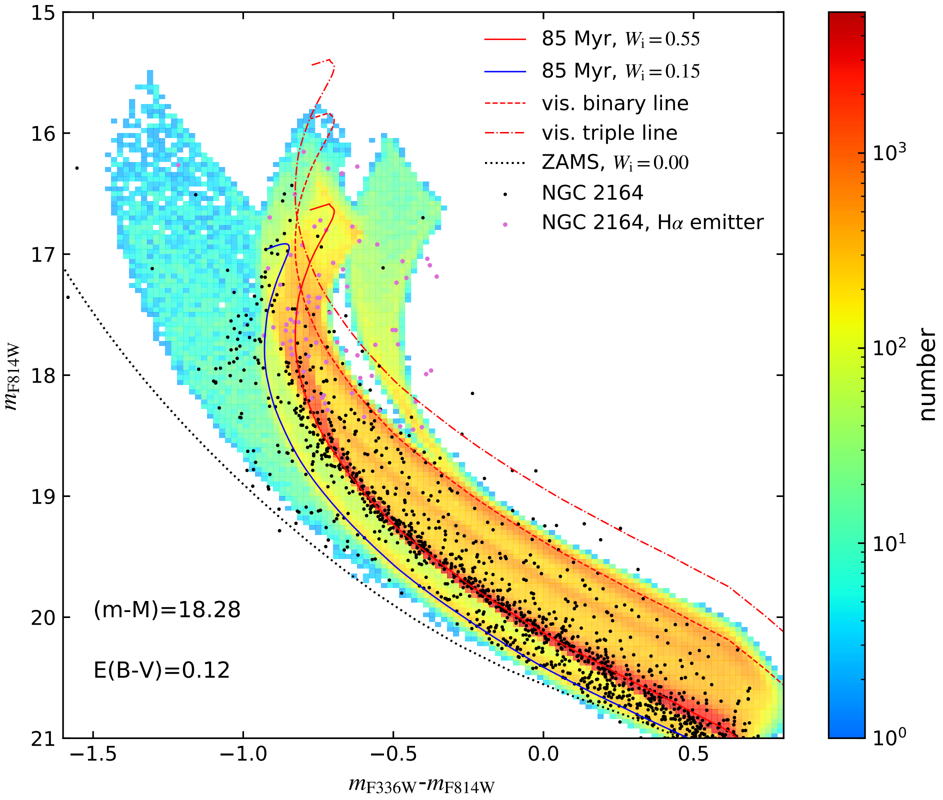

Figure 5.10: The same as Fig. 5.2, but for the synthetic cluster resembling the LMC cluster NGC 2164.

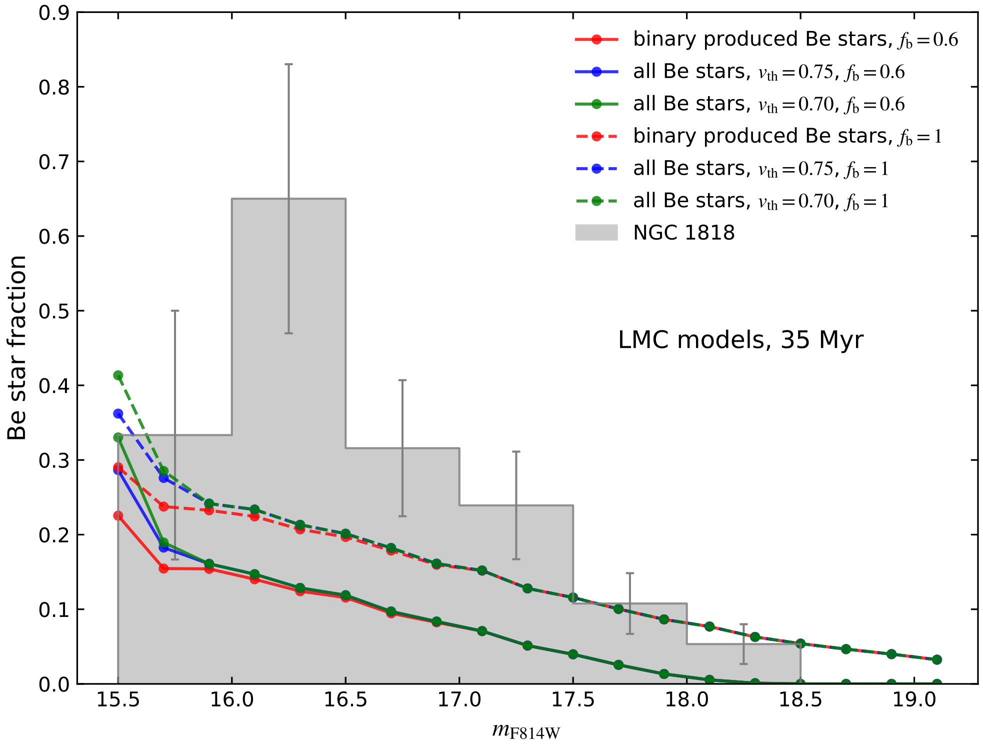

Figure 5.11: Same as Fig. 5.3, bur for the LMC cluster NGC 1818.

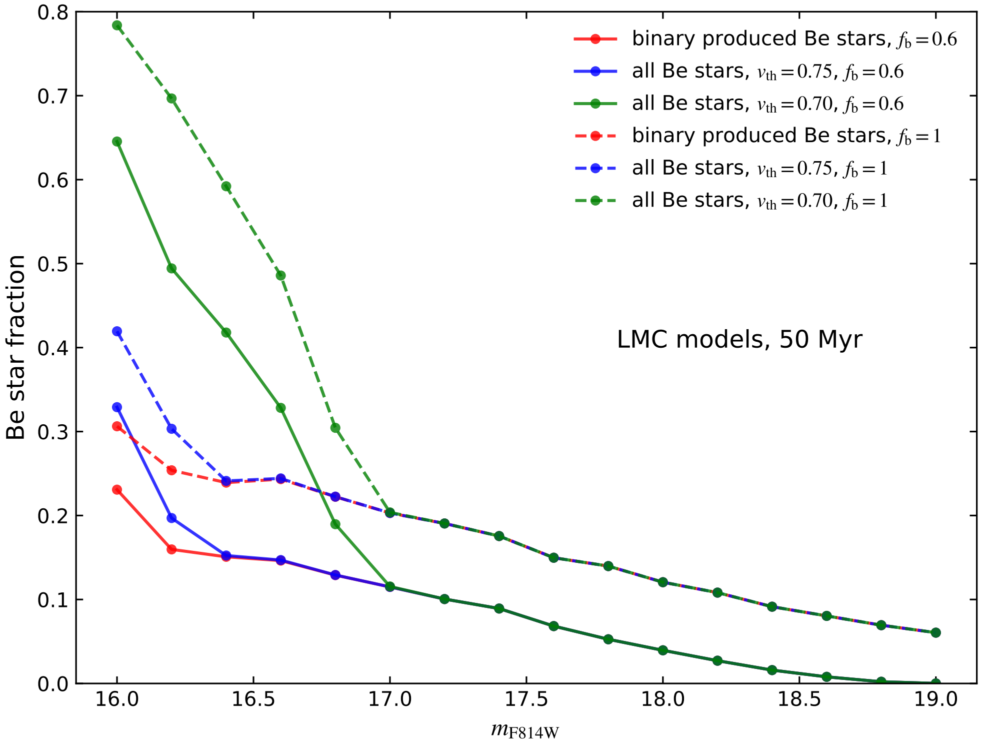

Figure 5.12: Same as Fig. 5.3, bur for the LMC cluster NGC 1755. We only show the theoretical predicted fractions in this figure as there is no Hα emission information for the observed stars in NGC 1755.

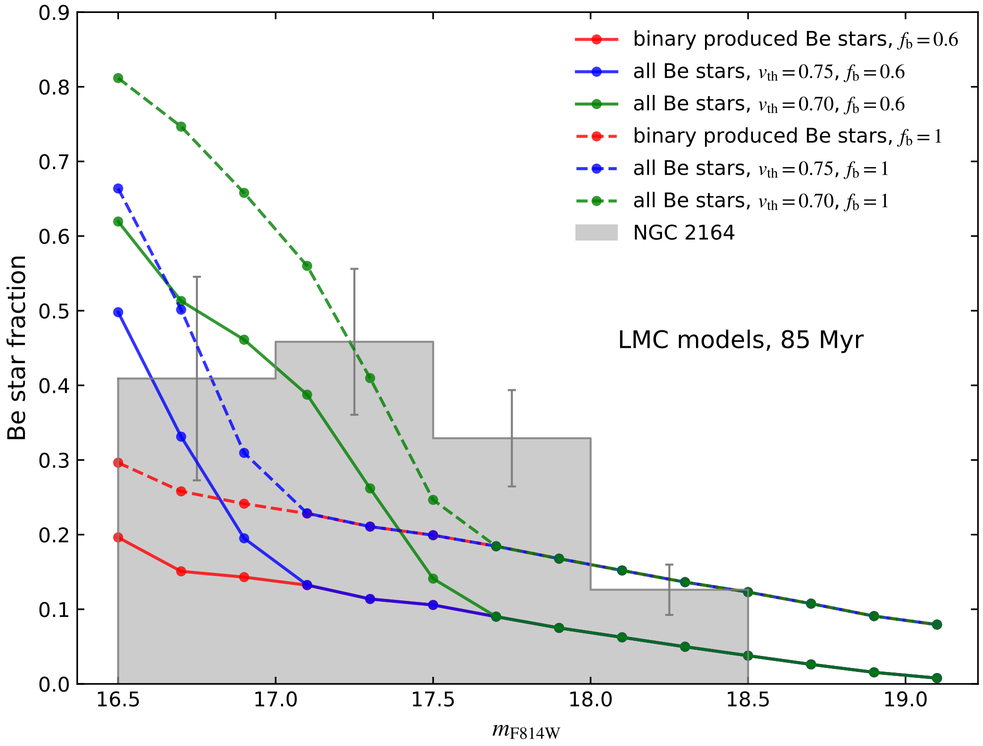

Figure 5.13: Same as Fig. 5.3, bur for the LMC cluster NGC 2164.

CHAPTER 6

Summary and Outlook

Massive stars are one of the most luminous objects in the sky and can dramatically influence the chemical composition and evolution of the star clusters, galaxies and our universe by their intense stellar wind and ionizing photons. Massive stars are believed to be connected to many spectacular objects or events, including Wolf-Rayet stars, supernovae, and gravitational waves. Therefore, it is essential to understand the structure and evolution of massive stars. However, there are many unsolved problems in massive star evolution, although enormous progress has been made on both the theoretical side and the observational side in the last decade. The main-sequence (MS) stage plays a prominent role in gauging massive star evolution, because it is the starting stage of massive stars, which contains the most straightforward physics, i.e. stable hydrogen burning, while the evolution of post-MS stars is highly affected by many uncertain physical processes, for example, strong stellar wind during the giant phase, strong internal mixing and dredge-up.

Star clusters offer unique laboratories to study the structure and evolution of massive stars, because star clusters are believed to contain a group of stars born simultaneously with the same initial chemical compositions. Therefore, the evolutionary stages of the stars in a cluster only depend on their masses. More massive stars evolve faster and end their MS evolution earlier than less mass stars. This leaves a turn-off feature of a star cluster in the color-magnitude diagram (CMD), which can be used to determine the age of the cluster. However, physical processes like rotation and binary interaction can significantly affect the structure and evolution of a star, which should ultimately affect the distribution of cluster stars in the CMD. This, in turn, means that the results from the studies based on the simple assumption that star clusters contain non-rotating single stars with the same initial conditions are dubious.

In this thesis, we mainly aim to explore the role of binary evolution in shaping the MS morphology of young Magellanic Cloud star clusters by comparing newly computed star models with recent high-precision photometric observations, thereby providing useful constraints on the formation and evolution of massive stars.

In Chapter 2, we examine the binary evolutionary induced MS features in our detailed binary models in which the two stars are assumed to be synchronized at the zero-age MS (ZAMS). We find that binary evolution leads to an extended MS turn-off by producing a population of blue stragglers via MS mergers and a population of near-critically-rotating Be stars via stable Case B mass transfer. Rejuvenation and slow rotation are the main reasons that make the MS merger products appear younger and brighter than the other MS stars. We predict the Be stars to reside on the right side of the turn-off with an extension in luminosity, which matches the observations.

However, in order to compare with real star clusters, we also need to take into account rotation. Rotation plays an important role in massive star evolution. Observations like long-duration gamma-ray bursts and MS O- and B-type stars with helium and nitrogen excesses cannot be explained without invoking rotation (Maeder and Meynet, 2000; Langer, 2012). In Chapter 3, we propose that two populations with one containing the stars rotating at around half of their critical velocities and the other one containing the stars rotating at less than 35% of their critical velocities are needed to explain the observed red and blue MSs in young star clusters. This bimodal velocity distribution agrees not only with the measured velocity distribution of the Large Magellanic Cloud (LMC) and Galactic field B/A type stars (Zorec and Royer, 2012; Dufton et al., 2013), but also with the sparse spectroscopically measured velocities of the red and blue MS stars in young star clusters (Marino et al., 2018; Sun, de Grijs et al., 2019; Sun, C. Li et al., 2019; Kamann, Bastian, Gossage et al., 2020).

The strength of rotational mixing is one of the most important unsolved problems. Though inefficient rotational mixing in our single star models explains the distribution of the observed turn-off stars better, we cannot entirely discard the possibility of efficient rotational mixing (as used in the SYCLIST models), because the turn-off stars are usually a mixture of single and binary evolutionary products. Fortunately, the development of the Multi Unit Spectroscopic Explorer (MUSE) makes the spectroscopic detection of the individual stars in the cluster cores possible, which may greatly help us to unveil the efficiency of rotational mixing in the near future.

Whereas bimodal velocity distribution is revealed in both field and cluster stars, its origin is still unknown. Stars ought to be born with fast rotation due to the excess angular momentum in their formation stages. Previous explanations on the origin of the slowly-rotating stars include tidal spin down, magnetic spin down, and the interaction between the stars and their disks during the formation scenario. In Chapter 4, we propose that binary MS mergers are responsible for the slowly-rotating blue MS stars. Unlike the previous studies that can only explain part of the observations, the binary MS merger origin of the blue MS stars succeeds in explaining the entire feature of the blue MS stars, including their distinct mass function and their spreading distribution between the ZAMS line and the position of the slowly-rotating single stars in the CMD. We find that an early merger rate peak, which is consistent with the latest binary formation simulations and the cluster observations, is required in explaining the large fraction of the blue MS stars in young star clusters.

3D magneto-hydrodynamical simulations show that the merger product of two massive MS stars is a slowly-rotating star accompanied by a strong magnetic field (Schneider, Ohlmann, Podsiadlowski, Röpke, Balbus, Pakmor and Springel, 2019). Therefore, MS mergers are promising in explaining the observed magnetic massive MS stars. The fact that the fraction of the blue MS stars ($\sim 20\%$) is slightly larger than the fraction of the observed magnetic massive MS stars ($\sim 10\%$, Ferrario et al. 2009) is probably attributed to magnetic field decay. Meanwhile, MS mergers may also explain the slowly-rotating nitrogen-enriched stars (Hunter et al., 2008). Further observations on rotation, surface chemical composition abundances, magnetic fields, and binarity of the blue MS stars in young star clusters are encouraged for our deep understanding of the origin of the magnetic fields and rotation in stars.

Considering all the above-mentioned findings, in Chapter 4, we, for the first time, propose that stars achieve their rotation in two different ways, that all stars are born with nearly half of their critical values, no matter whether they are in single stars or binaries. The close binaries merge due to either star evolution or orbital decay, and produce the slowly-rotating stars. We shed new light on the origin of the bimodal distribution of the spin, mass function, and magnetic field of stars.

In chapter 4, we also provide newly computed detailed binary models in which the two stars are born with 55% of their critical velocities. We find that binarity alone is adequate to explain all the observed MS features in young star clusters. To be more precise, pre-interaction binaries populate the red extension on top of the red MS stars; MS mergers account for the blue MS stars; while post-mass-transfer stars evolve to Be stars. Our theory is appealing because it explains all the observed MS components with coeval stars, based on a simple picture that all stars are born with the same rotation. Unfortunately, so far, there are not sufficient spectroscopic observations that can be used to test our theory. Here, we provide the observational signatures of each MS component predicted from our detailed binary models:

- red MS stars should have moderately fast rotation if they are single stars. If they are binaries, they should either have a slow rotation with a high mass ratio or a fast rotation with a low mass ratio.
- blue MS stars should have slow rotation, low binary fraction. They probably have a strong magnetic field and surface nitrogen enrichment.
- gap interlopers between the red and blue MS stars should either be single stars with rotational rates smaller than the red MS stars but faster than the blue MS stars, or be binaries with a short period in which the two star components are spun down by tides.
- visual binaries on top of the red MS stars should mainly be fast-rotating binaries or higher-order multiples.

More spectroscopic observations (e.g. by MUSE) on individual stars in young star clusters will come in the foreseeable future, which provides an excellent prospect to test our theory and gauge stellar evolution.

Another important finding in our work is that binary evolution is crucial in producing the Be stars. Understanding the origin of Be stars is vital in our understanding of single and binary star evolution. Single stars can only create Be stars near the end of their MS evolution, as long as they are not born as Be stars. The presence of the Be stars as faint as two magnitudes below the turn-off can only be explained by binary evolution. From another point of view, J. Bodensteiner, Shenar and Sana (2020) report a lack of MS companions in Be star populations, which contradicts the single evolution channel of Be stars. However, this study is based on limited samples in different data sets. More homogeneous observations are needed. While if binary evolution channel plays the dominant role, we would expect to see either runaway Be stars or Be stars with a more evolved star, i.e. a stripped He burning star, white dwarf (WD), neutron star (NS), or black hole (BH). The majority of the Be stars should be runaway stars, as a significant fraction of the binaries is disrupted by the supernova kick. Boubert and N. W. Evans (2018) find a high fraction of runaway Be stars with GAIA, which is consistent with the predictions from the binary evolution channel for the formation of Be stars. The system containing a Be star and a compact star may be detected as Be X-ray binaries, depending on the type of the compact star. Be+NS binaries are usually luminous in the X-ray band and thus are easy to detect. There are ~70 confirmed Be+NS systems in the Small Magellanic Cloud (SMC) (Coe and Kirk, 2015). In contrast, Be+BH and Be+WD binary systems are hard to detect, due to either a very long quiescent state or a very low X-ray luminosity. Despite the difficulties in detection, Be+BH and Be+WD systems have been detected. MWC 656 is the first binary system that is confirmed to contain a Be star and a BH (Casares et al., 2014). At the same time, there are few detected Be+WD systems in the SMC (Sturm et al., 2012; Coe, Kennea et al., 2020). New photometric devices and techniques like Transiting Exoplanet Survey Satellite (TESS) and optical interferometry are continuously enriching our knowledge of eclipsing binaries. The combinations of the indirect detections, like periodic radial velocity shift and the spectroscopic measurements of the OB stars, can help to identify Be binaries.

However, the fraction of the Be stars in our detailed binary models is too small to be comparable with the observations. The main reason is that a large number of binaries merge during Case B mass transfer based on our adopted merger criterion. In Chapter 5, we examine the maximum fraction of Be stars produced by binary evolution in star clusters by relaxing the merger criterion during Case B mass transfer. We adopt a method that allows us to build synthetic star clusters with merely single star models. In such population synthesis simulations, one can easily examine the effect of initial binary parameter distributions and the adopted physics on the distribution of the MS stars. After relaxing the merger criterion, we predict that the binary evolutionary induced Be stars occupy at most 30% of the turn-off MS stars, which is consistent with the previous study based on an analytic method (Hastings, Langer et al., 2021). However, this is still slightly smaller than the fraction of the observed Be stars. Single evolution channel for the formation of Be stars seems to be required to explain the remaining Be stars. However, whether a star can evolve to a Be star through single star evolution is sensitive to its initial rotational rate and the stellar wind mass loss. The intrinsic properties of Be stars in young star clusters might be unveiled with the upcoming observations on the rotation, surface chemical composition and binarity of Be stars.

All the above discussions are based on discrete star clusters with specific ages. In fact, we can also study the time evolution of our detailed single and binary models, for example, the time evolution of the distribution of each MS component and the time evolution of the fraction of each MS component. By comparing with the observed clusters with different ages, we can also constrain stellar evolution. From the observational side, people have observed, and are keeping observing star clusters. Taking the observed star clusters younger than 40 Myr for examples, there are only two known massive young clusters in the SMC, i.e. NGC 346 and NGC 330. While there are more clusters suitable to test our theory in the LMC (e.g. 30 Dor, NGC 2100, NGC 2004, NGC 1847, NGC 1818, NGC 2214) and the Milky Way (e.g. NGC 6231, h & χ Per, NGC 1960 & 581, NGC 457) (J. Bodensteiner, 2021). The upcoming observations on these clusters may offer excellent prospects for studying the time evolution of the cluster MS components. We need to point out that our theory is applicable in clusters up to ~700 Myr, when the turn-off star ($\sim 1.5\,\mathrm{M}_{\odot}$) starts to encounter magnetic braking. While the conclusion that binary evolution results in an extended MS turn-off holds in clusters up to 2 Gyr. Meanwhile, we can also investigate the effect of metallicity on the MS components in young star clusters. In fact, our group has started to compute detailed binary models with the Milky Way and LMC metallicity, which take into account similar physical processes as in this thesis.

Understanding the initial condition of stars and the most important physics in stellar evolution (e.g. mass transfer stability and mass transfer efficiency) is crucial to our understanding of the post-MS stars and supernova explosions. In particular, the binary systems containing a BH/NS and a massive O/B star will perhaps evolve to double compact systems that may eventually produce gravitational waves during their mergers. Langer, Schürmann et al. (2020) analyzed the LMC binary models and found ~3% of the LMC O/B stars in binaries to have BH companions. In the future, we can also perform a similar analysis taking into account the constraints proposed in this thesis, e.g. the distribution of stars' natal spins, and check how these constraints help to explain the observed gravitational wave events. We have come to the era of gravitational wave astronomy since the first detection of the two BH mergers by the Laser Interferometer Gravitational-Wave Observatory (LIGO) (B. P. Abbott,

R. Abbott, T. D. Abbott, Abernathy et al., 2016). The detection of the gravitational wave sources is expected to be significantly enlarged shortly, providing us with an unprecedented opportunity to gauge the most important physical processes in massive star evolution, including rotation, internal mixing, and binary interaction.

Appendix

APPENDIX A

Outcome of the grids of SMC binary models

In this appendix, we use Figs. A.1 to A.14. to show the evolutionary outcome of our grids of SMC binary models described in Chapter 2. The description of each evolutionary outcome is listed in the following:

- both dep. He: The binary models in which both of the stars are evolved up to He depletion.
- L2 overflow: The binary models that encounter L2 overflow. Such systems are expected to merge as soon as the L2 overflow occurs.
- upper $\dot{M}$ limit: The binary models that reach the merger criterion that the combined luminosity of the two stars is not sufficient to drive the required enhanced mass loss rate during mass transfer (see Section 2.2 for detail). Such systems are expected to merge as soon as the merger criterion is reached.
- lower $\dot{M}$ limit: Similar as the upper $\dot{M}$ limit criterion, but the excess material is assumed to be lost from the edge of the Keplerian disk of the accretor rather than the surface of the accretor. This is a less restrictive limit. The binary systems that reach this soft limit may merge, but we continue their evolution until other termination criteria are matched.
- inv. MT1: The binary models that encounter an inverse mass transfer (MT) when the primary star is on the main-sequence (MS) stage, while the secondary star has evolved off the MS stage. The evolution stops as soon as the inverse MT occurs.
- inv. MT2: The binary models that encounter an inverse MT when the primary star has evolved off the MS stage, meanwhile the secondary star has also evolved off the MS stage. The evolution stops as soon as the inverse MT occurs.
- inv. MT3: The binary models that encounter an inverse MT when the primary star has evolved off the MS stage, while the secondary star is on the MS stage. The evolution stops as soon as the inverse MT occurs.
- max $\dot{M}$: The binary models in which one of the star components' mass loss rate reaches the adopted maximum allowed value ($10^{-1}\,\mathrm{M}_{\odot}\mathrm{yr}^{-1}$). We stop the evolution when this criterion is met.

- convergence error1: The binary models that encounter a convergence error when the primary star is on the MS stage.
- convergence error2: The binary models that encounter a convergence error when the primary star has finished the MS evolution.
- had contact: The binary models that used to experience a contact phase.
- Case A/B MT boundary: The boundary between the binary models that undergo Case A and Case B mass transfer.

These figures are useful in understanding the binary parameters of the progenitors of the discrete MS components in young star clusters, especially the binary parameters that can result in Be stars (i.e. successful Case B binary systems) and blue stragglers (i.e. MS mergers) in star clusters.

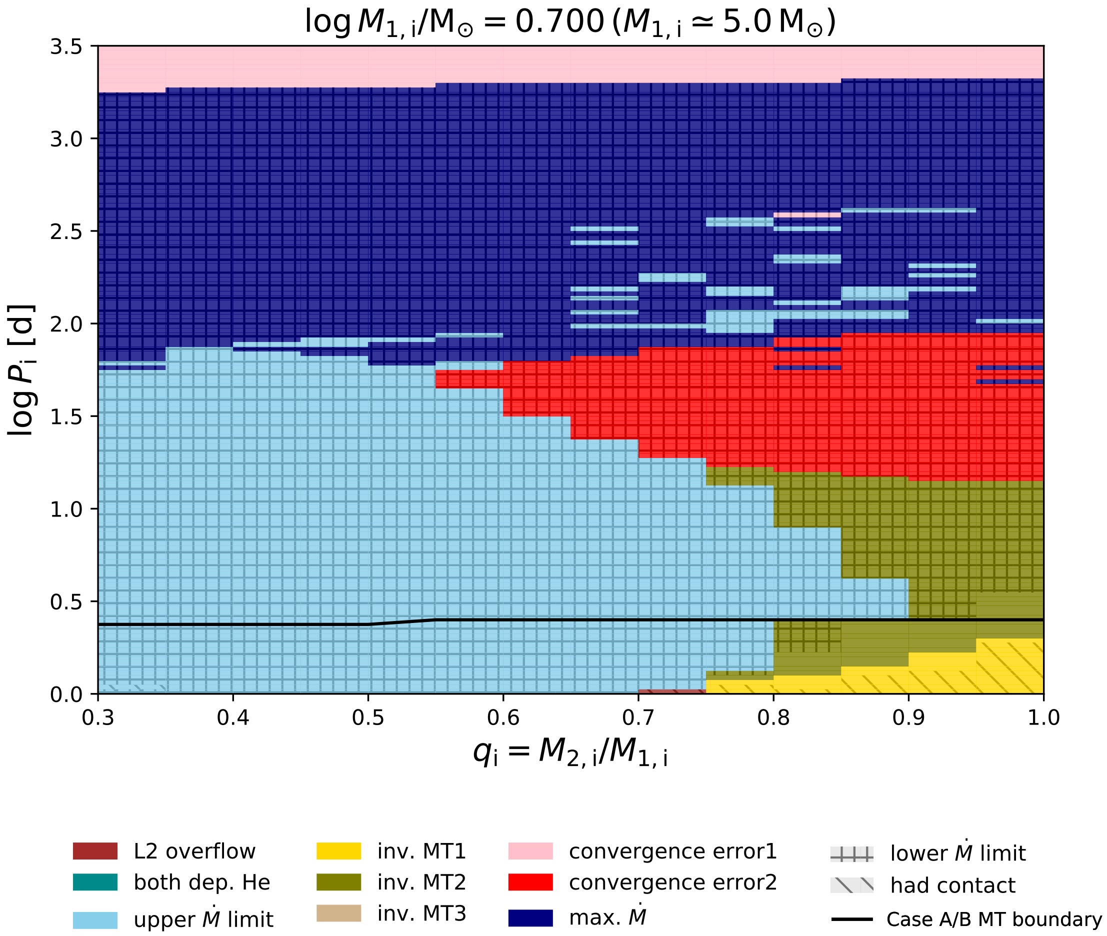

Figure A.1: Evolutionary outcome of the SMC-metallicity-like binary models with $\log M_{1,\mathrm{i}}/M_\odot = 0.700$ ($M \simeq 5.0\,\mathrm{M}_\odot$). Colors indicate the binary evolutionary outcome, explained in detail in the text of this appendix, of a binary model with particular initial parameters. The grey crosses mean the binary models that reach the adopted lower mass loss rate limit. While the grey hatched lines represent the binary models that encounter a contact phase during their evolution. The solid black line shows the boundary between the binary models that undergo Case A and Case B mass transfer.

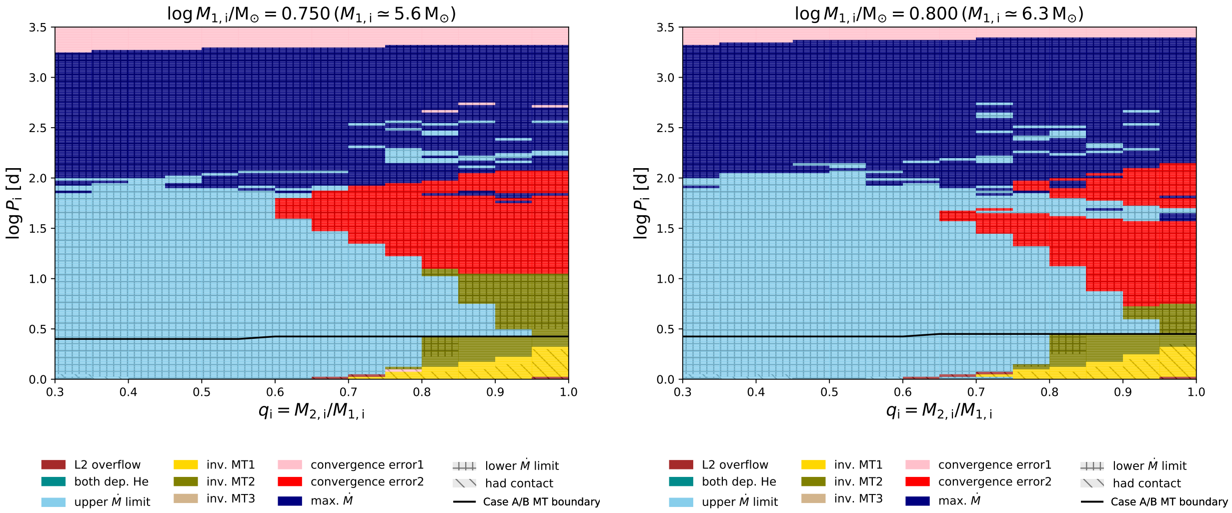

Figure A.2: Same as Fig. A.1, but for the binary models with $\log M_{1,\mathrm{i}}/M_\odot = 0.750\,(M \simeq 5.6\,\mathrm{M}_\odot)$ (left) and $\log M_{1,\mathrm{i}}/M_\odot = 0.800\,(M \simeq 6.3\,\mathrm{M}_\odot)$ (right).

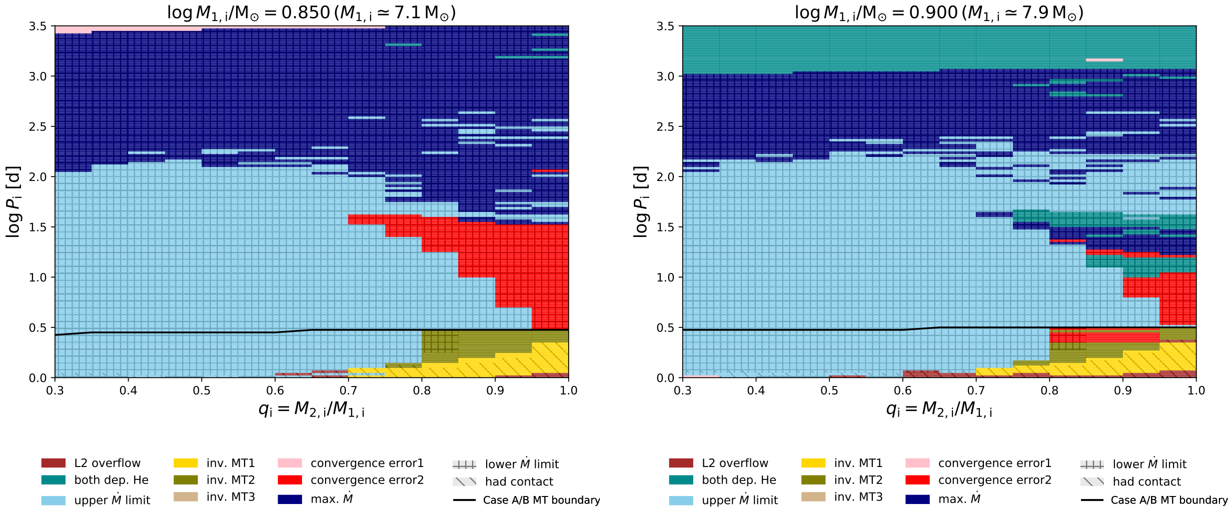

Figure A.3: Same as Fig. A.1, but for the binary models with $\log M_{1,\mathrm{i}}/M_\odot = 0.850\,(M \simeq 7.1\,\mathrm{M}_\odot)$ (left) and $\log M_{1,\mathrm{i}}/M_\odot = 0.900\,(M \simeq 7.9\,\mathrm{M}_\odot)$ (right).

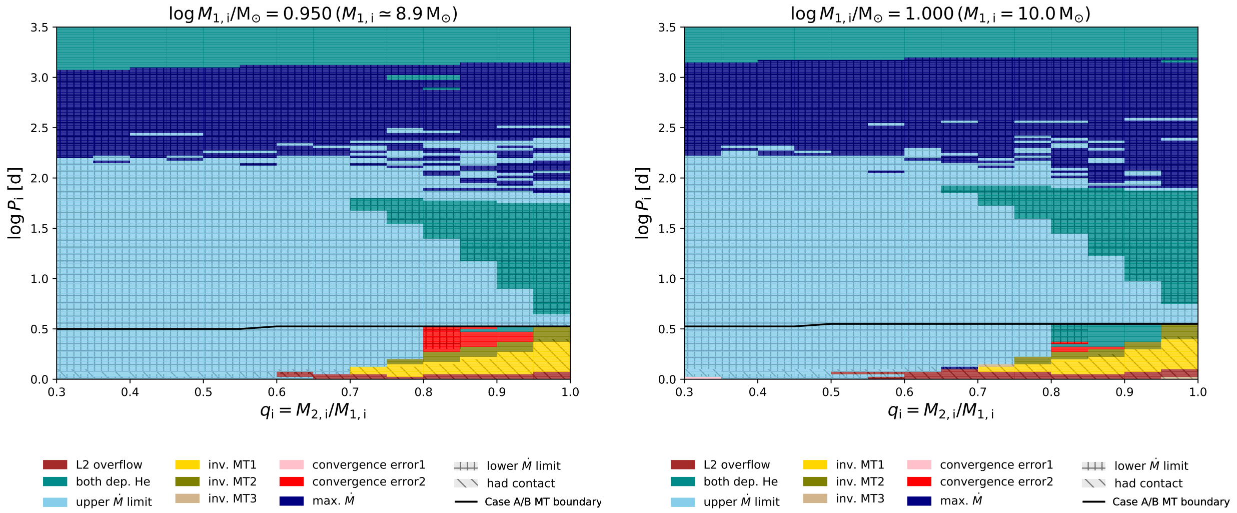

Figure A.4: Same as Fig. A.1, but for the binary models with $\log M_{1,\mathrm{i}}/M_\odot = 0.950\,(M \simeq 8.9\,\mathrm{M}_\odot)$ (left) and $\log M_{1,\mathrm{i}}/M_\odot = 1.000\,(M = 10.0\,\mathrm{M}_\odot)$ (right).

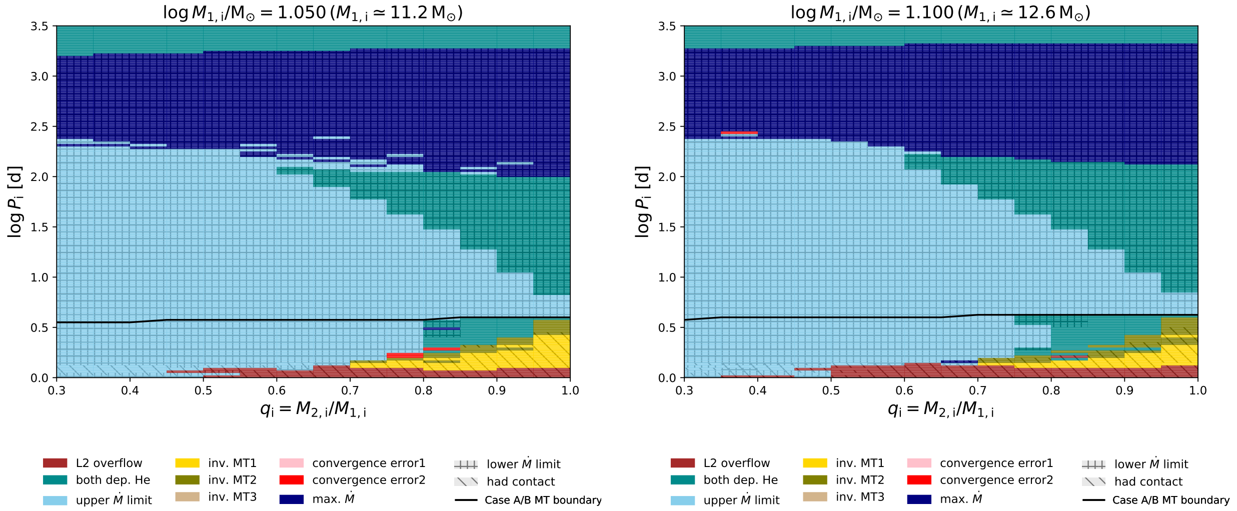

Figure A.5: Same as Fig. A.1, but for the binary models with $\log M_{1,\mathrm{i}}/M_\odot = 1.050\,(M \simeq 11.2\,\mathrm{M}_\odot)$ (left) and $\log M_{1,\mathrm{i}}/M_\odot = 1.100\,(M \simeq 12.6\,\mathrm{M}_\odot)$ (right).

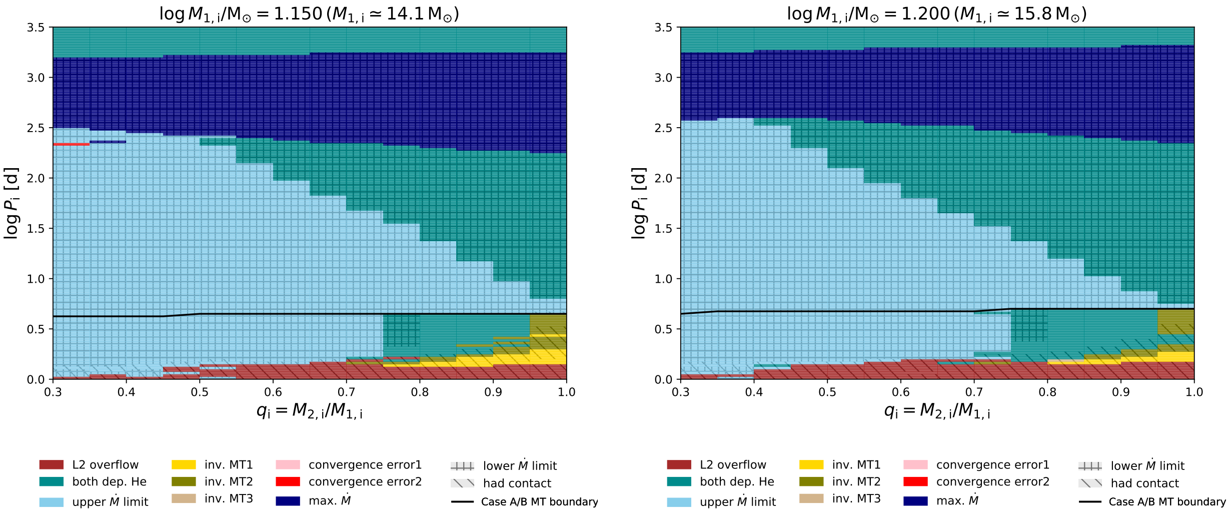

Figure A.6: Same as Fig. A.1, but for the binary models with $\log M_{1,i}/M_\odot = 1.150\,(M \simeq 14.1\,M_\odot)$ (left) and $\log M_{1,i}/M_\odot = 1.200\,(M \simeq 15.8\,M_\odot)$ (right).

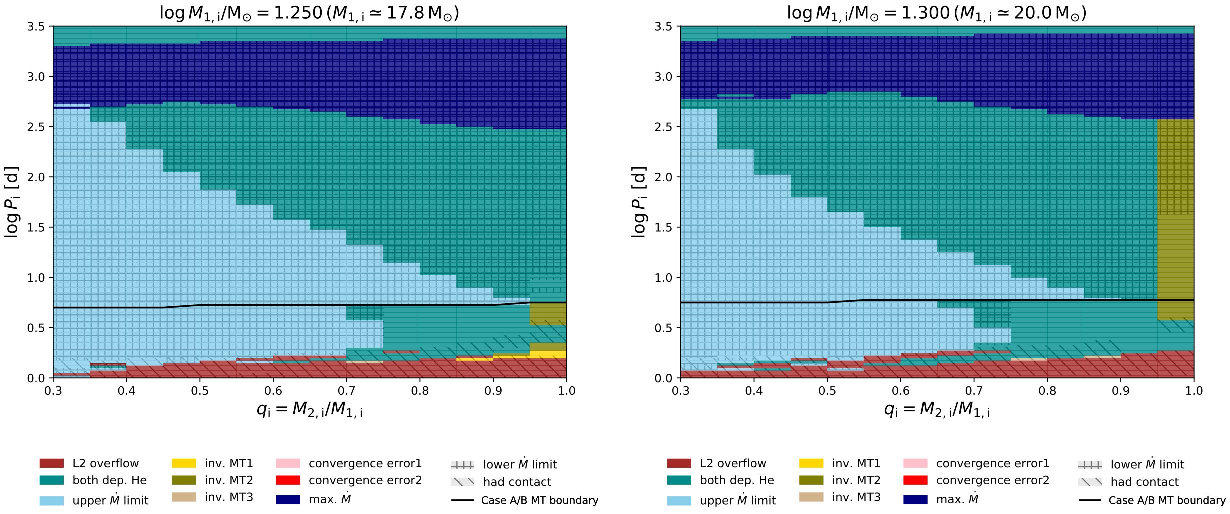

Figure A.7: Same as Fig. A.1, but for the binary models with $\log M_{1,i}/M_\odot = 1.250\,(M \simeq 17.8\,M_\odot)$ (left) and $\log M_{1,i}/M_\odot = 1.300\,(M \simeq 20.0\,M_\odot)$ (right).

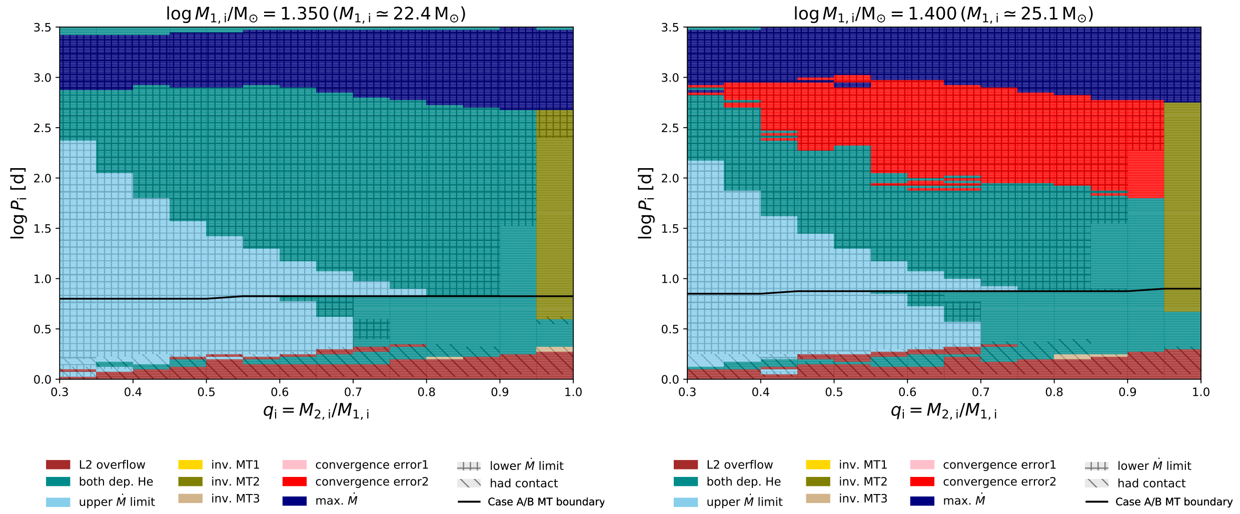

Figure A.8: Same as Fig. A.1, but for the binary models with $\log M_{1,\mathrm{i}}/M_\odot = 1.350\,(M \simeq 22.4\,\mathrm{M}_\odot)$ (left) and $\log M_{1,\mathrm{i}}/M_\odot = 1.400\,(M \simeq 25.1\,\mathrm{M}_\odot)$ (right).

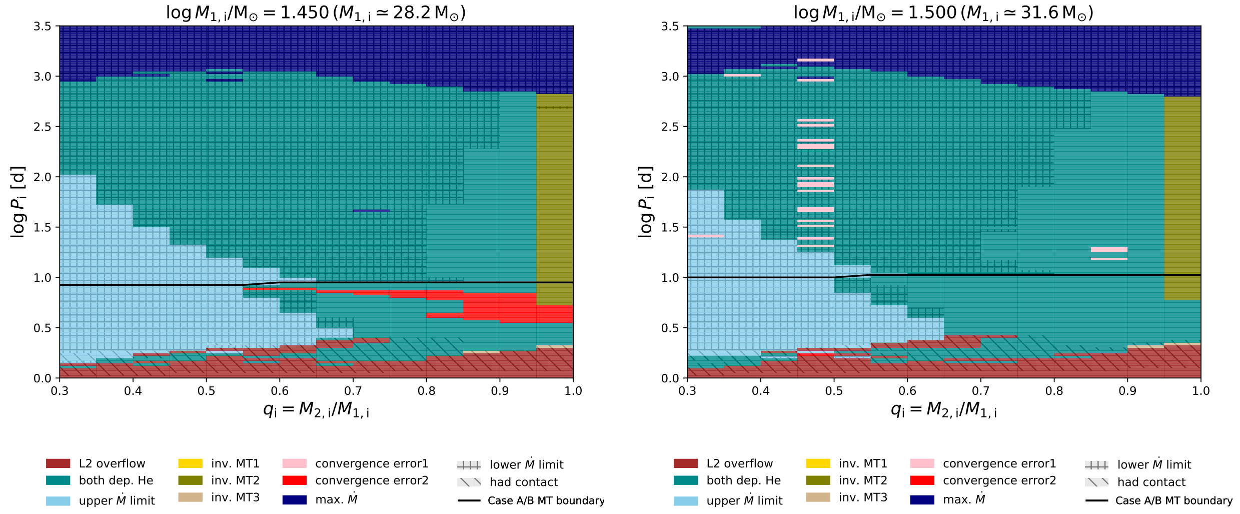

Figure A.9: Same as Fig. A.1, but for the binary models with $\log M_{1,\mathrm{i}}/M_\odot = 1.450\,(M \simeq 28.2\,\mathrm{M}_\odot)$ (left) and $\log M_{1,\mathrm{i}}/M_\odot = 1.500\,(M \simeq 31.6\,\mathrm{M}_\odot)$ (right).

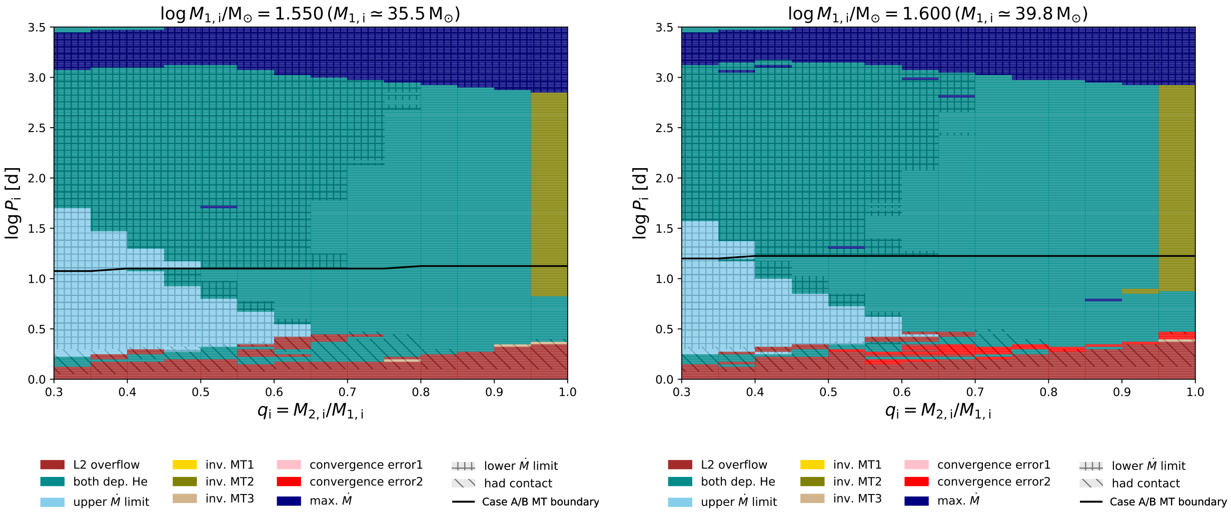

Figure A.10: Same as Fig. A.1, but for the binary models with $\log M_{1,i}/M_{\odot} = 1.550\,(M \simeq 35.5\,M_{\odot})$ (left) and $\log M_{1,i}/M_{\odot} = 1.600\,(M \simeq 39.8\,M_{\odot})$ (right).

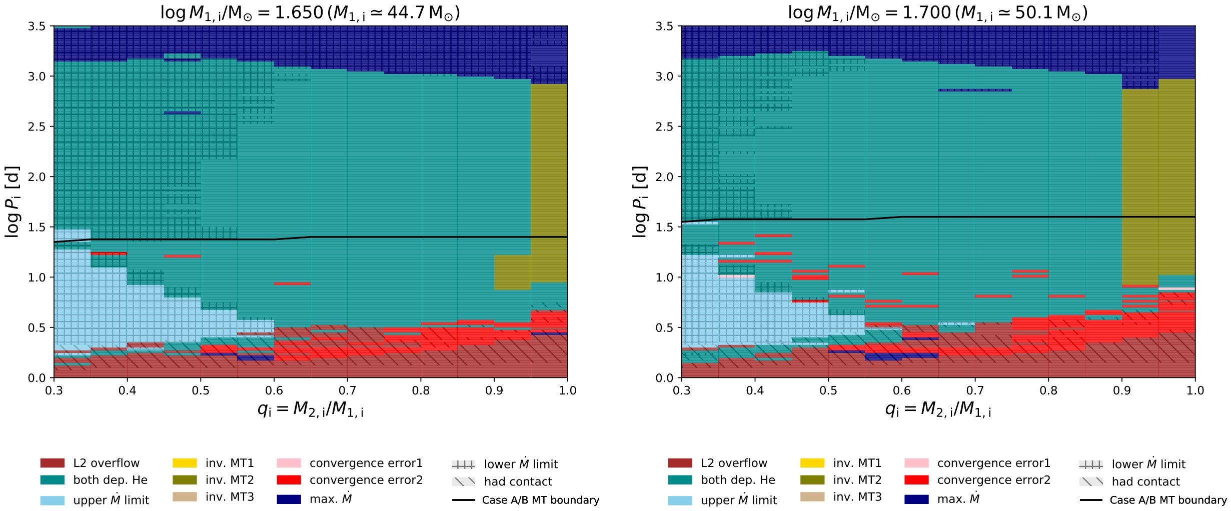

Figure A.11: Same as Fig. A.1, but for the binary models with $\log M_{1,i}/M_{\odot} = 1.650\,(M \simeq 44.7\,M_{\odot})$ (left) and $\log M_{1,i}/M_{\odot} = 1.700\,(M \simeq 50.1\,M_{\odot})$ (right).

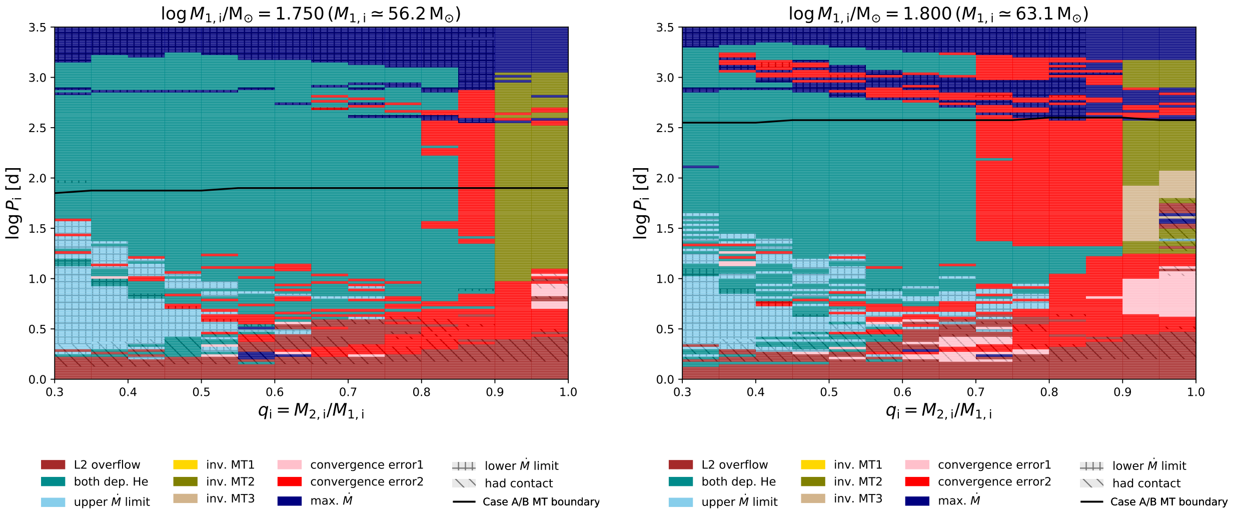

Figure A.12: Same as Fig. A.1, but for the binary models with $\log M_{1,\mathrm{i}}/M_\odot = 1.750\,(M \simeq 56.2\,\mathrm{M}_\odot)$ (left) and $\log M_{1,\mathrm{i}}/M_\odot = 1.800\,(M \simeq 63.1\,\mathrm{M}_\odot)$ (right).

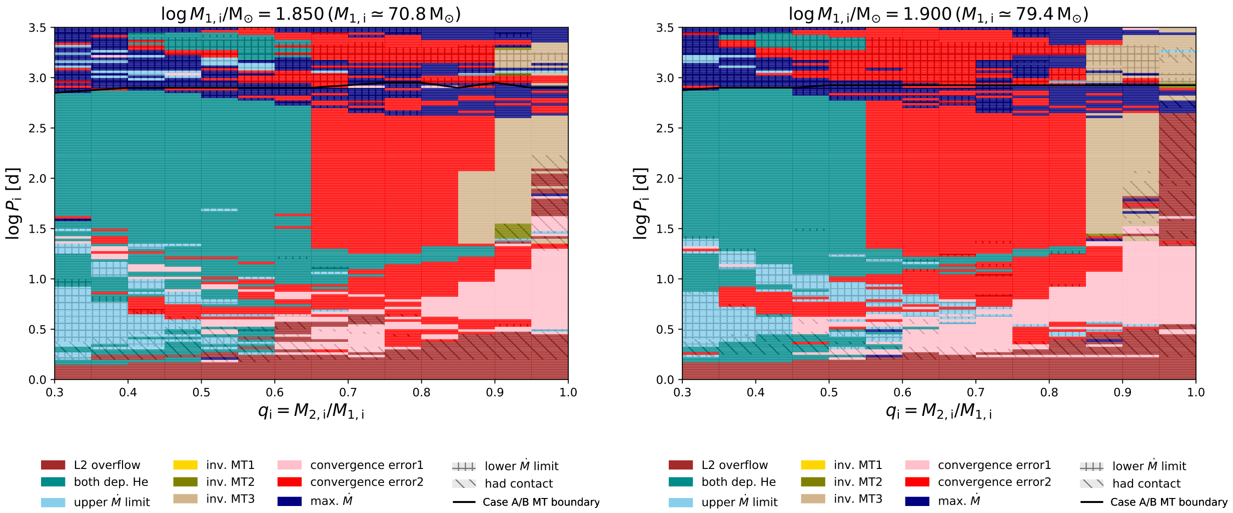

Figure A.13: Same as Fig. A.1, but for the binary models with $\log M_{1,\mathrm{i}}/M_\odot = 1.850\,(M \simeq 70.8\,\mathrm{M}_\odot)$ (left) and $\log M_{1,\mathrm{i}}/M_\odot = 1.900\,(M \simeq 79.4\,\mathrm{M}_\odot)$ (right).

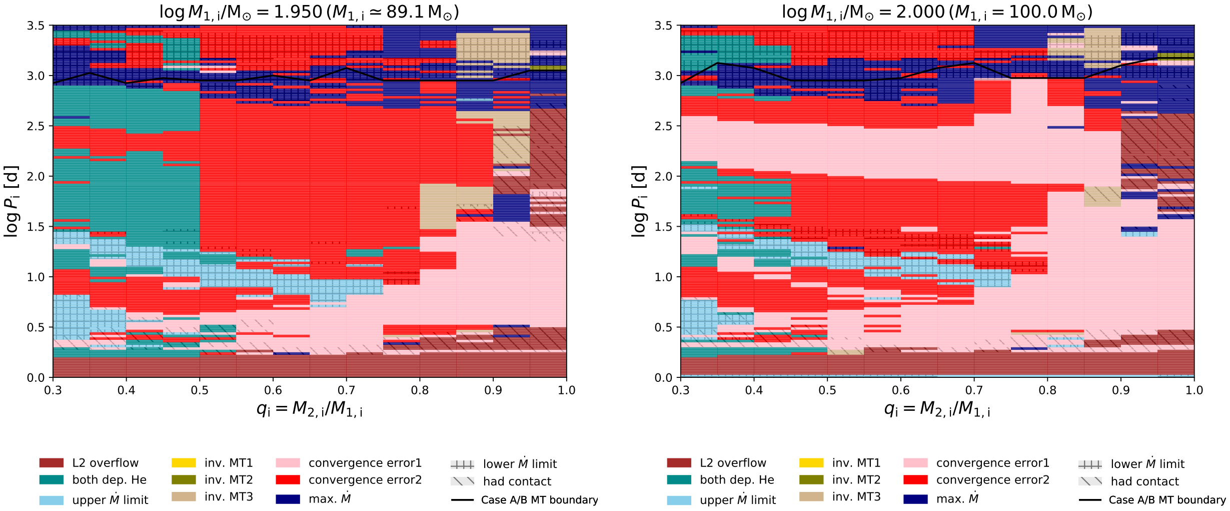

Figure A.14: Same as Fig. A.1, but for the binary models with $\log M_{1,\mathrm{i}}/M_\odot = 1.950$ ($M \simeq 89.1\,\mathrm{M}_\odot$) (left) and $\log M_{1,\mathrm{i}}/M_\odot = 2.000$ ($M = 100\,\mathrm{M}_\odot$) (right).

Bibliography

Abbott, B. P., R. Abbott, T. D. Abbott, M. R. Abernathy et al. (2016), *Observation of Gravitational Waves from a Binary Black Hole Merger*, Phys. Rev. Lett. **116**, 061102 061102, arXiv: `1602.03837 [gr-qc]` (cit. on pp. 2, 9, 120).

Abbott, B. P., R. Abbott, T. D. Abbott, F. Acernese, K. Ackley, C. Adams, T. Adams, P. Addesso, R. X. Adhikari, V. B. Adya, C. Affeldt, M. Afrough, B. Agarwal, M. Agathos, K. Agatsuma, N. Aggarwal, O. D. Aguiar, L. Aiello, A. Ain, P. Ajith, B. Allen, G. Allen, A. Allocca, P. A. Altin, A. Amato, A. Ananyeva, S. B. Anderson, W. G. Anderson, S. V. Angelova et al. (2017), *GW170814: A Three-Detector Observation of Gravitational Waves from a Binary Black Hole Coalescence*, Phys. Rev. Lett. **119**, 141101 141101, arXiv: `1709.09660 [gr-qc]` (cit. on p. 10).

Abbott, B. P., R. Abbott, T. D. Abbott, F. Acernese, K. Ackley, C. Adams, T. Adams, P. Addesso, R. X. Adhikari, V. B. Adya, C. Affeldt, M. Afrough, B. Agarwal, M. Agathos, K. Agatsuma, N. Aggarwal, O. D. Aguiar, L. Aiello, A. Ain, P. Ajith, B. Allen, G. Allen, A. Allocca, P. A. Altin, A. Amato, A. Ananyeva, S. B. Anderson, W. G. Anderson, S. Antier et al. (2017), *GW170104: Observation of a 50-Solar-Mass Binary Black Hole Coalescence at Redshift 0.2*, Phys. Rev. Lett. **118**, 221101 221101, arXiv: `1706.01812 [gr-qc]` (cit. on p. 14).

Abbott, B. P. et al. (2019), *GWTC-1: A Gravitational-Wave Transient Catalog of Compact Binary Mergers Observed by LIGO and Virgo during the First and Second Observing Runs*, Phys. Rev. X **9** (3) 031040, URL: `https://link.aps.org/doi/10.1103/PhysRevX.9.031040` (cit. on p. 10).

Abbott, R. et al. (2021a), *GWTC-2: Compact Binary Coalescences Observed by LIGO and Virgo during the First Half of the Third Observing Run*, Phys. Rev. X **11** (2) 021053, URL: `https://link.aps.org/doi/10.1103/PhysRevX.11.021053` (cit. on p. 10).

Abbott, R. et al. (2021b), *Observation of Gravitational Waves from Two Neutron Star-Black Hole Coalescences*, Astrophys. J. Letters **915**, L5 L5, arXiv: `2106.15163 [astro-ph.HE]` (cit. on p. 10).

Ahumada, J. A. and E. Lapasset (2007), *New catalogue of blue stragglers in open clusters*, Astron. Astrophys. **463** 789 (cit. on p. 31).

Atkinson, R. D. E. and F. G. Houtermans (1929), *Zur Frage der Aufbaumöglichkeit der Elemente in Sternen*, Zeitschrift fur Physik **54** 656 (cit. on p. 24).

Bastian, N., I. Cabrera-Ziri et al. (2017), *A high fraction of Be stars in young massive clusters: evidence for a large population of near-critically rotating stars*, Mon. Not. R. Astron. Soc. **465** 4795, arXiv: `1611.06705` (cit. on p. 39).

Bastian, N. and S. E. de Mink (2009), *The effect of stellar rotation on colour-magnitude diagrams: on the apparent presence of multiple populations in intermediate age stellar clusters*, Mon. Not. R. Astron. Soc. **398** L11, arXiv: `0906.1590 [astro-ph.GA]` (cit. on pp. 18, 39, 62, 71).

Bastian, N., S. Kamann, I. Cabrera-Ziri et al. (2018), *Extended main sequence turnoffs in open clusters as seen by Gaia - I. NGC 2818 and the role of stellar rotation*, Mon. Not. R. Astron. Soc. **480** 3739, arXiv: `1807.10779 [astro-ph.SR]` (cit. on pp. 38, 51, 62).

Bastian, N. and C. Lardo (2018), *Multiple Stellar Populations in Globular Clusters*, Ann. Rev. Astron. Astrophys **56** 83, arXiv: `1712.01286 [astro-ph.SR]` (cit. on p. 38).

Bastian, N. and J. Strader (2014), *Constraining globular cluster formation through studies of young massive clusters - III. A lack of gas and dust in massive stellar clusters in the LMC and SMC*, Mon. Not. R. Astron. Soc. **443** 3594, arXiv: `1407.2726 [astro-ph.GA]` (cit. on p. 18).

Bastian, N., S. Kamann, L. Amard et al. (2020), *On the origin of the bimodal rotational velocity distribution in stellar clusters: rotation on the pre-main sequence*, Mon. Not. R. Astron. Soc. **495** 1978, arXiv: `2005.01779 [astro-ph.SR]` (cit. on p. 64).

Baume, G. et al. (2007), *Extended star formation history of the star cluster NGC 2154 in the Large Magellanic Cloud*, Mon. Not. R. Astron. Soc. **375** 1077, arXiv: `astro-ph/0612174 [astro-ph]` (cit. on p. 18).

Baumgardt, H. and R. S. Klessen (2011), *The role of stellar collisions for the formation of massive stars*, Mon. Not. R. Astron. Soc. **413** 1810, arXiv: `1009.1189 [astro-ph.GA]` (cit. on p. 70).

Beasor, E. R. et al. (2019), *Discrepancies in the ages of young star clusters; evidence for mergers?*, Mon. Not. R. Astron. Soc. **486** 266, arXiv: `1903.05106 [astro-ph.SR]` (cit. on pp. 31, 34, 38).

Belczynski, K. et al. (2020), *Evolutionary roads leading to low effective spins, high black hole masses, and O1/O2 rates for LIGO/Virgo binary black holes*, Astron. Astrophys. **636**, A104 A104, arXiv: `1706.07053 [astro-ph.HE]` (cit. on p. 14).

Bodensteiner, J., T. Shenar and H. Sana (2020), *Investigating the lack of main-sequence companions to massive Be stars*, arXiv e-prints, arXiv:2006.13229 arXiv:2006.13229, arXiv: `2006.13229 [astro-ph.SR]` (cit. on pp. 9, 50, 105, 119).

Bodensteiner, J. (2021), *Observational imprints of binary evolution on B- and Be-star populations*, PhD thesis (cit. on p. 120).

Bodensteiner, J. et al. (2019), *The young massive SMC cluster NGC 330 seen by MUSE. I. Observations and stellar content*, arXiv: `1911.03477 [astro-ph.SR]` (cit. on pp. 24, 33).

Böhm-Vitense, E. (1958), *Über die Wasserstoffkonvektionszone in Sternen verschiedener Effektivtemperaturen und Leuchtkräfte. Mit 5 Textabbildungen*, Zeitschrift für Astrophysik **46** 108 (cit. on p. 4).

Boubert, D. and N. W. Evans (2018), *On the kinematics of a runaway Be star population*, Mon. Not. R. Astron. Soc. **477** 5261, arXiv: `1804.05849 [astro-ph.SR]` (cit. on p. 119).

Braithwaite, J. and H. C. Spruit (2004), *A fossil origin for the magnetic field in A stars and white dwarfs*, Nature **431** 819, arXiv: `astro-ph/0502043 [astro-ph]` (cit. on p. 66).

Brandt, T. D. and C. X. Huang (2015), *Rotating Stellar Models Can Account for the Extended Main-sequence Turnoffs in Intermediate-age Clusters*, Astrophys. J. **807**, 25 25, arXiv: `1504.04375 [astro-ph.SR]` (cit. on pp. 18, 39).

Britavskiy, N. et al. (2019), *The VLT-FLAMES Tarantula Survey. XXX. Red stragglers in the clusters Hodge 301 and SL 639*, Astron. Astrophys. **624**, A128 A128, arXiv: `1902.09891 [astro-ph.SR]` (cit. on pp. 31, 34).

Brott, I. et al. (2011), *Rotating massive main-sequence stars. I. Grids of evolutionary models and isochrones*, Astron. Astrophys. **530**, A115 A115, arXiv: `1102.0530 [astro-ph.SR]` (cit. on pp. 4, 8, 24–26, 31, 32, 41, 43, 44, 58, 71, 72).

Cantiello, M. and N. Langer (2010), *Thermohaline mixing in evolved low-mass stars*, Astron. Astrophys. **521**, A9 A9, arXiv: `1006.1354 [astro-ph.SR]` (cit. on pp. 25, 42).

Cantiello, M., S. .-.-C. Yoon et al. (2007), *Binary star progenitors of long gamma-ray bursts*, Astron. Astrophys. **465** L29, arXiv: `astro-ph/0702540 [astro-ph]` (cit. on p. 9).

Carciofi, A. C. et al. (2008), *On the Determination of the Rotational Oblateness of Achernar*, Astrophys. J. Letters **676** L41, arXiv: `0801.4901 [astro-ph]` (cit. on p. 8).

Carini, R. et al. (2020), *MUSE Observations of NGC330 in the Small Magellanic Cloud: Helium Abundance of Bright Main-sequence Stars*, Astron. J. **159**, 152 152, arXiv: `2002.02906 [astro-ph.SR]` (cit. on p. 88).

Casares, J. et al. (2014), *A Be-type star with a black-hole companion*, Nature **505** 378, arXiv: `1401.3711 [astro-ph.SR]` (cit. on p. 119).

Castro, N. et al. (2014), *The spectroscopic Hertzsprung-Russell diagram of Galactic massive stars*, Astron. Astrophys. **570**, L13 L13, arXiv: `1410.3499 [astro-ph.SR]` (cit. on p. 71).

Chaboyer, B. and J.-P. Zahn (1992), *Effect of horizontal turbulent diffusion on transport by meridional circulation*, Astron. Astrophys. **253** 173 (cit. on pp. 25, 42, 72).

Chauville, J. et al. (2001), *High and intermediate-resolution spectroscopy of Be stars 4481 lines*, Astron. Astrophys. **378** 861 (cit. on p. 8).

Chen, X. and Z. Han (2002), *Low- and intermediate-mass close binary evolution and the initial-final mass relation - II. Non-conservative case with convective overshooting*, Mon. Not. R. Astron. Soc. **335** 948 (cit. on p. 10).

Chiosi, C. and C. Summa (1970), *On the Evolution of OB Stars from the Main Sequence to the Helium Exhaustion Phase*, Astrophys. Space Sci. **8** 478 (cit. on p. 5).

Choi, J. et al. (2016), *Mesa Isochrones and Stellar Tracks (MIST). I. Solar-scaled Models*, Astrophys. J. **823**, 102 102, arXiv: `1604.08592 [astro-ph.SR]` (cit. on p. 42).

Claret, A. and G. Torres (2016), *The dependence of convective core overshooting on stellar mass*, Astron. Astrophys. **592**, A15 A15 (cit. on pp. 4, 42, 71).

Coe, M. J., J. A. Kennea et al. (2020), *Swift J004427.3-734801 - a probable Be/white dwarf system in the Small Magellanic Cloud*, Mon. Not. R. Astron. Soc. **497** L50, arXiv: `2005.02891 [astro-ph.HE]` (cit. on p. 120).

Coe, M. J. and J. Kirk (2015), *Catalogue of Be/X-ray binary systems in the Small Magellanic Cloud: X-ray, optical and IR properties*, Mon. Not. R. Astron. Soc. **452** 969, arXiv: `1506.01920 [astro-ph.HE]` (cit. on p. 119).

Cordoni, G. et al. (2018), *Extended Main-sequence Turnoff as a Common Feature of Milky Way Open Clusters*, Astrophys. J. **869**, 139 139, arXiv: `1811.01192 [astro-ph.SR]` (cit. on pp. 38, 64).

Correnti, M., P. Goudfrooij, A. Bellini et al. (2017), *Dissecting the extended main-sequence turn-off of the young star cluster NGC 1850*, Mon. Not. R. Astron. Soc. **467** 3628, arXiv: `1612.08746 [astro-ph.SR]` (cit. on pp. 18, 39, 64, 71).

Correnti, M., P. Goudfrooij, T. H. Puzia et al. (2015), *New constraints on the star formation history of the star cluster NGC 1856*, Mon. Not. R. Astron. Soc. **450** 3054, arXiv: `1504.03299 [astro-ph.SR]` (cit. on p. 18).

D'Antona, F., M. Di Criscienzo et al. (2015), *The extended main-sequence turn-off cluster NGC 1856: rotational evolution in a coeval stellar ensemble*, Mon. Not. R. Astron. Soc. **453** 2637, arXiv: `1508.01932 [astro-ph.SR]` (cit. on pp. 18, 39).

D'Antona, F., A. P. Milone et al. (2017), *Stars caught in the braking stage in young Magellanic Cloud clusters*, Nature Astronomy **1**, 0186 0186, arXiv: `1707.07711 [astro-ph.SR]` (cit. on pp. 24, 31, 38, 39, 62, 64).

De Greve, J. P. and C. De Loore (1992), *Evolution of massive close binaries*, Astron. Astrophys. Supp. **96** 653 (cit. on p. 10).

de Mink, S. E., M. Cantiello et al. (2009), *Rotational mixing in massive binaries. Detached short-period systems*, Astron. Astrophys. **497** 243, arXiv: `0902.1751 [astro-ph.SR]` (cit. on p. 9).

de Mink, S. E., N. Langer et al. (2013), *The Rotation Rates of Massive Stars: The Role of Binary Interaction through Tides, Mass Transfer, and Mergers*, Astrophys. J. **764**, 166 166, arXiv: `1211.3742 [astro-ph.SR]` (cit. on pp. 24, 31).

de Mink, S. E., H. Sana et al. (2014), *The Incidence of Stellar Mergers and Mass Gainers among Massive Stars*, Astrophys. J. **782**, 7 7, arXiv: `1312.3650 [astro-ph.SR]` (cit. on p. 26).

Detmers, R. G. et al. (2008), *Gamma-ray bursts from tidally spun-up Wolf-Rayet stars?*, Astron. Astrophys. **484** 831, arXiv: `0804.0014` (cit. on p. 25).

Domiciano de Souza, A., M. Hadjara et al. (2012), *Beyond the diffraction limit of optical/IR interferometers. I. Angular diameter and rotation parameters of Achernar from differential phases*, Astron. Astrophys. **545**, A130 A130 (cit. on p. 8).

Domiciano de Souza, A., P. Kervella et al. (2003), *The spinning-top Be star Achernar from VLTI-VINCI*, Astron. Astrophys. **407** L47, arXiv: `astro-ph/0306277 [astro-ph]` (cit. on p. 8).

Donati, J. .-.-F. and J. D. Landstreet (2009), *Magnetic Fields of Nondegenerate Stars*, Ann. Rev. Astron. Astrophys **47** 333, arXiv: `0904.1938 [astro-ph.SR]` (cit. on p. 66).

Dufton, P. L. et al. (2013), *The VLT-FLAMES Tarantula Survey. X. Evidence for a bimodal distribution of rotational velocities for the single early B-type stars*, Astron. Astrophys. **550**, A109 A109, arXiv: `1212.2424 [astro-ph.SR]` (cit. on pp. 31, 32, 38, 39, 53, 59, 62, 66, 73, 118).

Dunstall, P. R. et al. (2011), *The VLT-FLAMES survey of massive stars: Nitrogen abundances for Be-type stars in the Magellanic Clouds*, Astron. Astrophys. **536**, A65 A65, arXiv: `1109.6661 [astro-ph.SR]` (cit. on p. 105).

Dupree, A. K. et al. (2017), *NGC 1866: First Spectroscopic Detection of Fast-rotating Stars in a Young LMC Cluster*, Astrophys. J. Letters **846**, L1 L1, arXiv: `1708.03386 [astro-ph.GA]` (cit. on pp. 51, 62).

Eddington, A. S. (1925), *Circulating currents in rotating stars*, The Observatory **48** 73 (cit. on pp. 7, 71).

Eggleton, P. P. (1983), *Aproximations to the radii of Roche lobes.*, Astrophys. J. **268** 368 (cit. on p. 10).

Eggleton, P. P. and L. Kiseleva-Eggleton (2001), *Orbital Evolution in Binary and Triple Stars, with an Application to SS Lacertae*, Astrophys. J. **562** 1012, arXiv: `astro-ph/0104126 [astro-ph]` (cit. on p. 70).

Ekström, S. et al. (2008), *Evolution towards the critical limit and the origin of Be stars*, Astron. Astrophys. **478** 467, arXiv: `0711.1735 [astro-ph]` (cit. on pp. 4, 8, 33, 41, 49, 58, 66, 74, 96).

Endal, A. S. and S. Sofia (1976), *The evolution of rotating stars. I. Method and exploratory calculations for a 7 M sun star.*, Astrophys. J. **210** 184 (cit. on p. 42).

– (1978), *The evolution of rotating stars. II. Calculations with time-dependent redistribution of angular momentum for 7 and 10 M sun stars.*, Astrophys. J. **220** 279 (cit. on pp. 7, 38).

Espinosa Lara, F. and M. Rieutord (2011), *Gravity darkening in rotating stars*, Astron. Astrophys. **533**, A43 A43, arXiv: `1109.3038 [astro-ph.SR]` (cit. on p. 78).

Evans, C. J. et al. (2005), *The VLT-FLAMES survey of massive stars: Observations in the Galactic clusters NGC 3293, NGC 4755 and NGC 6611*, Astron. Astrophys. **437** 467, arXiv: `astro-ph/0503655 [astro-ph]` (cit. on p. 44).

Ferrario, L. et al. (2009), *The origin of magnetism on the upper main sequence*, Mon. Not. R. Astron. Soc. **400** L71 (cit. on pp. 66, 118).

Fossati, L. et al. (2016), *Evidence of magnetic field decay in massive main-sequence stars*, Astron. Astrophys. **592**, A84 A84, arXiv: `1606.07599 [astro-ph.SR]` (cit. on p. 66).

Frank, J., A. King and D. Raine (2002), *Accretion Power in Astrophysics*, 3rd ed., Cambridge University Press (cit. on p. 11).

Fricke, K. (1968), *Instabilität stationärer Rotation in Sternen*, Zeitschrift für Astrophysik **68** 317 (cit. on pp. 7, 71).

Gaia Collaboration, C. Babusiaux et al. (2018), *Gaia Data Release 2. Observational Hertzsprung-Russell diagrams*, Astron. Astrophys. **616**, A10 A10, arXiv: `1804.09378 [astro-ph.SR]` (cit. on p. 62).

Gaia Collaboration, A. Helmi et al. (2018), *Gaia Data Release 2. Kinematics of globular clusters and dwarf galaxies around the Milky Way*, Astron. Astrophys. **616**, A12 A12, arXiv: `1804.09381 [astro-ph.GA]` (cit. on p. 45).

Georgy, C., S. Ekström, P. Eggenberger et al. (2013), *Grids of stellar models with rotation. III. Models from 0.8 to 120 $M_\odot$ at a metallicity $Z = 0.002$*, Astron. Astrophys. **558**, A103 A103, arXiv: `1308.2914 [astro-ph.SR]` (cit. on p. 31).

Georgy, C., S. Ekström, A. Granada et al. (2013), *Populations of rotating stars. I. Models from 1.7 to 15 $M_\odot$ at $Z = 0.014$, 0.006, and 0.002 with Ω/Ω_{crit} between 0 and 1*, Astron. Astrophys. **553**, A24 A24, arXiv: `1303.2321 [astro-ph.SR]` (cit. on p. 39).

Glatt, K. et al. (2008), *Age Determination of Six Intermediate-Age Small Magellanic Cloud Star Clusters with HST/ACS*, Astron. J. **136** 1703, arXiv: `0807.3744 [astro-ph]` (cit. on p. 18).

Glebbeek, E. and O. R. Pols (2008), *Evolution of stellar collision products in open clusters. II. A grid of low-mass collisions*, Astron. Astrophys. **488** 1017, arXiv: `0806.0865 [astro-ph]` (cit. on p. 88).

Glebbeek, E., E. Gaburov et al. (2013), *Structure and evolution of high-mass stellar mergers*, Mon. Not. R. Astron. Soc. **434** 3497, arXiv: `1307.2445 [astro-ph.SR]` (cit. on pp. 86, 88).

Goldreich, P. and G. Schubert (1967), *Differential Rotation in Stars*, Astrophys. J. **150** 571 (cit. on pp. 7, 71).

Gossage, S. et al. (2019), *Combined Effects of Rotation and Age Spreads on Extended Main-Sequence Turn Offs*, Astrophys. J. **887**, 199 199, arXiv: `1907.11251 [astro-ph.SR]` (cit. on pp. 39, 41).

Goudfrooij, P., L. Girardi et al. (2014), *Extended Main Sequence Turnoffs in Intermediate-age Star Clusters: A Correlation between Turnoff Width and Early Escape Velocity*, Astrophys. J. **797**, 35 35, arXiv: `1410.3840 [astro-ph.SR]` (cit. on p. 18).

Goudfrooij, P., T. H. Puzia et al. (2011), *Population Parameters of Intermediate-age Star Clusters in the Large Magellanic Cloud. III. Dynamical Evidence for a Range of Ages Being Responsible for Extended Main-sequence Turnoffs*, Astrophys. J. **737**, 4 4, arXiv: `1105.1317 [astro-ph.SR]` (cit. on pp. 18, 38, 64).

Gratton, R. G., E. Carretta and A. Bragaglia (2012), *Multiple populations in globular clusters. Lessons learned from the Milky Way globular clusters*, Astron. Astrophys. Rev. **20**, 50 50, arXiv: `1201.6526 [astro-ph.SR]` (cit. on pp. 17, 62).

Grevesse, N., A. Noels and A. J. Sauval (1996), "Standard Abundances", *Astronomical Society of the Pacific Conference Series; volume 99. Proceedings of the sixth (6th) annual October Astrophysics Conference in College Park; Maryland; 9-11 October 1995; San Francisco: Astronomical Society of the Pacific (ASP); |c1996; edited by Stephen S. Holt and George Sonneborn, p.117*, ed. by S. S. Holt and G. Sonneborn, vol. 99, Astronomical Society of the Pacific Conference Series 117 (cit. on p. 43).

Hamann, W.-R., L. Koesterke and U. Wessolowski (1995), *Spectral analyses of the Galactic Wolf-Rayet stars: hydrogen-helium abundances and improved stellar parameters for the WN class*, Astron. Astrophys. **299** 151 (cit. on p. 72).

Hastings, B., N. Langer et al. (2021), *Stringent upper limit on Be star fractions produced by binary interaction*, Astron. Astrophys. **653**, A144 A144, arXiv: `2106.12263 [astro-ph.SR]` (cit. on pp. 9, 21, 79, 97, 102, 104, 106, 120).

Hastings, B., C. Wang and N. Langer (2020), *The single star path to Be stars*, Astron. Astrophys. **633**, A165 A165, arXiv: `1912.05290 [astro-ph.SR]` (cit. on pp. 8, 33, 41, 42, 49, 55, 57, 58, 66, 74, 96).

Heger, A., C. L. Fryer et al. (2003), *How Massive Single Stars End Their Life*, Astrophys. J. **591** 288, arXiv: `astro-ph/0212469 [astro-ph]` (cit. on p. 2).

Heger, A., N. Langer and S. E. Woosley (2000), *Presupernova Evolution of Rotating Massive Stars. I. Numerical Method and Evolution of the Internal Stellar Structure*, Astrophys. J. **528** 368, eprint: `astro-ph/9904132` (cit. on pp. 7, 25, 42, 71).

Heger, A., S. E. Woosley and H. C. Spruit (2005), *Presupernova Evolution of Differentially Rotating Massive Stars Including Magnetic Fields*, Astrophys. J. **626** 350, eprint: `astro-ph/0409422` (cit. on pp. 25, 72).

Howarth, I. D. et al. (2015), *The VLT-FLAMES Tarantula Survey. XXIII. Two massive double-lined binaries in 30 Doradus*, Astron. Astrophys. **582**, A73 A73, arXiv: `1508.05791 [astro-ph.SR]` (cit. on p. 29).

Huang, W., D. R. Gies and M. V. McSwain (2010), *A Stellar Rotation Census of B Stars: From ZAMS to TAMS*, Astrophys. J. **722** 605, arXiv: `1008.1761 [astro-ph.SR]` (cit. on pp. 8, 39, 49, 62, 66, 73, 96).

Hunter, I. et al. (2008), *The VLT FLAMES Survey of Massive Stars: Rotation and Nitrogen Enrichment as the Key to Understanding Massive Star Evolution*, Astrophys. J. Letters **676** L29, arXiv: `0711.2267` (cit. on p. 118).

Iben Icko, J. (1967), *Stellar Evolution Within and off the Main Sequence*, Ann. Rev. Astron. Astrophys **5** 571 (cit. on p. 62).

Inno, L. et al. (2016), *The Panchromatic View of the Magellanic Clouds from Classical Cepheids. I. Distance, Reddening, and Geometry of the Large Magellanic Cloud Disk*, Astrophys. J. **832**, 176 176, arXiv: `1609.03554 [astro-ph.GA]` (cit. on p. 45).

Ivanova, N. (2014), *Binary Evolution: Roche Lobe Overflow and Blue Stragglers*, 1st ed., Springer, Berlin, Heidelberg, ISBN: 978-3-662-44433-7 (cit. on p. 13).

Kamann, S., N. Bastian, S. Gossage et al. (2020), *How stellar rotation shapes the colour-magnitude diagram of the massive intermediate-age star cluster NGC 1846*, Mon. Not. R. Astron. Soc. **492** 2177, arXiv: `2001.01731 [astro-ph.SR]` (cit. on pp. 39, 52, 62, 65, 66, 86, 118).

Kamann, S., N. Bastian, T. .-.-O. Husser et al. (2018), *Cluster kinematics and stellar rotation in NGC 419 with MUSE and adaptive optics*, Mon. Not. R. Astron. Soc. **480** 1689, arXiv: `1807.10612 [astro-ph.GA]` (cit. on p. 51).

Klement, R. et al. (2019), *Prevalence of SED Turndown among Classical Be Stars: Are All Be Stars Close Binaries?*, Astrophys. J. **885**, 147 147 (cit. on p. 33).

Köhler, K. et al. (2015), *The evolution of rotating very massive stars with LMC composition*, Astron. Astrophys. **573**, A71 A71, arXiv: `1501.03794 [astro-ph.SR]` (cit. on p. 35).

Korntreff, C., T. Kaczmarek and S. Pfalzner (2012), *Towards the field binary population: influence of orbital decay on close binaries*, Astron. Astrophys. **543**, A126 A126, arXiv: `1205.6311 [astro-ph.SR]` (cit. on pp. 67, 81, 87).

Kozai, Y. (1962), *Secular perturbations of asteroids with high inclination and eccentricity*, Astron. J. **67** 591 (cit. on p. 70).

Kurucz, R. L. (1970), *Atlas: a Computer Program for Calculating Model Stellar Atmospheres*, SAO Special Report **309** (cit. on pp. 43, 72).

Kurucz, R. L. (1993), *SYNTHE spectrum synthesis programs and line data* (cit. on pp. 43, 72).

Labadie-Bartz, J. et al. (2017), *Photometric Variability of the Be Star Population*, Astron. J. **153**, 252 252, arXiv: `1609.08449 [astro-ph.SR]` (cit. on p. 79).

Langer, N. (1998), *Coupled mass and angular momentum loss of massive main sequence stars*, Astron. Astrophys. **329** 551 (cit. on pp. 25, 30, 78).

– (2012), *Presupernova Evolution of Massive Single and Binary Stars*, Ann. Rev. Astron. Astrophys **50** 107, arXiv: `1206.5443 [astro-ph.SR]` (cit. on pp. 2, 8, 9, 25, 29, 49, 96, 118).

Langer, N., M. F. El Eid and K. J. Fricke (1985), *Evolution of massive stars with semiconvective diffusion*, Astron. Astrophys. **145** 179 (cit. on p. 5).

Langer, N., K. J. Fricke and D. Sugimoto (1983), *Semiconvective diffusion and energy transport*, Astron. Astrophys. **126** 207 (cit. on p. 25).

Langer, N., C. Schürmann et al. (2020), *Properties of OB star-black hole systems derived from detailed binary evolution models*, Astron. Astrophys. **638**, A39 A39, arXiv: `1912.09826 [astro-ph.SR]` (cit. on p. 120).

Langer, N., S. Wellstein and J. Petrovic (2003), "On the evolution of massive close binaries", *A Massive Star Odyssey: From Main Sequence to Supernova*, ed. by K. van der Hucht, A. Herrero and C. Esteban, vol. 212 275 (cit. on pp. 9, 12).

Li, C., R. de Grijs et al. (2017), *Discovery of Extended Main-sequence Turnoffs in Four Young Massive Clusters in the Magellanic Clouds*, Astrophys. J. **844**, 119 119, arXiv: `1706.07545 [astro-ph.SR]` (cit. on pp. 16, 38, 62).

Li, C., W. Sun et al. (2019), *Extended Main-sequence Turnoffs in the Double Cluster h and χ Persei: The Complex Role of Stellar Rotation*, Astrophys. J. **876**, 65 65, arXiv: `1904.02005 [astro-ph.SR]` (cit. on pp. 17, 24, 31, 38, 62).

Lim, B. et al. (2019), *Extended main sequence turn-off originating from a broad range of stellar rotational velocities*, Nature Astronomy **3** 76, arXiv: `1811.01593 [astro-ph.SR]` (cit. on p. 38).

Lin, M.-K., M. R. Krumholz and K. M. Kratter (2011), *Spin-down of protostars through gravitational torques*, Mon. Not. R. Astron. Soc. **416** 580, arXiv: `1105.3205 [astro-ph.SR]` (cit. on p. 66).

Liu, Q. Z., J. van Paradijs and E. P. J. van den Heuvel (2006), *Catalogue of high-mass X-ray binaries in the Galaxy (4th edition)*, Astron. Astrophys. **455** 1165, arXiv: `0707.0549 [astro-ph]` (cit. on pp. 9, 49, 96).

Mackey, A. D. and P. Broby Nielsen (2007), *A double main-sequence turn-off in the rich star cluster NGC 1846 in the Large Magellanic Cloud*, Mon. Not. R. Astron. Soc. **379** 151, arXiv: `0704.3360 [astro-ph]` (cit. on p. 18).

Mackey, A. D., P. Broby Nielsen et al. (2008), *Multiple Stellar Populations in Three Rich Large Magellanic Cloud Star Clusters*, Astrophys. J. Letters **681** L17, arXiv: `0804.3475 [astro-ph]` (cit. on p. 38).

Maeder, A. (1987), *Evidences for a bifurcation in massive star evolution. The ON-blue stragglers.*, Astron. Astrophys. **178** 159 (cit. on pp. 8, 31).

Maeder, A. and G. Meynet (1987), *Grids of evolutionary models of massive stars with mass loss and overshooting - Properties of Wolf-Rayet stars sensitive to overshooting.*, Astron. Astrophys. **182** 243 (cit. on p. 4).

– (1996), *Diffusive mixing by shears in rotating stars.*, Astron. Astrophys. **313** 140 (cit. on p. 7).

Maeder, A. and G. Meynet (2000), *The Evolution of Rotating Stars*, Ann. Rev. Astron. Astrophys **38** 143, arXiv: `astro-ph/0004204 [astro-ph]` (cit. on pp. 6, 38, 118).

Mahy, L. et al. (2019), *The Tarantula Massive Binary Monitoring: III. Atmosphere analysis of double-lined spectroscopic systems*, arXiv e-prints, arXiv:1912.08107 arXiv:1912.08107, arXiv: `1912.08107 [astro-ph.SR]` (cit. on p. 29).

Mamajek, E. E. et al. (2015), *IAU 2015 Resolution B2 on Recommended Zero Points for the Absolute and Apparent Bolometric Magnitude Scales*, arXiv e-prints, arXiv:1510.06262 arXiv:1510.06262, arXiv: `1510.06262 [astro-ph.SR]` (cit. on pp. 43, 72).

Marchant, P., N. Langer, P. Podsiadlowski, T. M. Tauris, S. de Mink et al. (2017), *Ultra-luminous X-ray sources and neutron-star-black-hole mergers from very massive close binaries at low metallicity*, Astron. Astrophys. **604**, A55 A55, arXiv: `1705.04734 [astro-ph.HE]` (cit. on pp. 12, 24, 25).

Marchant, P., N. Langer, P. Podsiadlowski, T. M. Tauris and T. J. Moriya (2016), *A new route towards merging massive black holes*, Astron. Astrophys. **588**, A50 A50, arXiv: `1601.03718 [astro-ph.SR]` (cit. on pp. 8, 25, 29, 42).

Marino, A. F. et al. (2018), *Different Stellar Rotations in the Two Main Sequences of the Young Globular Cluster NGC 1818: The First Direct Spectroscopic Evidence*, Astron. J. **156**, 116 116, arXiv: `1807.04493 [astro-ph.SR]` (cit. on pp. 39, 51–53, 57, 62, 65, 66, 118).

Martinet, S. et al. (2021), *Convective core sizes in rotating massive stars. I. Constraints from solar metallicity OB field stars*, Astron. Astrophys. **648**, A126 A126, arXiv: `2103.03672 [astro-ph.SR]` (cit. on p. 71).

McSwain, M. V. and D. R. Gies (2005), *The Evolutionary Status of Be Stars: Results from a Photometric Study of Southern Open Clusters*, Astrophys. J. Supp. **161** 118, arXiv: `astro-ph/0505032 [astro-ph]` (cit. on p. 33).

Mermilliod, J. .-.-C. and A. Maeder (1986), *Evolution of massive stars : comparison of cluster sequences and models with mass loss.*, Astron. Astrophys. **158** 45 (cit. on p. 4).

Meynet, G. and A. Maeder (1997), *Stellar evolution with rotation. I. The computational method and the inhibiting effect of the μ-gradient.*, Astron. Astrophys. **321** 465 (cit. on p. 42).

Milone, A. P., L. R. Bedin, G. Piotto and J. Anderson (2009), *Multiple stellar populations in Magellanic Cloud clusters. I. An ordinary feature for intermediate age globulars in the LMC?*, Astron. Astrophys. **497** 755, arXiv: `0810.2558 [astro-ph]` (cit. on pp. 16, 18, 38, 62).

Milone, A. P., L. R. Bedin, G. Piotto, A. F. Marino et al. (2015), *Multiple stellar populations in Magellanic Cloud clusters - III. The first evidence of an extended main sequence turn-off in a young cluster: NGC 1856*, Mon. Not. R. Astron. Soc. **450** 3750, arXiv: `1504.03252 [astro-ph.SR]` (cit. on p. 38).

Milone, A. P., A. F. Marino, F. D'Antona, L. R. Bedin, G. S. Da Costa et al. (2016), *Multiple stellar populations in Magellanic Cloud clusters - IV. The double main sequence of the young cluster NGC 1755*, Mon. Not. R. Astron. Soc. **458** 4368, arXiv: `1603.03493 [astro-ph.SR]` (cit. on pp. 16, 18, 38, 44, 46, 62).

Milone, A. P., A. F. Marino, F. D'Antona, L. R. Bedin, G. Piotto et al. (2017), *Multiple stellar populations in Magellanic Cloud clusters - V. The split main sequence of the young cluster NGC 1866*, Mon. Not. R. Astron. Soc. **465** 4363, arXiv: `1611.06725 [astro-ph.SR]` (cit. on pp. 38, 44, 46).

Milone, A. P., A. F. Marino, M. Di Criscienzo et al. (2018), *Multiple stellar populations in Magellanic Cloud clusters - VI. A survey of multiple sequences and Be stars in young clusters*, Mon. Not. R. Astron. Soc. **477** 2640, arXiv: `1802.10538 [astro-ph.SR]` (cit. on pp. 9, 17, 18, 24, 33, 38, 39, 43–46, 48, 62–64, 66, 70–73, 96).

Milone, A. P., G. Piotto, L. R. Bedin et al. (2012), *The ACS survey of Galactic globular clusters. XII. Photometric binaries along the main sequence*, Astron. Astrophys. **540**, A16 A16, arXiv: `1111.0552 [astro-ph.SR]` (cit. on pp. 98, 99).

Milone, A. P., G. Piotto, A. Renzini et al. (2017), *The Hubble Space Telescope UV Legacy Survey of Galactic globular clusters - IX. The Atlas of multiple stellar populations*, Mon. Not. R. Astron. Soc. **464** 3636, arXiv: `1610.00451 [astro-ph.SR]` (cit. on pp. 17, 62).

Mucciarelli, A. et al. (2014), *No Evidence of Chemical Anomalies in the Bimodal Turnoff Cluster NGC 1806 in the Large Magellanic Cloud*, Astrophys. J. Letters **793**, L6 L6, arXiv: `1409.0259 [astro-ph.SR]` (cit. on pp. 18, 38, 62).

Niederhofer, F., C. Georgy et al. (2015), *Apparent age spreads in clusters and the role of stellar rotation*, Mon. Not. R. Astron. Soc. **453** 2070, arXiv: `1507.07561 [astro-ph.SR]` (cit. on pp. 18, 31, 35, 39, 64, 71).

Niederhofer, F., M. Hilker et al. (2015), *No evidence for significant age spreads in young massive LMC clusters*, Astron. Astrophys. **575**, A62 A62, arXiv: `1501.02275 [astro-ph.GA]` (cit. on p. 64).

Packet, W. (1981), *On the spin-up of the mass accreting component in a close binary system*, Astron. Astrophys. **102** 17 (cit. on pp. 9, 29).

Paczynski, B. (1991), *A Polytropic Model of an Accretion Disk, a Boundary Layer, and a Star*, Astrophys. J. **370** 597 (cit. on pp. 12, 96).

Palla, F. and S. W. Stahler (1993), *The Pre-Main-Sequence Evolution of Intermediate-Mass Stars*, Astrophys. J. **418** 414 (cit. on p. 82).

Paxton, B., L. Bildsten et al. (2011), *Modules for Experiments in Stellar Astrophysics (MESA)*, Astrophys. J. Supp. **192**, 3 3, arXiv: `1009.1622 [astro-ph.SR]` (cit. on pp. 24, 41, 71).

Paxton, B., M. Cantiello et al. (2013), *Modules for Experiments in Stellar Astrophysics (MESA): Planets, Oscillations, Rotation, and Massive Stars*, Astrophys. J. Supp. **208**, 4 4, arXiv: `1301.0319 [astro-ph.SR]` (cit. on pp. 7, 24, 41, 42, 71).

Paxton, B., P. Marchant et al. (2015), *Modules for Experiments in Stellar Astrophysics (MESA): Binaries, Pulsations, and Explosions*, Astrophys. J. Supp. **220**, 15 15, arXiv: `1506.03146 [astro-ph.SR]` (cit. on pp. 24, 25, 41, 71, 78).

Paxton, B., R. Smolec et al. (2019), *Modules for Experiments in Stellar Astrophysics (MESA): Pulsating Variable Stars, Rotation, Convective Boundaries, and Energy Conservation*, Astrophys. J. Supp. **243**, 10 10, arXiv: `1903.01426 [astro-ph.SR]` (cit. on pp. 7, 29, 35, 36, 41, 42, 44, 71, 78, 97).

Peimbert, M., V. Luridiana and A. Peimbert (2007), *Revised Primordial Helium Abundance Based on New Atomic Data*, Astrophys. J. **666** 636, arXiv: `astro-ph/0701580 [astro-ph]` (cit. on p. 43).

Perlmutter, S. et al. (1999), *Measurements of Ω and Λ from 42 High-Redshift Supernovae*, Astrophys. J. **517** 565, arXiv: `astro-ph/9812133 [astro-ph]` (cit. on p. 1).

Petit, V. et al. (2013), *A magnetic confinement versus rotation classification of massive-star magnetospheres*, Mon. Not. R. Astron. Soc. **429** 398, arXiv: `1211.0282 [astro-ph.SR]` (cit. on p. 66).

Petrovic, J., N. Langer and K. A. van der Hucht (2005), *Constraining the mass transfer in massive binaries through progenitor evolution models of Wolf-Rayet+O binaries*, Astron. Astrophys. **435** 1013, arXiv: `astro-ph/0504242 [astro-ph]` (cit. on pp. 9, 25, 29).

Pietrzyński, G. et al. (2013), *An eclipsing-binary distance to the Large Magellanic Cloud accurate to two per cent*, Nature **495** 76, arXiv: `1303.2063 [astro-ph.GA]` (cit. on p. 45).

Pols, O. R. et al. (1991), *The formation of Be stars through close binary evolution.*, Astron. Astrophys. **241** 419 (cit. on pp. 9, 33, 49, 96).

Popham, R. and R. Narayan (1991), *Does accretion cease when a star approaches breakup?*, Astrophys. J. **370** 604 (cit. on pp. 12, 96).

Raguzova, N. V. and S. B. Popov (2005), *Be X-ray binaries and candidates*, Astronomical and Astrophysical Transactions **24** 151, arXiv: `astro-ph/0505275 [astro-ph]` (cit. on pp. 9, 49, 96).

Railton, A. D., C. A. Tout and S. J. Aarseth (2014), *Pre-Mainsequence Stellar Evolution in N-Body Models*, Pub. Astron. Soc. Australia **31**, e017 e017, arXiv: `1402.3323 [astro-ph.SR]` (cit. on p. 82).

Rain, M. J. et al. (2021), *The Blue Straggler Population of the Open Clusters Trumpler 5, Trumpler 20, and NGC 2477*, Astron. J. **161**, 37 37, arXiv: `2010.06884 [astro-ph.SR]` (cit. on p. 86).

Ramírez-Agudelo, O. H. et al. (2015), *The VLT-FLAMES Tarantula Survey. XXI. Stellar spin rates of O-type spectroscopic binaries*, Astron. Astrophys. **580**, A92 A92, arXiv: `1507.02286 [astro-ph.SR]` (cit. on pp. 31, 66).

Ramírez-Tannus, M. C. et al. (2021), *A relation between the radial velocity dispersion of young clusters and their age. Evidence for hardening as the formation scenario of massive close binaries*, Astron. Astrophys. **645**, L10 L10, arXiv: `2101.01604 [astro-ph.SR]` (cit. on p. 67).

Rivinius, T., A. C. Carciofi and C. Martayan (2013), *Classical Be stars. Rapidly rotating B stars with viscous Keplerian decretion disks*, Astron. Astrophys. Rev. **21**, 69 69, arXiv: `1310.3962 [astro-ph.SR]` (cit. on pp. 35, 39–41, 49, 96).

Russell, H. N. (1914), *Relations Between the Spectra and Other Characteristics of the Stars*, Popular Astronomy **22** 275 (cit. on p. 24).

Sackmann, I. .-.-J. and S. P. S. Anand (1970), *Structure and Evolution of Rapidly Rotating B-Type Stars*, Astrophys. J. **162** 105 (cit. on p. 8).

Salpeter, E. E. (1955), *The Luminosity Function and Stellar Evolution.*, Astrophys. J. **121** 161 (cit. on p. 26).

Sana, H., S. E. de Mink et al. (2012), *Binary Interaction Dominates the Evolution of Massive Stars*, Science **337** 444, arXiv: `1207.6397 [astro-ph.SR]` (cit. on pp. 9, 24, 67, 99).

Sana, H., M. C. Ramírez-Tannus et al. (2017), *A dearth of short-period massive binaries in the young massive star forming region M 17. Evidence for a large orbital separation at birth?*, Astron. Astrophys. **599**, L9 L9, arXiv: `1702.02153 [astro-ph.SR]` (cit. on p. 67).

Sanyal, D., L. Grassitelli et al. (2015), *Massive main-sequence stars evolving at the Eddington limit*, Astron. Astrophys. **580**, A20 A20, arXiv: `1506.02997 [astro-ph.SR]` (cit. on p. 25).

Sanyal, D., N. Langer et al. (2017), *Metallicity dependence of envelope inflation in massive stars*, Astron. Astrophys. **597**, A71 A71, arXiv: `1611.07280 [astro-ph.SR]` (cit. on p. 25).

Schneider, F. R. N., R. G. Izzard, S. E. de Mink et al. (2014), *Ages of Young Star Clusters, Massive Blue Stragglers, and the Upper Mass Limit of Stars: Analyzing Age-dependent Stellar Mass Functions*, Astrophys. J. **780**, 117 117, arXiv: `1312.0607 [astro-ph.SR]` (cit. on p. 31).

Schneider, F. R. N., R. G. Izzard, N. Langer et al. (2015), *Evolution of Mass Functions of Coeval Stars through Wind Mass Loss and Binary Interactions*, Astrophys. J. **805**, 20 20, arXiv: `1504.01735 [astro-ph.SR]` (cit. on pp. 24, 29, 41, 64, 65).

Schneider, F. R. N., S. T. Ohlmann, P. Podsiadlowski, F. K. Röpke, S. A. Balbus and R. Pakmor (2020), *Long-term evolution of a magnetic massive merger product*, Mon. Not. R. Astron. Soc. **495** 2796, arXiv: `2005.05335 [astro-ph.SR]` (cit. on p. 86).

Schneider, F. R. N., P. Podsiadlowski et al. (2016), *Rejuvenation of stellar mergers and the origin of magnetic fields in massive stars*, Mon. Not. R. Astron. Soc. **457** 2355, arXiv: `1601.05084 [astro-ph.SR]` (cit. on pp. 9, 25, 44, 47, 66, 83).

Schneider, F. R. N., S. T. Ohlmann, P. Podsiadlowski, F. K. Röpke, S. A. Balbus, R. Pakmor and V. Springel (2019), *Stellar mergers as the origin of magnetic massive stars*, Nature **574** 211, arXiv: `1910.14058 [astro-ph.SR]` (cit. on pp. 25, 65, 66, 86, 118).

Schootemeijer, A., Y. Götberg et al. (2018), *Clues about the scarcity of stripped-envelope stars from the evolutionary state of the sdO+Be binary system φ Persei*, Astron. Astrophys. **615**, A30 A30, arXiv: `1803.02379 [astro-ph.SR]` (cit. on p. 33).

Schootemeijer, A. and N. Langer (2018), *Wolf-Rayet stars in the Small Magellanic Cloud as testbed for massive star evolution*, Astron. Astrophys. **611**, A75 A75, arXiv: `1709.08727 [astro-ph.SR]` (cit. on p. 41).

Schootemeijer, A., N. Langer et al. (2019), *Constraining mixing in massive stars in the Small Magellanic Cloud*, Astron. Astrophys. **625**, A132 A132, arXiv: `1903.10423 [astro-ph.SR]` (cit. on pp. 5, 41, 42, 71).

Schwarzschild, M. and R. Härm (1958), *Evolution of Very Massive Stars.*, Astrophys. J. **128** 348 (cit. on p. 5).

Shao, Y. and X.-D. Li (2014), *On the Formation of Be Stars through Binary Interaction*, Astrophys. J. **796**, 37 37, arXiv: `1410.0100 [astro-ph.HE]` (cit. on pp. 9, 96).

Sills, A., T. Adams and M. B. Davies (2005), *Blue stragglers as stellar collision products: the angular momentum question*, Mon. Not. R. Astron. Soc. **358** 716, arXiv: `astro-ph/0501142 [astro-ph]` (cit. on p. 86).

Sills, A., J. A. Faber et al. (2001), *Evolution of Stellar Collision Products in Globular Clusters. II. Off-Axis Collisions*, Astrophys. J. **548** 323, arXiv: `astro-ph/0008254 [astro-ph]` (cit. on p. 88).

Spruit, H. C. (2002), *Dynamo action by differential rotation in a stably stratified stellar interior*, Astron. Astrophys. **381** 923, eprint: `astro-ph/0108207` (cit. on pp. 7, 25, 42, 72).

Stothers, R. B. and C. .-.-W. Chin (1985), *Stellar evolution at high mass with convective core overshooting.*, Astrophys. J. **292** 222 (cit. on p. 4).

Sturm, R. et al. (2012), *A new super-soft X-ray source in the Small Magellanic Cloud: Discovery of the first Be/white dwarf system in the SMC?*, Astron. Astrophys. **537**, A76 A76, arXiv: `1112.0176 [astro-ph.HE]` (cit. on p. 120).

Sun, W., R. de Grijs et al. (2019), *Stellar Rotation and the Extended Main-sequence Turnoff in the Open Cluster NGC 5822*, Astrophys. J. **876**, 113 113, arXiv: `1904.03547 [astro-ph.SR]` (cit. on pp. 39, 118).

Sun, W., C. Li et al. (2019), *Tidal-locking-induced Stellar Rotation Dichotomy in the Open Cluster NGC 2287?*, Astrophys. J. **883**, 182 182, arXiv: `1908.06530 [astro-ph.SR]` (cit. on pp. 39, 62, 66, 118).

Tassoul, J.-L. (1978), *Theory of rotating stars* (cit. on p. 6).

Tauris, T. M. and E. P. J. van den Heuvel (2006), "Formation and evolution of compact stellar X-ray sources", *Compact stellar X-ray sources*, vol. 39 623 (cit. on p. 12).

Tokovinin, A. and M. Moe (2020), *Formation of close binaries by disc fragmentation and migration, and its statistical modelling*, Mon. Not. R. Astron. Soc. **491** 5158, arXiv: `1910.01522 [astro-ph.SR]` (cit. on pp. 65, 67).

van Bever, J. and D. Vanbeveren (1997), *The number of B-type binary mass gainers in general, binary Be stars in particular, predicted by close binary evolution.*, Astron. Astrophys. **322** 116 (cit. on pp. 9, 96).

– (1998), *The rejuvenation of starburst regions due to massive close binary evolution*, Astron. Astrophys. **334** 21 (cit. on pp. 18, 24).

van Rensbergen, W. et al. (2011), *Mass loss out of close binaries. The formation of Algol-type systems, completed with case B RLOF*, Astron. Astrophys. **528**, A16 A16, arXiv: `1008.2620 [astro-ph.SR]` (cit. on p. 96).

Vink, J. S., A. de Koter and H. J. G. L. M. Lamers (2001), *Mass-loss predictions for O and B stars as a function of metallicity*, Astron. Astrophys. **369** 574, eprint: `astro-ph/0101509` (cit. on p. 72).

von Zeipel, H. (1924), *The radiative equilibrium of a rotating system of gaseous masses*, Mon. Not. R. Astron. Soc. **84** 665 (cit. on pp. 8, 38).

Wang, C. et al. (2020), *Effects of Close Binary Evolution on the Main-sequence Morphology of Young Star Clusters*, Astrophys. J. Letters **888**, L12 L12, arXiv: `1912.07294 [astro-ph.SR]` (cit. on pp. 9, 12, 18, 41, 43, 44, 47, 49, 64, 66, 67, 74, 78, 83, 96).

Wang, L., D. R. Gies and G. J. Peters (2018), *Detection of Additional Be+sdO Systems from IUE Spectroscopy*, Astrophys. J. **853**, 156 156, arXiv: `1801.01066 [astro-ph.SR]` (cit. on p. 33).

Wasiutynski, J. (1946), *Studies in Hydrodynamics and Structure of Stars and Planets*, Astrophysica Norvegica **4** 1 (cit. on p. 7).

Wellstein, S. and N. Langer (1999), *Implications of massive close binaries for black hole formation and supernovae*, Astron. Astrophys. **350** 148, eprint: `astro-ph/9904256` (cit. on p. 78).

Wellstein, S., N. Langer and H. Braun (2001), *Formation of contact in massive close binaries*, Astron. Astrophys. **369** 939, eprint: `astro-ph/0102244` (cit. on pp. 9, 12).

Wu, D.-H. et al. (2018), *TTV-determined Masses for Warm Jupiters and Their Close Planetary Companions*, Astron. J. **156**, 96 96, arXiv: `1807.02217 [astro-ph.EP]` (cit. on p. 70).

Yang, W. (2018), *The Effects of Binary Stars on the Color-Magnitude Diagrams of Young-age Massive Star Clusters*, Astrophys. J. **860**, 132 132, arXiv: `1805.03905 [astro-ph.SR]` (cit. on pp. 41, 64).

Yang, W., S. Bi et al. (2013), *The Effects of Rotation on the Main-sequence Turnoff of Intermediate-age Massive Star Clusters*, Astrophys. J. **776**, 112 112, arXiv: `1304.5865 [astro-ph.SR]` (cit. on pp. 18, 39).

Yang, W., X. Meng et al. (2011), *The Contributions of Interactive Binary Stars to Double Main-sequence Turnoffs and Dual Red Clump of Intermediate-age Star Clusters*, Astrophys. J. Letters **731**, L37 L37, arXiv: `1103.3128 [astro-ph.SR]` (cit. on pp. 18, 24, 31, 41).

Yang, W. and Z. Tian (2017), *The Effects of the Overshooting of the Convective Core on Main-sequence Turnoffs of Young- and Intermediate-age Star Clusters*, Astrophys. J. **836**, 102 102, arXiv: `1701.05963 [astro-ph.SR]` (cit. on p. 71).

Yoon, S. .-.-C. and N. Langer (2005), *Evolution of rapidly rotating metal-poor massive stars towards gamma-ray bursts*, Astron. Astrophys. **443** 643, arXiv: `astro-ph/0508242 [astro-ph]` (cit. on p. 8).

Yoon, S. .-.-C., N. Langer and C. Norman (2006), *Single star progenitors of long gamma-ray bursts. I. Model grids and redshift dependent GRB rate*, Astron. Astrophys. **460** 199, arXiv: `astro-ph/0606637 [astro-ph]` (cit. on pp. 8, 42).

Yoon, S. .-.-C., S. E. Woosley and N. Langer (2010), *Type Ib/c Supernovae in Binary Systems. I. Evolution and Properties of the Progenitor Stars*, Astrophys. J. **725** 940, arXiv: `1004.0843 [astro-ph.SR]` (cit. on p. 9).

Zorec, J. and F. Royer (2012), *Rotational velocities of A-type stars. IV. Evolution of rotational velocities*, Astron. Astrophys. **537**, A120 A120, arXiv: `1201.2052 [astro-ph.SR]` (cit. on pp. 38, 39, 53, 59, 62, 66, 67, 73, 82, 118).

List of Figures

1.1 The orbital plane of the Roche equipotential for binary systems with a mass ratio of 0.25. M_1 and M_2 are the mass of the two stars, while CM is the center mass of the system. L_1 to L_5 are the Lagrange points. The inner Lagrange point L1 is the place where mass flows from one star to another. Credit: Frank, King and Raine (2002). . 11

1.2 Radius evolution as a function of time of a $5\,M_\odot$ star. The evolutionary phases and different types of mass transfer are indicated in the figure. Credit: Tauris and van den Heuvel (2006). 12

1.3 A binary evolution example with the StarTrack population synthesis code from the zero-age main sequence (ZAMS) to the merger of the two black holes. The evolution started with two massive stars with masses of $94.6\,M_\odot$ and $62.5\,M_\odot$, in a separation of 4941 solar radii. The initial eccentricity is 0.61. In this figure, MS, HG, WR star, BH mean main-sequence, Hertzsprung gap, Wolf-Rayet star and black hole, respectively. CE and CHeB mean common envelope phase and core helium burning phase, respectively. In this binary evolution example, a Wolf-Rayet star is assumed to be directly collapse into a black hole without a supernova after its nuclear burning stage. Credit: Belczynski et al. (2020). 14

1.4 Schematic diagram of cluster star distribution in the Hertzsprung-Russell diagram/color-magnitude diagram. Stars in different evolutionary stages are indicated by different markers. In particular, the grey region means that the stars luminous enough to be here have evolved off their main-sequences. 15

1.5 Age estimation of various open clusters based on their turn-off positions in the color-magnitude diagram. The lines are the theoretical isochrones that can best fit the observed cluster star distributions. The age of a cluster can be obtained by the right y-axis according to its turn-off. Source: Australia Telescope Outreach and Education; Credit: Mike Guidry, University of Tennessee. 16

1.6 Color-magnitude diagram of the main-sequence stars in the Large Magellanic Cloud cluster NGC 2164 observed by Hubble Space Telescope. The black and purple dots correspond to the observed main-sequence stars without and with photometric excess in the narrow Hα band. Distinct main-sequence components are indicated in the figure. Data is from Milone, Marino, Di Criscienzo et al. (2018). 17

2.1 Distribution of our binary models in the Hertzsprung-Russell diagram at six different times, as indicated. Only the visually brighter component of each binary is plotted, for all models where at least one of the two stars still undergoes core hydrogen burning. Dark blue dots correspond to models that have not yet interacted with a companion. Yellow dots indicate the products of the merger of two core hydrogen burning stars. Red dots indicate stars that have undergone rapid (thermal timescale) accretion of matter from a companion. Green dots represent stars undergoing nuclear timescale accretion at the selected time. Below the age, we indicate the approximate MS turnoff mass for the non-interacting stars. We indicate the binary produced MS features in Panel (d). 27

2.2 Evolution of both components of three example binary models in the HR diagram (left panels), with a zoom of the MS region (right panels). All three models start with the same primary model (donor star, green lines) of 15.85 $M_{\odot}$. The initial mass of the secondary stars (mass gainer, blue lines) is 12.68 $M_{\odot}$ in the top two systems, and 9.51 $M_{\odot}$ in the third. The dashed lines in the right panels represent single-star isochrones for 8, 12, and 15 Myr, and solid dots on the evolutionary tracks with the corresponding colors mark the positions of the binary components at these ages. The black star symbols mark the pre-supernova position of the primary stars. The gray triangles in the bottom panels mark the merger event. The donor stars in the top and the bottom models start mass transfer during core hydrogen burning (Case A mass transfer), and the donor in the middle model starts mass transfer after core hydrogen exhaustion (Case B mass transfer). 28

2.3 Star cluster animation to show their evolution in the Hertzsprung-Russell diagram, with colors indicating the ratio of rotation to critical rotation velocity. Evolutionary tracks of non-rotating single stars are shown as gray lines, with initial masses quoted. We evolve our cluster from an age of 0.02 Myr up to 40 Myr, corresponding to a turnoff mass of $\sim 8\,M_{\odot}$. The three example binaries shown in Fig. 2.2 are marked with special symbols, such that triangles, circles and squares indicate examples a, b, and c, respectively. The video duration is 20 s. 30

2.4 Distribution of 10,000 simulated single stellar models (colored dots) obtained from interpolating in the dense grid of the single-star evolution model of Brott et al. (2011), taking into account the initial mass function and the distribution of the initial rotation velocities derived by Dufton et al. (2013), at 15 Myr. The color represents the ratio of rotation to critical rotation velocity at an age of 15 Myr, according to the color bar to the right. Overlaid are our binary-evolution models models using grey and black dots, at the same age, with black indicating a ratio of rotation to critical rotation velocity above 0.98. 32

2.5 Age spread Δt inferred by the extended MS turnoff from the binary models as a function of cluster age t. To determine the apparent age of the extended turnoff stars in our simulated clusters, we first generate a series of single-star isochrones and then fit these isochrones via two methods, first, using the bluest MS star, and second, using the brightest MS star as to be fitted by the isochrone. Examples are shown in Panels (b) to (f), where the solid gray line describes the best-fitting isochrone for the first, and the dashed gray line describes the best-fitting isochrone for the second method. The model stars used for these fits are indicated by grey star symbols. In Panel (a) we show average of the result from the two methods for 33 different times as green symbols, where the examples from Panels (b) to (f) are marked by blue squares. The error bars represent the difference in the results from the two methods. The gray straight line represents a linear fit to the data as $\Delta t = 0.518t - 0.510$. We also show the results for two Galactic and two LMC clusters of Beasor et al. (2019). Here, we took the age derived from the lowest luminosity red supergiant as the true cluster age (Beasor et al., 2019; Britavskiy et al., 2019), and show the age discrepancy with the ages derived from the stellar luminosity function (red) and the brightest turnoff star (purple). We display our analytic estimate (Eq. 2.1) with a cyan line. 34

3.1 Color difference between the rotating and non-rotating LMC models as a function of magnitude at four different ages, which are ZAMS and the derived ages for three young LMC clusters NGC 1755 (80 Myr), NGC 2164 (100 Myr) and NGC 1866 (200Myr) (Milone, Marino, Di Criscienzo et al., 2018). The solid and dashed lines denote our MESA models and the SYCLIST models, respectively, with color indicating initial rotational rate. The formally labelled fractional critical angular velocities for the SYCLIST models in their web interface are shown in the parentheses. Shaded areas exhibit the effect of gravity darkening. Dots with error bars in the last three panels indicate the color difference between the star number distribution peaks of the observed blue and red main-sequence stars in the above-mentioned three clusters (see fig. 5 in Milone, Marino, D'Antona, Bedin, Da Costa et al. 2016 for NGC 1755, fig. 13 in Milone, Marino, Di Criscienzo et al. 2018 for NGC 2164, and fig. 6 in Milone, Marino, D'Antona, Bedin, Piotto et al. 2017 for NGC 1866 on the number distribution of the blue and red main-sequence stars, respectively). 46

3.2 Left: high-precision HST observation of the LMC cluster NGC 1818. The black and red dots are normal main-sequence stars and stars with a brightness excess in the Hα narrow band filter. The red errorbars on the left indicate one sigma photometry error at corresponding magnitudes. Right: isochrone fit for the red and blue main sequences of NGC 1818, using the SYCLIST models and our MESA models. For the SYCLIST models, we take the fit in Milone, Marino, Di Criscienzo et al. (2018), using 40 Myr isochrones of the non-rotating models and the models with labelled 90% of critical angular velocities (roughly equal to 50% of critical linear velocities under the MESA definition) to fit the observed blue and red main sequences, indicated by the solid orange line and the dashed green line, respectively. While for our MESA models, we employ 30 Myr isochrones of the non-rotating models and the models with 50% of critical linear velocities to fit the observed blue and red main sequences, denoted by the solid red line and the dashed blue line, respectively. The adopted distance modulus and reddening in each fit are listed. The small grey arrow shows how the isochrones will move if we add 0.05 to $E(B-V)$. 48

3.3 Minimum initial velocity for a star to reach a specific velocity at the end of its main-sequence evolution. The upper left and right panels show the results of our LMC metallicity models by assuming 1% of center H or 0.1% of center H left as the criterion of the terminal-age main sequence, respectively. While the lower panels correspond to the results of our SMC metallicity models under different terminal-age main sequence criteria. Colors indicate the velocity of a star at its terminal main sequence. Each dot on the lines represents one mass in our single star model grids. The top x-axis indicates the corresponding turn-off age of each mass in models with $W_{\mathrm{i}} = 0.5$. 50

3.4 Left: distribution of the main-sequence stars with spectroscopic measurement (Marino et al., 2018) in the CMD. The red main-sequence stars, blue main-sequence stars, and Be stars with Hα emission lines are designated by triangles, squares and asterisks, respectively, with color indicating the measured $v\sin i$ values. The main-sequence stars and the Hα emitters observed by the Hubble Space Telescope are shown by the black and red dots, respectively. Lower right: comparison between the model predicted average surface equatorial velocity and the spectroscopic measurements. The symbols with error bars correspond to the observations, using the same symbol types as the left panel. The solid lines and dashed lines represent the average surface equatorial velocity (times $\pi/4$ to account for a random orientation) of our MESA models at 30 Myr and the SYCLIST models at 40 Myr (the ages used in the isochrone fitting in Fig. 3.2). Color coding is the same as Fig. 3.1. Upper right: comparison between our theoretical predicted $v\sin i$ distributions (color dotted steps) and the observed $v\sin i$ of the red (solid black steps) and the blue (solid grey steps) main-sequence stars. For the theoretical predictions, we perform a Monte Carlo simulation by assuming a random orientation angle distribution and normalise the results to a total number of 15 for each initial rotation, which is similar to the number of the blue (14) and red main-sequence (16) stars with spectroscopic analysis. 51

3.5 Evolutionary tracks of 5 $M_\odot$ star models with LMC-like (left) and SMC-like (right) metallicities. The solid blue, dashed orange and dotted purple lines denote our MESA models, the SYCLIST models, and the MIST models, respectively. The adopted metallicity Z in different model sets are listed in the legend. In each model set, stellar evolutionary tracks from left to right correspond to models with increasing initial rotational velocity, with values listed in the legend. Numbers in the parentheses indicate the formally labelled fractional critical angular velocities in the SCYLIST web interface. 54

3.6 Current surface He (left) and N (right) abundances as a function of magnitude of our MESA models and the SYCLIST models shown in Fig. 3.2. The upper two x-axis show the corresponding mass derived from our MESA models and the SYCLIST models that are used to fit the red main-sequence. 56

3.7 Surface N abundances of our MESA models with LMC metallicity (left) and SMC metallicity (right) at the end of their main sequences (when 1% of H is left in the center). The x-axis shows models' initial mass, with corresponding turn-off ages showing on the top x-axis. The solid lines with different colors indicate different initial rotational rates. 56

3.8 Same as Fig. 3.1, but color differences are calculated with respect to the $W_\mathrm{i} = 0.2$ models. 57

3.9 Same as Fig. 3.1, but color differences are calculated with respect to the $W_\mathrm{i} = 0.3$ models. 58

3.10 Same as Fig. 3.2, but we only show our MESA models and use pairs of isochrones of the $W_\mathrm{i} = 0.55$ and $W_\mathrm{i} = 0.20$ models (left), and the $W_\mathrm{i} = 0.60$ and $W_\mathrm{i} = 0.30$ models (right) to fit the the observed red and blue main sequences in NGC 1818. 59

3.11 Ratio between current surface rotation velocity and the critical velocity as a function of magnitude for our our MESA models at 30 Myr (solid line) and the SYCLIST models at 40 Myr (dashed line). Colors indicate the ratio between the initial rotation velocity and the critical velocity, which is the same as Fig. 3.1.The adopted model age, distance modulus and reddening for each model set are the same as the right panel of Fig. 3.2. 60

4.1 **a**: Color-magnitude diagram of the stars (black dots) in the main-sequence region of the Large Magellanic Cloud open star cluster NGC 1755 based on high-quality HST photometry (Milone, Marino, Di Criscienzo et al., 2018). Typical errors at different magnitudes are shown with red error bars on the right. **b**: Isochrone fit for the red (major) main sequence of NGC 1755, signified by the densest stellar concentration, using stellar models with a rotation parameter of $W_{\rm i} = 0.65$ (red solid line), and identification of the blue main-sequence stars (blue circles; cf., Sec. 4.5.1). The solid blue line represents the corresponding isochrone of single star models with $W_{\rm i} = 0.35$ Here, $W_{\rm i} = v_{\rm rot,i}/v_{\rm crit,i}$ is the ratio between rotational velocity and break-up velocity at the zero-age main sequence. The red dashed line shows the positions of the equal-mass binaries in which both components have $W_{\rm i} = 0.65$. The grey dashed line indicates the zero-age main-sequence line of non-rotating stars. The adopted age, distance modulus $(m - M)_0$ and reddening $E(B - V)$ are indicated. The stars between the two thin horizontal dotted lines are used in our mass function analysis (see Sec. 4.5.3). The right y-axis shows the stellar mass according to the mass-magnitude of the fast rotating stellar models. 63

4.2 **a** and **c**: Cumulative number distribution of red main-sequence (red lines) and blue main-sequence stars (blue lines) in NGC 1755 as a function of their mass, as derived from the stellar model isochrones. Dashed lines display distributions according to the best-fitting power-law mass function. The shading reflects one sigma errors of our power-law fitting, and correspond to the error of the power law indices given in the legend. The dashed black lines show the distributions predicted by a power law with index $\gamma = -2.35$ (the traditional Salpeter IMF), assuming the same total number of stars as the corresponding number in the observed populations. We show the apparent magnitudes for given masses on the top of the figures. **b** and **d**: Residuals, i.e., difference between the colored solid and dashed lines in Panels a and c, as a function of mass, with a residual of zero indicated by the grey dashed lines. 65

4.3 Color-magnitude diagram with lines of constant merger times, overplotted on the distribution of the main-sequence stars in NGC 1755, with blue open circles indicating blue main-sequence stars. Solid lines of given colors provide the location of merger products which formed from equal-mass binaries at the indicated time (see color scale) and were then evolved to the current cluster age. The merger products have 35% critical rotation immediately after the merger event. The blue main-sequence stars above the grey horizontal dotted line are considered in the merger time estimation (see Sec. 4.5.2). The isochrone fitting to the red MS (solid red line), the zero-age main-sequence line (dashed grey), and the adopted distance modulus and reddening are the same as panel b of Fig. 4.1. 68

4.4 **a** (upper panel): Merger rate, expressed as number of merger events per Myr, as function of time, as derived for NGC 1755. This histogram is obtained by taking in to account a Gaussian probability distribution of the merger rotation over the time range displayed in Panel b for each star, and summing up their contributions in each time bin of width 1 Myr. The shaded area indicates bootstrapped 1σ estimates. **b** (bottom panel): Magnitude versus merger time of the blue main-sequence stars in NGC 1755 (blue horizontal error bars). Magnitude errors are small and are not shown here (see Fig. 4.1). The upper and lower limits of the merger time are derived from the minimum and maximum rotation velocities consistent with the color, individually for each star. A time of 60 Myr corresponds to today. 69
4.5 As panel b of Fig. 4.1, but for the Small Magellanic Cloud cluster NGC 330 and the Large Magellanic Cloud clusters NGC 1818 and NGC 2164. The adopted distance moduli and reddenings are indicated (see also Tab. 4.1). 75
4.6 Color-magnitude diagram of NGC 1755, with isochrones derived from our single star models with different initial rotational rates, as indicated in the legend. The adopted distance modulus and reddening are the same as panel b of Fig. 4.1, as are the isochrones with a rotation parameter of $W_\mathrm{i} = 0.35$ and $W_\mathrm{i} = 0.65$. The right y-axis displays the stellar masses derived from the mass-magnitude relation of the models with 65% of critical rotation initially. 76
4.7 As panel b of Fig. 4.1 but for the indicated stars clusters, where stellar models with different initial rotational velocities ($W_\mathrm{i} = 0.55$ and $W_\mathrm{i} = 0.15$) are employed to fit the red and blue main-sequences of the clusters (see legends). The adopted distance moduli and reddenings are indicated both in the figure and in Tab. 4.1. 77
4.8 Distribution of our detailed binary evolution models in the color-magnitude diagram at an age of 30 Myr. Distance modulus and reddening are assumed as panel b of Fig. 4.7. Each open symbol indicates a binary model (or a binary merger product), showing the combined magnitude and color of the two stars (or the magnitude and color of the binary merger product). Circles indicate detached binary models containing two main-sequence stars, while squares correspond to semi-detached binary models containing two main-sequence stars. Diamonds designate main-sequence merger products. Crosses correspond to binary models containing a main-sequence star and a stripped helium burning star, while pentagons denote binary models containing a main-sequence star and a compact companion. The semi-detached systems are marked in grey, while the color for other open symbols shows the current rotational velocity of either the visually brighter component in a binary model or of a binary merger product. The observed main-sequence stars and Hα emitters are overplotted with small black and purple dots, respectively. The isochrones and zero-age main-sequence line are the same as those in panel b of Fig. 4.7. 80
4.9 Contamination of the blue main-sequence from binary evolution (non-mergers) at different ages. Red and blue dots correspond to the fraction of binary models containing two main-sequence stars and binary models containing a main-sequence star and a He burning star, that will be classified as blue main-sequence stars, with respect to all the binary models, respectively. 81
4.10 As Fig. 4.2, but for the Small Magellanic Cloud cluster NGC 330. 83
4.11 As Fig. 4.2, but for the Large Magellanic Cloud cluster NGC 1818. 84

4.12 As Fig. 4.2, but for the Large Magellanic Cloud cluster NGC 2164. 84

4.13 Dependence of the derived mass function slope on the borderline between the blue and the red main-sequence stars. The borderline is obtained by shifting the isochrone for the blue main sequence by Q times the color separation between the isochrones for the blue and the red main sequences. We consider Q values between 0 and 1, in intervals of 0.2, as well as $Q = 0.5$. Different errorbars correspond to different clusters. We avoid to plot the errorbars at the same Q values to make them distinct. The black dashed line marks the slope of the Salpeter IMF $\gamma = -2.35$. 85

4.14 As Fig. 4.4, but the results are derived based on the isochrone fitting and blue main-sequence star identification shown in the top left panel of Fig. 4.7. 89

4.15 As panel b of Fig. 4.4, but for all four clusters: the Small Magellanic Cloud cluster NGC 330, and the Large Magellanic Cloud clusters NGC 1818, NGC 1755 and NGC 2164. 90

4.16 Relative rejuvenation versus post-merger stellar mass. t is the cluster age of NGC 1755, which also indicates the most recent incidence time of the merger. t_{app} is the apparent age of the merger product as measured by single star isochrones, for a fixed merger time of $t = 60$ Myr. The five lines correspond to five different mass ratios as indicated by their color (see legend). Each dot on the line corresponds to one computed binary model (see Sec. 4.5.4). 91

4.17 As Fig. 4.3, but adopting different mass ratios for the precursor binaries of the merger models. The thin solid lines correspond to the merger models rotating at 35% of their critical velocities. We only show models of mergers for a merger incidence time of 60 Myr. The isochrone for the red MS (thick solid red line), and the zero-age main-sequence line (dashed grey) are the same as in panel b of Fig. 4.1. 92

4.18 As panel b of Fig. 4.4, also showing lines for models resulting from mergers with mass ratios (q) of 0.2, 0.4, 0.6 and 0.8. 93

4.19 Fraction of the suspected triple stars or higher order multiples out of all main-sequence stars, based on the equal-mass binary lines in the CMDs (see panel b of Fig. 4.1, and Fig. 4.5), as function of absolute magnitude for stars in four young Magellanic Cloud clusters in different magnitude intervals. The horizontal width of the error bars correspond to the magnitude intervals, while the vertical error bars reflect the Poisson error. 94

5.1 Estimate of binary fraction and mass ratio distribution in NGC 330. Shadow areas in Panel A delineate the stars employed. The boundary of these areas is explained in detail in the text. The red and blue solid lines correspond to the isochrones of 30 Myr fast-rotating and slowly-rotating single stars, respectively, while the red dashed line shows the position of the equal-mass binaries comprised of two fast-rotating stars. Panel B displays the derived binary fraction, with different colors representing different fractions of initially synchronized binaries that contain two slowly-rotating stars. Dashed lines express the mean binary fractions in the whole considered magnitude range. In Panel C, we exhibit the normalized fraction of high mass ratio binaries ($q \geq 0.5$) in three bins of $0.5 \leq q < 0.65$, $0.65 \leq q < 0.8$ and $0.8 \leq q \leq 1$. Different colors correspond to different magnitude intervals. The fraction is normalized such that the mass ratio bin is 0.05, and the sum of the fraction in the considered mass ratio range is 1 in each magnitude interval. The grey dashed lines are the mean values in the three magnitude intervals. 98
5.2 The synthetic star cluster resembling NGC 330 based on merely single star models. Color indicates the number of the simulated stars in each pixel. Observed main-sequence stars with and without Hα emission are overplotted with the black and purple dots, respectively. The binary evolutionary induced Be star models are shifted upwards and rightwards by 0.2 mag to better match the position of the observed Hα emitters. We do not normalize the number of the simulated stars to the number of the observed stars to avoid producing discrete main-sequence features in the color-magnitude diagram. The solid red and blue lines correspond to the isochrones of the fast- and slowly-rotating star models, respectively. While the dashed and dotted dashed red lines show the positions of the fast-rotating equal-mass binary and triple star models, respectively. 101
5.3 Predicted and observed Be fraction in NGC 330 as a function of magnitude. The solid and dashed lines correspond to the predictions based on binary fractions of 0.6 and 1, respectively. The red lines mean that we only consider binary produced Be star models, while the blue (green) lines mean that we treat all star models with velocities larger than 75% (70%) of their critical values as Be star models, regardless of their origins. The grey bars illustrate the observed Be star fraction with the Poisson errors plotted on top. 103
5.4 Similar as Fig. 5.3, but the mass ratio threshold for the stable and unstable mass transfer is removed in the simulation. 104
5.5 The same as Fig. 5.1, but for the LMC cluster NGC 1818. 107
5.6 The same as Fig. 5.1, but for the LMC cluster NGC 1755. 108
5.7 The same as Fig. 5.1, but for the LMC cluster NGC 2164. 109
5.8 The same as Fig. 5.2, but for the synthetic cluster resembling the LMC cluster NGC 1818. 110
5.9 The same as Fig. 5.2, but for the synthetic cluster resembling the LMC cluster NGC 1755. 111
5.10 The same as Fig. 5.2, but for the synthetic cluster resembling the LMC cluster NGC 2164. 112
5.11 Same as Fig. 5.3, bur for the LMC cluster NGC 1818. 113
5.12 Same as Fig. 5.3, bur for the LMC cluster NGC 1755. We only show the theoretical predicted fractions in this figure as there is no Hα emission information for the observed stars in NGC 1755. 114
5.13 Same as Fig. 5.3, bur for the LMC cluster NGC 2164. 115

A.1 Evolutionary outcome of the SMC-metallicity-like binary models with $\log M_{1,\mathrm{i}}/M_{\odot} = 0.700$ ($M \simeq 5.0\,\mathrm{M}_{\odot}$). Colors indicate the binary evolutionary outcome, explained in detail in the text of this appendix, of a binary model with particular initial parameters. The grey crosses mean the binary models that reach the adopted lower mass loss rate limit. While the grey hatched lines represent the binary models that encounter a contact phase during their evolution. The solid black line shows the boundary between the binary models that undergo Case A and Case B mass transfer. 127
A.2 Same as Fig. A.1, but for the binary models with $\log M_{1,\mathrm{i}}/M_{\odot} = 0.750$ ($M \simeq 5.6\,\mathrm{M}_{\odot}$) (left) and $\log M_{1,\mathrm{i}}/M_{\odot} = 0.800$ ($M \simeq 6.3\,\mathrm{M}_{\odot}$) (right). 128
A.3 Same as Fig. A.1, but for the binary models with $\log M_{1,\mathrm{i}}/M_{\odot} = 0.850$ ($M \simeq 7.1\,\mathrm{M}_{\odot}$) (left) and $\log M_{1,\mathrm{i}}/M_{\odot} = 0.900$ ($M \simeq 7.9\,\mathrm{M}_{\odot}$) (right). 128
A.4 Same as Fig. A.1, but for the binary models with $\log M_{1,\mathrm{i}}/M_{\odot} = 0.950$ ($M \simeq 8.9\,\mathrm{M}_{\odot}$) (left) and $\log M_{1,\mathrm{i}}/M_{\odot} = 1.000$ ($M = 10.0\,\mathrm{M}_{\odot}$) (right). 129
A.5 Same as Fig. A.1, but for the binary models with $\log M_{1,\mathrm{i}}/M_{\odot} = 1.050$ ($M \simeq 11.2\,\mathrm{M}_{\odot}$) (left) and $\log M_{1,\mathrm{i}}/M_{\odot} = 1.100$ ($M \simeq 12.6\,\mathrm{M}_{\odot}$) (right). 129
A.6 Same as Fig. A.1, but for the binary models with $\log M_{1,\mathrm{i}}/M_{\odot} = 1.150$ ($M \simeq 14.1\,\mathrm{M}_{\odot}$) (left) and $\log M_{1,\mathrm{i}}/M_{\odot} = 1.200$ ($M \simeq 15.8\,\mathrm{M}_{\odot}$) (right). 130
A.7 Same as Fig. A.1, but for the binary models with $\log M_{1,\mathrm{i}}/M_{\odot} = 1.250$ ($M \simeq 17.8\,\mathrm{M}_{\odot}$) (left) and $\log M_{1,\mathrm{i}}/M_{\odot} = 1.300$ ($M \simeq 20.0\,\mathrm{M}_{\odot}$) (right). 130
A.8 Same as Fig. A.1, but for the binary models with $\log M_{1,\mathrm{i}}/M_{\odot} = 1.350$ ($M \simeq 22.4\,\mathrm{M}_{\odot}$) (left) and $\log M_{1,\mathrm{i}}/M_{\odot} = 1.400$ ($M \simeq 25.1\,\mathrm{M}_{\odot}$) (right). 131
A.9 Same as Fig. A.1, but for the binary models with $\log M_{1,\mathrm{i}}/M_{\odot} = 1.450$ ($M \simeq 28.2\,\mathrm{M}_{\odot}$) (left) and $\log M_{1,\mathrm{i}}/M_{\odot} = 1.500$ ($M \simeq 31.6\,\mathrm{M}_{\odot}$) (right). 131
A.10 Same as Fig. A.1, but for the binary models with $\log M_{1,\mathrm{i}}/M_{\odot} = 1.550$ ($M \simeq 35.5\,\mathrm{M}_{\odot}$) (left) and $\log M_{1,\mathrm{i}}/M_{\odot} = 1.600$ ($M \simeq 39.8\,\mathrm{M}_{\odot}$) (right). 132
A.11 Same as Fig. A.1, but for the binary models with $\log M_{1,\mathrm{i}}/M_{\odot} = 1.650$ ($M \simeq 44.7\,\mathrm{M}_{\odot}$) (left) and $\log M_{1,\mathrm{i}}/M_{\odot} = 1.700$ ($M \simeq 50.1\,\mathrm{M}_{\odot}$) (right). 132
A.12 Same as Fig. A.1, but for the binary models with $\log M_{1,\mathrm{i}}/M_{\odot} = 1.750$ ($M \simeq 56.2\,\mathrm{M}_{\odot}$) (left) and $\log M_{1,\mathrm{i}}/M_{\odot} = 1.800$ ($M \simeq 63.1\,\mathrm{M}_{\odot}$) (right). 133
A.13 Same as Fig. A.1, but for the binary models with $\log M_{1,\mathrm{i}}/M_{\odot} = 1.850$ ($M \simeq 70.8\,\mathrm{M}_{\odot}$) (left) and $\log M_{1,\mathrm{i}}/M_{\odot} = 1.900$ ($M \simeq 79.4\,\mathrm{M}_{\odot}$) (right). 133
A.14 Same as Fig. A.1, but for the binary models with $\log M_{1,\mathrm{i}}/M_{\odot} = 1.950$ ($M \simeq 89.1\,\mathrm{M}_{\odot}$) (left) and $\log M_{1,\mathrm{i}}/M_{\odot} = 2.000$ ($M = 100\,\mathrm{M}_{\odot}$) (right). 134

List of Tables

3.1 The adopted fitting models and the corresponding parameters for the LMC cluster NGC 1818. 48

4.1 Basic information of the studied clusters and the parameters adopted in fitting the observed red and blue main sequences with our single star models. 74
4.2 Slopes γ and uncertainties of the mass functions derived for the red and blue main-sequence stars in four clusters. The last column shows the number ratio between the blue main-sequence stars and all stars. 83

Acknowledgements

Finally, I have finished this thesis, which is a landmark in my life. The journey to this achievement is long and challenging, but is fruitful. There are so many people I would like to thank from the deep of my heart, without whom all my accomplishments are impossible.

The first one I would like to thank is Norbert, who gave me the opportunity to carry out my PhD study in Bonn and provided me with all the necessary supports. I have learnt from him innumerable things, in terms of both science and attitude to work. His passion for science leaves a deep impression on me. He keeps working hard and is always excited by intriguing topics and ideas. From the science point, he is undoubtedly an expert in massive stars, and is always helpful when I am stuck with my projects. He is trustworthy because of his strictness in science, which really touches and impacts me. Another thing I have learnt from him is how to think like a scientist, which is vital to my future career. Apart from science, he also touches me with his patience and his tolerance. I have encountered many difficulties and failures during my research. I indeed felt depressed at those times, but I never feel entirely desperate, because I know he is always there to help and to support me. His door is always open to those who have whatever problems. I never fear difficulties and darkness because of him. Thanks, Norbert! Studying with you is one of the luckiest things in my life. I firmly believe that all the knowledge and characters I have learnt from you are invaluable and will benefit my career and my life.

I would then like to thank our group members, in particular Abel and Ben, who have close cooperation with me. I have also learnt a lot from discussions with other group members, Götz, Jonathan, Luca, Koushik, Christoph, Xiao-Tian, Harim, Athira, and the previous members in the stellar group, Thomas, Zheng-Wei, Martin, Nathan, David, Daniel, John, Patrick, Koh, and in particular Pablo, who laid the foundation of my research projects. I really enjoy the interesting and valuable discussions with our group members. I would also like to thank Elisabeth and Sabine, who have done all the necessary things to allow me to study with ease in Bonn.

Then I want to give my gratefulness to Hugues and Julia in Leuven, who have made enormous contributions to my research. I appreciate Hugues's help in my postdoctoral application. I would also like to thank Danny, Antonino, Alex, Selma, Norberto and Lee for their help and constructive suggestions in my research projects. I could not have done my work without their assistance.

I deeply thank my previous supervisor, Xiang-Dong Li, and many of my previous teachers, who have taught me how to study, think and live. At last, it is time to thank my parents and my friends who are always on my side and are there to help when I need them. Thanks to Dong-Hong Wu, Bing Liu, Shuang Wang and so on. I want to say I miss you so much. I would like to especially thank and congratulate my old friend Yu-Xin Lin, who has just obtained her PhD degree in Bonn. Thank you for accompanying me these years, encouraging me and bringing me so much happiness. Words cannot explain my thankfulness to the people who have provided me with their favour. The precious memory with all of you is a treasure in my life.

List of Publications

Published in refereed journals

- **Wang, C.**, Langer, N., Schootemeijer, A. et al. 2020, ApJ, 888, L12:
  "Effects of Close Binary Evolution on the Main-sequence Morphology of Young Star Clusters"
- Hastings, B., Langer, N., **Wang, C.**, et al. 2021, A&A, 653, A144:
  "A stringent upper limit on Be star fractions produced by binary interaction"
- Bodensteiner, J., Sana, H., **Wang, C.**, et al. 2021, A&A, 652, A70:
  "The young massive SMC cluster NGC 330 seen by MUSE. II. Multiplicity properties of the massive-star population"
- Hastings, B., **Wang, C.**, Langer, N. 2020, A&A, 633, 165:
  "The single star path to Be stars"
- Langer, N., Schürmann, C., ...**Wang, C.** et al. 2020, A&A, 638, 39:
  "Properties of OB star-black hole systems derived from detailed binary evolution models"
- Schootemeijer, A., Langer, N., Grin, N., **Wang, C.** 2019, A&A, 625, 132:
  "Constraining mixing in massive stars in the Small Magellanic Cloud"

Submitted to refereed journals

- **Wang, C.**, Langer, N., Schootemeijer, A. et al., submitted to Nature Astronomy:
  "Stellar mergers as the origin of the blue main-sequence band in young star clusters"
- Antoniadis, J., Aguilera-Dena, D. R., ... **Wang, C.** et al. submitted to A &A Letter:
  "Explodability fluctuations of massive stellar cores enable asymmetric compact object mergers like GW190814"

Published in conference proceedings

Wang, C., Langer, N., Gräfener, G. et al. 2019, IAUS, 346, 78:
"Formation of the SMC WO+O binary AB8"

Curriculum Vitae

Personal Details

Name	Chen Wang
Date of Birth	27.09.1990
Email	cwang@astro.uni-bonn.de

Education

2009–2013	BSc in Astronomy, School of Astronomy and Space Science, Nanjing University, China.
2013–2016	MSc in Astrophysics, School of Astronomy and Space Science, Nanjing University, China.
2016–2021	PhD in Astrophysics, Argelander Institute for Astronomy, Universität Bonn, Germany.

Teaching Experiences

2019–2020	Teaching assistant for the course of “Stellar Structure and Evolution", Universität Bonn, Germany.